Structure and Reactivity study of beta Zeolite and Al metal clusters using Density Functional Theory

Thesis submitted to the

University of Pune

for the Degree of

Doctor of Philosophy in Chemistry

By

Bhakti S. Kulkarni

Physical Chemistry Division
National Chemical Laboratory
Pune – 411 008

December 2010

Declaration

I, Bhakti S. Kulkarni, hereby declare that the work incorporated in this thesis entitled,

Structure and Reactivity study of beta Zeolite and Al metal clusters

using Density Functional Theory

submitted by me for the degree of Doctor of Philosophy to the University of Pune is the record of the work I have carried out at the Physical Chemistry Division, National Chemical Laboratory, Pune – 411 008 from April 2008 to December 2010 under the supervision of Dr. Sourav Pal, is original and has not formed the basis of award of any degree or diploma. Such material as has been obtained from other sources has been duly acknowledged in this thesis.

Date: _____

Bhakti S. Kulkarni
Physical Chemistry Division,
National Chemical Laboratory,
Pune – 411 008

Certificate

CERTIFIED THAT the work done in the thesis entitled,

Structure and Reactivity study of beta Zeolite and Al metal clusters

using Density Functional Theory

submitted by **Bhakti S. Kulkarni** for the degree of Doctor of Philosophy to the University of Pune, was carried out by the candidate under my supervision in the Physical Chemistry Division, National Chemical Laboratory, Pune - 411 008, India. Such material as has been obtained from other sources has been duly acknowledged in the thesis.

Date:

_____ _____

Dr. Sailaja Krishnamurty
(Co-advisor)

CECRI, Karaikudi

Prof. Dr. Sourav Pal
(Research Guide)

Physical Chemistry Division,
National Chemical Laboratory,
Pune – 411 008

To My Family and

Dear ones

Acknowledgments

"Would you tell me, please, which way I ought to go from here?"
"That depends a good deal on where you want to get to," said the Cat.
"I don't much care where--" said Alice.
"Then it doesn't matter which way you go," said the Cat.
"--so long as I get SOMEWHERE," Alice added as an explanation.
"Oh, you're sure to do that," said the Cat, "if you only walk long enough."
-Lewis Caroll (Alice in Wonderland)

Whenever I read this dialogue from a famous fairy tale, it always reminds me words of my Supervisor, Dr. Sourav Pal, who motivated us in the field of scientific research by saying, "PhD is a mile stone and research is a life long journey." It is my great pleasure to thank my research guide, Dr. Pal for giving me opportunity to join his lab in NCL and a freedom given to work on my favorite topic. He has been a fantastic adviser, who taught me how to do research in an individualistic way. I would especially like to mention our classes, where he introduce us and make understand basic and advance knowledge of quantum chemistry without which this work would not have been possible. I really appreciate his way of imagining things and his good sense of humor.

I owe a special debt to my co–supervisor Dr. Sailaja Krishnamurty for introducing me to the field of *ab* initio molecular dynamics. I thank Sailaja for her sincere and continuous support during the last year of my degree, especially the Al–cluster study. It has been really fun to learn shell scripting under her guidance. I must acknowledge Sailaja for the enriching discussions which helped improve the quality of my work on many an occasion. I will always remember a conversation during which she said that science should be a passion and not a profession.

I am obliged to Director, NCL for providing me the infrastructure to carry out the work presented in this thesis. I am grateful to Indo-French project funding for my earlier Fellowship and also CSIR for awarding me the direct Senior Research Fellowship. I thank Dr. Annick Goursot for the useful discussions and advice on the work of zeolite modeling. I am thankful to DST for providing the timely financial support to participate in MCBR-II, Germany. I cannot forget the Dept. of Chemistry, where I took my first lessons in the field of research. I acknowledge Prof. Gadre and Dr. Gejji for acquainting me to the field of computational chemistry.

The present thesis work would have been difficult without the association of my labmates in NCL. My thanks goes to Akhilesh and Prashant, for helping me with the basic computational chemistry during the initial phase of my research. Special thanks goes to Sophy, Saikat and Nayana, for making me very comfortable in the group and treating me more as a friend than as a junior. I would miss the homely company of Sophy at many occasions. I am particularly grateful to Sharan for teaching me how to use VASP and for his tremendous help during the initial phase of

my Ph.D. In the last year of my Ph.D., I also had the fortune of interacting with the new scientists of our thriving group: Dr. Kumar Vanka, Dr. Neelanjana Sengupta, and Dr. Sudip Roy. I have had great fun interacting with my batchmates Arijit, Subrata, Lalitha, Rahul, Tuhina, Ideh, Deepti, Sumantra, and Sapna. I must specially mention Himadri for being a competent System Administrator which kept the cluster running. I cannot do without thanking Shobhana for her patient listening, sweet cheering, and for being a wonderful friend. I should also acknowledge our youngest team members Mudit, Jitendra, Sayali, Debarati, Shantanu, Kamalika, Anagha and Divya for their camaraderie.

I am very lucky to get kind and unwavering support from my both families. My parents made tremendous sacrifices to ensure that I had good education. I thank u Mom and Dad for your seamless patience, words of wisdom, and the independence that you gave. I also acknowledge my grandfather for his encouragement to complete this higher education. I thank my elder sisters Sulakshana and Adit for their sincere concern and good counsel. Gratefully, I thank my husband, Sharang, for understanding the importance that this Ph.D. holds for me, for motivating me in this crucial period of degree, for appreciating my aspirations, and for his unconditional encouragement and adjustments. I dedicate this thesis to Mom, Dad and Sharang. For this and more, I am forever in their debt. Sharang, you and our baby, have been my inspiration in whatever I have done and achieved till now.

Date: _____

Bhakti S. Kulkarni

Contents

	List of abbreviations	i
	List of figures	iii
	List of tables	vi
	List of publications	viii
	Abstract	x
1	**Introduction**	**1**
1.1	General Overview	3
1.1.1	Catalysts and reaction energetics	3
1.1.2	Types of catalysts	4
1.1.3	Applications, Advantages and Disadvantages	6
1.1.4	Motivation for Theoretical Investigation	10
1.2	**Metal Oxide Framework: Zeolite**	12
1.2.1	General Features	12
1.2.2	Applications and Advantages	14
1.2.3	Enhancement of catalyst by doping: Recent studies and advances	15
1.2.4	Characterization: Experiment and Theory	17
1.3	**Metal Clusters**	20
1.3.1	General Features	20
1.3.2	Enhancement of catalyst by melting: Recent studies and advances	23
1.3.3	Characterization: Experiment and Theory	27
1.4	**Motivation and outline of the thesis**	31
1.5	References	32

2	**Theoretical Methods and Computational Aspects**	**43**
2.1	**The many-body problem**	44
2.1.1	Born-Oppenheimer approximation	44
2.1.2	Hartree approximation	45
2.1.3	Hartree-Fock approximation	46
2.1.4	Beyond Hartree-Fock	48
2.2	**Density functional theory**	48
2.2.1	Thomas-Fermi theory	48
2.2.2	Hohenberg-Kohn theorems	49
2.2.3	Kohn-Sham equations	51
2.24	Exchange-correlation functionals	53
2.3	**Molecular dynamics**	54
2.3.1	Equations of motions	55
2.3.2	Numerical integration	56
2.4	***Ab initio* molecular dynamics**	57
2.4.1	Born-Oppenheimer molecular dynamics	57
2.4.2	Car-Parrinello molecular dynamics	60
2.5	**Plane wave-pseudopotential method**	62
2.5.1	Bloch’s theorem and plane wave basis	62
2.5.2	Pseudopotentials	63
2.6	**Interpretation of Data using analysis tools**	65
2.6.1	Optimization Techniques	65
2.6.2	Structure and Bonding	66

2.6.3	Conceptual DFT: Reactivity Descriptors	69
2.6.4	MD analysis tool	73
2.7	References	75
3	**Properties of Sn-BEA Vs. Ti-BEA**	**78**
3.1	Introduction	78
3.2	Methodology and Computational Details	82
3.3	Results and Discussion	86
3.3.1	Structure of Sn-BEA and Ti-BEA	86
3.3.2	Energetics of Sn-BEA and Ti-BEA	88
3.3.3	Lewis Acidity of Sn-BEA and Ti-BEA	90
3.3.4	Hydrophilicity of Sn-BEA and Ti-BEA	92
3.4	Conclusions	95
3.5	References	97
4	**Role of plane wave cut-off in structural and energy convergence**	**101**
4.1	Introduction	101
4.2	Simulation Model	104
4.3	Computational Details	106
4.4	Results and Discussion	108
4.5	Conclusions	116
4.6	References	117
5	**Probing Lewis Acidity of Sn- and Ti-BEA using**	**120**

	industrially important ligands	
5.1	Introduction	121
5.2	Simulation Model	123
5.3	Computational Details	125
5.4	Results and Discussion	126
5.4 (a)	Structural deformation of T-BEA framework upon ligand adsorption	126
5.4 (b)	Energetics of interacting T-BEA and Ligands (L)	131
5.4 (c)	Reactivity of T-BEA towards Ligands (L)	135
5.5	Conclusions	139
5.6	References	141
6	**Role of Structure and Bonding of Al Clusters in the adsorption of N_2**	**145**
6.1	Introduction	145
6.2	Computational Details	148
6.3	Results and Discussion	150
6.3(a)	Size dependence of the reactivity: Ground State Geometries of Al clusters and their Interaction with N_2	150
6.3(b)	Influence of melting on the reactivity: High Energy Al_{13} cluster conformations and their Interaction with N_2	162
6.3(c)	Activation Barriers for interactive Al_{13}--N_2 complexes	170
6.4	Conclusion and Scope	171
6.5	References	173

7	**Thermodynamic study describing chemisorption of N_2**	**176**
7.1	Introduction and methodology	176
7.2	Results and Discussion	178
7.2(a)	Ionic motion of Al clusters	178
7.2(b)	Molecular dynamic simulation of Al_{13}--N_2 complexes at RT	181
7.3	Conclusion and Scope	185

List of Abbreviations

The following abbreviations, in alphabetical order, that have been used in this thesis:

AIMD	*Ab initio* molecular dynamics
BEA	Beta
BOMD	Born-Oppenheimer molecular dynamics
BZ	Brillouin zone
CC	Coupled cluster
CI	Configuration interaction
CPMD	Car-Parrinello molecular dynamics
DFT	Density functional theory
ELF	Electron Localization Function
FF	Fukui Function
FMO	Frontier Molecular Orbitals
GAMESS	General Atomic Molecular and Electronic Structural System
GGA	Generalized gradient approximation
HF	Hartree-Fock
HK	Hohenberg-Kohn
HOMO	Highest Occupied Molecular Orbital
IR	Infra Red
KS	Kohn-Sham
LDA	Local density approximation
LUMO	Lowest Occupied Molecular Orbital
MC	Monte Carlo
MD	Molecular dynamics
MOT	Molecular Orbital Theory
MP	Møller-Plesset
MSD	Mean square Displacements
PW91	Perdew and Wang 1991
PP	Pseudopotentional

RMS-BLF	Root mean square-Bond length fluctuations
USPP	Ultra-soft pseudopotential
VASP	Vienna *ab initio* simulations package
XRD	X-Ray Diffraction

List of Figures

Figure 1.1	Energy profiles highlighting role played by catalyst	3
Figure 1.2	Phase distinguish as in Hetero- and Homogeneous catalyst	4
Figure 1.3	NH_3 synthesis over Heterogeneous Metal surface catalyst	5
Figure 1.4	Homogeneous Acid catalysts	6
Figure 1.5	Different classic Catalysts	7
Figure 1.6	The three structural units of a zeolite. (a) Primary, (b) Secondary and (c) Unit Cell	13
Figure 1.7	Extended structure of a zeolite (MFI) consisting of several unit cells	14
Figure 1.8	Growth pattern observed in Au clusters	21
Figure 2.1	Flowchart displaying the steps involved in the Born-Oppenheimer Molecular Dynamics algorithm	59
Figure 2.2	A schematic diagram of an atomic all-electronic wavefunction and the corresponding atomic pseudo wavefunction	64
Figure 2.3	Illustrative ELF	69
Figure 3.1	Crystallographically defined 9 T sites of BEA. The gray spheres represent the Si sites.	83
Figure 3.2	The cluster models cut from the optimized periodic Sn and Ti-BEA systems.	85
Figure 4.1	Optimized T-BEA unit cell with interaction of H_2O molecule at T1 site.	105
Figure 4.2	**(a)** Total energy of Sn-BEA + H_2O as a function of PW	107

	cut-off at default FFT grid. **(b)** Interaction energy of Ti-BEA and H_2O as a function of PW cut-off at default FFT grid.	
Figure 4.3	Ti-BEA nuclear–nuclear repulsion energy (Ewald energy) (eV) as a functionof PW cut-off (eV).	110
Figure 4.4	H_2O total energy (eV) as a function of PW cut-off (eV).	111
Figure 4.5	**(a)** Ti-BEA + H_2O total energy (eV) as a function of PW cut-off (eV). **(b)** Sn-BEA total energy (eV) as a function of PW cut-off (eV).	112
Figure 4.6	**(a)** Ti-BEA and H_2O Interaction energy (eV) as a function of PW cut-off (eV). **(b)** Sn-BEA and H_2O Interaction energy (eV) as a function of PW cut-off (eV).	113
Figure 4.7	**(a)** HOMO and **(b)** LUMO of Ti-BEA+H_2O	114
Figure 4.8	ELF at 0.65 of Sn-BEA+H_2O	116
Figure 5.1	The Crystallographically defined BEA unit cell with Ti at T1 site.	124
Figure 5.2	Optimized T-BEA/NH_3	125
Figure 5.3	Optimized T-BEA/CH_3OH	125
Figure 5.4	Optimized T-BEA/H_2O showing axial (ax) and equatorial (eq) splitting of TO_4 unit	129
Figure 5.5a	Sn-BEA--H_2O: SA-SB, covalent interaction	138
Figure 5.5b	Sn-BEA--CH_3CN: SA-HB, weakly electrostatic interaction	138
Figure 5.5c	Ti-BEA--NH_3: HA-SB, weakly electrostatic interaction	138
Figure 5.5d	Ti-BEA--CH_3CN: HA-HB, ionic interaction	138
Figure 6.1	Al_2 and its N_2 interaction from ELF and FMO	151
Figure 6.2	Al_3 and its N_2 interaction from ELF and FMO	153
Figure 6.3a	Al_{13} (I_h) and its N_2 interaction from ELF and FMO	154
Figure 6.3b	Al_{13} (I_h) another perspective	155
Figure 6.3b	Al_{13} (I_h--N_2) another perspective	155
Figure 6.4	Al_{30} and its N_2 interaction from ELF and FMO	159
Figure 6.5	Al_{100} and its N_2 interaction from ELF and FMO	161
Figure 6.6	Al_{13} (D_h) and its N_2 interaction from ELF and FMO	163

Figure 6.7	Al_{13} high energy configurations and its N_2 interaction from ELF and FMO	168
Figure 6.8	Interaction energy as a function of cluster size	172
Figure 7.1	Two modes of N_2 interactions	178
Figure 7.2	MSD curves for Al_{13} cluster	179
Figure 7.3	MSD curves for Al_{100} cluster	180
Figure 7.4	Characteristic Bond Length Fluctuations	183-184

List of Tables

Table 1.1	Examples of major industrial processes using heterogeneous catalysis	9
Table 1.2	Metal Cluster Catalyzed reactions	26
Table 3.1	Optimized Structural Parameters of Sn-BEA.	87
Table 3.2	Optimized Structural Parameters of Ti-BEA.	87
Table 3.3	Cohesive Energies of All the 9 T Sites of Sn-BEA and Ti-BEA	89
Table 3.4	Energies of the HOMO, LUMO and HOMO-LUMO Gaps of the 9 T Sites of Sn-BEA and Ti-BEA	90
Table 3.5	Mulliken and Lowdin Charges of Sn and Ti Atoms in their Respective Configurations	92
Table 3.6	Condensed Electrophilic (f^+) and Nucleophilic (f^-) FFs of the 9 T Sites of Sn-BEA and Ti-BEA	93
Table 3.7	Structural Parameters and Binding Energies (BEs) of Sn-BEA and Ti-BEA in the Presence of H_2O	94
Table 4.1	Convergence of various geometrical parameters of T-BEA+H_2O as a function of plane wave cut-off.	109
Table 5.1	Optimized structural parameters of Sn-BEA and Ti-BEA	127
Table 5.2	Optimized structural parameters of T-BEA--L adducts	128
Table 5.3	HOMO, LUMO energies of Lewis bases and T-BEA--L adducts	132
Table 5.4	Chemical Potential, Hardness and Philicity descriptors for L and T-BEA--L	137
Table 6.1	Structural and Electronic Properties of Al_{13} (I_h) and its N_2 Complex	156

Table 6.2	Structural and Electronic Properties of Al_{30} and its N_2 Complex	160
Table 6.3	Structural and Electronic Properties of Al_{13} (D_h) and its N_2 Complex	164
Table 6.4	Electronic Properties of H1, H2 (Al_{13}) and its N_2 Complex	169

List of Publications

This thesis is based on the following papers, which are referred to in the text by their Roman numerals:

I. A comparative study of structural, acidic and hydrophobic properties of Sn-BEA with Ti-BEA using periodic density functional theory, Sharan Shetty, Bhakti. S. Kulkarni, D.G. Kanhere, Annick Goursot and Sourav Pal, J. Phys. Chem. B 112, **2008,** 2573-2579.

II. Influence of plane wave cut-off on structural and electronic properties in Sn-BEA and Ti-BEA zeolite water molecule interaction, Bhakti S. Kulkarni, Sailaja Krishnamurty, Sourav Pal, Chemical Physics Letters, 484, Issues 4-6, **2010**, 374-379.

III. Probing Lewis acidity and reactivity of Sn- and Ti-beta zeolite using industrially important moieties: A periodic density functional study, Bhakti S. Kulkarni, Sailaja Krishnamurty, Sourav Pal, J. Mol. Catal. A: Chemical, 329, Issues 1-2, **2010**, 36-43.

Iς. Density Functional Theory Based Understanding on the Reactivity of N_2 Molecule on Al_n (n = 2, 3, 13, 30 and 100) Clusters, Bhakti S. Kulkarni, Sailaja Krishnamurty, Sourav Pal, manuscript under review.

ς. Thermodynamic study describing chemisorption of N_2 on Al metal clusters, Bhakti S. Kulkarni, Sailaja Krishnamurty, Sourav Pal, manuscript under preparations.

The following papers are co-authored by me but are not included in this thesis:

- Reactivity descriptors and electron density analysis for ligand chemistry: A case study of 2,2'-bipyridine and its analogues, Bhakti. S. Kulkarni, Akhilesh Tanwar, Sourav Pal, J. Chem. Sci. 119, **2007**, 489–499.
- Bond length variations: Electron number profiles and transferable atomic sizes, Parthasarathy Ganguly, Bhakti S. Kulkarni, Sourav Pal, J. Mol. Str., 936, Issues 1-3, **2009**, 1-8.

Abstract

The development of new catalysts is a key objective for a cleaner and sustainable chemistry. Two important families of catalysts coexist nowadays. Metal clusters with variable number of atoms and zeolites with a flexible framework, reaching high activity and selectivity for a large class of chemical reactions, finely tunable by phase transitions and doping, respectively. The structure of the catalyst itself can be studied by a variety of spectroscopic and crystallographic techniques. The surface of the solid presents a variety of sites, including defects such as steps with variable coordination for the active element. Moreover, the nature of the surface can change upon the reaction conditions, and its structure is more difficult to characterize from microscopy and spectroscopy. The determination of the active site is hence a challenge, and most probably several possible *ab initio* methods based on Quantum-chemistry and thermodynamics are helpful tool to extract necessary information on them.

Thus, the main motivation of this thesis is to use a computational approach to model two classes of catalytic materials, zeolites and metal clusters, to understand the reactivity related to their unique structural features. In the thesis, we will be specifically studying beta zeolite doped with tetravalent Sn and Ti atoms. The Sn- and/or Ti-BEA presents new promising mechanisms in various oxidation and reduction reactions enhancing industrial applications, yet their several structural and electronic properties are inaccessible through experiments. Motivated by this problem, we try to resolve some of the loop holes of the structural differences and connect it to reactivity. To the other end, in the thesis, we have performed DFT based calculations to study theoretically the ground state structure, electronic structure and chemical bonding of Al clusters with N_2 molecule. This study is extrapolated to thermodynamics using AIMD technique to understand the chemisorption of N_2 on Al clusters.

The organization of the thesis will be as follows:

Chapter 1 Introduction

In Chapter 1 we will begin by giving a brief introduction to general definition of catalyst and general terms related to it, such as energetics, type of catalysts, their advantages and applications. Thereafter in next section, we will focus on the zeolites, describing the enhancement of their catalytic properties by doping. This will be followed by providing a brief discussion on the recent experimental and theoretical research advances. In last section, we describe the peculiar surprises of metal cluster resulting in their stability and size sensitivity. Similarly, the enhancement of metal clusters by melting is discussed with several examples in the proceeding section. In addition at the end we will review selected metal cluster reports including Al clusters. We will end the chapter by describing the motivation behind the research carried out and by presenting an outline of the thesis.

Chapter 2 Theoretical background

In Chapter 2 we will present an outline of the theoretical framework behind the methodology used in the most part of the work presented in the thesis. We will begin with a brief introduction to the many-body problem by talking about the Hartree approximation, the Hartree-Fock (HF) approximation, and the methods which go beyond HF. This will be followed by a discussion on the use of density functional theory (DFT) as an alternative route for performing such calculations. Next a description of the concepts of molecular dynamics and *ab initio* molecular dynamics will be given. We will also explain and compare the ideas and algorithms behind Born-Oppenheimer molecular dynamics and Car-Parrinello molecular dynamics. Lastly, we will illuminate on the implementation of the plane wave-pseudopotential molecular dynamics method in the program package of VASP for performing solid-state calculations. Several descriptors, FF, ELF, FMO, RMS and MSD used to discuss the reactivity are also shortly elaborated.

Chapter 3 Properties of Sn-BEA Vs. Ti-BEA

Periodic density functional theory has been employed to characterize the differences in the structural, Lewis acidic and hydrophilic properties of Sn-BEA and Ti-BEA. We show that the incorporation of Sn increases the Lewis acidity of BEA compared to the incorporation of Ti. Hence, the present work gives insight into the role of Sn in increasing the efficiency of the oxidation reactions. The results also justify that the percentage of Sn substituted in BEA is less than Ti. The structural analysis shows that the first coordination shell of Sn is larger than that of Ti. However, the second coordination of both sites remains the same. The water adsorption properties of these substituted zeolites are quantified. Moreover, we explain the higher Lewis acidity of Sn than the Ti site on the basis of the Fukui functions and charge population analysis.

Chapter 4 Role of plane wave cut-off in structural and energy convergence

Periodic systems are best described by the pseudo-potential methods. However, the accuracy of its description depends on the cut-off of plane wave basis. This is much more critical in the case of weak interactions, where a clear understanding on the influence of plane wave cut-off on the structural and electronic properties is not readily available in the literature. In the present work, we have taken a metal substituted beta zeolite–H_2O complex for understanding this objective. Our studies show that while a lower cut-off of 500 eV is sufficient for the convergence of the structural parameters, description of energy-dependent properties necessitates a high cut-off value.

Chapter 5 Probing Lewis Acidity of Sn- and Ti-BEA using industrially important ligands

The Lewis acidic nature and reactivity of two industrially important catalysts, viz., Sn and Ti substituted beta zeolite (T-BEA) are analyzed using a unique combination of structural parameters, energetics and reactivity descriptors. To achieve this purpose, we adsorb the industrially important moieties (L) namely NH_3, H_2O, CH_3OH, CH_3CN on the active sites of T-BEA. The analysis of the structural properties of these complexes reveals that TO_4 shows typical characteristic splitting 120°/90°, close to bipyramidal geometry as compared to tetrahedral symmetry observed in the bare T-BEA. This is associated with small variations in the framework bond lengths ($\geq$ 0.08 Å) and a substantially large variation of bond angles ($\leq$ 10˚) in all the ligand-zeolite complexes. Further in both cases of Sn and Ti substituted beta zeolite, ligand interacts at optimum inter-atomic bond distance. Our interaction energies show that adsorption of all ligand moieties is stronger at Sn center than that of Ti. In general, the order of stability of the different T-BEA adducts is NH_3>H_2O>CH_3OH>CH_3CN. The ligand interaction is associated with the corresponding bond elongation and bond reduction of the adsorbed molecules on catalyst active site, which can be taken as measure of red or blue shifted frequencies. Finally, the global descriptors of reactivity justify the fact that soft acid, Sn-BEA, interacts strongly with soft bases following the Pearson's HSAB principle. However, hard acid, Ti-BEA interacts with soft bases to form a stable Lewis adduct. Furthermore, the HOMO-LUMO gap of all Sn-BEA--L adducts is lower than that of Ti-BEA--L adducts indicating to its higher Lewis acidic nature compared to Ti-BEA.

Chapter 6 Role of Structure and Bonding of Al Clusters in the adsorption of N_2

Reactivity of Aluminum Clusters has been found to exhibit size sensitive variations. This work is motivated by a recent report predicting higher reactivity of melted Aluminum clusters towards the N_2 molecule as compared to the non-melted Al clusters. We attempt to understand the underlying electronic and structural factors influencing the adsorption of N_2 molecule (a prerequisite for the reactivity) on ground state geometry (a non-melted structure) of various Al clusters. The results show that the adsorption energy is of the order of 8-10 kcal/mol and does not vary with respect to the cluster size and the electronic properties of the ground state geometry. The structural and electronic properties of high energy conformations of Al clusters (a

melted cluster) are also analyzed to explain their higher reactivity towards N_2 molecule.

Chapter 7 Thermodynamic study describing chemisorption of N_2

In this chapter, we address the dynamic interactions of N_2 with Al_{13} clusters at Room Temperature (RT). For this study, we obtain the high energy conformation (melted structures) of Al_{13} cluster from the high temperature simulations. The phase transition of the Al_{13} clusters over all temperatures is verified using MSD and RMS-BLF descriptors. Similarly, we address the phase transition of Al_{100} cluster over three different temperatures. The results clearly show that the melted structure forms Al_n--N_2 cluster with more ease compared to non-melted structure. In addition, finite temperature simulation suggests the multiple Al-N bond formation which is not clearly seen from static calculations [chapter 6]. For understanding the interaction strength of N_2, This outcome is supported with various structural properties such as average bond lengths and average interaction energies.

CHAPTER 1

Introduction

*"Everything's got a **moral**, if only you can find it."*

-Lewis Caroll (Alice in Wonderland)

In the 20th century, advances in chemical sciences changed our lives. It has shaped our modern technological society by supplying us with energy, medicines, crop protection, foodstuffs, and new materials worldwide. Unfortunately, even though chemistry is the science with the highest impact on our everyday lives, chemicals and the chemical industry have a poor public image. This is partly due to hazardous and polluting nature of traditional chemical processes. Today, the escalating costs of petrochemicals, and the increasing energy and raw material demands in Asian emerging markets, are forcing a change. Two popular terms associated with this change are sustainability, or sustainable development. A sustainable society is one that meets the needs of the current generation without sacrificing the ability to meet the needs of future generations. Sustainable development can be reached using the strategic goals, the practical approaches, and the operational and monitoring tools. For example, if you use less or no solvent, and replace stoichiometric reagents with

catalytic cycles, reactor space–time yields go up [1].

To achieve this objective, research into catalytic materials is developing rapidly, so as to elucidate their fundamental properties for synthesizing specifically-tailored materials for various applications. In addition, finding new applications such as providing environment friendly process using the existing knowledge about these important and remarkable materials is a ongoing research problem. As pressure increases on the World's finite and dwindling supplies of hydrocarbons, obtained mainly from crude oil developments, the use of **zeolites** and **metal clusters** as catalysts to render known **hydrocarbon cracking** and **oxidation chemistry** is more efficient. Designing such materials requires invention, experiment-ation, and developing an **understanding** of the **fundamentals** of their **structure, bonding and reactivity**. Advances in theoretical methods are likely to play an increasing role in predicting the features and synthetic viability of modified and novel catalyst structures.

In this chapter we begin by giving a brief introduction to definition of catalyst, type of catalysts and the general overview on the use of these materials as the novel catalyst including their advantages and applications, in Section 1.1. The detail discussion associated with zeolite and recent advances in their application is done in Section 1.2. In Section 1.3 we discuss a selected interesting metal cluster materials and their catalytic potential. We end the chapter by describing the motivation behind the research carried out herein and by presenting an outline of this thesis in Section 1.4.

1.1 General Overview

Catalyst is a substance that can cause a change in the rate of a chemical reaction without itself being consumed in the reaction; the changing of the reaction rate by use of a catalyst is called catalysis. Substances which increase the rate of reaction are called positive catalysts or, simply, catalysts, while substances which decrease the rate of reaction are called negative catalysts or inhibitors.

1.1.1 Catalysts and reaction energetics

One of the high impact industrial applications of catalyst is lowering the hard conditions of reaction processes. Catalysts enable reactions to occur much faster or at lower temperatures by providing an alternative pathway of lower activation energy for a reaction. This is done by inducing some changes in reactants while the catalyst remains chemically unchanged. This can be observed on a Boltzmann distribution and energy profile diagram, Figure 1.1.

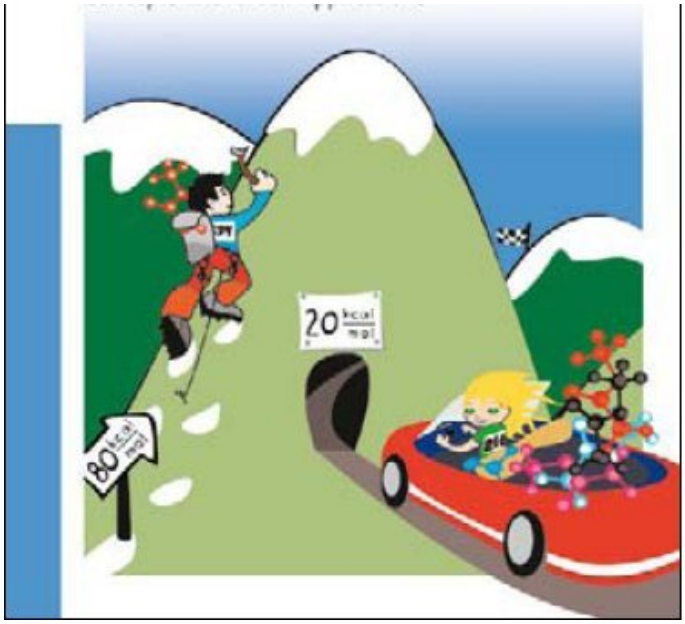

Figure 1.1: Energy profiles highlighting role played by catalyst

In short, catalysts reduce the amount of energy needed to start and complete a

chemical reaction. Molecules that would not have had the energy to react or have low energies so that they probably would have taken a long time to react are able to react in the presence of a catalyst. As the catalyst is not consumed in the process, each catalyst molecule can participate in many consecutive cycles, so we need only a small amount of catalyst relative to the substrate. The substrate/catalyst ratio reflects the catalyst's efficiency, which is measured in terms of turnover number.

1.1.2 Types of catalysts

Catalysts are divided into two main types - heterogeneous and homogeneous. Heterogeneous catalysts are present in a different phase from that of the reactants (e.g. a solid catalyst in a liquid reaction mixture), whereas homogenous catalysts are in the same phase (e.g. a dissolved catalyst in a liquid reaction mixture). This difference is clearly brought out in Figure 1.2.

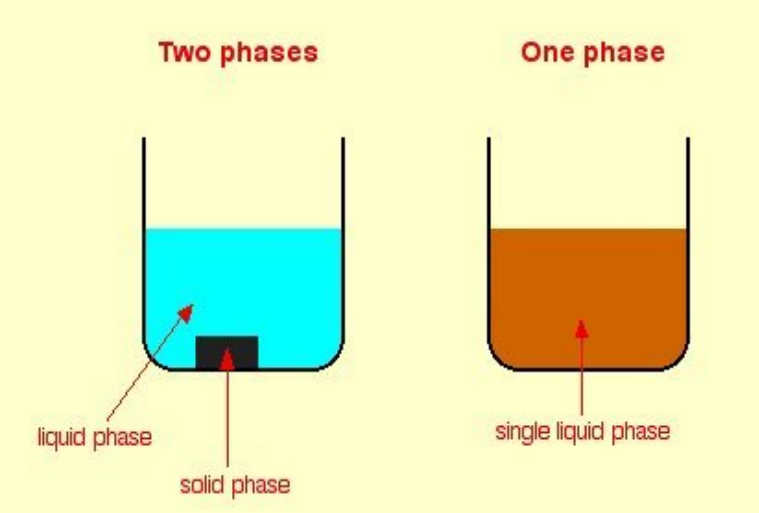

Figure 1.2: Phase distinguish as in Hetero- and Homogeneous catalyst

A simple model for heterogeneous catalysis involves the catalyst providing a surface on which the reactants are temporarily adsorbed. For example, in Haber process (which is used to manufacture ammonia), finely divided iron acts as a heterogeneous catalyst. The active site in the metal participates in partial weak

bonding with the reactant gases. As a result, the bonds within the reactant are weakened and are held in close proximity to each other (see Figure 1.3). In this way the particularly strong triple bond in nitrogen is weakened. Following this, hydrogen and nitrogen atoms are brought closer than would be the case in the gas phase, thus the rate of reaction increases. Turn Over Number (TON) and Turn Over Frequency (TOF) per active site, or per gram catalyst are the important terms in heterogeneous catalysis. This is because one does not know exactly how many active sites are on the surface. Other such commonly used heterogeneous catalysts include vanadium oxide in the contact process, nickel surface in the manufacture of margarine, alumina and silica in the cracking of alkanes and platinum rhodium palladium surfaces as catalytic converters in car engines.

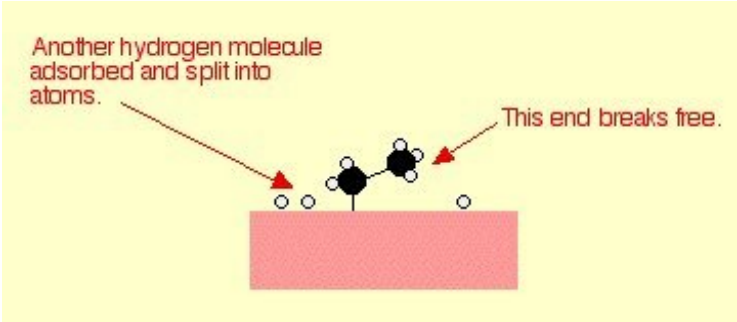

Figure 1.3: NH_3 synthesis over Heterogeneous Metal surface catalyst

A typical example of homogeneous catalysts (see Figure 1.4) are $H^+(aq)$ (which acts as a catalyst in esterification) and chlorine free radicals (in the breakdown of ozone). Chlorine free radicals are formed by the action of ultraviolet radiation on chlorofluorocarbons (CFCs). They react with ozone forming oxygen molecules and regenerating chlorine free radicals as follows:

$$Cl(.) + O(3) \rightarrow ClO(.) + O(2)$$

$$ClO(.) + O \rightarrow Cl(.) + O(2)$$

Homogenous catalysts generally react with one or more reactants to form a chemical intermediate that reacts to form the final reaction product, in the process regenerating

the catalyst. Following is a typical reaction scheme, where C represents the catalyst:

$$A + C \rightarrow AC \ (1) \quad B + AC \rightarrow AB + C \ (2)$$

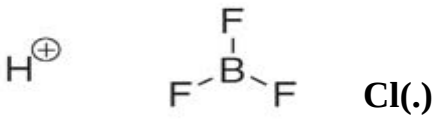

Figure 1.4: Homogeneous Acid catalysts

In homogeneous catalysis, the TON is the number of cycles that a catalyst can run through before it deactivates, i.e., the number of A molecules that one molecule of catalyst can convert into B molecules. The TOF is simply TON/time, i.e., the number of A molecules that one molecule of catalyst can convert into B molecules in one second, minute, or hour. Thus, the catalyst opens a selective route to the desired product. There are various kinds of product selectivity.

1.1.3 Applications, Advantages and Disadvantages

There are many different catalyst compounds (Figure 1.5). They range from the proton, H^+, through Lewis acids, organo-metallic complexes, organic and inorganic polymers, all the way to enzymes. However, their application is based on the type of reaction to be catalyzed.

The main categories of reactions catalyzed by homogeneous catalysts are: dissociation and coordination; oxidative addition; reductive elimination; insertion and migration; de-insertion and β-elimination; and nucleophilic attack on a coordinated substrate. Many homogeneous catalysts are based on a (transition) metal atom that is stabilized by a ligand or simply called as organo-metallic complexes. The ligand is usually an organic molecule that attaches to the metal atom. The main advantage of an organo-metallic homogeneous catalyst is the tunability of catalyst's property by changing this ligand. Selecting the right metal and the right ligand can improve the catalyst's activity, selectivity, and stability. The most commonly used homogeneous organo-metallic compounds as catalyst include $Rh[P(Ph)_3]_3Cl$, $Cr(CO)_6$,

$IrCl(CO)[P(C_6H_5)_3]_2$, $Ti(OiPr)_4$, $Cu(OTf)_2$, $Ni[P(Ph)_3]_3$, DIOP, BINAP, dpp-benzene, Xantphos, $Ni(CO)_4$ and many more.

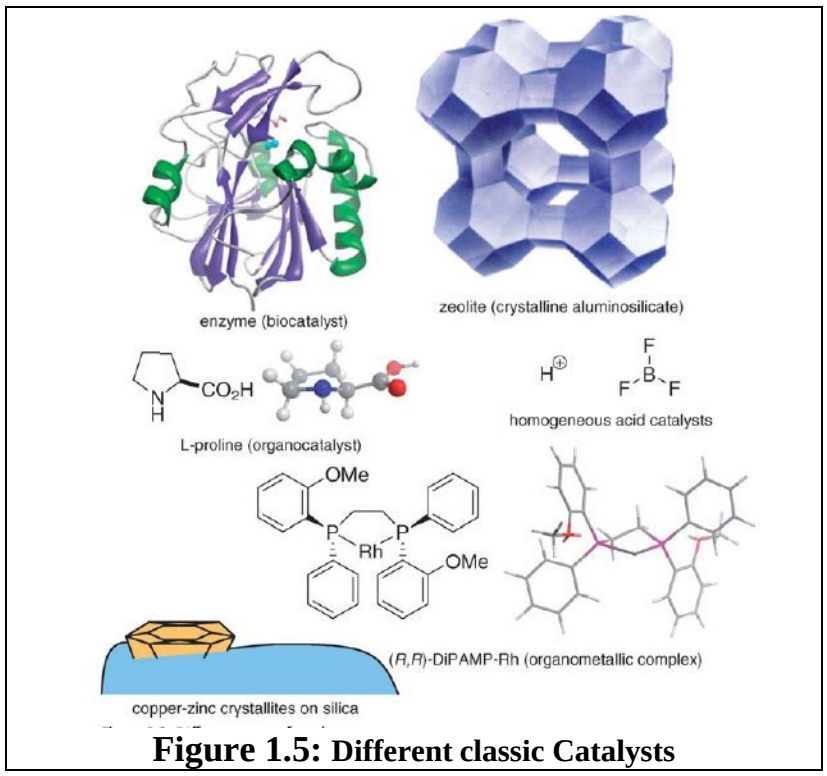

Figure 1.5: Different classic Catalysts

Apart from this some species without metal co-ordination helps to speed up various organic reactions. This typically points the classic acid/base catalysis simply by H^+ and OH^-. Examples include aldol reactions, esterifications and trans-esterifications, and synthesis of nitroaromatics such as 2-methyl-1, 3, 5-trinitrobenzene. Brønsted acids catalyze reactions by protonating nucleophilic sites such as lone pairs on O or N atoms or alkene pi-bonds. Organocatalysis is a subtype of acid catalysis. The catalysts are small organic molecules, predominantly composed of C, H, O, N, S, and P atoms. These molecules are often Lewis acids or bases. Organocatalysts display several advantages over organometallic complexes: They are typically inexpensive, readily available, and many of them are air-and water-stable. The fact that they contain no metals is an advantage in itself: There is no need for metal separation and recovery at the end of the reaction. Moreover, organocatalysts

are usually much less toxic than their organo-metallic counterparts. The typical examples of organocatalysts are piperidine praline, Cinchona alkaloid.

Significantly, two of the seven Nobel Prizes in chemistry given this century were awarded for achievements in homogeneous catalysis: In 2001 William Knowles [2] and Ryoji Noyori [3] shared the prize with Barry Sharpless [4] for their contributions to asymmetric hydrogenation and oxidation catalysis, respectively. Four years later, Yves Chauvin [5], Robert Grubbs [6], and Richard Schrock [7] shared the prize for their contribution to metathesis catalysis.

The main advantage of homogeneous catalysis is the high activity and selectivity, which can be tuned by changing the catalyst's molecular properties. Moreover, homogeneously catalyzed reactions are not hampered by surface effects, phase transfer limitations or mass-transfer problems. All the catalytic sites are accessible and every single metal atom is a potential active site. Despite these advantages, the main disadvantage is the problem of catalyst separation, recovery and recycling [8]. Most homogeneous catalysts are thermally sensitive, and decompose below 150°C. Thus distillation, even at reduced pressure, will lead to catalyst decomposition. Low-pressure distillation is also problematic, because a catalyst optimized for working under the high-pressure reaction conditions may undergo undesirable side-reactions under reduced pressure. This often prevents their scientific successes from becoming commercial ones.

On the contrary, heterogeneous catalysis covers all the cases where the catalyst and the substrate are in different phases. However, heterogeneous catalysis, usually refer to a system where the catalyst is a solid and the reactants are gases or liquids. Most of the heterogeneous catalysis was developed for the applications in petrochemicals and bulk-chemicals industries. Due to reactivity and process size considerations, these industries favor continuous processes at high temperatures. This meant that working with solid catalysts and gaseous reactants was often the best option. Table 1.1 lists some of the common examples of heterogeneous catalysts and the respective industrial processes. Other common model catalyst systems include thin metal and oxide films [9], glassy metals [10], supported catalysts based on

chemical vapor deposition [11], and supported homometallic and bimetallic clusters and oxides [12].

Process	Catalyst	Reactants	Products	End usage
Haber–Bosch NH_3 synthesis	magnetite (Fe)	H_2, N_2	NH_3	fertilizer, gunpowder, explosives
Methanol synthesis [11]	$Cu/ZnO/Al_2O_3$	CO, CO_2, H_2	CH_3OH	bulk chemicals, fuel
Fischer–Tropsch [12]	Co, Fe	coal, natural gas	C_5-C_{11} hydrocarbons	automotive fuel
Cracking [13]	clays	long alkanes, C_{12+}	C_7-C_9 alkanes	fuel, detergents
Alkylation [14]	zeolites, clays, silicates	C_3-C_5 alkanes	C_7-C_9 isoalkanes	high-octane fuel
Dehydrogenation/reforming	Pt/Al_2O_3	alkanes	alkenes	polymers, bulk chemicals
Hydrodesulfurization [15,16]	Co/Mo sulfides	diesel fuel	sulfur-free diesel	automotive fuel
Hydrocracking [2]	Pt on zeolites or aluminosilicates	aromatics mixture	saturated hydrocarbons	automotive/aviation fuel
Isomerization [17]	H-ZSM-5 zeolites	xylenes, toluene	*p*-xylene	polymers, bulk chemicals
Polymerization [18]	Ti, Ziegler–Natta	ethene	poly(ethylene)	polymers, bulk chemicals
Oxidation [19]	vanadium oxide	xylenes	phthalic acids	polymers

Table 1.1: Examples of major industrial processes using heterogeneous catalysis

Solid catalysts are also used in clean energy applications such as fuel cells [13], solar energy conversion [14], and energy storage cycles [15]. The most preferred material for various chemical processes is the metallic surface. Another such recently developed noticeable catalytic materials constitute clusters of various metallic and non-metallic elements. The cluster size varies from few to several hundred atom's combination. Experiments have demonstrated that the properties of clusters uniquely depend on their size and composition and that they evolve differently [16]. These tiny surfaces exhibit the emphatic chemical and physical properties. This leads to potential applications of these materials in oxidation chemistry. Especially the melted analogues of these clusters are helpful in bringing down the tedious reaction. The latter characteristic of these clusters are hence useful to change the traditional high temperature, pressure demanding processes in applications like hydrocarbon cracking, diffusion, polymerization etc. Nevertheless, not all heterogeneous catalysis occurs on metal surfaces. Zeolites, for example, are excellent solid acid catalysts. These are porous crystalline structures of metal oxides, often made from silicon, aluminum, and oxygen. By substituting cations in the zeolite framework, one can create Bronsted [30b] and/or Lewis acid sites. These highly crystalline materials can be synthesized to exact specifications, including the setup of identical active sites at uniform distances.

One important advantage of heterogeneous catalysis is the ease of catalyst separation. In gas/solid systems the catalyst is easily separated and cleaned, and in

liquid/solid systems it can be simply filtered. Such solid acids have an important advantage over HF, HCl, or H_2SO_4: They are easily isolated from the product mixture and require no neutralization [17]. This means no salt waste, and considering the enormous production volumes in the petrochemical industry, this is a big advantage even when the acid is used in catalytic amounts [18]. In addition these materials are susceptible to all temperature and pressure ranges. Only to sustain such conditions, specially designed equipment is needed in industrial processes.

1.1.4 Motivation for Theoretical Investigation

At first glance, heterogeneous catalysis seems overwhelming. It is the more varied and the most complicated of the two catalysis sub disciplines, combining physical, inorganic, organic and organo-metallic chemistry, surface science, and materials science. From the outside, the process seems extremely simple: reactants enter the reactor, and products leave it. Inside, things are much more complicated: reactants must diffuse through the catalyst pores, adsorb on its surface, travel to the active site, react there, and desorbs back to the gas phase. All of these steps happen at the molecular level (also called the microscopic). However, the catalyst itself is a macroscopic object, with an intricate surface structure, and physical interactions at the macroscopic level also affect the reaction outcome. This is what makes heterogeneous catalysis so complicated. Unlike the situation for molecular catalysts, the bulk parameters such as particle size, shape, and mechanical strength are crucial here. The surface interactions hold the key to the catalyst's activity, selectivity, and stability. Two other crucial factors are mass transfer and heat transfer.

At the microscopic level, metal crystal surfaces show various steps and kinks. Strikingly, it is often precisely at these irregular points that catalysis happens. This is because the surface atoms at those spots are not fully coordinated, and thus have more options for interacting with substrate molecules [19]. However, one can predict the properties and performance of new catalysts [18, 20] by combining the data from high-throughput experimentation with statistical analysis and descriptor models (*in-silico* design). The development of XRD, in situ IR, mass spectrometry, EXAFS and NMR analysis techniques enables today's chemist to study reaction kinetics, and

examine catalytic intermediates under true reaction conditions. The latter type of modeling deals with catalyst descriptors, structure/activity and structure/property relationships [21]. There are various levels of catalyst descriptors, ranging from very simple ones based on composition parameters to ones based on high-level quantum computations. This leads to a better understanding of reaction mechanisms and exciting new reactions. By using reactive probe molecules, we can qualify and quantify the type and number of active sites. First, we can easily change a single parameter in the model, thus observing the influence of this parameter on the reaction. Such simulations are essential in industrial process design, where any changes in the reactor configuration are very costly. Second, computer models can help identify the properties of new catalysts and materials, including ones that are difficult (or indeed impossible) to synthesize in the laboratory. In addition to all of the above, we can simulate any experimental conditions, including reactions at extreme temperatures and pressures using dynamics, which are difficult to set up in the laboratory. Modeling the structure/activity relationships of such catalysts can save not just much synthetic effort but also it saves chemical and financial wastage. In addition, Simulations let us observe reactions and species that are inaccessible by experiment, such as the transfer of single protons, intermediates and even the transition states.

Thus main aim of the present thesis is to apply the Density Functional Theory to investigate the structure-property relationship of two different classes of chemical systems. One of the aspects is to deal with the structural, electronic properties and reactivity differences of Sn-BEA and Ti-BEA zeolite in a crystalline phase by DFT with PBC. The other aspect is to use a combined, DFT and MD approach basically known as AIMD, to study the structural, bonding properties and hence finally reactivity of Al metal clusters.

We in the next section give an introduction to these two systems of study.

1.2 Metal Oxide Framework: Zeolite

‘‘La Roca magica’’ (the magical rock), so printed a Cuban newspaper [22], in applaud of one of its country’s greatest mineral resources—Zeolites. The first zeolite was identified in 1756 by the Swedish mineralogist (Baron) Friedrich Axel Cronstedt, who observed that on heating the stones he had gathered, in a blow-pipe flame, they danced about in a froth of hot liquid and steam, appearing as if the stones themselves were boiling. He thus coined the name ‘‘zeolite’’ which from Greek derivation (zein, ‘‘to boil’’; lithos, ‘‘a stone’’) means ‘‘stones that boil’’ [23]. The phenomenon he observed provides a vital clue to an essential property of zeolites, which is their ability to absorb a substantial proportion of water, and indeed of other liquids.

1.2.1 General Features

Zeolites are crystalline aluminosilicates with composition represented by the empirical formula,

$$M_xD_y[Al_x+2ySi_n-(x+2y)O_{2n}]mH_2O$$

where x is the number of monovalent cations, y is the number of bivalent cations, n is cation valence, and m is the number of water molecules in the zeolite formula [24, 25]. The structure of a zeolite consists of a three dimensional framework of SiO_4 and AlO_4 tetrahedra, each of which contains a silicon or an aluminum atom in the center. They are termed as TO_4 tetrahedron (Fig. 1.6(a)), where T is Si or Al. The oxygen atoms are shared between the adjoining tetrahedra units which can be present in various ratios and arranged in different ways. The combination of several aluminosilicate rings then leads to the formation of structural channels and cavities. The diameter of these channels or pores range from 0.3 to 1.0 nm. The smallest pore size is formed by a eight ring pore with diameters 0.3 to 0.4 nm e.g. zeolite A, A medium pore zeolite, is a ten ring pore with a 0.4 to 0.6 nm in diameter, such as ZSM-5. Large pore zeolites are with twelve ring pores with 0.8 nm, e.g. zeolite beta [26]. The extra-large pore zeolites are with fourteen ring pores with 1.0 nm, e.g. UTD-1. Structure commission of IZA registered approximately 130 molecular sieve structures but only about 15 of them have commercial interest till now:

- From natural zeolites mordenite, chabazite, erionite, and clinoptilolite.
- From synthetic zeolites A, X, Y, mordenite, L, ZSM-5, Beta, ferrierite, MCM-22, SAPO-34, SAPO-11.

A zeolite with a two or three dimensional channel system can have a better catalytic activity involving physical or chemical adsorption [26b]. Diffusion of molecules also depends on the number of channels [24, 25].

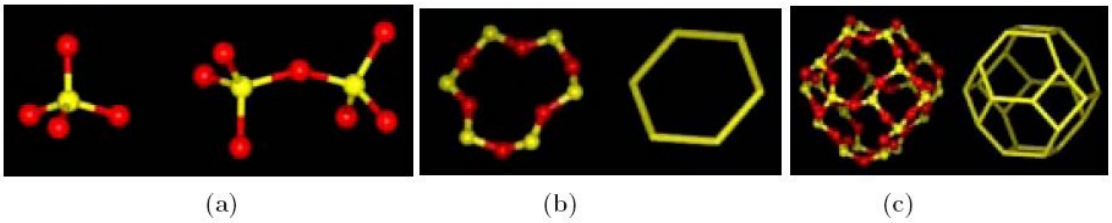

Figure 1.6: The three structural units of a zeolite. (a) Primary, (b) Secondary and (c) Unit Cell

The structural formula of a zeolite is based on the crystallographic unit cell formula $M_{x/n}.[(Al_2O_3)_x.(SiO_2)_y].wH_2O$, where x and y are total number of tetrahedra per unit cell and y/x is usually 1 to 5, and w is the number of water molecules in the unit cell, M is the metal cation or proton of valence n, to produce electrical neutrality, since for each Al tetrahedron in the lattice there is an overall charge of -1. The sum x+y is the total number of tetrahedra in the unit cell. The portion [ ] above represents framework composition. In most zeolite structures the primary structural TO_4 tetrahedra (Fig. 1.6(a)) are assembled into secondary building units (Fig. 1.6(b)), which may be simple polyhedras such as cubes, hexagons and octahedral [26]. The final structure framework (unit cell) consists of assemblies of these secondary units. The framework may be considered in terms of large polyhedra building blocks forming characteristic cages. For example, sodalite and sodalite Y can both be generated by the truncated octahedron known as beta-cage. Extended structure of zeolite MFI with pores and channels formed from several unit cells is shown in Figure 1.7.

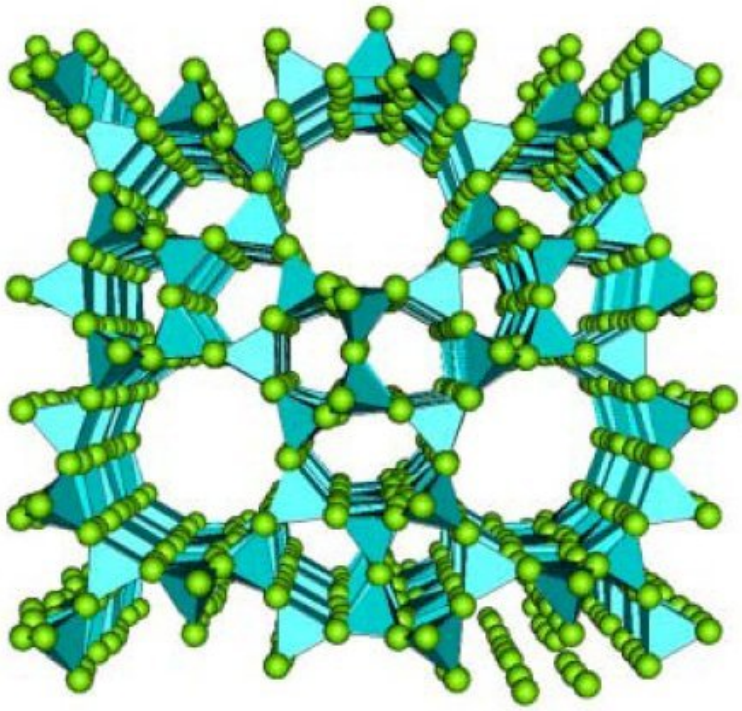

Figure 1.7: Extended structure of a zeolite (MFI) consisting of several unit cells

1.2.2 Applications and Advantages

Today, mainly synthetic zeolites are used widely in petroleum refining and chemical processes and natural zeolites are utilized mainly in many non catalytic applications.

Zeolites selectively adsorb or reject different molecules and hence, act as molecular sieves. The molecular sieve action may be total or partial, depending upon the conditions, such as the pore size of the zeolite, size of the diffusing molecule and moreover, the activation energy of the molecule to pass through the channels. Zeolites are microporous materials widely used as heterogeneous catalysts, where the shape and selectivity plays an important role. The above properties of zeolites are responsible for widespread industrial applications of zeolites, as ion exchangers, selective adsorbents [27]. More importantly, they have been used in oil and petrochemical industries as oxidation or reduction catalyst in many processes such as cracking, isomerization and alkylation [28-30a]. Recently, they have been shown to

have applications in optical switching, microwave absorption, optical data storage, etc.

From the catalytic viewpoint the following factors can be utilized in catalysis: acidity of zeolites (for some reactions also basicity), redox properties (zeolites contain suitable metals), multifunctional character of specially prepared modified forms of zeolites, shape selectivity of zeolites. Proton-donor Bronsted acid sites [30b] are generated by isomorphous substitution of tetravalent silicon by trivalent cations [30c] and mainly by aluminum. Alternatively, extra–framework cations, either monovalent (e.g. Na^+ or K^+), or divalent (e.g. Ca^{2+}, Sr^{2+}) are incorporated into the extra–framework sites [24, 25 30]. Experiments have shown that there are some 'free' hydroxyl groups present on the zeolite framework, which are also responsible for acidity. On the contrary, Lewis acid sites arise from the isomorphous substitution of more electronegative atom such as Ti, Sn, etc, at the active sites. Due to the high electronegativity, they have ability to accept a pair of electrons and are probable sites for oxidation reactions [31, 32]. Also, Lewis electron acceptor sites are formed by thermal treatment of silicon-rich H-forms of zeolites, e.g. ZSM-5 by dehydroxylation of Si-OH-M groups (M is trivalent cation) [33].

In addition, zeolites also show non catalyzed utilizations as: 1. Sorption and separation processes in detergents and cleaning of waste waters. 2. Improving physical and chemical properties of soils and used as dietary additive to the feedstuff and sorption material in agriculture. 3. Increasing chemical resistance of cement-based composites and sorption efficiency of the mineral filler in geosynthetic clay liner in building industry and environmental engineering, respectively.

In the present thesis we have characterized such Lewis acid sites in Sn and Ti substituted beta zeolite. In addition, we compare their Lewis acidity and hydrophillicity, which are extremely crucial factors in industrial applications.

1.2.3 Enhancement of catalyst by doping: Recent studies and advances

The chemical substitution of Si by some other atoms like Ge, Sn, Ti, etc., can relax the zeolite framework and can affect a certain chemical reactions taking place within the zeolite [34, 35]. The catalytic properties of zeolites, in which the Si atoms are substituted by the metal ions like titanium or vanadium, occur not due to Bronsted acidity [30b]. There are no O-H groups or counter ions present, because there is no surplus charge in the framework. In case of vanadium the oxidation state +v leads to formation of a V=O double bond. The high potential of zeolites in Lewis acid catalyzed reactions origins directly from the incorporated tetravalent T-atoms [36], attributed to their electronegative nature. Since all tetrahedra sites are exposed to the pore volume, zeolites possess a very high surface area compared to inorganic solids. Zeolite frameworks are not rigid, and at higher temperatures the shape and dimensions of the pore openings and the channels are more flexible. Although various frameworks, such as mordenite, chabazite, ferrierite, ZSM-5, MCM-22 were in common commercial practice, a large pore zeolites as silicalite and beta were chosen for the incorporation by the transition metals.

The first synthesis of the titanosilicalite, TS-1, with MFI structure was achieved on 1983, and its unique catalytic activity in oxidation reactions with hydrogen peroxide, led to fast progress of investigation on the heterogeneous catalytic oxidation and reveal a new possibility for economical and ecological attractive industrial production of many chemicals [37, 38]. Consequently, detailed investigation of TS-1 with different physical methods and catalytic tests for oxidation reactions of alkanes, alkenes, and aromatic hydrocarbons, with hydrogen peroxide as oxidant under mild conditions were published in literature [39] Ten years after that, the research group of Corma *et. al.* has published a direct synthesis of titanium containing materials with the framework of beta (BEA) [40, 41]. In these two zeolites the framework Ti atoms possess tetrahedral coordination, an octahedral coordination is realized in the zeolite ETS-10 [42]. The main difference between TS-1 and Ti-Al-BEA, are the larger channels and the presence of Al in the BEA. The former feature allows larger molecules to enter in the zeolite pore, while the presence of Al causes the Bronsted acidity [30b] of the zeolite, which can lead to further acid catalyzed consecutive reactions. Thus, Ti-Al-BEA is broadly applicable and exhibits higher

activity than TS-1 [43]. On the other hand sometimes the selectivity of the catalytic reactions is diminished. Due to acidity of the aluminium sites, Ti-Al-BEA enhances the rate of secondary reactions and causes decomposition of desired epoxides. There are various methods reported to suppress this additional acidity, and one obvious way is to synthesize Al free BEA. However, recent experiments with hydrophobic Al free Ti-Beta (Ti-BEA) showed that although a clear benefit in epoxide selectivity was obtained, the epoxidation activity was still lower than for TS-1 [44]. The successful catalytic results obtained with Ti zeolites motivated researchers to synthesize zeolites containing other transition metals in framework positions. Tin and zirconium have been incorporated tetrahedrally into the framework of zeolite beta [45] and interesting catalytic properties, different from those of Ti zeolites, have been observed in the products.

Recently, Sn-BEA was shown to have better catalytic activity than Ti-BEA [20]. Al-free-Sn BEA was first synthesized by Mal and Ramaswamy, who predicted that the Sn atom should be tetrahedrally coordinated [45a]. Corma *et. al*. showed for the first time that the Sn-BEA acts as an efficient catalyst for the Baeyer–Villiger oxidation (BVO) reaction in the presence of H_2O_2 [20]. They further showed the probable reaction mechanism of the Baeyer–Villiger oxidation reaction, in which the carbonyl group of the ketone is initially activated, and then followed by a reaction with the non activated H_2O_2, in contrast to what occurs in the Ti-BEA zeolite [20]. Later, it was also shown by Corma *et. al.* that Sn-BEA acts as a better catalyst than the Ti-BEA for the MPVO reaction [46, 47]. The increase in the activity of BEA by the substitution of Sn can be rationalized by the higher atomic size and electronegativity than the Ti atom, leading to stronger Lewis acid sites. This shows that the combined property of large pore dimension and high Lewis acidity of Sn-BEA makes it a highly active stereo-selective catalyst for many oxidation and reduction reactions.

1.2.4 Characterization: Experiment and Theory

It is known that the crystallographically inequivalent T-sites will have different activity and shape selectivity due to the differences in the topological environment

around the T-sites. Hence, in the isomorphically substituted zeolites, it is important to understand the nature of the active sites and to precise their structures. Experimental techniques such as X-ray diffraction, diffraction, and magic-angle-spinning (MAS) NMR, MAS and IR spectroscopy have been used to investigate the coordination of the active T-sites in the zeolite and their interaction with organic molecules [47-50]. The hydrophobic Ti-BEA was characterised by EXAFS–XANES, showing again the same geometry for the Ti sites that was observed before for Ti-Al-BEA and for TS-1. Similarly, Sn119 MAS NMR spectrum and *in situ* EXAFS spectroscopy of Sn-BEA confirmed that the Sn atoms have a tetrahedral coordination and XRD could identify those unique sites for Sn substitution [46-48]. It is clear, then, that an intrinsic difference in the activity of the Ti/Sn sites must exist and this should be related to electronic effects in relation to the Ti/Sn atoms. This is further supported by the fact that solvents with different electron donating capabilities influence differently the catalytic behavior of TS-1, Ti-BEA and Sn-BEA [51].

However, in zeolites such as Sn-BEA or Ti-BEA, in which the concentration of the Sn or Ti is low in the framework, it becomes difficult to obtain the structural features of the local active sites by using these experimental techniques [48, 49]. Various quantum-mechanical methods have been implemented to study the structural and electronic properties of the active sites in zeolites. Finite or cluster models of an active site cut out of the zeolite crystal have been used for theoretical investigations, in which the dangling bonds of the cluster are saturated by hydrogen atoms. The reviews by Sauer and co-workers may be referred for detailed study on the cluster models of zeolites [52]. The advantage of using the cluster model is that it avoids artificial periodicity for systems with large Al and cation content and is computationally cheap. It is also a better model for representing the active sites on the surface. However, cluster models neglect the effect of long-range interactions and some artificial states are introduced due to the atoms lying at the boundary of the truncated fragment. Periodic methods are the only way to overcome all these problems, as they include the long-range electrostatic interactions. One can refer to these studies for the further comparison of clusters model versus the periodic model calculations [52, 53].

Sastre *et. al.* have carried out cluster calculations on the Ti-BEA and TS-1 using ab initio Hartree–Fock and density functional theory [54]. On the basis of the LUMO energies, they characterized the acidity of these two zeolites and proved that Ti-BEA is more Lewis acidic than TS-1 [54]. Dimitrova and Popova have done a cluster model study on Al, B, Ti, and V incorporated into BEA and further studied their interaction with the peroxo group [55]. Their study showed that the incorporation of Ti is energetically more favorable than the other atoms and Ti increases the oxidizing power of the peroxo group. Zicovich-Wilson and Dovesi carried out periodic Hartree–Fock calculations on Ti-containing zeolites such as SOD, CHA, and alpha-quartz (QUA) [56]. Interestingly, they showed that the substitution of Si atoms by Ti atoms in a zeolite is an endothermic process when evaluated with respect to pure silico zeolite. They also proved that the incorporation of Ti within the zeolite framework is thermodynamically less favorable than the formation of extra framework TiO_2 clusters. This explains the difficulty of synthesizing high Ti content zeolites [56]. Very recently, Damin *et. al.* analyzed the interaction of Ti-CHA with various molecules such as NH_3, H_2O, H_2CO, and CH_3CN using a periodic approach [57]. Moreover, there have been several studies on other zeolites by using a periodic description [58]. Recently, Rozanska *et. al.* have used a periodic approach to study the chemisorption of several organic molecules in zeolites [59]. To confirm the peculiarities of Sn-BEA, analogous experiment on Sn-BEA and CH_3CN adsorption has been recently carried out by Corma and co-workers [60]. Their study predicted a blue shifted $\Delta\upsilon$(CN) stretching frequency of +42 cm^{-1}. In addition, to study the structure-activity relation in Sn-BEA catalyst they carried out a computational study based on a cluster model approach. Interestingly, to study the influence on reactive site, their model comprised of reaction sites accompanied by various functional groups. In the past, [61-65] main attention has been devoted to study of the Ti (IV) center reactivity in various zeolites such as TS-1, CHA etc. through the adsorption of NH_3 and H_2O like basic moieties. Bordiga *et. al.* [65] studied the adsorption of CD_3CN and pyridine on Ti centers of the TS-1. They confirmed their results with the experimental vibrational spectra.

As the epoxidation of olefins and few other reactions such as, the Meerwein–Ponndorf–Verley reaction, BVO are catalyzed by these Lewis acids, we thought that differences in the Lewis acidity of the Ti and Sn in both structures could be responsible for their different catalytic behavior. Quantum chemical calculations can yield useful information regarding the electronic properties of these materials [66] and its relation with Lewis acidity. Motivated by this, in the present work, we examine the effect of the incorporation of Sn and Ti in BEA using a periodic model of beta zeolite. Indeed, when the number of substituted Si atoms per unit cell is very small (here 1/64), the system can be assumed periodic.

Thus the aim of this thesis is to characterize the Lewis acidity of titanium and tin centers in Ti-BEA and Sn-BEA zeolites, respectively and its relation with structural factors.

1.3 Metal Clusters

Clusters are aggregates of atoms or molecules, intermediate in size between individual atom and bulk. There are many different types of clusters, such as metallic clusters, molecular clusters, organic clusters and quantum dots. Clusters are different from both molecules and solids, and for this reason can have very different properties. Molecules are characterized by having definite and unique structure and specific composition. On the other hand clusters may be composed of any number of particles and have a tendency to grow. Figure 1.8 shows typical growth pattern observed in Au clusters.

1.3.1 General Features

Metal clusters are among the more complex and interesting ones. As the dimension of the metal clusters goes on decreasing quantum effects becomes much more prominent and affect the behavior of e.g. the B. E., ionization potentials, polarizabilities, optical spectra, etc. [67]. Such changes in the electronic structure can affect the bonding and other physical and chemical properties of metal clusters. As the number of particles of

the cluster becomes larger, the number of locally stable structures (isomers) of the cluster grows rapidly. Mainly theoretical and experimental research has been focused on the evolution of properties with size, particularly those, such as structural, electronic, magnetic and optical properties [68-70]. The most interesting are the metal clusters where the transition from a localized (covalent or ionic) to a delocalized (metallic like) bonding occurs as the size of the cluster increases [68, 69, 71]. Structure and stability are the most important properties of the metal clusters, which can be correlated with the type of atom–atom bonds formed in the metal cluster and later to its application.

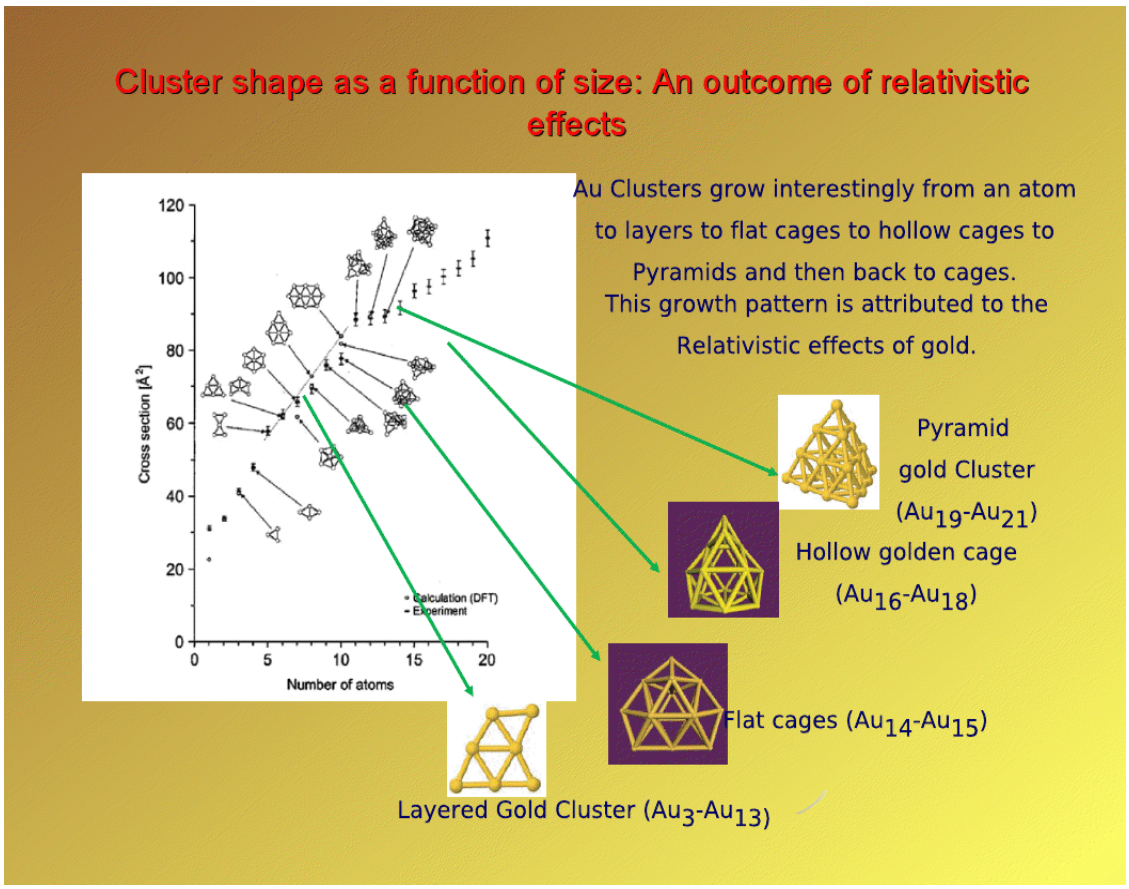

Figure 1.8: Growth pattern observed in Au clusters

In general there are four types of bonds which can be distinguished within the metal clusters viz. covalent, ionic, metallic and van der Waal [69]. Among these clusters, covalent and ionic clusters are supposed to be the most stable clusters due to strong inter-atomic bonds. Recently, metal cluster stability is linked to the presence of aromaticity and/or anti-aromaticity [72]. In a combined experimental and theoretical work, Li *et. al.* [73] for the first time showed the existence of aromaticity in XAl_4^- (where, X=Li, Na, Cu) clusters.

During the study of the structural properties of metal clusters, it has been found that some clusters have unusual stability than others and were termed to be 'magic clusters' [71, 73b]. The stability of these magic clusters was analogous to the stability seen in atoms and nuclei due to shell closing. Magic clusters show significant peaks in the mass spectra and are easily distinguishable via mass spectrometry techniques. These kind of metal clusters were first observed in the mass spectra of Na [74]. Knight *et. al.* used a mass spectra of the alkali clusters to show that the most stable clusters consist of 2, 8, 20, 40,... atoms, which interestingly coincides with the magic numbers observed in nuclei with 2, 8, 20, 40,... nucleons [75]. Magic numbers are different for different clusters and depend on the electronic structure and the geometry of the cluster. The interactions between the rare gas atoms are of van der Waal's type and hence the stability of the magic clusters in these systems is due to the atomic packing and atomic shell closure. However, in simple alkali or alkaline earth metals the atoms interact more strongly and hence the formation of magic clusters is due to the electronic shell closure [75-78]. Al_7^+ and Al_{14}^+ appear as magic clusters in some mass spectra of Al clusters. An unstable homoatomic metal cluster can be converted to a stable 'magic' cluster by doping with a single impurity [79-83]. For example, Al_7C^-, Sn doped Li_n, doping of Al_{13} cluster by a tetravalent atom.

Metal clusters can be classified as homoatomic and heteroatomic (or mixed) clusters. Homoatomic metal clusters contain same type of atomic species; on the other hand heteroatomic clusters are made up of different type of atomic species. Extensive theoretical and experimental studies have been carried out on the structural and electronic properties of homoatomic metal clusters such as Li, Na, K, Al, Sn etc. [76, 84-87]. In the last decade, similar investigations have been extended to study the

heteroatomic clusters, but comparatively to a lesser extent than the homoatomic metal clusters. One of the reasons for this would be the complexity produced by the additional interactions of the unlike atoms (hetero interactions) within the heteroatomic clusters. In small clusters, even a single impurity is expected to influence the structural and electronic properties [79-81]. For instance, Kaneher and co-workers have studied the structural and electronic properties of Sn doped Li_n clusters using AIMD simulations [83]. Binary clusters such as A_xB_y also belong to the class of mixed clusters [88]. Chacko *et. al.* have worked on some Al_4X_4 mixed clusters where (X=Li, Na, K, Be, Mg, B and Si) [73, 89]. The other interesting works on mixed–metal clusters are on GaAs, AlAs, [90], AuIn [91]. Changing the stoichiometry of different kinds of atoms provides another interesting way of improving the reactivity and selectivity of clusters in the context of catalysis. Another crucial factor which enhances reactivity of metal cluster dramatically is melting. The melting transitions of isolated metal nano clusters have received a lot of attention recently. Well-defined melting transitions have been observed and implied in many applications for metal clusters with fewer than 100 atoms.

1.3.2 Enhancement of catalyst by melting: Recent studies and advances

It is now well established that metal clusters with 10–10^3 atoms can display transitions i. e. melting between solid like and liquid like states. The transitions have first order characteristics and have been observed in experiments by means of a peak in the heat capacity due to the latent heat. Experimental studies on the phase transitions have now been performed for a variety of cluster materials including sodium [92-99], tin [100-101], gallium [102-104], sodium chloride [105], and aluminum [106-110] and these measurements have stimulated a number of theoretical studies [111-115]. The experimental studies of cluster melting have revealed significant size dependent fluctuations in the melting temperatures.

Pawlow a century ago [116] predicted that the melting points of small particles are depressed due to the increase in the surface-to-volume ratio. Sodium and aluminum clusters have been the most widely studied materials for the phase

transition. For sodium clusters it appears that variations in the melting temperatures are correlated with geometric shell closings [117]. For the aluminum clusters studied so far, both geometry and the electronic structure are important [110, 118]. A number of recent simulations have shown that cluster melting can be preceded by structural transitions [119, 120]. For example, using a Gupta potential, Li *et. al.* found that structural transitions between low enthalpy geometries (the ground state, icosahedral, and cuboctahedral) occur for Au_{55} at temperatures well below the melting temperature [121]. Cleveland *et. al.* found that for Au_{146} and Au_{459} the melting process is punctuated by solid-to-solid structural transformations from the ground state to higher enthalpy icosahedral structures which are precursors to melting [122]. Schebarchov and Handy discovered that structural transitions occur in the solid part of a coexisting solid-liquid Ni_{1415} cluster [123a]. In the case of palladium clusters, transitions from both fcc and decahedral ground states to icosahedral structures precede melting [123b]. Experimental evidence for structural transitions in isolated metal clusters is scarce. Ion mobility measurements have revealed some examples for both aluminum [124a] and gold [124b]. Low temperature dips in the heats capacities for Al_{56}^{+} –Al_{62}^{+} have been attributed to exothermic structural transitions annealing [106, 108].

These phase transitions, however, are not found to be strictly size consistent. That is, as size of cluster decreases there are no linear drop in their melting temperature. For instance, the extensive first principle thermodynamic simulations [125] on Al_{13} and Ga_{13} show higher than bulk melting temperatures. Upon doping with carbon a substantial reduction in melting is observed, thus allowing to tune finite temperature properties of small clusters. Doping causes lot of structural rearrangement of atoms within the cluster enhancing its reactivity, whereas, melting induces less coordination enhancing the catalytic activity. In the last decade, various clusters of Au, Pt and Pd are utilized vastly for their high catalytic reactivity [126]. Bulk gold is well-known to be chemically inert; the metal does not react with oxygen in air. However, it is now well established that gold clusters differ from bulk as they have several surface and corner atoms that have low coordination and hence adopt geometries that are extremely active for catalyzing certain oxidation reactions [127].

Some of the unique properties observed in these gold clusters are better response properties [128], and different melting behavior [129]. Several interesting findings on Au clusters have been summarized in a recent review on theoretical chemical calculations on gold [130]. One of the important applications of Au clusters has been for CO oxidation. In this context, the interaction of ground state geometry of Au clusters with O_2 [131] and CO [132] has been widely studied. Moreover, it has now recently been reported that in some cases the higher energy conformations have better adsorption properties as compared to the ground state cluster [132b, 133]. Many additional reports have shown that this activity of neutral clusters which depends upon the type of sites exposed and their ability to absorb or donate electrons can be elevated by phase transitions. Although, no explicit study on phase transitions of Pt and Pd all-metal cluster is reported so far, these are well known catalysts in many applications. The scope of catalytic reactions initiated by these above mentioned metal clusters is given in Table 1.2. Considering the two critical issues, abundance and cost, the expensive materials like Au, Pt are best replaced by Al metal clusters.

Many recent studies have proved the potential use of Al metal clusters as catalyst in varied applications [134]. A major breakthrough addressed by M. F. Jarrold [135] motivated us to study the novel features of Al clusters, where they discuss the reactivity of N_2 on a Al_{100} cluster. They have determined the melting temperature of Al_{100} using heat capacity measurements following which the ion beam experiments are used to investigate the reaction between the cluster and molecular N_2. They show above the melting transition, the activation barrier for N_2 adsorption decreases nearly by 1 eV. The importance of Al-N reaction has also motivated Romanowski *et. al.* [136] to perform a theoretical study of N_2 reaction with liquid Al metal. They have determined the activation barrier for dissociative chemisorption of N_2 to be 3.0 eV. They propose that the melting decreases the surface energy, and atoms in liquid are mobile and better able to adjust the N_2 molecule. Hence, previous studies on N_2 adsorption conclude that the atoms on the surface of the liquid cluster move to minimize their energy, lowering the activation barrier.

Apart from the enhanced mobility, detailed information on the reactivity of various Al clusters and the reacting sites within them has not yet been clearly

obtained.

Reaction
alkene isomerization
reduction of CO and of ketones
alkene hydrogeneration
hydroformylation of alkenes
ketone hydrogenation
Fischer-Tropsch-synthesis
hydrogenation of alkyl cyanides and -isocyanides
synthesis of methanol from CO and H_2
synthesis of polyols from CO and H_2
hydrogenation of nitrobenzene to aniline
hydrogenation of amides
alkyne hydrogenation
alkyne cyclization to arenes
aminomethylation [a]
hydroxymethylation [b]
water gas shift reaction

Table 1.2: Metal Cluster Catalyzed reactions

A very little understanding is available concerning the role of structure and bonding of Al clusters on the adsorption reactivity of the cluster. The catalytic reactivity is always attributed to specific and precise structural rearrangement of atoms in the material. It is worthwhile to correlate the above two parameters to their reactivity. Thus, the interesting questions are: "Is the chemisorption of N_2 molecule a consequence of highly different structure of Al cluster following the phase transition? Do the changes in structure modify the chemical bonding property within the cluster thereby enhancing its reactivity or the higher reactivity is completely due the dynamical rearrangement of atoms within cluster? Does this reactivity vary as a function of cluster size?"

To answer the above questions, in this thesis, we have studied systematically the adsorption behavior of N_2 on Al cluster as a function of cluster size. We also address the issue of conformational changes following the phase transition and

their impact on N_2 adsorption.

1.3.3 Characterization: Experiment and Theory

Cluster production is one of the most important steps in cluster studies. To produce them, one can either aggregate the particles or break them directly from a solid or in liquid. These can be produced in the form of colloidal particles. Mostly, the studies have been focused on the formation of clusters in the gaseous phase by using cluster sources. One of the most popular sources to produce metal cluster is the supersonic jet. The other two sources to produce clusters are the gas aggregation and the surface source. However, in laser vaporization technique the clusters are produced from the surface of a solid material by particle or photon impact or by a high electric field. Smalley and coworkers were the first to combine a laser ablation method and a supersonic beam. In this source, metal vapor is produced by the pulsed-laser ablation of a rod of the material to be investigated. This source can be considered as the hybrid of the supersonic jet and the gas aggregation source [16]. All known spectroscopic techniques such as optical, [137] infrared, photoelectron, [16] have been applied to study the poperties of clusters. Photodetachement and photodissociation techniques have allowed us to gain insight into the electronic properties of charged clusters.

Jarrold *et. al.*, have investigated the photodissociation of aluminum cluster ions [77]. The first attempt to measure the ionization energies of aluminium clusters by laser vaporization was by Cox *et. al.* [138]. Information on the structural and bonding properties can be obtained through vibrational spectroscopy. Very recently, Fielicke *et. al.* used far-infrared spectroscopy to determine the structures of cationic vanadium clusters containing 6 to 23 atoms [139]. Recently, structures of silver and gold cluster ions have been studied by collision cross section [140]. However, none of these experimental techniques or studies could reveal the evidence of catalytic nature of the gold clusters against their noble metallic phase. Gold clusters are the excellent demonstration, where theory has played a immodest role in determining their notabilities. Satya Bulusu *et. al.* reported theoretical grounds of hollow golden cages. Their recent work has shown that gold has some unique properties such as strong relativistic effects and aurophilic attraction, which likely play a key role in allowing

the formation of these unusual golden cages. Gold anion clusters of 13 atoms or fewer possess planar structures, whereas a cluster of 20 (Au_{20}) possesses a pyramidal structure and also examine the intermediate structures resulting in the high reactivity [141a]. The same authors also demonstrate planar-to-tubular structural transition in boron clusters: B_{20} as the embryo of single-walled boron nanotubes using theoretical simulations [141b].

In this new era, a computer simulation has led to a novel way of doing science that combines both theory and experiments. The finite number of atoms considered in the metal clusters makes these systems ideal for theoretical studies. They can also help and guide the experimental work. Theoretical approaches used to study cluster science are either based on the first principle methods, such as HF, CI, DFT or classical approximations such as jellium model, tight binding etc.

Classical Approaches

Jellium model is one of the simplest and widely used theoretical model to study the electronic properties of metal clusters. It is simple enough to be applied to spherical metal clusters ranging up to few thousand atoms. Jellium model completely ignores the ionic core structure and replaces it by an uniform positive charge as being smeared out over the entire volume of the cluster, while the valence electrons are free to move within this homogeneously distributed positively charged background. The electronic energies are calculated self-consistently to obtain the energy levels [69, 71, 142]. This approach is thus particularly suitable for systems with rather delocalized valence electrons such as bulk metal. According to the jellium model clusters with closed electronic shells have the spherical shapes, while clusters with partially filled or opened electron shells are deformed. Hence, the background of the jellium model can be modified according to the shape of the cluster. The initial work by Ekardt has succesfully shown that the jellium model can account for the experimentally observed properties [143]. A number of characteristic properties of metal clusters such as static polarizabilities, collective electronic excitations (plasmons), ionization potentials as well as the so called ’magic numbers’ can be explained in terms of jellium model and its extensions [142, 143].

The limitation of using the jellium model is obvious since it neglects the ionic perturbation. It fails to understand the properties of covalent and ionic solids, where the electrons are localized in the bonding region. Thus jellium model has a limited range of applications which include the group Ia metals, alkaline earth metals and to some extent the transition metals. Nevertheless, the model cannot compete with the conventional *ab initio* quantum chemical methods to study the properties of less than 20 atoms cluster. Reviews by Brack [144] and W. de Heer [67b] are suggested for the detailed study of the jellium model and its applications.

***Ab initio* Approaches**

Although classical and semi-classical approaches are successful in describing the stability and structural properties of the metal clusters [142, 143], very little information on the electronic structure and related properties such as polarizabilities, optical spectra and ionization potentials of small clusters is available through these approximations. Moreover, the hybridization taking place within the atoms cannot be explained on the grounds of classical and semi-classical theories. The most widely used *ab initio* method to calculate the ground state properties are the HF and DFT. The post HF method such as DFT, CI, CC have been used to calculate the excited state properties of metal clusters [32]. Many techniques, such as simulated annealing, conjugate gradient, Newton-Raphson have been employed for searching the potential energy surface to find the lowest energy configuration. Simulated annealing technique begins by heating the cluster at a very high temperature and then cooling or quenching it slowly, hence probing the thermally accessible regions of the phase space [145]. In a series of papers, the electronic structure of the clusters composed of Ia–group metal atoms and of IIa–group atoms have been investigated at the *ab initio* level [146]. Other studies on mixed metal clusters have also been carried out at the *ab initio* levels [147].

In the last decade combined approach of DFT and MD has been employed to study the ground state and dynamical properties of metal clusters [148]. In this approach the electronic potential derived from the DFT is combined with the classical MD equation, during the motion of nuclei to develop an efficient combined electron–

ion minimization. This approach was first proposd by Car and Parrinello [149]. This technique also helps in studying the melting of clusters. Thermodynamical simulations are based on the concepts such as temperature, pressure, equipartition, phase transition, [150] conformational search of clusters etc [151]. These simulations are carried out in a micro-canonical ensemble (constant energy) or in a canonical ensemble (constant temperature) [152].

1.4 Motivation and outline of the thesis

Presently variety of materials that are of industrially important processes are under investigation, but none of these are found to be the replacement of zeolites in the petroleum cracking. In addition, development in the zeolites and metal clusters render the new mechanisms for oxidation chemistry, unlike the traditional routes, drastically influencing the yield and reactor-time space. In view of this fact the current need, therefore, today is to bring about breakthroughs in the existing technologies as well as design new materials with major modifications. Experiments in this context are time consuming and also demand a lot of human and financial resources. In comparison, computation is a fast, promising and cost effective tool to monitor this task. In this decade, there are plenty of examples found where theory and simulations have played significant role in supporting experiments and evaluating materials. Thus, main aim of the present thesis is to understand the reactivity of two classes of catalyst zeolites and metal clusters using *ab initio* methods in computer simulations.

The outline of the thesis is as follows. Chapter 2 provides the theoretical background of the computational techniques employed in this work. In the succeeding chapters 3-5, results from our theoretical studies on the Sn-BEA and Ti-BEA are presented. Specifically, chapter 3 deals with the comparative study of structural, acidic and hydrophillic properties of Sn-BEA and Ti-BEA using p-DFT. In chapter 4, influence of plane wave cut-off on structural and electronic properties with example of Sn-BEA and Ti-BEA zeolite water molecule interaction is discussed. The strength of interaction of various ligands with Sn-BEA Vs. Ti-BEA, concluding the trend of reactivity is outlined in the chapter 5. Chapter 6 and 7 deals with the catalytic reactivity issues of Al metal clusters. Chapter 6, in general is first principle study on the role of structure and bonding of Al clusters in the adsorption of N_2 molecule. The contributing thermodynamic factors behind the chemisorption of N_2 molecule, first on the Al_{13} cluster and then on the Al_{100} cluster, is focused separately in chapter 7.

1.5 References

[1] G. Rothenberg, Catalysis: Concepts and Green Applications, WILEY-VCH Verlag GmbH & Co. KGaA, Weinheim, 2008.

[2] W.S. Knowles, Asymmetric hydrogenations (Nobel Lecture). Angew. Chem. Int. Ed., 41 (2002) 1998.

[3] R. Noyori, Asymmetric catalysis: science and opportunities (Nobel Lecture 2001). Adv. Synth. Catal., 345 (2003) 15.

[4] K. B. Sharpless, Searching for new reactivity (Nobel Lecture). Angew. Chem. Int. Ed., 41 (2002) 2024.

[5] Y. Chauvin, Olefin metathesis: the early days (Nobel Lecture). Angew. Chem. Int. Ed., 45 (2006) 3740.

[6] R. H. Grubbs, Olefin-metathesis catalysts for the preparation of molecules and materials (Nobel Lecture). Angew. Chem. Int. Ed., 45 (2006) 3760.

[7] R. R. Schrock, Multiple metal–carbon bonds for catalytic metathesis reactions (Nobel Lecture). Angew. Chem. Int. Ed., 45 (2006) 3748.

[8] B. Cornils, and W. A. Herrmann, Concepts in homogeneous catalysis: the industrial view. J. Catal., 216 (2003) 23.

[9] (a) C. M. Friend, K. T. Queeney, and D. A. Chen, Structure and reactivity of thin-film oxides and metals. Appl. Surf. Sci., 142 (1999) 99. (b) D. R. Rainer, D. W. Goodman, Thin films as model catalysts. NATO ASI Ser. E: Appl. Sci., 331(1997) 27.

[10] A. Baiker, Metallic glasses in heterogeneous catalysis. Faraday Discuss. Chem. Soc. 87 (1989) 239.

[11] S. H. Kim, and G. A. Somorjai, Surface science of single-site heterogeneous olefin polymerization catalysts. Proc. Natl. Acad. Sci. USA, 103 (2006) 15 289.

[12] (a) M. Frank, and M. Baumer, From atoms to crystallites: adsorption on oxide supported metal particles. Phys. Chem. Chem. Phys., 2 (2000) 3723. (b) W. T. Wallace, B. K. Min, Goodman, The nucleation, growth, and stability of oxide-supported metal clusters. Top. Catal., 34 (2005) 17. (c) D. R. Rainer, C. Xu, D. W. Goodman, Characterization and catalysis studies of small metal particles on

planar model oxide supports. J. Mol. Catal. A: Chem., 119 (1997) 307.

[13] (a) S.S.C. Chuang, Catalysis of solid oxide fuel cells. Catalysis, 18 (2005) 186. (b) L. Carrette, K. A. Friedrich, U. Stimming, Fuel cells: principles, types, fuels, and applications. Chem. Phys. Chem., 1 (2000) 163.

[14] (a) P. V. Kamat, N. M. Dimitrijevic, Colloidal semiconductors as photocatalysts for solar energy conversion. Solar Energy, 44 (1990) 83. (b) N. Serpone, A decade of heterogeneous photo catalysis in our laboratory: pure and applied studies in energy production and environmental detoxification. Res. Chem. Intermed., 20 (1994) 953.

[15] (a) B. Zaidman, H. Wiener, and Y. Sasson, Formate salts as chemical carriers in hydrogen storage and transportation. Int. J. Hydr. Energy, 11 (1986) 341. (b) H. Wiener, B. Zaidman, and Y. Sasson, Storage of energy by solutions of alkali formate salts. Solar Energy, 43 (1989) 291.

[16] H. Haberland, Clusters of Atoms and Molecules: Theory, Experiment, and Clusters of Atoms. Springer–Verlag, Heidelberg, 1994.

[17] T. Okuhara, Water-tolerant solid acid catalysts. Chem. Rev., 102 (2002) 3641.

[18] M.A. Harmer, Q. Sun, Solid acid catalysis using ion-exchange resins. Appl. Catal. A: Gen., 221 (2001) 45.

[19] (a) H. S. Taylor, Mechanism of catalytic processes. J. Ind. Eng. Chem., 13 (1920) 75. (b) H. S. Taylor, A theory of the catalytic surface. Proc. R. Soc. (London), 108A (1925) 105. (c) H. S. Taylor, The mechanism of activation at catalytic surfaces. Proc. R. Soc. (London), 113A (1926) 77.

[20] A. Corma, L. T. Nemeth, M. Renz, and S. Valencia, Sn-zeolite beta as a heterogeneous chemoselective catalyst for Baeyer–Villiger oxidations. Nature, 412 (2001) 423.

[21] (a) A. Corma, Inorganic solid acids and their use in acid-catalyzed hydrocarbon reactions. Chem. Rev., 95 (1995) 559. (b) C. D. Chang, and A. J. Silvestri, The conversion of methanol and other O compounds to hydrocarbons over zeolite catalysts. J. Catal., 47 (1977) 249.

[22] F. A. Mumpton, Proc. Natl. Acad. Sci. U. S. A., 96 (1999) 3463.

[23] A. F. Cronstedt, Kongl. Vetenskaps Akad. Handl. Stockholm, 17 (1756) 120.

[24] R. M. Barrer. Zeolites and Clay Minerals as Sorbents and Molecular Sieves, Academic, London, 1978.

[25] D. W. Breck. Zeolite Molecular Sieves. Structure, Chemistry, and Use, wiley–Interscience, new. York., 1974.

[26] (a) W. M. Meier, D. H. Olson Atlas of Zeolites Structure Types Juris Druck: Zurich and Polycrystal Book Service: Pittsburgh, 1978. (b) A. G. Pelmenschikov and R. A. van Santen, J. Phys. Chem. 97 (1993) 10678.

[27] Studies in Surface Science and Catalysis. Edited by P. J. Grobet, W. J. Mortier, E. F. Vansant, G. Schulz–Ekloff. Amsterdam, 37, 1988.

[28] Introduction to Zeolite Science and Practice. Edited by H. van Bekkum, E. M. Flanigen, P. A. Jacobs and J. C. Jansen. Elsevier, Amsterdam, 58, 2001.

[29] R. Szostak. Molecular Sieves. Blackie Academic, 1998.

[30] (a) Modelling of Structure and Reactivity in Zeolites. Edited by, C. R. A. Catlow, Academic Press. 1992. (b) R. A. van Santen and G. J. Kramer, Chem. Rev. 95 (1995) 637. (c) A. M. Vos, K. H. L. Nulens, F. De Proft, R. A. Schoonheydt, P. Geerlings. J. Phys. Chem. B 106 (2002) 2026.

[31] A. Carati, C. Flego, E. Previde Massara, R. Millini, L. Carluccio, W.O. Parker Jr, G. Bellussi. Microporous and Mesoporous Materials. 30 (1999) 137.

[32] A. Corma, P. Esteve, A. Martinez. J. Catal. 161 (1996) 11.

[33] J. Čejka, and B. Wichterlova, Catal. Rev. 44 (2002) 375.

[34] X. Yang. J. Phys. Chem. 99 (1995) 1276.

[35] M. Hunger, T. Horvath, G. Engelhardt, H. G. Karge. Stud. Surf. Sci. Catal. 756, (1995).

[36] M. G. Clerici, P. Ingallina, J. Catal. 140 (1993) 71.

[37] (a)B. Notarri, Appl. Catal. A, 97 (1993) N16. (b) C. Neri, B. Anfossi, F. Buonomo, EP 100 (1986) 119. (c) A. Espoito, M. G. Clerici, F. Buonomo, U. Romano, Brit. Pat. 2. 116. 974 (1985).

[38] (a) M. Taramasso, G. perego, B. Notarri, US Pat. 4. 410. 501 (1983). (b) C. D. Chang, S. D. Hellring, US pat. 4. 578. 521 (1986). (c) G. Bellussi, M. G. Clerici, F. Bounomo, U. Romano, A. Esposito, B. Notari, EP 0. 200. 260 (1986).

[39] (a) C. B. Khouw, C. B. Dartt, J. A. Labinger, M. E. Davis, J. Catal. 149 (1994)

195. (b) B. Notari, "Innovation in Zeolite Material Science", Amsterdam, Stud. Surf. Sci. Catal., 37, 413 (1987).

[40] (a) M. A. Camblor, A. Corma, A. Martinez, J. Perez-Pariente, J. Chem. Soc., Chem. Commun., 599 (1992). (b) M. A. Camblor, A. Corma, J. Perez-Pariente, Zeolites, 13 (1993) 82. (c) M. A. Camblor, A. Corma, A. Martinez, J. Perez-Pariente, 3rd International Symposium on Heterogeneous catalysis and Fine Chemicals, April 5-8, 1993, Poitiers, France (1993) C139.

[41] G. Perego, G. Bellussi, C. Gorono, M. Taramasso, A. Esposito, Stud. Surf. Sci. Catal. 28 (1986) 129.

[42] E. Borello, C. Lamberti, S. Bordiga, A. Zecchina, Appl. Phys. Lett. 71 (1997) 2319.

[43] M. A. Camblor, A. Corma, A. Martinez, J. Perez-Pariente, J. Chem. Soc. Chem. Commun. 589 (1992).

[44] T. Blasco, M. A. Camblor, A. Corma, P. Esteve, A. Martinez, C. Prieto, S. Valencia, J. Chem. Soc. Chem. Comm. (1996) 2367.

[45] (a) N. K. Mal, A. V. Ramaswamy, Chem. Commun. 425 (1997). (b) M. Renz, T. Blasco, A. Corma, R. Jensen, L. T. Nemeth, Chem. Eur. J. 8 (2002) 4708. (c) [10] Y. Zhu, G. Chuah, S. Jaenicke, J. Catal. 227 (2004) 1.

[46] A. Corma, M. E. Domine, L. Nemeth, S. Valencia, J. Am. Chem. Soc. 124 (2002) 3194.

[47] A. Corma, M. E. Domine, S. Valencia, J. Catal. 215 (2003) 294.

[48] M. Renz, T. Blasco, A. Corma, V. Formes, R. Jensen, L. Nemeth, Chem. Eur. J. 8 (2002) 4708.

[49] (a) T. Blasco, M. A. Camblor, A. Corma, J. Perez-Pariente, J. Am. Chem. Soc. 115 (1993) 11806. (b) T. Blasco, M. A. Camblor, A. Corma, P. Esteve, J. M. Guil, A. Martinez,J. A. Perdigon-Melon, S. Valencia, J. Phys. Chem. B 102 (1998)75.

[50] (a) G. Valerio, A. Goursot, R. Vetrivel, O. Malkina, V. Malkin, and D. R. Salahub J. Am. Chem. Soc. 120 (1998) 11426. (b) S. Ganapathy, T. K. Das, R. Vetrivel, S. S. Ray, T. Sen, S. Sivasanker, L. Delevoye, C. Fernandez, and J. P. Amoureux J. Am. Chem. Soc. 120 (1998) 4752.

[51] A. Corma, P. Esteve, A. Martinez, J. Catal. 161 (1996) 11.

[52] (a) J. Sauer, Chem. Rev. 89 (1989) 199. (b) J. Sauer, P. Ugliengo, E. Garrone, V. R. Saunders, Chem. Rev. 94 (1994) 2095 .

[53] J-R. Hill, C. M. Freeman, B. Delley, J. Phys. Chem. A 103 (1999) 3772.

[54] G. Sastre, A. Corma, Chem. Phys. Lett. 302 (1999) 447.

[55] R. Dimitrova, M. Popova, Mol. Eng. 8 (1998) 471.

[56] C. M. Zicovich-Wilson, R. Dovesi, J. Phys. Chem. B 102 (1998) 1411.

[57] A. Damin, S. Bordiga, A. Zecchina, K. Doll, C. Lamberti, J. Chem. Phys. 118 (2003) 10183.

[58] (a) R. Shah, J. D. Gale, M. C. Payne, J. Phys. Chem. 100 (1996) 11688. (b) T. Demuth, J. Hafner, L. Benco, H. Toulhoat, J. Phys. Chem. B 104 (2000) 4593.

[59] X. Rozanska, T. Demuth, F. Hutschka, J. Hafner, R. A. van Santen, J. Phys. Chem. B 106 (2002) 3248.

[60] (a) M. Boronat, P. Concepcion, A. Corma, M. Renz. Catalysis Today 121 (2007) 39. (b) M. Boronat, P. Concepcion, A. Corma, M. T. Navarro, M. Renz, S. Valencia. Phys. Chem. Chem. Phys. 11 (2009) 2876.

[61] (a) E. A. Pidko, P. Mignon, P. Geerlings, R. A. Schoonheydt, R. A. van Santen. J. Phys. Chem. C 112 (2008) 5510. (b) F. Tielens, J. F. M. Denayer, I. Daems, G. V. Baron, W. J. Mortier, P. Geerlings. J. Phys. Chem. B 107 (2003) 11065.

[62] T. Blasco, M. A. Camblor, A. Corma, P. Esteve, J. M. Guil, A. Martinez, J. A. Perdigon-Melon, and S. J. valencia, J. Phys. Chem. B 102 (1998) 75.

[63] (a) I. Phpai, A. Goursot, F. Fajula, D. Plee, J. Weber. J. Phys. Chem.99 (1995) 12925. (b) S. Krishnamurty, R. K. Roy, R. Vetrivel, S. Iwata, and S. Pal, J. Phys. Chem. A 101 (1997) 7253. (c) R. Ch. Deka, R. Vetrivel, and S. Pal, J. Phys. Chem. A 103 (1999) 5978.

[64] (a) E. L. Meijer, R. A. van Santen, A. P. J. Jansen, J. Phys. Chem. A 103 (1999) 2553. (b) E. H. Teunissen, A. P. J. Jansen, R. A. van Santen, J. Phys. Chem. 99 (1995) 1873.

[65] (a) V. Bolis, S. Bordiga, C. Lamberti, S. Zecchina, F. Rivetti, G. Spano and G. petrini, Langmur, 15 (1999) 5753. (b) V. Bolis, S. Bordiga, C. Lamberti, S. Zecchina, A. Carati, F. Rivetti, G. Spano and G. petrini, Macroporous Mater. 30

(1999) 67. (c) F. Bonino, A. Damin, S. Bordiga, C. Lamberti, A. Zecchina, Langmuir 19 (2003) 2155. (d) A. Damin, S. Bordiga, C. Lamberti, A. Zecchina, K. Doll. J. Chem. Phys. 118 (2003) 10183. (e) S. Bordiga, A. Damin, F. Bonino, A. Zecchina, G. Spano, F. Rivetti, V. Bolis, C. Prestipino, and C. Lambeti, J. Phys. Chem. B 106 (2002) 9892. (f) A. Zecchina, S. Bordiga, G. Spoto, A. Damin, G. Berlier, F. Bonino, C. Prestipino and C. Lamberti, Top. Catal. 21 (2002) 67.

[66] (a) I. Pbpai, A. Goursot, F. Fajula, J. Phys. Chem. 98 (1994) 4654. (b) N. Jardillier, D. Berthomieu, A.Goursot, J. U. Reveles, A. M. Koster, J. Phys. Chem. B 110 (2006) 18440. (c) A. Martınez, A. Goursot, B. Coq, G. Delahay. J. Phys. Chem. B 108 (2004) 8823. (d) S. Krishnamurty, T. Heine, A. Goursot. J. Phys. Chem. B 107 (2003) 5728. (e) T. Heine, A. Goursot, G. Seifert, J. Weber. J. Phys. Chem. A 105 (2001) 620.

[67] (a) V. Bonacic-Koutecky, P. Fantucci, J. Koutecky. Chem. Rev. 91 (1991) 1035. (b) W. A. de Heer. Rev. Mod. Phys. 65 (1993) 611. (c) J. A. Alonso. Chem. Rev. 100 (2000) 637.

[68] Physics and Chemistry of Finite Systems: From Clusters to Crystals. edited by P. Jena. S. N. Khanna, B. K. Rao. Kluwer Academic, Dorderecht, Netherlands, Vol. 1 and Vol. 2 (1992).

[69] Clusters of Atoms and Molecules: Theory, Experiment, and Clusters of Atoms. edited by H. Haberland, Springer–Verlag, Heidelberg, (1994).

[70] Methods of Electronic Structure Calculations. Edited by V. Kumar, O. K. Andersen, A. Mookerjee. World Scientific, Singapore. pg. 317, (1994).

[71] Clusters and Nanostructuredl Materials edited by P. Jena, S. n. Behera. Nova Science Publishers. Inc. (1996).

[72] (a) S. Shetty, S. Pal and D. G. Kanhere, J. Phys. Chem. A 108 (2004) 628. (b) R. W. A. Havenith, P. W. Fowler, E. Steiner, S. Shetty, D. G. Kanhere and S. Pal, Phys. Chem. Chem. Phys. 6 (2004) 285.

[73] (a) X. Li, A. E. Kuznetsov, H–F. Zhang, A. I. Boldyrev, L–S. Wang. Science. 291 (2001) 859. (b) X. Li, H. Wu, X-B. Wang, L-S. Wang. Phys. Rev. Lett. 81, 1909, (1998).

[74] T. P. Martin, Phys. Rep. 273(1996) 199.

[75] W. D. Knight, K. Clemenger, W. A. de Heer, W. A. Saunders. Phys. Rev. B 31 (1985) 1539.

[76] M. Y. Chou, M. L. Cohen. Phys. Lett.A 113 (1986) 420.

[77] U. Ray, M. F. Jarrold, J. E. Bower. J. S. Kraus. Chem. Phys. Lett. 159 (1989) 221.

[78] (a) J. A. Harris, R. S. Kidwell, J. A. Northby. Phys. rev. Lett. 53 (1984) 2390. (b) O. Echt, K. Sattler, E. Recknagel. Phys. Rev. Lett. 47 (1981) 1121.

[79] V. Kumar, Y. Kawazoe Appl. Phys. Lett. 83 (2003) 2677.

[80] C. Thomas, W.-J. Zheng, T. P. Lippa, S.-J. Xu, S. A. Lyapustina, and K. H. Bowen, Jr. J. Chem. Phys. 114 (2001) 9895.

[81] J. Zhao, B. Liu, H. Zhai, R. Zhou, G. Ni, Z. Xu Solid. State. Commun. 122 (2002) 543.

[82] V. Kumar, V. Sundarajan. Phys. Rev. B 57 (1998) 4939.

[83] K. Joshi, D. G. Kanhere. Phys. Rev. A 65 (2002) 043203.

[84] V. Bonacic-Koutecky, P. Fantucci, J. KouteckÂ´y. Chem. Rev. 91 (1991) 1035.

[85] (a) L. Hanley, S. L. Anderson. J. Phys. Chem. 91 (1987) 5161. (b) L. Hanley, S. L. Anderson. J. Chem. Phys. 89 (1988) 2848.

[86] (a) M. F. Jarrold, J. E. Bower. J. Am. Chem. Soc. 110 (1988) 70. (b) M. F. Jarrold, J. E. Bower. Chem. Phys. Lett. 144 (1988) 311.

[87] (a) B. K. Rao, P. Jena. Phys. Rev. B 32 (1985) 2058. (b) P. Jena, B. K. Rao, R. M. Nieminen. Solid State Commun. 59 (1986) 509. (c) P. Fantucci, J. Koutecky, G. Pacchioni. J. Chem. Phys. 88 (1988) 325. (d) P. Blaise, F. Spiegelmann, D. Maynau, J. P. Malrieu. Phys. Rev. B 41 (1990) 5566.

[88] S. Shetty, S. Pal and D. G. Kanhere. J. Chem. Phys. 118 (2003) 7288.

[89] S. Chacko, M. Deshpande, D. G. Kanhere. Phys. Rev. B 64 (2003) 155409.

[90] W. Andreoni. Phys. Rev. B 45 (1992) 4203.

[91] M. Heinebrodt, N. Malinowski, F. Tast, W. Branz, I. M. L. Billas, and T. P. Martin. J. Chem. Phys. 110 (1999) 9915.

[92] M. Schmidt, R. Kusche, W. Kronmüller, B. von Issendorf, and H.Haberland, Phys. Rev. Lett. 79 (1997) 99.

[93] M. Schmidt, R. Kusche, B. von Issendorf, and H. Haberland, Nature London 393 (1998) 238.

[94] M. Schmidt, R. Kusche, T. Hippler, J. Donges, W. Kronmüller, B. von Issendorff, and H. Haberland, Phys. Rev. Lett. 86 (2001) 1191.

[95] M. Schmidt and H. Haberland, C. R. Phys. 3 (2002) 327.

[96] M. Schmidt, J. Donges, Th. Hippler, and H. Haberland, Phys. Rev. Lett. 90 (2003) 103401.

[97] H. Haberland, T. Hippler, J. Donges, O. Kostko, M. Schmidt, and B. von Issendorff, Phys. Rev. Lett. 94 (2005) 035701.

[98] F. Chirot, P. Feiden, S. Zamith, P. Labastie, and J. M. L'Hermite, J. Chem. Phys. 129 (2008) 164514.

[99] C. Hock, S. Strassburg, H. Haberland, B. von Issendorff, A. Aguado, and M. Schmidt, Phys. Rev. Lett. 101 (2008) 023401.

[100] A. A. Shvartsburg and M. F. Jarrold, Phys. Rev. Lett. 85 (2000) 2530.

[101] G. A. Breaux, C. M. Neal, B. Cao, and M. F. Jarrold, Phys. Rev. B 71 (2005) 073410.

[102] G. A. Breaux, R. C. Benirschke, T. Sugai, B. S. Kinnear, and M. F. Jarrold, Phys. Rev. Lett. 91 (2003) 215508.

[103] G. A. Breaux, D. A. Hillman, C. M. Neal, R. C. Benirschke, and M. F. Jarrold, J. Am. Chem. Soc. 126 (2004) 8628.

[104] G. A. Breaux, B. Cao, and M. F. Jarrold, J. Phys. Chem. B 109 (2005) 16575.

[105] G. A. Breaux, R. C. Benirschke, and M. F. Jarrold, J. Chem. Phys. 121 (2004) 6502.

[106] G. A. Breaux, C. M. Neal, B. Cao, and M. F. Jarrold, Phys. Rev. Lett. 94 (2005) 173401.

[107] C. M. Neal, A. K. Starace, M. F. Jarrold, K. Joshi, S. Krishnamurty, and D. G. Kanhere, J. Phys. Chem. C 111 (2007) 17788.

[108] C. M. Neal, A. K. Starace, and M. F. Jarrold, Phys. Rev. B 76 (2007) 054113.

[109] M. F. Jarrold, B. Cao, A. K. Starace, C. M. Neal, and O. H. Judd, J. Chem. Phys. 129 (2008) 014503.

[110] A. K. Starace, C. M. Neal, B. Cao, M. F. Jarrold, A. Aguado, and J. M. López, J. Chem. Phys. 129 (2008) 144702.

[111] W. Zhang, F. Zhang, and Z. Zhu, Phys. Rev. B 74 (2006) 033412.

[112] Z. H. Li and D. G. Truhlar, J. Am. Chem. Soc. 130 (2008) 12698.

[113] P. J. Hsu, J. S. Luo, S. K. Lai, J. F. Wax, and J.-L. Bretonnet, J. Chem. Phys. 129 (2008) 194302.

[114] J. G. O. Ojwang', R. van Santen, G. J. Kramer, A. C. T. van Duin, and W A. Goddard, J. Chem. Phys. 129 (2008) 244506.

[115] S. M. Ghazi, S. Zorriasatein, and D. G. Kanhere, J. Phys. Chem. A 113 (2009) 2659.

[116] P. Pawlow, Z. Phys. Chem. 65 (1909) 1.

[117] (a) H. Haberland, T. Hippler, J. Donges, O. Kostko, M. Schmidt, and B. V. Issendorff, Phys. Rev. Lett. 94 (2005) 035701. (b) A. Aguado and J. M. López, Phys. Rev. Lett. 94 (2005) 233401. (c) A. Aguado, J. Phys. Chem. B 109 (2005) 13043. (d) E. G. Noya, J. P. K. Doye, D. J. Wales, and A. Aguado, Eur. Phys. J. D 43 (2007) 57.

[118] A. K. Starace, C. M. Neal, B. Cao, M. F. Jarrold, A. Aguado, and J. M. López, J. Chem. Phys. 131 (2009) 044307.

[119] (a) C. M. Neal, A. K. Starace, and M. F. Jarrold, J. Phys. Chem. A 111 (2007) 8056. (b) F. Chirot, P. Feiden, S. Zamith, P. Labastie, and J. M. L'Hermite, J. Chem. Phys. 129 (2008) 164514. (c) M. F. Jarrold and E. C. Honea, J. Phys. Chem. 95 (1991) 9181.

[120] (a) C. M. Neal, G. A. Breaux, B. Cao, A. K. Starace, and M. F. Jarrold, Rev. Sci. Instrum. 78 (2007) 075108. (b) J. Bohr, Int. J. Quantum Chem. 84 (2001) 249. (c) D. Poland, J. Chem. Phys. 126 (2007) 054507.

[121] T. X. Li, S. M. Lee, S. J. Han, and G. H. Wang, Phys. Lett. A 300 (2002) 86.

[122] C. L. Cleveland, W. D. Luedtke, and U. Landman, Phys. Rev. Lett. 81 (1998) 2036.

[123] (a)D. Schebarchov and S. C. Hendy, Phys. Rev. Lett. 95, 116101 2005. (b) D. Schebarchov and S. C. Hendy, Phys. Rev. B 73 2006 (121402 (R)).

[124] (a) M. F. Jarrold and J. E. Bower, J. Chem. Phys. 98 (1993) 2399. (b) P. Weis, T. Bierweiler, E. Vollmer, and M. M. Kappes, J. Chem. Phys. 117 (2002) 9293.

[125] P. Chandr `achud, K. Joshi. D. G. Kanhere, Phys. Rev. B, 76 (2007) 235423.

[126] (a) H. S. De, S. Krishnamurty and S. Pal, J. Phys. Chem. C, 113 (2009), 7101. (b) H. S. De, S. Krishnamurty and S. Pal, J. Phys. Chem. C, 114 (2010) 6690.

[127] (a) M. Haruta, Gold Bull. 37 (2004) 27. (b) M. Haruta, M. Date, Appl. Catal., A 222 (2001) 427.

[128] (a) U. Landman, W. D. Luedtke, N. A. Burnham, R. Colton, J. Science 248 (1990) 454. (b) Y. Yang, S. Chen, Nano Lett. 3 (2003) 75. (c) P. Pyykko, Inorg. Chim. Acta 358 (2005) 4113.

[129] S. Krishnamurty, G. S. Shafai, D. G. Kanhere, B. Soule de Bas, M. J. Ford, J. Phys. Chem. A 111 (2007) 10769.

[130] P. Pykko, Chem. ReV. 37 (2008) 1967.

[131] (a) W. T. Wallace, R. B. Wyrwas, R. L. Wheten, R. Mitric, V. Bonacic-Koutecky, J. Am. Chem. Soc. 125 (2003) 8408. (b) B. von Issendorff, H. Hakkinen, M. Moseler, U. Landman, Chem. Phys. Chem. 8 (2007) 157. (c) C. Luo, W. Fa, J. Dong, J. Chem. Phys. 125 (2006) 84707. (d) D. G. Barton, S. Podkolzin, J. Phys. Chem. B 109 (2005) 2262. (e) L. Barrio, P. Lui, J. Rodriguez, J. M. Campos-Martin, J. L. G. Fierro, J. Phys. Chem, C 111 (2007) 19001. (f) W. T. Wallace, R. L. Wheten, J. Am. Chem. Soc. 124 (2002) 7499.

[132] (a) M. Okumura, M. Haruta, Y. Kitagawa, K. Yamaguchi, Gold. Bull. 40 (2007) 40. (b) S. Chretien, H. Metiu, J. Chem. Phys. 126 (2007) 104701. (c) K. J. Naresh, K. R. S. Chandrakumar and Swapan K. Ghosh, J. Phys. Chem. C, 113 (41), (2009) 17885–17892.

[133] (a) G. Shafai, S. Hong, M. Bertino, T. S. Rahman, J. Phys. Chem. C 113 (2009) 12072.

[134] (a) R. Ferrando, J. Jellinek, R. L. Johnston, Chem. Rev. Washington, D. C. 108 (2008) 845. (b) A. O. Orlov, I. Amlani, G. H. Bernstein, C. S. Lent, G. L. Snider, Science 277 (1997) 928. (c) M. Valden, X. Lai, D. W. Goodman, Science 281 (1998) 1647.

[135] B. Cao, A. K. Starace, O. H. Judd, M. F. Jarrold, J. Am. Chem. Soc. 131 (2009) 2446.

[136] Z. Romanowski, S. Krukowski, I. Grzegory, S. Porowski, J. Chem. Phys. 114 (2001) 6353.

[137] D. M. Mann, H. P. Broida. J. Appl. Phys. 44 (1973) 4950.

[138] D. M. Cox, D. J. Trevor, R. L. Wheten, A. Kaldor. J. Phys. Chem. 92 (1988) 421.

[139] A. Fielicke, A. Kirilyuk, C. Ratsch, J. Behler, M. Scheffler, G. von Helden, G. Meijer. Phys. Rev. Lett. 93 (2004) 023401.

[140] P. Weis, T. Bierweiler, S. Glib, M. M. Kappes. Chem. Phys. Lett. 355 (2002) 355.

[141] (a) S. Bulusu, X. Li, L-S. Wang, and X. C. Zeng, Proc. Natn. Acad. Sci. 103 (2006) 8326. (b) B. Kran, S. Bulusu, H-J. Zhai, S. Yoo, X. C. Zeng, and L-S. Wang, 102 (2005) 961.

[142] W. D. Knight, W. A. De Heer, W. A. Saunders, K. Clemenger, M. Y. Chou, M. L. Cohen. Chem. Phys. Lett. 134 (1987) 1.

[143] W. Ekardt. Phys. Rev. B 29 (1984) 1558.

[144] M. Brack. Rev. Mod. Phys. 65 (1993) 677.

[145] S. Kirkpatrick, C. D. Gelatt, M. P. Vecchi. Science 220 (1983) 671.

[146] I. Boustani, W. Pewestorf, P. Fantucci, V. Bonacic-Koutecky, J. Koutecky. Phys. Rev. B B35 (1987) 9437.

[147] P. Jena, S. N. Khanna, B. K. Rao, Microclusters. Edited by S. Sugano, Y. Nishina, S. Ohnishi. Springer–Verlag, Heidelberg, (1987)

[148] Ph. D. Thesis, Sharan Shetty, Pune University (2005).

[149] R. Car, M. Parrinello. Phys. Rev. Lett. 55 (1985) 2471.

[150] G. Galli, R. Martin, R. M. Car, M. Parrinello. Science 250 (1990) 1547.

[151] (a) P. Ballone, W. Andreoni, R. Car, M. Parrinello. Phys. Rev. Lett. 60 (1988) 271. (b) D. Hohl, R. O. Jones, R. Car, M. Parrinello. Phys. rev. Lett. 139 (1987) 540.

[152] M. P. Allen, D. J. Tildesley. Computer Simulation of Liquids. Claredon Press, Oxford (1987).

CHAPTER 2

Theoretical Methods and Computational Aspects

Abstract:

As discussed in chapter 1, the aim of the thesis is to address the structure-property relationship of two heterogeneous catalysts viz. zeolite and metal clusters. This chapter is devoted to some of the theoretical approaches used for the description of periodic and non-periodic systems. The methodology used in both cases is based on Density Functional Theory. Later, we also discuss the AIMD technique based on the DFT, to study the adsorption properties of metal clusters. Finding the ground state geometry and the properties associated with material has been a central goal of many researchers. Both these methodologies will be elaborated in this chapter.

In the last decade, various quantum mechanical methods have been implemented to treat the electronic structure of molecules, clusters and solids. We begin Section 2.1 with a brief introduction to the many-body problem by discussing the Born-Oppenheimer approximation, Hartree approximation, Hartree-Fock theory, and methods beyond Hartree-Fock. In Section 2.2 we provide a summary of density functional theory which is as an alternative route for performing such calculations. Special attention is given to the Hohenberg-Kohn theorems, Kohn-Sham equations, and the different exchange-correlations functionals. In Section 2.3 a description of the concepts of molecular dynamics is given while the foundations of *ab initio* molecular dynamics are laid in Section 2.4. In Section 2.4 we explain and compare the ideas and

algorithms behind Born-Oppenheimer molecular dynamics and Car-Parrinello molecular dynamics. Lastly, the implementation of the above mentioned methods via the plane wave-pseudopotential approach employed in Vienna *ab initio* simulations package (VASP) for performing solid-state calculations is discussed in section 2.5. In the last section 2.6 of this chapter, we discuss the interpretation of the data obtained from these theoretical calculations. For further detailed information on the other theoretical methods, interested reader is referred to the review by Payne et al. [1a]

2.1 The many-body problem

Any given system composed of N electrons and M nuclei can be determined by solving the Schrödinger equation. The *time-independent Schrödinger equation* [1b] has the form

$$H\Psi = E\Psi \tag{2.1.1}$$

where Ψ is the wavefunction of the system, E is the energy eigenvalue and H is the Hamiltonian operator. H is the sum of the kinetic energy T and potential energy V operators and can be written as

$$H = -\sum_{i=1}^{N}\frac{\hbar^2}{2m}\nabla_i^2 - \sum_{A=1}^{M}\frac{\hbar^2}{2M_A}\nabla_A^2 + \frac{1}{2}\sum_{i\neq j}^{N}\frac{e^2}{r_{ij}} + \frac{1}{2}\sum_{A\neq B}^{M}\frac{Z_A Z_B e^2}{R_{AB}} - \sum_{i=1}^{N}\sum_{A=1}^{M}\frac{Z_A e^2}{r_{iA}} \tag{2.1.2}$$

In the above equation the first two terms are the kinetic energies of N electrons with masses m and M nuclei with masses M_A, the third term is the electrostatic repulsion between electrons separated by r_{ij}, fourth term is the electrostatic repulsion between nuclei separated by R_{AB} and the last term is the Coulombic attraction between electrons and nuclei r_{iA} distance apart.

2.1.1 Born-Oppenheimer approximation

Since nuclei have much larger masses their velocities are consequently smaller

compared to electrons. The *Born-Oppenheimer approximation* [2] assumes that the nuclei are fixed which amounts to removing the second term in Equation (2.1.2). Due to the above approximation, the fourth term is a constant and is included in the total energy after calculating the wavefunction. These simplifications result in the electronic Hamiltonian operator (H_e):

$$H_e = -\sum_{i=1}^{N} \frac{1}{2}\nabla_i^2 + \sum_{i\neq j}^{N} \frac{1}{r_{ij}} - \sum_{i=1}^{N}\sum_{A=1}^{M} \frac{Z_A e^2}{r_{iA}} \qquad (2.1.3)$$

The conceptual and numerical problems related to the electron-electron interactions (second term) in Equation (2.1.3) are the most challenging to deal with. An elementary scheme would be to set the corresponding terms to zero implying that the *N* electrons move completely independent of each other. Then the total wavefunction **Ψ**

$$\Psi = \psi_1(r_1)\psi_2(r_2)...\psi_N(r_N) \qquad (2.1.4)$$

becomes a product of *N* one-electron wavefunctions ψ_i. However such a Hamiltonian is very archaic and hence electron-electron interactions must be calculated.

2.1.2 Hartree approximation

To have the similaristic model of electron-electron interactions, under the Hartree approximation each electron is thought of as moving in a field built by all other electrons. The electron-electron interactions then depend only on the positions of the electron under consideration which moves in an electronic sea made by the rest of the electrons. The second term in Equation (2.1.3) can therefore be approximated as a sum of one-electron potentials v_i

$$\sum_{i\neq j}^{N} \frac{1}{r_{ij}} \approx \sum_{i=1}^{N} v_i(r_i) = \sum_{i=1}^{N} \int \frac{\rho(r_j) - |\psi_i(r_j)|^2}{|r_i - r_j|} dr_j \qquad (2.1.5)$$

where ψ_i is the orbital for the i^{th} electron. The solution of Hartree approximation needs to be derived self-consistently because calculation of ψ_i depends on $\Sigma(1/r_{ij})$ which in turn is defined in terms of ψ_i. The total wavefunction is still expressed as the *Hartree product* as given in Equation (2.1.4). However it is not antisymmetric with respect to exchange of electrons and does not account for the Pauli exclusion principle. In order to bring in the Pauli exclusion principle one has to go beyond the Hartree method.

2.1.3 Hartree-Fock approximation: Slater determinant

Thus, the many electron wavefunction **Ψ** may be approximated in the form of a *Slater determinant* composed of an antisymmetrized product of *N* orthonormal spin orbitals $\psi_i(x)$ for all the electrons, where each $\psi_i(x)$ is a product of a spatial orbital $\varphi_k(r)$ and a spin function $\sigma(s) = \alpha(s)$ *or* $\beta(s)$.

$$\Psi_{HF} = \frac{1}{\sqrt{N!}} \begin{vmatrix} \psi_1(x_1)...\psi_2(x_1).....\psi_N(x_1) \\ \psi_1(x_2)...\psi_2(x_2).....\psi_N(x_2) \\ ..... \\ ..... \\ \psi_1(x_N)...\psi_2(x_N).....\psi_N(x_N) \end{vmatrix} \equiv \frac{1}{\sqrt{N!}} \det[\psi_1\psi_2....\psi_N] \qquad (2.1.6)$$

In the *Hartree-Fock (HF) approximation* [3] the orthonormal spin orbitals that minimize the total energy is given by

$$E[\Psi] = \frac{\langle \Psi \mid H \mid \Psi \rangle}{\langle \Psi \mid \Psi \rangle} \qquad (2.1.7)$$

for the above determinant form of Ψ_{HF} are found. The normalization integral $\langle \Psi_{HF} \mid \Psi_{HF} \rangle$ is equal to 1 and energy is given by the formula

$$E_{HF} = \langle \Psi_{HF} \mid H \mid \Psi_{HF} \rangle = \sum_{i=1}^{N} H_i + \frac{1}{2} \sum_{i,j=1}^{N} (J_{ij} - K_{ij}) \qquad (2.1.8)$$

where
$$H_i = \int \psi_i^*(x)\left[-\frac{1}{2}\nabla^2 + v(x)\right]\psi_i(x)dx \tag{2.1.9}$$

$$J_{ij} = \iint \psi_i(x_1)\psi_i^*(x_1)\frac{1}{r_{12}}\psi_j^*(x_2)\psi_j(x_2)dx_1dx_2 \tag{2.1.10}$$

$$K_{ij} = \iint \psi_i^*(x_1)\psi_j(x_1)\frac{1}{r_{12}}\psi_i(x_2)\psi_j^*(x_2)dx_1dx_2 \tag{2.1.11}$$

The J_{ij} are called C*oulomb integrals* and K_{ij} are called *exchange integrals*. Minimization of Equation (2.1.8) subject to the orthogonalization conditions gives the HF differential equations

$$F\Psi_i(x) = \sum_{j=1}^{N}\varepsilon_{ij}\psi_j(x) \tag{2.1.12}$$

where
$$F = -\frac{1}{2}\nabla^2 + v + g = -\frac{1}{2}\nabla^2 + v + j - k \tag{2.1.13}$$

and j and k are the Coulomb and exchange operators respectively. In the HF scheme the one-electron effective potential has the form $v + g$, where v is the potential of an electron in the external field and g is equal to sum of Coulomb potential, taking into account the repulsion of the other electrons, and the exchange potential, which has no classical interpretation and is caused by the antisymmetrization of the one-electron functions in the expressions for ψ. The Coulomb and exchange potentials for each ψ_i depend on the solutions ψ_j of all the other equations with j≠i. Therefore the HF equations form a system of interrelated equations that is solved by the *self-consistency method*.

Even if the HF equations are correctly solved, the method eventually turns out to be theoretically incomplete. Despite the correct treatment of electronic exchange within the HF theory, electronic correlation is totally missing. Consequently the *correlation energy* may be defined as the difference between the correct energy and that of the HF solution i.e. $E_{corr} \equiv E - E_{HF}$. Therefore, for including correlation one has

to go beyond the HF theory.

2.1.4 Beyond Hartree-Fock (Correlation energy)

Some instances of the different methods that take correlation effects into account are the Møller-Plesset (MP) perturbation theory [4], configuration interaction (CI) [5] and coupled cluster (CC) [6]. In perturbation theory the difference between the exact Hamiltonian and sum of one electron operators is introduced as a perturbation to the unperturbed HF solution. Correlation corrections can be derived to a chosen order. Another way to include correlation is to work with a multi-determinant wavefunction instead of the single-determinant wavefunction. This approach is used in CI and CC methods. Treatment of exchange and correlation follows another route in the density functional theory which is covered in the next section.

2.2 Density functional theory

The *density functional theory* (DFT) [7] allows one to move away from the *N*-electron wavefunction **Ψ** and its associated Schrödinger equation and replace them by the much simpler electron density *ρ(r)* and its corresponding calculation scheme. The history of using electron density as the basic variable began with the pioneering work of Thomas and Fermi.

2.2.1 Thomas-Fermi theory

Thomas [8] and Fermi [9] proposed in 1927 that statistical considerations can be used to estimate the distribution of electrons in an atom. In this method the kinetic energy is approximated as an explicit functional of density, idealized as non-interacting electrons in a homogeneous gas with a density equal to the local density at the given point. Neglecting the exchange and correlation terms, the *Thomas-Fermi (TF) total energy* of an atom with a nuclear charge Z in terms of electron density is given by

$$E_{TF}[\rho(r)] = C_F \int \rho^{5/3}(r)dr - Z\int \frac{\rho(r)}{r}dr + \frac{1}{2}\iint \frac{\rho(r)\rho(r')}{|r-r'|}drdr' \quad (2.2.1)$$

where the Fermi coefficient C_F = 2.871. Assuming that for the ground state of an atom the electron density minimizes the energy functional $E_{TF}[\rho(r)]$ under the constraint

$$N = N[\rho(r)] = \int \rho(r)dr \tag{2.2.2}$$

Applying the method of Lagrange multipliers to incorporate the constraint, the ground-state electron density must satisfy the variational principle

$$\delta\left\{E_{TF}[\rho] - \mu_{TF}\left(\int \rho(r)dr - N\right)\right\} = 0 \tag{2.2.3}$$

which yields

$$\mu_{TF} = \frac{\delta E_{TF}[\rho]}{\delta\rho(r)} = \frac{5}{3}C_F\rho^{2/3}(r) - \left[\frac{Z}{r} - \int \frac{\rho(r_2)}{|r - r_2|}dr_2\right] \tag{2.2.4}$$

Hence, the TF theory involves solving the Equation (2.2.4) under the constraint (2.2.2) and inserting the resulting electron density in Equation (2.2.1) to yield the total energy.

The TF theory though allows the explicit calculation of an atom's total energy, its accuracy is low. The errors for the total energies of atoms are relatively large and still more for molecules which are unstable within the TF theory. Due to these reasons, this method was considered as an oversimplified model.

2.2.2 Hohenberg-Kohn theorems

The modern formulation of density functional theory originated with the fundamental theorems of Hohenberg and Kohn [10]. The *first Hohenberg-Kohn (HK) theorem* states that: *The external potential v(r) is determined, within a trivial additive constant, by the electron density* $[\rho(r)]$. Since $[\rho(r)]$ determines the number of

electrons, it follows that $[\rho(r)]$ also determines the ground-state wavefunction **Ψ** and all other properties such as kinetic energy $T[\rho(r)]$, potential energy $V[\rho(r)]$ and total energy $E[\rho(r)]$ of the system. Hence the ground state expectation value of any observable, including the total energy, is a unique functional of the ground-state electron density $[\rho(r)]$.

$$E_v[\rho] = T[\rho] + V_{ne}[\rho] + V_{ee}[\rho] = \int \rho(r)v(r)dr + F_{HK}[\rho] \qquad (2.2.5)$$

where

$$F_{HK}[\rho] = T[\rho] + V_{ee}[\rho] \qquad (2.2.6)$$

The *second HK theorem* states that: *For a trial density* $\tilde{\rho}(r)$ *such that* $\tilde{\rho}(r) \geq 0$ *and* $\int \tilde{\rho}(r)dr = N$,

$$E_0 \leq E_v[\tilde{\rho}] \qquad (2.2.7)$$

This provides a variational principle such that the search for the lowest-energy wavefunction $\mathbf{\Psi_0(r)}$ can be replaced by a search for the lowest energy electron density $[\rho_0(r)]$and the ground-state energy E_0 is given as the minimum of the functional $E_v[\rho_0(r)]$.

The classical part of the electron-electron interaction $V_{ee}[\rho(r)]$ in Equation (2.2.6) is the Coulomb potential energy

$$J[\rho] = \frac{1}{2}\iint \frac{\rho(r_1)\rho(r_2)}{|r_2 - r_1|}dr_1 dr_2 \qquad (2.2.8)$$

In the TF theory $V_{ee}[\rho(r)]$ is replaced by $J[\rho(r)]$ and kinetic energy $T[\rho(r)]$ is taken from the theory of a non-interacting uniform electron gas. This constitutes a direct approach for calculating $T[\rho(r)]$ and therefore the total energy if the electron density is known but only approximately. It would however be preferable to correctly

calculate $T[\rho(r)]$ as it forms the leading part of the total energy. Kohn and Sham proposed introducing orbitals into the problem allowing more accurate computation of $T[\rho(r)]$ with a small residual correction that is handled separately.

2.2.3 Kohn-Sham equations

For a system of noninteracting electrons the kinetic energy is

$$T_0 = \sum_{i=1}^{N} n_i \langle \psi_i | -\frac{1}{2}\nabla^2 | \psi_i \rangle \tag{2.2.9}$$

and the electron density is

$$\rho(r) = \sum_{i=1}^{N} n_i \, | \psi_i(x) |^2 \tag{2.2.10}$$

with x including both space and spin coordinates. Here ψ_i and n_i are the natural spin orbitals and their occupation numbers respectively. Using orbitals to calculate the kinetic energy is an indirect though accurate approach.

Kohn and Sham [11] replaced the interacting many-body problem by a corresponding noninteracting particle system with the same density in an appropriate external potential. The total energy functional is then expressed in atomic units as

$$E[\rho(r)] = T_0[\rho(r)] + \frac{1}{2}\iint \frac{\rho(r)\rho(r')}{|r-r'|} dr dr' + E_{XC}[\rho(r)] + \int \rho(r) v(r) dr \tag{2.2.11}$$

In the above equation the first term is the kinetic energy functional of the system of noninteracting electrons with the same density, the second term is the classical Coulomb energy for the electron-electron interaction, the third term is energy functional incorporating all the many-body effects of exchange and correlation and the last term is the attractive Coulomb potential provided by the fixed nuclei.

The construction of the *Kohn-Sham (KS) functional* is based on the

assumption that the exact ground state density can be represented by the ground state density of an auxiliary system of noninteracting particles. The solution of the KS auxiliary system can be viewed as the minimization problem of the KS functional with respect to the density. This leads to *N* KS equations

$$\left[-\frac{1}{2}\nabla^2 + v_{eff}(r)\right]\psi_i(r) = \varepsilon_i\psi_i(r) \tag{2.2.12}$$

and

$$\rho(r) = \sum_i^N \sum_s |\psi_i(r,s)|^2 \tag{2.2.13}$$

Here ε_i are eigenvalues, ψ_i are KS orbitals and v_{eff} is the effective potential

$$v_{eff}(r) = v(r) + \int \frac{\rho(r')}{|r-r'|}dr' + v_{XC}(r) \tag{2.2.14}$$

that is the sum of potential from the nuclei, a Hartree-style potential and the potential for exchange and correlation. The latter is defined as

$$v_{XC}(r) = \frac{\partial E_{XC}[\rho(r)]}{\partial\rho(r)} \tag{2.2.15}$$

In Equation (2.2.14) $v_{eff}(r)$ depends on $[\rho(r)]$. Hence the KS Equations (2.2.12), (2.2.13) and (2.2.14) have to be solved self-consistently. Therefore, in a DFT calculation one begins with a guess for $[\rho(r)]$ for constructing $v_{eff}(r)$ from Equation (2.2.14). After the first iteration we get a new electron density from which the Hartree and exchange-correlation potentials are generated to yield a new potential. This process is repeated until self-consistency is achieved.

2.2.4 Exchange-correlation functionals

In the KS equations while the kinetic energy is incorporated correctly, a challenge in DFT is the search for a good approximation of the exchange-correlation functional $E_{XC}[\rho(r)]$. One of the many approaches is the *local density approximation (LDA)* [11]. The LDA exchange-correlation energy functional is given as

$$E_{XC}^{LDA}[\rho] = \int \rho(r)\varepsilon_{XC}[\rho(r)]dr \tag{2.2.16}$$

where $E_{XC}[\rho(r)]$ is the exchange-correlation energy per particle of a uniform electron gas of density $[\rho(r)]$. The exchange part of $E_{XC}[\rho(r)]$ can be expressed analytically by that of a homogeneous electron gas.

$$\varepsilon_X[\rho(r)] = -C_X\rho(r)^{1/3}, \quad C_X = \frac{3}{4}\left(\frac{3}{\pi}\right)^{1/3} \tag{2.2.17}$$

The correlation part may be obtained from perturbation theory or from Quantum Monte Carlo method. The corresponding exchange-correlation potential and KS equation then become

$$v_{XC}^{LDA}(r) = \frac{\delta E_{XC}^{LDA}}{\delta\rho(r)} = \varepsilon_{XC}[\rho(r)] + \rho(r)\frac{\partial\varepsilon_{XC}[\rho(r)]}{\partial\rho} \tag{2.2.18}$$

$$\left[-\frac{1}{2}\nabla^2 + v(r) + \int\frac{\rho(r')}{|r-r'|}dr' + v_{XC}^{LDA}(r)\right]\psi_i(r) = \varepsilon_i\psi_i(r) \tag{2.2.19}$$

The self-consistent solution of Equation (2.2.19) defines the *LDA method*. Application of LDA amounts to assuming that the exchange-correlation energy for a nonuniform system can be obtained by applying uniform electron gas results to infinitesimal portions of the nonuniform electron distribution and then summing over all individual

contributions.

LDA is expected to work for systems with slowly varying electron densities. However it was failure for even semiconductors and insulators due to large cancellations in the exchange part. Hence further improvements are called for. A route to bring about this improvement is to take into account the gradient of the electron density. The idea is to include $\partial\rho(r)/\partial r$ as well as $\rho(r)$ to describe the exchange hole. This is implemented via the method of *generalized gradient approximation* (GGA) in which the exchange-correlation energy functional is written as

$$E_{XC}^{GGA}[\rho(r)] = \int \rho(r) F[\rho(r), \nabla\rho(r)] dr \qquad (2.2.20)$$

In 1986 the exchange part of $E_{XC}^{GGA}[\rho(r)]$ was proposed by Perdew and Wang (PW86) [12] and another correction was developed by Becke in 1988 (B88) [13]. Gradient corrections to the correlation part were proposed in 1986 by Perdew (P86) [14], in 1991 by Perdew and Wang (PW91) [15], in 1988 by Lee, Yang and Parr (LYP) [16] and in 1996 by Perdew, Burke and Ernzerhof (PBE) [17]. In all our density functional calculations the PW91 GGA functional and B3LYP GGA functional has been employed.

2.3 Molecular dynamics

The aim of *molecular dynamics* (MD) is to model the detailed microscopic dynamical behavior of many different types of systems as found in chemistry, physics or biology. In such a scenario, the motions of nuclei must be taken care as a function of time and temperature.

In the MD method, nuclear motion of the particles is described using the laws of Newton's mechanics whereby every new distribution is derived from the previous one by using the interactions between the particles. For an i^{th} particle of the system, the total potential energy at time $t_0=0$ is computed as a sum of all pair interactions u_{ij}

$$u(\vec{r}_i) = \sum_j u_{ij}(\vec{r}_i, \vec{r}_j) \tag{2.3.1}$$

Once this is obtained, the force acting on the particle can be calculated as

$$\vec{f}_i = -\nabla u(\vec{r}_i) \tag{2.3.2}$$

which causes an acceleration

$$\vec{a}_i = \frac{\vec{f}_i}{m} \tag{2.3.3}$$

This in turn modifies the initial velocity $\vec{v}_i$ to $\vec{v}_i'$ and then every particle is allowed to move with that velocity over a short period of time Δt. This produces new positions $\vec{r}_i'$ for all the particles at time $t_1 = t_0 + \Delta t$. Next the potential energies u_i', forces $\vec{f}_i'$ and velocities $\vec{v}_i''$ are calculated for this new distribution. This procedure is repeated for a large number of times. Therefore MD simulations can describe systems that evolve in time. The new positions are derived from the Newtonian laws of motion and are therefore deterministic.

2.3.1 Equations of motion

The Hamiltonian for a system of N particles moving under the influence of a potential function $U(R^N)$ is given by

$$H(R^N, P^N) = \sum_{I=1}^{N} \frac{P_I^2}{2M_I} + U(R^N) \tag{2.3.4}$$

where R^N and P^N are the sets containing all the positions and momenta respectively. The forces are derived from the potential

$$F_I(R^N) = -\frac{\partial U(R^N)}{\partial R_I} \tag{2.3.5}$$

The equations of motion are according to Hamilton's equations

$$\dot{R}_I = \frac{\partial H}{\partial P_I} = \frac{P_I}{M_I} \; ; \; \dot{P}_I = -\frac{\partial H}{\partial R_I} = -\frac{\partial U}{\partial R_I} = F_I(R^N) \tag{2.3.6}$$

From which the Newton's second law is obtained

$$M_I \ddot{R}_I = F_I(R^N) \tag{2.3.7}$$

The equations of motion are integrated and atomic trajectories are followed on the potential energy surface.

2.3.2 Numerical integration

The numerical integration techniques are applied on a discretization of time and a repeated calculation of the forces on the particles during the MD simulation. These methods must have the properties of (a) long time energy conservation to ensure that we stay on the constant energy hypersurface and short time reversibility and (b) short time reversibility so that the discrete equation still exhibit the time reversible symmetry of the original differential equations.

A computationally efficient scheme is the *Verlet algorithm* [18]. To derive it $\vec{r}_i(t)$ is expanded forward and backward in time in the third order of Taylor expansion.

$$\vec{r}_i(t+\delta t) = \vec{r}_i(t) + \vec{v}_i(t)\delta t + \frac{1}{2m_i}\vec{f}_i(t)(\delta t)^2 + \frac{1}{6}\vec{b}_i(t)(\delta t)^3 + O((\delta t)^4) \tag{2.3.8}$$

$$\vec{r}_i(t-\delta t) = \vec{r}_i(t) - \vec{v}_i(t)\delta t + \frac{1}{2m_i}\vec{f}_i(t)(\delta t)^2 - \frac{1}{6}\vec{b}_i(t)(\delta t)^3 + O((\delta t)^4) \tag{2.3.9}$$

Adding we get, $$\vec{r}_i(t+\delta t) = 2\vec{r}_i(t) - \vec{r}_i(t-\delta t) + \frac{1}{m_i}\vec{f}_i(t)(\delta t)^2 + O((\delta t)^4) \tag{2.3.10}$$

Subtraction yields $$\vec{v}_i(t) = \frac{1}{2(\delta t)}[\vec{r}_i(t+\delta t) - \vec{r}_i(t-\delta t)] + O((\delta t)^3) \qquad (2.3.11)$$

A MD simulation is usually performed for a fixed number of particles N inside a fixed volume. The initial values for positions and velocities are chosen together with an appropriate time step. The first part of the simulation is the equilibration phase in which strong fluctuations may occur. Once all the important quantities are sufficiently equilibrated, the actual simulation is performed. The time evolution of such a microcanonical ensemble is accumulated over many time steps. Finally observables are calculated from the trajectory as time averages which are thought of as being comparable to experimentally observed ensemble averages.

2.4 *Ab initio* molecular dynamics

The basic idea underlying every *ab intio molecular dynamics* (AIMD) method is to compute the forces acting on the nuclei from electronic structure calculations that are performed on-the-fly as the MD trajectory is generated. In this way the electronic variables are not generated beforehand, but are considered as active degrees of freedom. This implies, that given a suitable approximate solution of the many-electron problem, chemically complex systems can also be handled by MD. Thus, one has to select a particular approximation for solving the Schrödinger equation.

2.4.1 Born-Oppenheimer molecular dynamics

The most commonly employed approach to AIMD is the *Born-Oppenheimer molecular dynamics* (BOMD) in which the electronic problem is solved using DFT for obtaining the ground state eigenvalue. The steps involved in the Born-Oppenheimer Molecular Dynamics algorithm are displayed in Figure 2.1. For an interacting system of electrons with classical nuclei fixed at positions $\{R^N\}$, the total ground state energy can be found by minimizing the KS energy functional (as defined in Equation 2.2.11)

$$\min_{\Psi_0}\left\{\left\langle \Psi_0 \mid H_e \mid \Psi_0 \right\rangle\right\} = \min_{\{\phi_i\}} E^{KS}\left[\{\phi_i\}, R^N\right] \tag{2.4.1}$$

with respect to orbitals which are subject to the orthonormality constraint

$$\left\langle \phi_i \middle| \phi_j \right\rangle = \delta_{ij} \tag{2.4.2}$$

The corresponding Lagrangian for BOMD is therefore

$$L_{BO}(R^N, \dot{R}^N) = \sum_{I=1}^{N} \frac{1}{2} M_I \dot{R}_I^2 - \min_{(\phi_i\})} E^{KS}[\{\phi_i\}, R^N] \tag{2.4.3}$$

and the equations of motion are

$$M_I \ddot{R}_I = -\nabla_I \left[\min_{(\phi_i\})} E^{KS}[\{\phi_i\}, R^N] \right] \tag{2.4.4}$$

The forces between nuclei needed for the implementation of BOMD are

$$\frac{d}{dR_I}\left[\min_{(\phi_i\})} E^{KS}[\{\phi_i\}, R^N] \right] \tag{2.4.5}$$

Once the initial forces are calculated they are next fed into a numerical integration procedure together with a set of initial velocities for the nuclei, and a step of molecular dynamics is carried out, yielding a new set of positions and velocities. At the new nuclear positions, the energy functional is minimized again and a new set of forces is obtained and used to perform another step of MD propagation. This procedure is repeated until an entire trajectory has been generated. These steps involved in BOMD are displayed in the form of a flowchart presented in Fig. 2. which tells that BOMD requires a full self-consistent density functional minimization of energy and its derivative at each point.

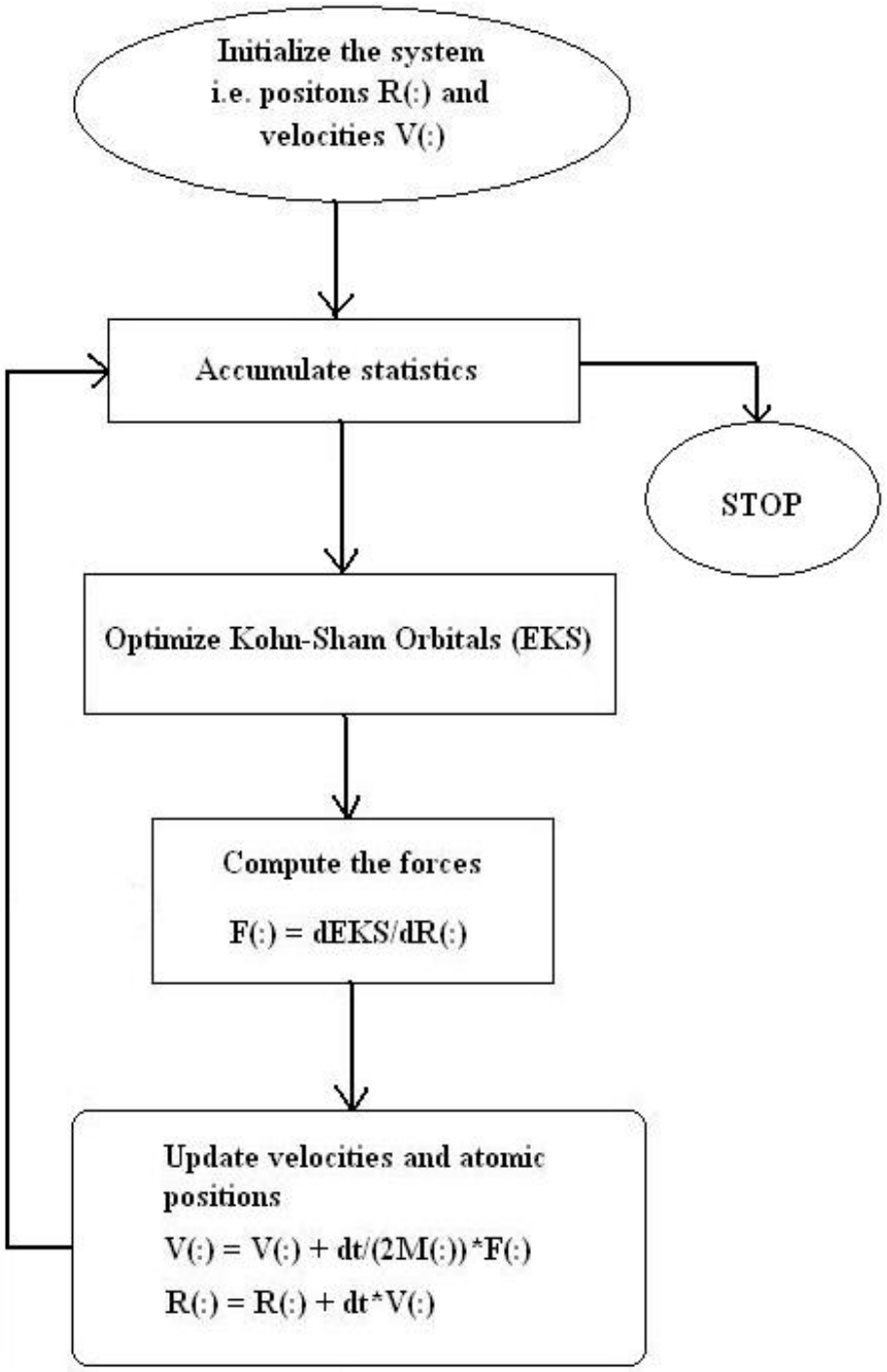

Figure 2.1: Flowchart displaying the steps involved in the Born-Oppenheimer Molecular Dynamics algorithm

For cutting down computational expenses it would therefore be appealing to have an approach that does not require exact calculation of ground state energy at every step. An elegant alternative to BOMD was proposed by Car and Parrinello [19a].

2.4.2 Car-Parrinello molelcular dynamics

Car-Parrinello molecular dynamics (CPMD) [19a] is an efficient way to combine a quantum chemical description of electron dynamics and a classical description of nuclei dynamics in a unique framework. The Car-Parinello approach exploits the time-scale separation of fast electronic and slow nuclear motion. This is achieved by mapping the two-component quantum/classical problem onto a two-component purely classical problem with two separate energy scales.

In CPMD the extended energy functional E^{KS} is considered to be dependent on $\{\Phi_i\}$ and R^N. In classical mechanics the force of the nuclei is obtained as the derivative of a Lagrangian with respect to the nuclear positions. Similarly, a functional derivative with respect to the orbitals, which if also interpreted as classical fields, would yield the force on the orbitals. Car and Parinello postulated the following Lagrangian using E^{KS}

$$L_{CP}(R^N,\dot{R}^N,\{\phi_i\},\{\dot{\phi}_i\})=\sum_{I=1}^{N}\frac{1}{2}M_I\dot{R}_I^2+\sum_i\frac{1}{2}\mu\langle\dot{\phi}_i|\dot{\phi}_i\rangle-\varepsilon^{KS}[\{\phi_i\},R^N] \tag{2.4.9}$$

and the equations of motion are

$$M_I\ddot{R}_I(t)=-\frac{\partial E^{KS}}{\partial R_I}+\sum_{ij}\Lambda_{ij}\frac{\partial}{\partial R_I}\langle\phi_i|\phi_j\rangle \tag{2.4.10}$$

$$\mu\ddot{\phi}_i(t)=-\frac{\delta E^{KS}}{\delta\langle\phi_i|}+\sum_j\Lambda_{ij}|\phi_j\rangle \tag{2.4.11}$$

where μ is the "fictitious mass" or inertia parameter assigned to the degrees of freedom. The forces needed for the implementation of CPMD can be obtained as the

partial derivatives of the KS energy functional with respect to both the nuclear positions and the KS orbitals

$$F(\Phi_i) = -f_i H^{KS} \phi_i \tag{2.4.12}$$

$$F(R_I) = -\frac{\partial E^{KS}}{\partial R_I} \tag{2.4.13}$$

The forces in Equation (2.4.13) are the same forces as in BOMD but in BOMD these were derived under the condition that the wavefunctions are optimized and are therefore are only correct up to the accuracy achieved in the wavefunction optimization. In CPMD these are the correct forces and calculated from analytic energy expressions are correct to machine precision.

In CPMD we begin with a starting configuration for which the KS equation is solved for the electrons. Next the forces are evaluated as the derivative of E^{KS} with respect to nuclear positions as given in Equation (2.4.13). In the same nuclear step the fictitious forces acting on the orbitals are calculated as the functional derivative of E^{KS} with respect to orbitals (see Equation (2.4.12)). This is followed by an update of the nuclear and electronic configurations and another step of MD is performed. For generating a trajectory these steps are continuously repeated.

It is noticeable that only one electronic step is performed for all the nuclear steps and hence the computationally demanding full electronic minimization is executed only for the starting configuration. If μ is small then the new electronic configuration corresponding to the new nuclear configuration will be already near enough to the exact ground state. On the other hand if μ is large then it ensures the use of reasonably large time steps, in order to have a fast integration of the equations.

In addition to above mentioned fundamental concepts, several new MD approaches are developed by many researchers which are not only conceptually simpler but are computationally much more economic than the conventional approaches . For example, S. K. Ghosh and co-workers [19b, 19c] recently proposed a one dimensional descriptor (energy, electron transfer) approach to multidimensional dynamical processes in condensed phase.

However, in the present thesis we use only the AIMD, BOMD approach, to obtain and study the melted surfaces of Al metal clusters.

2.5 Plane wave-pseudopotential method

This section discusses the implementation of the *plane wave-pseudopotential method* within the program code VASP [20,21] used during the course of this work for calculating properties of solids. In an extended solid-state material the number of nuclei and electrons is of the order one mole. The computational problem of solving Schrödinger's equation involves diagonalization of large matrices of the order of one mole X one mole. This challenging task is simplified by exploiting the translational symmetry properties of the crystal in question.

2.5.1 Bloch's theorem and plane wave basis

In an infinite crystal which is translationally invariant under a lattice translation T, the effective KS potential υ_{eff} as defined in Equation (2.2.14) possesses the periodicity of the lattice

$$v_{eff}(r + T) \equiv v_{eff}(r) \tag{2.5.1}$$

Further, in order to satisfy the KS equations one must have

$$\psi_i(k, r + T) = e^{ikT}\psi_i(k, r) \tag{2.5.2}$$

This results in the *Bloch's theorem* [22] for the KS orbitals according to which ψ_i(k,r) can be written as a product of a function $u_i(k,r)$ that has the periodicity of the lattice and a *plane wave* $e^{ik.r}$ with k being a vector in the first *Brillouin zone* (BZ), i.e.

$$\psi_i(k, r) = e^{ikr}u_i(k, r) \tag{2.5.3}$$

The periodic function can be expanded in the plane wave basis as

$$u_i(r,k) = \frac{1}{\sqrt{\Omega_{cell}}} \sum_G c_i(G,k) \exp[iG.r] \tag{2.5.4}$$

where Ω_{cell} is the volume of the primitive cell and G are the reciprocal lattice vectors. In the above form the $\psi_i(k,r)$'s are k-dependent. The complete set of G vectors is infinite and evaluating sums over all such vectors would be computationally expensive. Since orbitals and densities tend to become smooth at small scales, i.e. the plane wave components become negligible for large G vectors, therefore during calculations the infinite sums over G vectors and cells can be truncated.

2.5.2 Pseudopotentials

The most common *pseudopotential* (PP) approach is the *frozen core approximation* which is based on the fact that physical and chemical properties of crystals mostly depend on the distribution of the valence electrons. Hence the core electrons can be considered to be "frozen" while keeping intact the core electron distribution of the isolated atom in the crystal environment. In turn, the long range interactions of the core are accounted for by PPs.

Conventionally the PP is constructed by satisfying four general criteria:

(a) the valence pseudo-wavefunction Φ_l^{PS} must be the same as the all-electron (AE) wavefunction Φ_l^{AE} outside a given cut-off radius R_{cut},

(b) the charge enclosed within R_{cut} must be equal for the two wavefunctions, i.e.

$$\int_0^{R_{cut}} \left|\Phi_l^{PS}(r)\right|^2 dr = \int_0^{R_{cut}} \left|\Phi_l^{AE}(r)\right|^2 dr \tag{2.5.5}$$

and is normalized such that

$$\int_0^{\infty} \left|\Phi_l^{PS}(r)\right|^2 dr = \int_0^{\infty} \left|\Phi_l^{AE}(r)\right|^2 dr = 1 \tag{2.5.6}$$

This is commonly referred to as *norm-conservation*,

(c) Φ_{PS} must not have any radial nodes within the core region and,

(d) the valence AE and PP eigenvalues must be equal. These features are illustrated in Figure 2.2.

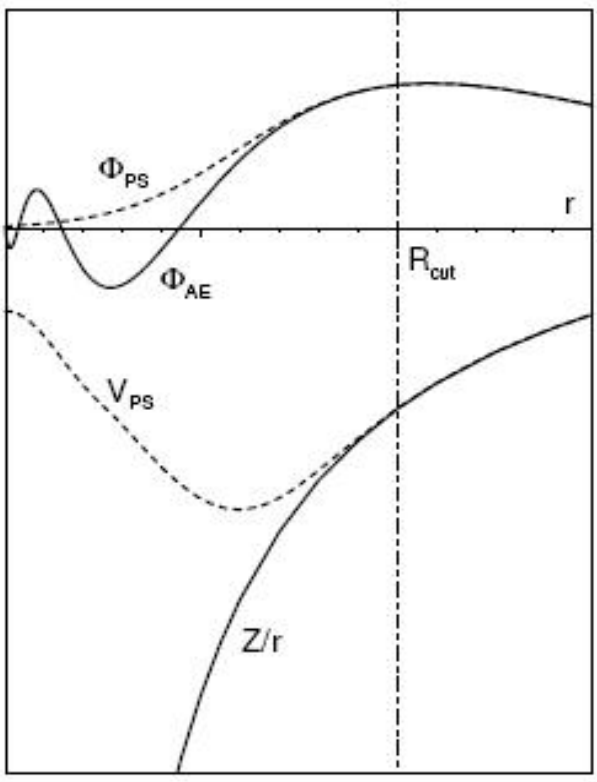

Figure 2.2: A schematic diagram of an atomic all-electronic wavefunction (solid line) and the corresponding atomic pseudo wavefunction (dashed line) together with the respective external Coulomb potential (solid line) and pseudopotential (dashed line).

Application of PPs has various advantages. It leads to a reduction in the number of electrons in the system and thereby allows for faster calculations and a simplified treatment of bigger systems. PPs also allow for a considerable reduction of the basis set size. The pseudized valence wavefunctions are nodeless functions and therefore require less basis functions for an accurate description. Furthermore the relativistic effects connected to the core electrons are incorporated into the PPs without complicating the calculations of the final system. Most importantly, PPs are transferable which implies that the same PP would be adequate for an atom in all

possible chemical environments. This proves particularly useful during a simulation in which a change of environment is expected, such as in case of chemical reactions and phase transitions.

2.6 Interpretation of Data using analysis tools

VASP [20, 21] is a package for performing geometry optimization and AIMD simulations with the use of DFT potential and PBC. It is a useful package for simulating periodic solids and hence uses plane wave basis set in conjunction with Vanderbilt's ultra–soft pseudopotentials. However, finite cluster or molecules can also be simulated by using a supercell. Its an all–purpose code for carrying out AIMD simulations. The AIMD approach implemented in VASP is based on BOMD concept, where an exact evaluation of the instantaneous electronic ground state is obtained from DFT at each MD step using efficient matrix diagonalization schemes. The optimization techniques discussed in the next section are efficiently implemented in VASP.

2.6.1 Optimization Techniques

Optimization techniques are used to drive the system in the minimum energy configuration. Once the initial configuration is defined the next step is to find its minimum energy structure. A variety of optimization techniques have been suggested. The final ground state geometry is considered only when the ions and the electrons are in their minimum energy configurations.

Conjugate gradient

The conjugate gradient method [1a] provides simple and efficient way to locate the minimum of a particular system. The initial direction is taken to be the negative of the gradient at the starting point. A subsequent conjugate direction is then constructed from a linear combination of the new gradient and the previous direction that minimized the function. It should be noted that at each point the gradients are orthogonal but the directions are conjugate. Since the minimization along the

conjugate directions is independent, the dimensionality of the vector space explored in this technique reduces by one at each iteration. When the dimensionality of the function has been reduced to zero, there are no directions left in which to minimize the function, so the trial vector must be at the minimum. In this technique, the search direction is generated using the information from all the sampling points along the conjugate gradient path.

quasi-Newton

A quasi-Newton (variable metric) algorithm [23] is used to relax the ions into their instantaneous ground state. The forces and the stress tensor are used to determine the search directions for finding the equilibrium positions (the total energy is not taken into account). This algorithm is very fast and efficient close to local minima, but fails badly if the initial positions are a bad guess. Since the algorithm builds up an approximation of the Hessian matrix it requires very accurate forces, otherwise it will fail to converge. This method works very well for the systems initial guess lying close to the minima. It implicitly calculates an approximation of the inverse Hessian matrix by taking into account information from previous iterations. On start up, the initial Hessian matrix is diagonal. Information from old steps (which can lead to linear dependencies) is automatically removed from the iteration history, if required. The number of vectors kept in the iterations history (which corresponds to the rank of the Hessian matrix must not exceed the degrees of freedom. Naively the number of degrees of freedom is 3*(NIONS-1). But symmetry arguments or constraints can reduce this number significantly.

2.6.2 Structure and Bonding

To study the ground state properties of a system it is necessary to obtain the ground state geometry of the system. Location of global minimum of any system is a complicated problem. The geometry optimization belongs to the problem of minimizing an N-dimensional function with respect to a set of coordinates. Hence the problem becomes much more complicated as the dimension of the system increases. None of the optimization schemes discussed in the earlier section can guarantee for

the search of global minimum. The only way to find the global minimum is to find same minimum energy configuration in a number of different calculations. Another direct approach is to study the structure and bonding pattern to insure the optimum values of these properties.

Bonding

Bonding in chemical systems can be described either as localized or delocalized. The covalent, ionic, hydrogen and polar bonds belong to the localized bonding character, while metallic bonding belongs to the other class. The characterization of chemical bonds is a qualitative rather than a quantitative exercise. Bader used the topological description of electron density ρ(r) as a tool to understand the bonding in various chemical systems. However, it is known that, electron density alone does not easily reveal the consequences of the Pauli exclusion principle on the bonding.

Electron Localization Function

Becke and Edgecombe proposed ELF, [24] which has been used to examine electron localization in atoms, molecules and solids. The idea was based on the measure of the probability of finding an electron in the neighborhood of another electron with the same spin. Several reviews have discussed in depth the application of ELF. [25]– [28] ELF can be viewed as a local measure of the Pauli repulsion between electrons owing to the exclusion in three dimensional spaces. It therefore makes it possible to define regions of space that are associated with different electron pairs in a molecular or a solid. The ELF is defined as

$$\eta(r) = \frac{1}{1 + (\frac{D_p}{D_h})^2} \qquad (2.6.1)$$

$$D_h = (\frac{3}{10})(3\pi^2)^{5/3} * \rho^{5/3} \qquad (2.6.2)$$

$$D_p = \frac{\frac{1}{2}\sum_i |\nabla\psi|^2 - \frac{1}{8}|\nabla\rho|^2}{\rho} \qquad (2.6.3)$$

$$\rho = \sum_{i=1}^{N} |\psi(r)|^2 \qquad (2.6.4)$$

where the sum in Eqn. 2.6.4 is over all the occupied orbitals. D_h is the kinetic energy of the electron gas having the same density or one can say its the value of D_p in a homogeneous electron gas. This clearly shows that for a homogeneous electron distribution the value of ELF will be equal to 0.5. According to the definition, the ELF values lie between zero and one. Chemical systems in which, in the vicinity of one electron, no other electron with the same spin may be found, that is, where electrons are alone, or form pairs of antiparallel spins, for instance as occurs in bonding pairs or lone pairs. In this case, the Pauli principle has little influence on their behavior and the ELF value tends to 1. However, if the probability of finding the electron in the vicinity of other electron is high than the ELF value decreases.

Examination of each term in the Eqn. 2.6.3 is quite revealing. First term is the total kinetic energy of N noninteracting fermions in the ground state, whereas the second term is what the kinetic energy density at a point in space would be if only one occupied orbital contributed to the electron density at the point. The latter term is a lower bound for the former. Eqn. 2.6.3 quantifies the amount of Pauli repulsion at a given point r in space. As a result the 'excess' Pauli kinetic energy is small in region where the electrons are localized as discussed above.

Figure 2.3 shows the ELF pictures of two different molecular systems viz methyl acetate and benzene. Region (a) of the methyl acetate shows a localization region at the center of C–C bond, indicating a covalent bond. The double bond character is shown by the region (b). Region (d) and (e) indicate a lone pair of electrons on the O atoms. ELF of benzene clearly shows a symmetric electron localization pattern. Hence, indicating a resonance or delocalized state. In the present work ELF has been used to understand the localized and weak bonding in Sn or Ti–Beta zeolite and water complex. Later, it has been used to analyze the bonding pattern of the Al metal clusters and eventually how this changes due to N_2 adsorption.

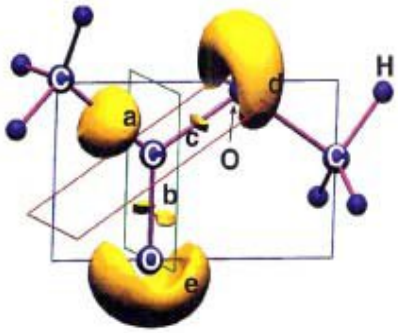

Figure 2.3: (a) Methyl acetate

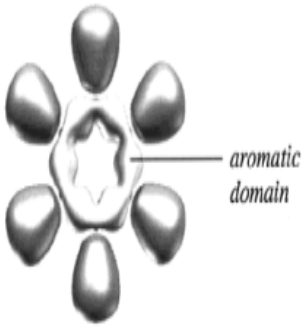

Figure 2.3: (b) Benzene

2.6.3 Conceptual DFT: Reactivity Descriptors

Based on the famous Hohenberg and Kohn theorems [10], DFT provided a sound basis for the development of computational strategies for obtaining information about the energetics, structure, and properties of (atoms and) molecules at much lower costs than traditional *ab initio* wave function techniques. On the other hand, a second branch of DFT has developed since the late 1970s, called **"conceptual DFT"** by its protagonist, R. G. Parr [29]. A breakthrough in the dissemination of this approach was the publication in 1989 of Parr and Yang's 'Density Functional Theory of Atoms and Molecules' [7], which not only promoted "conceptual DFT" but, certainly due to its inspiring style, attracted the attention of many chemists. Many of such chemical phenomena can be understood and predicted by some theoretical quantities that have a direct relationship with the characteristic sets of important chemical properties. These quantities are, in general, called descriptors. The reactivity descriptors are very much pertinent to the reactivity of the molecular systems and are intended to provide a qualitative and semi-quantitative measure of the extent to which a particular site will be affected in a given condition. In the last two centuries, there have been several attempts to explain the nature of bonding and reactivity of molecular systems based on some intuitive ideas, models and empirical rules in terms of the reactivity descriptors [30-32]. In particular, the concept of the highest occupied molecular orbital (HOMO) and lowest unoccupied molecular orbital (LUMO) developed by Fukui (frontier molecular orbital theory) [33], Mulliken's donor acceptor concept (overlap and orientation principle) [34] and Pearson's hardness and softness concept

(Hard-Soft Acid-Base principle) [35]. These descriptors or principles have made a profound impact on our understanding of the experimental observations at the microscopic level in an elegant way. Formulation and concept of some of these reactivity descriptors is summarized as follows.

Localized Fukui Functions

The site-selectivity of a chemical system, cannot, however, be studied using the global descriptors of reactivity such as electronegativity. For this, appropriate local descriptors need to be defined. An appropriate definition of local softness s(r) is given by 2.65

$$s(r) = \left(\frac{\partial \rho(r)}{\partial N}\right)_{v(r)} \left(\frac{\partial N}{\partial \mu}\right)_{v(r)} = f(r)S \qquad (2.6.5)$$

Such that

$$\int s(r)d(r) = S \qquad (2.6.6)$$

Where $f(r)$ is defined as the Fukui function (FF). It is obvious that local softness, s, contains the same information as the Fukui function as well as additional information about the molecular softness. FF can be interpreted either as the change of the electron density $\rho(r)$ at each point r when the total number of electrons is changed or as the sensitivity of a system's chemical potential to an external perturbation at a particular point r

$$f(r) = \left(\frac{\partial \rho(r)}{\partial N}\right)_{v(r)} = \left(\frac{\partial \mu}{\partial v(r)}\right)_{N} \qquad (2.6.7)$$

The latter point of view, by far the most prominent in the literature, faces the N-discontinuity problem of atoms and molecules, leading to the introduction of both right- and left-hand-side derivatives, both to be considered at a given number of electrons, $N = N_0$:

$$f^{+}(r) = \left(\frac{\partial \rho(r)}{\partial N}\right)^{+}_{v(r)} \qquad (2.6.8)$$

For a nucleophilic attack provoking an electron increase in the system, and

$$f^{-}(r) = \left(\frac{\partial \rho(r)}{\partial N} \right)^{-}_{v(r)} \qquad (2.6.9)$$

For a electrophilic attack provoking an electron decrease in the system.

Although, in principle, the neutral or N_0-electron system's electron density contains all information needed for the evaluation of the Fukui function, most studies in the literature have been carried out in the so-called finite difference method, approximating

$$f^{+}(r) \approx \rho_{N_0+1}(r) - \rho_{N_0}(r) \qquad (2.7.0)$$

And

$$f^{-}(r) \approx \rho_{N_0}(r) - \rho_{N_0-1}(r) \qquad (2.7.1)$$

A third function describing radical attack, $f^{0}(r)$, is then obtained as the arithmetic average of $f^{+}(r)$ and $f^{-}(r)$. To obtain the local information, Atom condensed Fukui functions were first introduced by Yang *et al*, based on idea of integrating the Fukui function over atomic regions, similar to procedure followed in population analysis technique. Combined with finite difference approximation, this yields working equations of the type

$$f_A^{+} = q_{A,N_0+1} - q_{A,N_0} \qquad (2.7.2)$$

$$f_A^{-} = q_{A,N_0} - q_{A,N_0-1} \qquad (2.7.3)$$

Where, $\boldsymbol{q}_{A,N0}$ denotes the electronic population of atom A of reference system. In *ab initio* calculations these numbers are obtained mostly by a Mulliken and Lowdin population analysis. However, the surplus or depleted charges on each atom in a system derived by Mulliken and/or Lowdin population scheme, itself serves as a reactivity descriptors, predicting the electrophilic and/or nucleophilic nature of a particular atom in that chemical environment.

HOMO-LUMO analysis

Since the derivative of 2.6.7 is not known exactly, there are various different strategies to calculate, in an approximate way, the Fukui function. Two different finite-difference approaches can be followed. Separate calculations of (N_0 + 1) and (N_0 – 1) electrons simply by relaxation of orbitals from the neutral system. This

approach has been known as the 'relaxed orbital' approach. On the contrary, assuming that the shape of molecular orbitals does not change when a small amount of charge is added or subtracted, Yang *et. al.* calculated the derivative of 2.6.7 as, governing electrophilic attack,

$$f^{-}(\vec{r}) \approx \rho_{HOMO}(\vec{r}) \qquad (2.7.4)$$

Governing nucleophilic attack,

$$f^{+}(\vec{r}) \approx \rho_{LUMO}(\vec{r}) \qquad (2.7.5)$$

And governing radical attack,

$$f^{0}(\vec{r}) \approx \frac{1}{2}\left[\rho_{HOMO}(\vec{r}) + \rho_{LUMO}(\vec{r})\right] \qquad (2.7.6)$$

known as the 'frozen orbital' approximation, where $d\rho$ is same as $d\rho_{valance}$. Under frozen orbital approximation atom-condensed Fukui functions will be nothing but the respective atomic population of HOMO or LUMO orbitals. FMO theory predicts that the preferable electrophilic reaction in a molecule will take place at the site where the relative density of the HOMO is high and the position, which has a relatively high LUMO density, is preferable for the nucleophilic reaction.

Pearson's definitions of Hardness and Softness

The general idea of classifying reagents with respect to their chemical behavior stimulated further research on the physical properties of the complexes. Among all, the work contributed by Pearson is considered to be one of the most important works and it has been found to be very useful for correlating and better understanding of a very large amount of chemical information in terms of the hard and soft parameters. Later on these concepts were coined as HASB principle around 1963. He has actually classified the molecular systems in terms of the hard-soft acid-base in a general way: Hard acid: acceptors or nucleophiles, Soft acid: Low positive charge, Hard base: donors or electrophiles, Soft base: Low electronegativity. HSAB principle says that there is an extra stabilization if hard acids bind to coordinate with hard bases and soft acids bind to coordinate with soft bases. A more interesting idea is the one that relates the hard-hard and soft-soft character, respectively, to ionic and covalent interaction [36-39]. A simple explanation for hard-hard interactions is by considering them to be

primarily electrostatic or ionic interactions. Here, we use these concepts to quantify the Lewis acidic nature of Sn and Ti substituted BEA zeolites and their interactive way with different Lewis bases. Thus, these reactivity descriptors have been used extensively for the study of site selectivity of atoms in a molecule. In this thesis, these quantities will be computed and are used to predict the inter-molecular reactivity trend.

2.6.4 MD analysis tool

The state of thermodynamic system and the motion of atoms within it is understood and analyzed through two standard parameters viz. RMS and MSD. We describe these two concepts in short below.

RMS

The δ_{rms} is a measure of fluctuations in the bond lengths averaged over all the atoms and over the total time span. It is defined as

$$\delta_{rms} = \frac{2}{N(N-1)} \sum_{i>j} \frac{(< r_{ij}^2 >_t - < r_{ij} >_t^2)^{1/2}}{< r_{ij} >_t} \qquad (2.7.7)$$

where N is the number of atoms in the system, r_{ij} is the distance between atoms i and j, and <...>t denotes a time average over the entire trajectory.

MSD

The MSD is another widely used parameter for analyzing a solid-like-to-liquid-like transition. In the present work, we calculate the MSD for individual temperatures over a given simulation, which is defined as

$$< r_I^2(t) >= \frac{1}{M} \sum_{m=1}^{M} [R_I(t_{0m} + t) - R_I(t_{0m})]^2 \qquad (2.7.8)$$

where R_I is the position of the I^{th} atom and we average over M different time origins t_{0m} spanning the entire trajectory. The MSD indicates the displacement of an atom in the cluster as a function of time. In the solid-like region, all atoms perform oscillatory

motion about fixed points resulting in negligible MSDs of individual atoms from their equilibrium positions. In a liquid-like state, on the other hand, atoms diffuse throughout the cluster and MSDs eventually reach a saturated value of the order of the square of the cluster radius. The liquid-like state hence represents a structure which has very less correlation of each atom with the neighboring one.

2.7 References

[1] (a) (a) M. C. Payne, M. P. Teter, D. C. Allan, T. A. Arias, J. D. Joannopoulos. Rev. Mod. Phys. **1992**, 64, 1045. (b) E. Schrödinger, *Ann. Phys.* **1926**, *79*, 361.

[2] M. Born and J. R. Oppenheimer, *Ann. Phys.* **1927**, *84,* 457.

[3] C. C. J. Roothaan, *Rev. Mod. Phys.* **1951**, *23*, 69.

[4] C. Møller and M. S. Plesset, *Phys. Rev.* **1934**, *46*, 618.

[5] C. D. Sherrill and H. F. Schaefer, *Adv. Quantum Chem.* **1999**, *34*, 143.

[6] R. J. Bartlett, *J. Phys. Chem.* **1989**, *93*, 1697.

[7] R. G. Parr and W. Yang, *Density functional theory of atoms and molecules*, Clarendon Press, New York **1989**.

[8] L. H. Thomas, *Proc. Cambr. Phil. Soc.* **1927**, *23*, 542.

[9] E. Fermi, *Z. Phys.* **1928**, *48*, 73.

[10]P. Hohenberg and W. Kohn, *Phys. Rev.* **1964**, *136*, 864.

[11]W. Kohn and L. J. Sham, *Phys. Rev.* **1965**, *140*, 1133.

[12]J. P. Perdew and Y. Wang, *Phys. Rev. B* **1986**, *33*, 8800.

[13]A. D. Becke, *Phys. Rev. A* **1988**, *38*, 3098.

[14]J. P. Perdew, *Phys. Rev. B* **1986**, *33*, 8822.

[15]J. P. Perdew and Y. Wang, *Phys. Rev. B* **1992**, *45*, 13244.

[16]C. Lee, W. Yang, and R. G. Parr, *Phys. Rev. B* **1988**, *37*, 785.

[17]J. P. Perdew, S. Burke, and M. Ernzerhof, *Phys. Rev. Lett.* **1996**, *77*, 3865.

[18]L. Verlet, *Phys. Rev.* **1969**, *57*, 98; *Phys. Rev.* **1967**, *165*, 201.

[19](a) R. Car and M. Parrinello, *Phys. Rev. Lett.* **1985**, *55*, 2471. (b) K. Dhole, A. Samanta and S. K. Ghosh, J. Phys. Chem. A, **2008**, *112* (22), 4879. (c) A. Samanta and S. K. Ghosh, J. Phys. Chem. A, **2008**, *112* (4), 752.

[20]G. Kresse and J. Hafner, *Phys. Rev. B* **1993**, *47*, 558.

[21]G. Kresse and J. Furthmüller, *Phys. Rev. B* **1996**, *54*, 11169.

[22]F. Bloch, *Z. Phys.* **1928**, *52*, 555.

[23]P. Pulay, Chem. Phys. Lett. **1980**, 73, 393.

[24]A. D. Becke and K. E. Egecombe. J. Chem. Phys. **1990,** 92, 5397.

[25]A. Savin, R. Nesper, S. Wengert, and T. F. Fasssler. Angew. Chem. Int. Ed. Engl. **1997**, 36, 1809.

[26]A. Savin, O. Jaspen, J. Fald, K. O. Anderson, H. Preuss, and H. G. von Schnering. Angew. Chem. Int. Ed. Engl. **1992,** 31, 187.

[27]U. Haussermann, S. Wengert, P. Hofmann, A. Savin, O. Jespen, and R Nesper.Angew. Chem. Int. Ed. Engl. **1994,** 33, 2069.

[28]F. Fuster, A. Sevin, B. Silvi. J. Phys. Chem. A **2000,** 104, 852.

[29]R. G. Parr, W. Yang, Annu. Rev. Phys. Chem. **1995**, 46, 701.

[30] (a) L. Pauling, The Nature of Chemical Bond and Structure of Molecule and Crystals;Oxford and IBH: New Delhi, **1967**. (b) S. Pal, K. R. S. Chandrakumar, J. Am. Chem. Soc. **2000,** 122, 4145. (c) K. R. S. Chandrakumar, S. Pal, J. Phys. Chem. A **2002,** 106, 5737. (d)K. R. S. Chandrakumar, S. Pal, J. Phys. Chem. A **2001,** 105, 4541. (e) S. K. Ghosh, Chem. Phys. Lett. **1990**, 172 77.

[31] (a) R. Mc Weeny, Coulson`s Valence, Oxford University Press , Oxford, **1979.** (b) R. K. Roy, S. Krishnamuthy, P. Geerlings, S. Pal, J. Phys. Chem. A **1998,** 102, 3746. (c) R. K. Roy, S. Pal, K. Hirao, J. Chem. Phys. **1999**, 110, 8236. (d) P. K. Chattaraj, B. Maiti, U. Sarkar, J. Phys. Chem. A **2003,** 107, 4973. (c) P. K. Chattaraj, J. Phys. Chem. A **2001**, 105, 511. (d) R. Parthasarathi, J. Padmanabhan, M. Elango, V. Subramanian, P.K. Chattaraj, Chem. Phys. Lett. **2004**, 394, 225.

[32] (a) Z. B. Maksic, Theoretical Models of Chemical Bonding: The Concept of the Chemical Bond; Ed.; Springer-Verlag: Berlin, **1990**. (b) S. Krishnamurthy, R. K. Roy, R. Vetrival, S. Iwata, S. Pal, J. Phys. Chem. A **1997**, 101, 7253. (c) R. G. Parr, P. K. Chattaraj J. Am. Chem. Soc. **1991**, 113, 1854 (d) J. Garza, R. Vargas, A. Cedillo, M. Galván, P. K. Chattaraj, Theor. Chem. Acc. **2006**, 115, 257.

[33]K. Fukui, Theory of Orientation and Stereo Selection; Springer-Verlag, Berlin **1975.**

[34](a) R. S. Mulliken, J. Am. Chem. Soc. **1952**, 74, 811. (b) L. E. Orgel, R. S. Mulliken, J. Am. Chem. Soc. **1957**, 79, 4839; (c) H. Tsubomura, R. S.

Mullikken, J. Am. Chem. Soc. **1960**, 82, 5966.

[35](a) R. G. Pearson, Hard and Soft Acids and Bases, Dowden, Hutchinson, and Ross, Stroudsburg, PA, **1973**; (b) R. G. Pearson, Chemical Hardness: Applications from Molecules to Solids; Wiley-VCH Verlag GMBH: Weinheim; **1997**.

[36](a) R. G. Pearson, J. Am. Chem. Soc. **1963**, 85, 3533; (b) R. G. Pearson, Science, **1966**, 151, 172.

[37]J. E. Huheey, Inorganic Chemistry: Principles of Structure and Reactivity; Harper and Row: New York, **1983**.

[38]G. Klopman, Chemical Reactivity and Reaction Path, Wiley, New York, **1974**.

[39]I. Fleming, Frontier Orbitals and Organic Chemical Reactions, Wiley, New York, **1976.**

[40]S. Nóse, Mol. Phys. 52, 255, **1984**.

CHAPTER 3

Properties of Sn-BEA Vs. Ti-BEA

Abstract:

Periodic density functional theory is employed to characterize the differences in the structural, Lewis acidic and hydrophilic properties of Sn-BEA and Ti-BEA. The results show that the incorporation of Sn increases the Lewis acidity of BEA compared to the incorporation of Ti, thereby increasing the efficiency of the oxidation reactions. The results also justify as to why the percentage of Sn substituted in BEA is less than of Ti. The structural analysis shows that the first coordination shell of Sn is larger than that of Ti. However, the second coordination of both sites remains the same. The water adsorption properties of these substituted zeolites are quantified. Finally, we explain the higher Lewis acidity of Sn than the Ti site on the basis of the Fukui functions and charge population analysis.

3.1 Introduction

Zeolite Beta (BEA) is used as one of the active catalysts for carrying out several organic reactions such as epoxidation of olefins [1], aromatic and aliphatic alkylation [2], acid catalyzed reactions [3], etc. Some of the important reactions which can be catalyzed by BEA include the Baeyer-Villiger oxidation (BVO) reaction and

the Meerwein-Ponndorf-Verley reduction of aldehydes and Oppenauer's oxidation of alchols (MPVO) reaction [4]. The reasons for using BEA as an efficient catalyst are its relatively large pore size, its flexible framework and its high acidity [5]. It is also well-established that the acidity of BEA can be finely tuned by the incorporation of various atoms such as B, Al, Ti, Zr, Fe, etc [6-9]. These sites substituted in the BEA framework act as an active Bronsted or Lewis acid sites depending upon their valence states [8]. Among various atoms, Ti substitution in a BEA framework leads to an active catalyst for epoxidation of olefins in the presence of H_2O_2 [7-10]. Other Ti zeolites, which have been successfully used for the oxidation of small organic molecules, are the titanium silicalites (TS-1, TS-2) [11]. Several studies have been reported to understand the differences of the activity and selectivity between these two zeolites [1,12]. Corma et al. have shown that these differences arise from the hydrophilic/hydrophobic nature of the Ti sites [1,9]. According to their report, Ti sites in TS are more hydrophobic than those in the Al-Ti-BEA. Hence, TS was preferred over Al-Ti-BEA when the solvent used in the reaction was prepared in an aqueous medium.

One of the challenges in this field is to increase the efficiency of a zeolite by substitution with other elements. Such an attempt has been made recently by incorporating Sn in BEA. Mal and Ramaswamy successfully synthesized the Al-free Sn-BEA [13]. In an interesting experimental work, Corma et al. showed that the incorporation of Sn in the BEA framework results in a more efficient catalyst for the BVO reaction in the presence of H_2O_2 [14]. In their study, a new mechanism was proposed for the oxidation of ketones. They showed that the Sn site in BEA activates the carbonyl group of the cyclohexanone followed by the attack of H_2O_2, unlike the Ti sites which initially activate the H_2O_2. This result was attributed to the higher Lewis acidity of the Sn site with respect to the Ti site. Hence, incorporation of Sn in BEA leads to a higher selectivity toward the formation of lactones in the BVO reaction as compared to that of Ti [14, 15]. On this background, highly selective MPVO reactions were carried out more efficiently with Sn-BEA than Ti-BEA [16]. In these studies, it was shown that the Sn site is situated within the framework and no extra framework Sn was detected. Although much of the experimental studies have

focused on the efficiency of the Sn-BEA, the higher Lewis acidity of the Sn site compared to the Ti site in BEA is still not understood. Recently, Sever and Root used the $M(OH)_4$ (M = Sn, Ti) cluster models to investigate the reaction pathways for the BVO reaction [17]. Their study supports the formation of a Criegee intermediate that contains a five-membered chelate ring with the tin center. Further, they conclude that the Baeyer-Villiger rearrangement of the chelated Criegee intermediate is the rate-determining step for the overall reaction. In addition, the Gibbs activation barrier for rearrangement of the chelated Criegee intermediate is over 17 kcal/mol less than the corresponding activation barrier for the nonchelated Criegee intermediate in the noncatalyzed mechanism. Thus the Lewis acidic tin center facilitates the rearrangement step by stabilizing the hydroxyl leaving group as the peroxo bond is cleaved in the transition state.

One of the important issues concerning the activity and selectivity of the zeolite is its hydrophobic/hydrophilic nature [18, 19]. It is known that, if the zeolite is hydrophilic in nature, the water present in the solvent poisons the active sites. This hinders the kinetics of the reaction and decreases the activity of the zeolite. Corma et al. have bypassed this problem by modifying the catalyst design, which allows the use of Sn-BEA in the presence of aqueous media [20]. Very recently, Boronat et al. have done theoretical calculations using a $Sn(OSiH_3)_3OH$ cluster model to understand the effect of H_2O during the BVO reaction [31]. Their results show that one water molecule is permanently attached to the Sn active site. To understand the water adsorption competence, Fois et al. continued the interaction study of water molecules with the Ti sites in Ti-offretite using Car-Parrinello molecular dynamics [21]. They found that, at higher loading of water molecules, the Ti atom expands its coordination number.

In the past decade, several experimental and theoretical studies have been employed to characterize the role of Ti sites at a microscopic level in various Ti-zeolite systems [1, 7, 22-26]. It has been revealed that due to the high crystallinity, low Ti content and large quadrupolar moment of Ti, accurate information on the Ti sites in BEA is not possible through experimental techniques [25]. Hence, it is necessary to use theoretical methods to explore the local behavior for, e.g., structure,

electronic and bonding properties of these sites. Sastre and Corma have used *ab initio* calculations to discuss the role of the Ti sites in Ti-BEA and TS-1 [26]. The energies of the lowest unoccupied molecular orbital (LUMO) of Ti-BEA and TS-1 with one Ti substituted in turn at every T site were shown to be different. Furthermore, the Ti sites in Ti-BEA were found to be more acidic than those in TS-1 and this acidity varies among all of the Ti sites in both zeolites [26]. This indicates that not only two different Ti-containing zeolites have different acidities, but also different T sites within a particular zeolite have varying acidities. Boronat et al. have also characterized the acidic characteristics of several transition metals substituted in BEA on the basis of LUMO energies [27].

Very recently, Bare et al. have used the EXAFS technique to investigate the Sn site in Sn-BEA [28]. They showed that Sn was not randomly distributed in BEA, and takes specific crystallographic sites, i.e., T5/T6 sites in their nomenclature, which corresponds to T1 and T2 in our nomenclature, following Newsam *et. al.* [29]. Surprisingly, they found that this substitution takes place through pairing of these sites, within the six-membered ring, i.e., two T1 or two T2. However, no explanation was given for this distribution. At the same time, in a theoretical work using a periodic approach based on density functional theory (DFT), we have proposed the sites for Sn substitution in BEA [30]. According to these results, T2 site is the most probable site for the Sn substitution based on thermodynamics consideration. Moreover, we found that the substitution of two Sn atoms per unit cell is thermodynamically unfavorable. This is consistent with the earlier experimental results.

As it can be seen from the above description, the incorporation of Sn in BEA proves to be a better catalytic site than Ti. Hence, detailed information on the differences in the properties of Sn and Ti sites in BEA, such as the quantification of the Lewis acidity, number of T atoms to be substituted in the unit cell and hydrophobicity, is of fundamental importance and is still to be resolved. The aim of the present theoretical study is to bring out the differences in these substituted BEA zeolites by analyzing their structural, electronic and water adsorption properties.

Moreover, we use the local reactivity descriptors such as the Fukui functions (FFs) and charge population to analyze the Lewis acidic strength of Sn and Ti sites.

3.2 Methodology and Computational Details

Several theoretical studies based on a classical as well as quantum potential have been proposed to study the properties of zeolites [26, 33-40]. It has been a practice to adopt cluster models cut from the zeolite crystals to study these properties. One of the obvious reasons to use the cluster model is that it is computationally cheap. Sauer et al. have conducted an extensive study of zeolites using cluster models [35, 36]. A periodic approach provides a more realistic description to study the properties of a crystal [39, 24]. Although zeolite catalysts are neither crystals nor periodic solids, it is more convenient to use periodic boundary conditions, when there are very few substituted sites per unit cell.

Earlier experimental studies have indeed proved that Sn and Ti sites in BEA are very few, that they are situated within the framework and during the BVO or MPVO reaction these sites do not dissociate from the framework [4a, 15]. In the present work, we have employed the periodic DFT to investigate the properties of Sn-BEA and Ti-BEA. The advantage of using periodic boundary conditions is that the long range electrostatic interactions are included within Ewald summations. The unit cell of BEA is shown in Figure 3.1. The instantaneous stationary electronic ground state is calculated by solving the Kohn-Sham equation based on DFT. The valence electrons have been represented by the plane waves in conjunction with the Vanderbilt's ultrasoft pseudopotentials (PPs) for the core [41]. It is worth mentioning that during the interaction between two systems the complete plane wave avoids the basis set superposition error. The exchange-correlation functional is expressed by the generalized gradient approximation (GGA) with the Perdew-Wang 91 (PW91) functional [42]. The calculations were restricted to the gamma point in the Brillouin zone sampling. The energy cutoff used for the plane waves was 21.83 Ry (300 eV). The interaction between the water molecule and the Sn and Ti sites in BEA was studied using an energy cutoff of 36.74 Ry (500 eV).

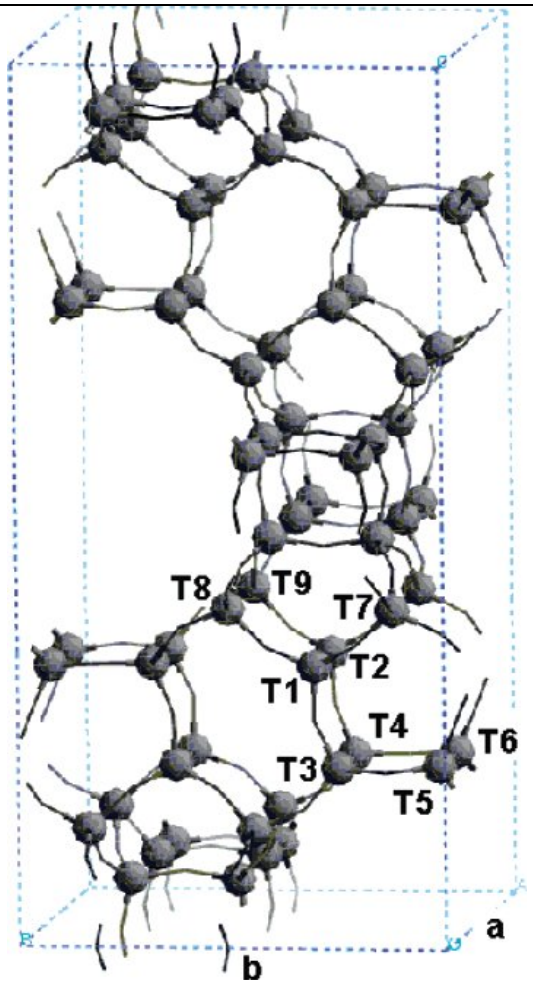

Figure 3.1: Crystallographically defined 9 T sites of BEA. The gray spheres represent the Si sites.

For large systems, such as the present study, our study is limited to 36.74 Ry cutoff and our calculations may not have converged with respect to the energy cutoff. A much higher energy cutoff value has been used for the description of hydrogen bonding in the context of plane waves for HF clusters [43] using standard norm conserving pseudopotentials. On the other hand, we have used ultrasoft pseudopotentials, which may require a much lower energy cutoff. Further, our calculation is on a true periodic system, which may require much less cutoff than the

free HF molecules enclosed in a box of 15 Å as in the work on HF clusters. For periodic systems, such as zeolites, cutoffs similar to the ones employed in the present study have been used [44] in earlier studies by others. However, it would be interesting to investigate the convergence of the adsorption energies with energy cutoffs for systems studied in this paper in the future.

The energies corresponding to the HOMO, LUMO, and HOMO-LUMO gaps are obtained using the periodic calculations at all nine T sites of Sn- and Ti-BEA. The above calculations have been performed by the VASP code [45]. The charge population and local reactivity descriptors have been calculated using the cluster model, cut from the optimized periodic systems of Sn-BEA and Ti-BEA. The cluster model cuts are represented in Figure 3.2. The clusters have been cut considering the most reactive T sites, i.e., T2 and T1 for Sn and Ti-BEA, respectively. The clusters have been terminated with the H atoms. These clusters were reoptimized by constraining the terminal H atoms and relaxing all of the other atomic positions. The cluster calculations have been carried out by the DFT approach and B3LYP functional with the basis set DZVP [46]. These calculations are done using the GAMESS program [50].

BEA is a high silica zeolite and consists of two different ordered polytypic series, viz., polymorph A and polymorph B [29]. It has two mutually perpendicular straight channels with a cross section of 0.76 nm * 0.64 nm which run along the *a* and *b* directions. Intersecting to these, at right angles, a helical channel of 0.55 nm * 0.55 nm also exists along the *c*-axis. This gives rise to a three-dimensional pore system of 12-membered ring aperture. The unit cell of an ideal fully siliceous BEA consists of 192 atoms with 64 Si and 128 O atoms distributed within the tetragonal lattice of dimensions of (12.6 * 12.6 * 26.2) Å. There are nine distinct crystallographically defined T sites, as shown in Figure 3.1. We adopt the experimental structure as defined by Newsam et al. and accordingly define the nine T sites in the unit cell of BEA [29]. The structural optimization of the Si and Sn- and Ti-BEA has been carried out in two steps. In the first step, the conjugate gradient method was used to optimize the unit cell of BEA. The optimization was considered to be achieved when the maximum forces on the atoms were less than 0.1 eV/Å.

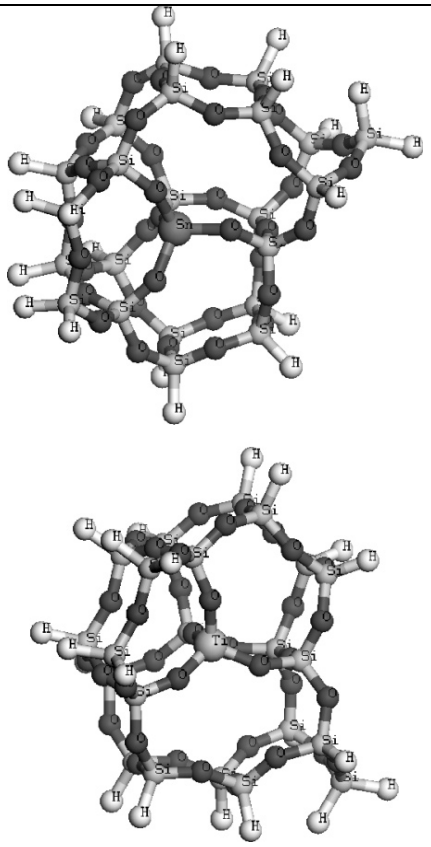

Figure 3.2: The cluster models cut from the optimized periodic Sn and Ti-BEA systems. The T sites are T2 and T1 for the Sn- and Ti-BEA systems, respectively.

In the second step, these optimized geometries were reoptimized with the quasi-Newton method unless the maximum force on the atoms was less than 0.06 eV/Å. One should note that during the optimization the cell shape of the unit cell has been fully relaxed, while keeping its volume constant. The reason is that the percentage of Sn and Ti in BEA is only 1/u.c. We expect that if the concentartion of the Sn or Ti is increased in BEA the volume of the cell along with the shape has to be relaxed. In the case of Sn- and Ti-BEA, each of the nine distinct T sites were substituted by Sn and Ti atoms (i.e., Si/(Sn or Ti)) 63/1, respectively, and were optimized. Once the active site in Sn- and Ti-BEA was confirmed, one water molecule was introduced near these

active sites and the same optimization procedure was followed as discussed above. The structural data for the Sn-BEA has been taken from a recent publication by us [30].

3.3 Results and Discussion

3.3.1. Structure of Sn-BEA and Ti-BEA: Tables 3.1 and 3.2 present the optimized structural details of all nine T sites of Sn-BEA and Ti-BEA, respectively. It should be noted that only the average bond distances and bond angles are presented. It can be seen from Table 3.1 that the Sn-O bond distances range between 1.908 and 1.917 Å, the Sn-O-Si bond angles range from 136 to 144.2° and the Sn-Si distance is around 3.241 Å. Very recently, Bare et al., with the help of the EXAFS technique, showed that the Sn-O bond distances and Sn-Si distances in Sn-BEA were around 1.906 and 3.5 Å, respectively [28]. This clearly shows that the theoretical results presented by us are in good agreement with the experimental results. However, the theoretical results of Bare et al. were not consistent with their experimental data. This may be due to keeping the shape of the unit cell fixed during the optimization and using the local density approximation in their study [28]. On the other hand, we have relaxed the lattice vectors of the unit cell during the optimization and also used the GGA exchange-correlation potential, as explained in the earlier section. The change in the local coordination of the T site in Sn-BEA compared to the Si-BEA has been illustrated in the earlier study.

Table 3.2 shows that the average Ti-O bond distances of the nine T sites in BEA vary from 1.794 to 1.799 Å. These values are in good agreement with the earlier works on Ti-BEA [7]. Compared to Sn-O bond distances; the Ti-O distances are smaller. This is due to the larger atomic size of Sn with respect to Ti. From the data of Tables 3.1 and 3.2, it can be noticed that the average Sn-O and Ti-O bond lengths are very similar for all T sites, whereas the corresponding bond angles have a large range of variation. Moreover, in both the Sn- and Ti-BEA models, the largest average angles belong to the T1 and T2 sites. The average experimental values of T1-O-T and T2-O-T angles in the unsubstituted Si-BEA are 155.3 and 155.9°, respectively, and they also

correspond to the largest T-O-T angles in the framework. If we compare Sn and Ti substituted in the framework with Si, we get the expected

Table 3.1: Optimized Structural Parameters of Sn-BEA. Average Sn-O Bond Lengths, Sn-O-Si Bond Angles and Sn-Si Distances of All the 9 T Sites of Sn-BEA

T–sites	Sn–O (Å)	Sn–O–Si (deg)	Sn–Si (Å)
T1	1.911	143.5	3.336
T2	1.909	144.2	3.341
T3	1.910	140.6	3.241
T4	1.917	136.0	3.281
T5	1.913	142.2	3.297
T6	1.910	141.2	3.297
T7	1.911	140.6	3.282
T8	1.908	140.0	3.282
T9	1.912	137.8	3.270

Table 3.2: Optimized Structural Parameters of Ti-BEA. Average Ti-O Bond Lengths, Ti-O-Si Bond Angles and Ti-Si Distances of All the 9 T Sites of Ti-BEA

T–sites	Ti–O (Å)	Ti–O–Si (deg)	Ti–Si (Å)
T1	1.799	151.7	3.302
T2	1.797	152.4	3.304
T3	1.794	145.0	3.220
T4	1.797	145.4	3.233
T5	1.799	148.1	3.257
T6	1.799	148.5	3.263
T7	1.794	149.0	3.269
T8	1.795	147.4	3.249
T9	1.798	144.0	3.225

order for average T-O bond lengths Sn-O > Ti-O > Si-O, with around 0.12-0.15 Å difference at each replacement. The average T1-O-T or T2-O-T bond angles vary as Sn-O-Si < Ti-O-Si < Si-O-Si. These Ti-O-Si bond angles which range between 144 and 152° are larger than the Sn-O-Si bond angles with a range between 136.0-143.5°. Due to the angular flexibility, the Ti-Si distance differs only by ~0.04 Å from the Sn-Si distance. Although the first coordination shell radius of Ti is smaller than that of Sn, the second coordination shells are at similar distances. The adaptation of the BEA framework to Sn and Ti substitution results thus in a quite localized deformation of the siliceous framework. Hence, we can infer that the difference in adsorption properties between Sn- and Ti-BEA should be mainly due to the electronic differences of these sites.

3.3.2. Energetics of Sn-BEA and Ti-BEA: In this subsection, we discuss the thermodynamic stability of Sn-BEA and Ti-BEA. This is done by calculating the cohesive energies for each of the nine T sites in Sn-BEA and Ti-BEA. Cohesive energy of a solid is defined as the difference between the energy of the bulk (solid) at equilibrium and the energy of the constituent atoms in their ground state [30]. Cohesive energy does not account for the kinetic formation of the system, nor for the different nature of the synthesis intermediates generated in aqueous solution, which can generate different routes for the solid growth. The cohesive energies of all nine substituted T sites of Sn-BEA and Ti-BEA are given in Table 3.3. In our earlier investigation, we showed that the substitution of Sn in the BEA framework decreases the cohesive energy [30]. Hence, the incorporation of Sn in BEA is thermodynamically less stable than the Si-BEA. On this basis, we explained the fact that the incorporation of Sn in the BEA framework is restricted. Interestingly, Bare et al. predicted the formation of Sn pairs as the active sites, where the two Sn atoms were shown to be on the opposite sides of a six-membered ring [28]. They showed that one of these pairs is present per 8 u.c. of BEA. Unfortunately, at present, it is out of scope to consider 8 u.c. of BEA. Nevertheless, we have carried out the calculations placing two Sn atoms per u.c. at the T1 and T2 (T5 and T6 according to Bare et al.) positions which are situated in the six-membered ring and are on the opposite side of each other (Figure 3.1). We found that this does not increase the cohesive energy. The

cohesive energy of Si-BEA is -1527.902 eV [30]. From Table 3.3; we see that the cohesive energy of Ti-BEA is about 3 eV higher than that of Si-BEA.

Table 3.3: Cohesive Energies of All the 9 T Sites of Sn-BEA and Ti-BEA

T site	Sn-BEA	Ti-BEA
T1	1521.387	1530.797
T2	1521.681	1530.767
T3	1521.468	1530.210
T4	1521.523	1530.045
T5	1521.405	1530.014
T6	1521.431	1530.570
T7	1521.457	1530.359
T8	1521.621	1530.415
T9	1521.323	1530.282

This indicates that the incorporation of Ti in BEA is thermodynamically more favorable than that of Sn. Among the nine T sites of Ti-BEA, we found that the T1 and T2 sites have the highest stability, and that T5 is the least stable. We have also calculated the cohesive energy with two Ti per u.c. (i.e., Ti/Si) 2/62 per u.c.). The two Ti atoms were incorporated at two different T2 positions at a distance of 9 Å. This reveals an increase in the cohesive energy of about 3 eV compared to one Ti per u.c. Thus Ti could be incorporated more easily in BEA than Sn. That these calculations are carried out on a dehydrated solid resulting from a thermodynamically driven synthesis, ignoring the effects of the various ingredients and formation conditions, i.e., the nature and energies of the synthesis intermediates. Nevertheless, these results are consistent with the earlier experimental works, where it has been shown that the amount of incorporated Ti is larger than that of Sn in BEA [7, 15].

3.3.3. Lewis Acidity of Sn-BEA and Ti-BEA: Earlier experimental studies have conjectured that Sn acts as a better Lewis acidic site than Ti in BEA [14-16]. Hence, Sn-BEA acts as a more active catalyst for the oxidation reactions. This motivated us to compare the Lewis acidity of Sn- and Ti-BEA. First, one must recall that the Lewis acidity, being related with an electron acceptor character, can be correlated with the global electron affinity of the solid. Qualitatively, LUMO energies can be used for a omparing between the electron affinities of Sn- and Ti-BEA [26, 27]. The HOMO and the LUMO energies, and their corresponding HOMO-LUMO gaps of Sn-BEA and Ti-BEA, have been reported in Table 3.4.

Table 3.4: Energies of the HOMO, LUMO and HOMO-LUMO Gaps of the 9 T Sites of Sn-BEA and Ti-BEA

T site	Sn-BEA			Ti-BEA		
	HOMO (eV)	LUMO (eV)	gap (eV)	HOMO (eV)	LUMO (eV)	gap (eV)
T1	-3.124	1.333	4.457	-3.135	1.417	4.552
T2	-3.125	1.366	4.491	-3.133	1.469	4.602
T3	-3.131	3.121	1.557	-4.688	1.548	4.669
T4	-3.117	1.421	4.538	-3.120	1.492	4.612
T5	-3.131	1.450	4.581	-3.152	1.500	4.652
T6	-3.120	1.426	4.546	-3.145	1.453	4.598
T7	-3.121	1.419	4.540	-3.156	1.486	4.642
T8	-3.117	1.497	4.614	-3.144	1.470	4.620
T9	-3.114	1.506	4.620	-3.121	1.454	4.575

Globally, the average LUMO energy among the Sn substituted models is lower than that for the Ti ones. In our earlier results on Sn-BEA, we have shown that out of the

nine T sites the T1 and the T2 sites have low LUMO energies compared to the other T sites, and would be the probable sites for the reaction [30]. Interestingly, T1 and T2 have been proposed as the most probable sites for Sn substitution from EXAFS experiments [28]. The two corresponding LUMO orbitals have similar low energies, making these two models good candidates as Lewis acids [27]. Both sites have also the smallest HOMO-LUMO gap. A smaller gap, in a solid, correlates with a larger global softness. The most probable Sn-BEA solids would thus correspond to the most Lewis acidic and the more "soft" models.

In the case of Ti-BEA, we can see from Table 3.4 that the T1 site has the lowest LUMO energy, whereas T3 has the highest. We can also notice that T1 and T2, which have the largest cohesive energies, have also low HOMO-LUMO gaps, with T1 having the smallest. Considering these two factors together, we propose that these sites would also be the most favorable sites for the substitution by Ti and also for the reaction to take place. We propose thus that, in both cases, Sn and Ti would be more probably substituted at the T1 and T2 sites. Considering their LUMO energies, about 0.1 eV lower for Sn-BEA, we can infer that Sn-BEA is more Lewis acidic than Ti-BEA. Moreover, with the corresponding HOMO-LUMO gaps being lower for Sn-BEA than for Ti-BEA, this also suggests that Sn-BEA is a softer acid. Despite its smaller radius, Ti has thus less ability to adapt to the various geometric environments, showing the behavior of a "harder" species.

Local reactivity descriptors such as condensed electrophilic and nucleophilic FFs and charge populations have been used to interpret the acidic strength of the Sn and Ti sites [47-49]. Table 3.5 describes the Mulliken and Lowdin charge populations. We can see from Table 3.5 that the positive charge on Sn is higher than that on Ti. This indicates that there is a charge buildup on the Ti compared to Sn. This probably arises due to the back-donation of electrons from the neighboring oxygen atoms to the empty d-orbitals of Ti, lowering its positive charge and therefore its Lewis acidity.

Table 3.5: Mulliken and Lowdin Charges of Sn and Ti Atoms in their Respective Configurations

T site	Mulliken	Lowdin
Sn	1.57	1.28
Ti	1.32	0.89

The values of electrophilic FFs (f^+) and nucleophillic FFs (f^-) obtained through the Lowdin population scheme are given in Table 3.6. The electrophilic (f_k^+) and nucleophilic (f_k^-) FFs of a particular k^{th} atom are defined as

$$f_k^+ \approx q_k^{N_{0+1}} - q_k^{N_0}$$

$$f_k^- \approx q_k^{N_0} - q_k^{N_{0-1}}$$

q_k values are the electronic population of the *k*th atom of a particular species.

It can be seen that the electrophilic FFs (Table 3.6) of Sn and Ti in their respective configurations are higher than those of the other atoms. This shows that the Sn and Ti sites act as the probable Lewis acidic sites for the nucleophilic attack. Interestingly, the Sn site is slightly more electrophilic than the Ti site. This clearly indicates the higher Lewis acidity of Sn compared to the Ti site.

3.3.4. Hydrophilicity of Sn-BEA and Ti-BEA: One of the important issues concerning the selectivity toward the organic molecules in zeolites is the hydrophobic/hydrophilic character of these catalysts [18]. Indeed, for reactions such as BVO and MPVO in the presence of aqueous solvents, zeolites containing both Lewis acidity and hydrophobicity would be the most appropriate [20, 31]. In fact, being a product of reaction, water is always present in the catalyst pores. However, this presence is not desirable, because its adsorption is competitive with that of reactants and also due to the product hydrolysis. On a perfect silicalite surface, water is physisorbed, i.e., its interaction energy is weak; mainly due to van der Waals forces. As soon as defects are present, water may bind to the silanols or dissociate and

react with the surface [32]. In order to be hydrophobic; zeolites must thus present less or no defects.

Table 3.6: Condensed Electrophilic (f^+) and Nucleophilic (f^-) FFs of the 9 T Sites of Sn-BEA and Ti-BEA

Atoms	Sn-BEA		Ti-BEA	
	f^+	f^-	f^+	f^-
T=Sn/Ti	0.2465	0.00265	0.2170	0.0024
Si	0.0267	0.0015	0.0245	0.0011
Si	0.0308	0.0009	0.0258	0.0013
Si	0.0255	0.0031	0.0236	0.0028
Si	0.0250	0.0037	0.0241	0.0030
O	0.0465	0.0002	0.0737	0.0003
O	0.0464	0.0048	0.0677	0.0038
O	0.0461	0.0075	0.0705	0.0037
O	0.0408	0.00373	0.0714	0.0002

If this is achieved, i.e., for highly hydrophobic samples, experimental results show that substituted Ti- BEA is much more hydrophobic than Sn-BEA [20]. Although it is difficult to compare Ti-BEA and Sn-BEA with a high loading of water, it is of particular interest to investigate, at the microscopic level, the coordination of Sn and Ti sites in the presence and absence of one water molecule. For this comparison, Sn and Ti have been located at sites T2 and T1, respectively. The full systems have then been optimized with a higher energy cutoff to account for the hydrogen bonding as mentioned in section 2.

Table 3.7 gives the averaged optimized T-O(BEA), T-OH_2 bond lengths, T-O-Si bond angles and T-Si distances, where (T) Sn and Ti. We can see that after hydration, the Sn-O distance has been increased by 0.013 Å and the Sn-O-Si angle is

also increased by about 3.2° with respect to the dehydrated Sn-BEA. The bond distance between the Sn site and the H_2O is 2.38 Å. The hydrated Ti-BEA shows a similar trend with a Ti-O bond length and the Ti-O-Si bond angle which have been increased by 0.025 Å and 2.3°, respectively. The Ti-OH_2 bond distance is 2.44 Å. We see that the Sn-OH_2 distance is shorter than Ti-OH_2. In order to understand the adsorption of the H_2O molecule to the T sites, we have calculated the binding energy (BE) of a single water molecule to the Sn and Ti sites in BEA (Table 3.7). This is done as follows

$$\mathbf{BE} = E_{\text{complex (BEA + H2O)}} - \{E_{\text{(BEA)}} + E_{\text{(H2O)}}\}$$

Table 3.7: Structural Parameters and Binding Energies (BEs) of Sn-BEA and Ti-BEA in the Presence of H_2O

Geometrical parameters	Sn-BEA	Sn-BEA+H_2O	Ti-BEA	Ti-BEA+H_2O
T-O Å (300 eV)	1.909	1.924	1.797	1.820
T-O Å (400 eV)	1.909	1.921	1.797	1.817
T-Si Å (300 eV)	3.33	3.34	3.33	3.35
T-Si Å (400 eV)	3.33	3.36	3.33	3.36
T-O-Si4 deg (300eV)	143.0	145.9	152.0	157.8
T-O-Si deg(400 eV)	143.0	145.2	152.0	157.7
T-OH_2 (300 eV)	-	2.43	-	4.07
T-OH_2 (600 eV)	-	2.44	-	3.84

As can be seen from Table 3.7, the BEs of a water molecule to the Sn and Ti sites are -32.07 and -13.0 kJ/mol, respectively. This clearly shows that the water molecule has an exothermic interaction with the Sn and Ti sites. This has been confirmed experimentally for Ti-BEA zeolite [7]. Furthermore, the Ti-BEA and H_2O complex is ~20 kJ/mol less stable than the Sn-BEA and H_2O complex. This also confirms the Sn site in BEA has high Lewis acidity and is more hydrophilic compared to Ti-BEA.

It must be recalled that interaction energies calculated with DFT based methods do not include van der Waals attractive contributions. In recent work, these dispersion terms have been added empirically [51] or using adequate correlation

functionals [52]. It is easy to give an a posteriori estimate of the van der Waals stabilization of water bound to the Sn or Ti sites in BEA, using an empirical correction. Using our optimized Sn and Ti structures, the van der Waals stabilization energy of the bound water molecule has been calculated using the universal force field [53]. The following energies have been found: -13.8 kJ/ mol for Sn-BEA and -10 kJ/mol for Ti-BEA. Since these empirical van der Waals terms are additive, one can infer that a water dimer would form a very low exothermic complex with the Sn-BEA model but would still be nonbonding with the Ti model. Hence, these results show that Ti-BEA is less hydrophilic than Sn-BEA. This confirms the earlier experimental findings [20a].

3.4 Conclusion

The present theoretical investigation reveals the differences between the Sn-BEA and Ti-BEA based on their structural, Lewis acidic and hydrophilic properties. Our analysis shows that the Sn and Ti atoms may occupy T2 and/or T1 crystallographic positions in BEA. Although the first coordination shell of Sn is larger than Ti, the second coordination shell in both model zeolites is similar. This explains the relaxation of the local environment of the substituted site. The structural data on Sn-BEA and Ti-BEA presented in this work are in good agreement with the earlier experimental studies. The cohesive energy results demonstrate that the incorporation of Ti is more favorable than Sn in BEA. Nevertheless, we show that Sn-BEA is more Lewis acidic than Ti, and hence proves to be a more efficient catalyst for the oxidation reactions than Ti-BEA. Interestingly, we have used the local reactivity descriptors such as condensed electrophilic and nucleophilic FFs to explain the higher Lewis acidic strength of Sn than Ti. The charge population analysis quantifies the back-donation of the electrons in Ti which is not seen in Sn. One of the important aspects concerning the activity and selectivty of the zeolite which we have addressed in the present work, is the hydrophilic nature of the Sn and Ti sites in BEA. Our results show that Sn-BEA is more hydrophilic than Ti-BEA.

Thus, the present study gives insight into the microscopic properties of the active sites in Sn-BEA and Ti-BEA and the differences between them, which would have been otherwise difficult to understand through experimental methods.

3.5 References

[1] Corma, A.; Esteve, P.; Martinez, A. *J. Catal.* **1996**, 161, 11.

[2] Bellussi, G.; Pazzuconi, G.; Perego, C.; Girotti, G.; Terzoni, G. *J. Catal.* **1995**, 157, 227.

[3] Creyghton, E. J.; Ganeshie, S. D.; Downing, R. S.; van Bekkum, H. *J. Mol. Catal.* **1997**, 115, 457.

[4] (a) Jansen, J. C.; Creyghton, E. J.; Njo, S. L.; van Koningsveld, H.; van Bekkum, H. *Catal. Today* **1997**, 38, 205. (b) Kunkeler, P. J.; Zuurdeeg, B. J.; van der Waal, J. C.; van Bokhoven, J. A.; Koningsberger, D. C.; van Bekkum, H. *J. Catal.* **1998**, 180, 234.

[5] (a) Wadlinger, R. L.; Kerr, G. T.; Rosinski, E. J. *U.S. Patent 3308069*, **1967**. (b) Tuan, V. A.; Li, S.; Noble, R. D.; Falconer, J. L. *EnViron. Sci. Technol.* **2003**, 37, 4007.

[6] (a) Sen, T.; Chatterjec, M.; Sivasanker, S. **1995**, 207. (b) de Me´norval, L. C.; Buckermann, W.; Figueras, F.; Fajula, F. *J. Phys. Chem.* **1996**, 100, 465 (c) Juttu, G. C.; Lobo, R. F. *Catal. Lett.* **1999**, 62, 99. (d) Dimitrova, R.; Neinska, Y.; Miha´lyi, M.; Pal-Borbe´ly, G.; Spassova, M. *Appl. Catal., A* **2004**, 266, 123. (e) Pe´rez-Ramirez, J.; Groen, J. C.; Bru¨ckner, A.; Kumar, M. S.; Bentrup, U.; Debbagh, M. N.; Villaescusa, L. A. *J. Catal.* **2005**, 232, 318.

[7] (a) Blasco, T.; Camblor, M. A.; Corma, A.; Pe´rez-Pariente *J. Am. Chem. Soc.* **1993**, 115, 11806. (b) van der Waal, J. C.; van Bekkum, H. *J. Mol. Catal.* **1997**, 124, 137. (c) Carati, A.; Flego, C.; Massara, P.; Millini, R.; Carluccio, L.; Parker W. O., Jr.; Bellussi, G. *Microporous Mesoporous Mater.* **1999**, 30, 137.

[8] van Santen, R. A.; Kramer, G. *J. Chem. Rev.* **1995**, 95, 637.

[9] Blasco, T.; Camblor, M. A.; Corma, A.; Esteve, P.; Guil, J. M.; Martinez, A.; Perdigo´n-Melo´n, J. A.; Valencia, S. *J. Phys. Chem. B* **1998**, 102, 75.

[10] (a) Saxton R. J.; Zajacek J. G.; Crocco G. L. *Zeolites* **1996**, 17, 315. (b) Corma, A.; Domine, M. E.; Gaona, J. A.; Navarro, M. T.; Rey, F.; Valencia, S. *Stud. Surf. Sci. Catal.* **2001**, 135, 1812.

[11] (a) Taramasso, M.; Perego, G.; Notari, B. *U.S. Patent 4,410,501* **1983**. (b) Reddy, J. S.; Sivasanker, S. *Catal. Lett.* **1991,** 11, 241. (c) Huybrechts, D. R. C.; De Bruycker, L.; Jacobs, P. A. *Nature* **1990**, 345, 240.

[12] (a) van der Waal, J. C.; Lin, P.; Rigutto, M. S.; van Bekkum, H. *Stud. Surf. Sci. Catal.* **1996**, 105B, 1093. (b) Corma, A.; Camblor, M. A.; Esteve, P.; Martı´nez, A.; Pe´rez-Pariente, J. *J. Catal.* **1994**, 145, 151.

[13] Mal, N. K.; Ramaswamy, A. V. *Chem. Commun.* **1997**, 425.

[14] Corma, A.; Nemeth, L. T.; Renz, M.; Valencia, S. *Nature* **2001**, 412, 423.

[15] Renz, M.; Blasco, T.; Corma, A.; Forne´s, V.; Jensen, R.; Nemeth, L. *Chem. Eur. J.* **2002**, 8, 4708.

[16] Corma, A.; Domine, M. E.; Nemeth, L.; Valencia, S. *J. Am. Chem. Soc*. **2002**, 124, 3194.

[17] (a) Sever, R. R.; Root, R. W. *J. Phys. Chem. B* **2003**, 107, 10521. (b) Sever, R. R.; Root, R. W. *J. Phys. Chem. B* **2003**, 107, 10848.

[18] Corma, A. *J. Catal.* **2003**, 216, 298.

[19] Stelzer, J.; Paulus, M.; Hunger, M.; Weitkamp, J. *Microporous Mesoporous Mater.* **1998**, 22, 1.

[20] (a) Corma, A.; Domine, M. E.; Valencia, S. *J. Catal.* **2003**, 215, 294. (b) Corma, A.; Renz, M. *Chem. Commun.* **2004**, 550. (c) Corma, A.; Forne´s, V.; Iborra, S.; Mifsud, M.; Renz, M. *J. Catal.* **2004**, 221, 67.

[21] Fois, E.; Gamba, A.; Spano´, E. *J. Phys. Chem. B* **2004**, 108, 154.

[22] Zicovich-Wilson, C. M.; Dovesi, R.; Corma, A. *J. Phys. Chem. B* **1999**, 103, 988.

[23] (a) Pei, S.; Zajac, G.; Kaduk, J.; Faber, J.; Boyanov, B.; Duck, D.; Fazzini, D.; Morrison, Yang, D. *Catal. Lett.* **1993**, 21, 333. (b) Lopez, A.; Tuilier, M.; Guth, J.; Delmotte, L.; Popa, J. *J. Solid State Chem.* **1993**, 102, 480. (c) Scarano, D.; Zecchina, A.; Bordiga, S.; Geobaldo, F.; Spoto, G.; Petrini, G.; Leofanti, G.; Padovan, M.; Tozzola, G. *J. Chem. Soc., Faraday Trans.* **1993**, 89, 4123. (d) Neurok, M.; Manzer, L. E. *J. Chem. Soc., Chem. Commun.* **1996**, 1133.

[24] Zicovich-Wilson, C. M.; Dovesi, R. *J. Phys. Chem. B* **1998**, 102, 1411.

[25] (a) Notary, B. *Catal. Today* **1993**, 18, 163. (b) Berger, S.; Bock, W.; Marth, C.; Raguse, B.; Reetz, M. *Magn. Reson. Chem.* **1990**, 28, 559.

[26] Sastre, G.; Corma, A. *Chem. Phys. Lett.* **1999**, 302, 447.

[27] Boronat, M.; Corma, A.; Renz, M.; Viruela, R. M. *Chem. Eur. J.* **2006**, 12, 7076.

[28] Bare, S. R.; Kelly, S. D.; Sinkler, W.; Low, J. J.; Modica, F. S.; Valencia, S.; Corma, A.; Nemeth, L. T. *J. Am. Chem. Soc.* **2005**, 127, 12924.

[29] Newsam, J. M.; Treacy, M. M. J.; Koetsier, W. T.; de Gruyter, C. B. *Proc. R. Soc. London, Ser. A* **1988**, 420, 375.

[30] Shetty, S.; Pal, S.; Kanhere, D. G.; Goursot, A. *Chem. Eur. J.* **2006**, 12, 518.

[31] Boronat, M.; Corma, A.; Renz, M.; Sastre, G.; Viruela, P. M. *Chem. Eur. J.* **2005**, 11, 6905.

[32] (a) Ma, Y.; Foster, A. S.; Nieminen, R. M. *J. Chem. Phys.* **2005**, 122, 144709. (b) Mischler, C.; Horbach, J.; Kob, W.; Binder, K. *J. Phys.: Condens. Matter* **2005**, 17, 4005.

[33] Jentys, A.; Catlow, C. *Catal. Lett.* **1993**, 22, 251.

[34] Neurok, M.; Manzer, L. E. *J. Chem. Soc., Chem. Commun.* **1996**, 1133.

[35] de Man, A. J. M.; Sauer, J. *J. Phys. Chem.* **1996**, 100, 5025.

[36] Sauer, J. *Chem. Rev.* **1989**, 89, 199.

[37] Valerio, G.; Goursot, A.; Vetrivel, R.; Malkina, O.; Malkin, V.; Salahub, D. R. *J. Am. Chem. Soc.* **1998**, 120, 11426.

[38] Maurin, G.; Bell, R. G.; Devautour, S.; Henn, F.; Giuntini, J. C. *Phys. Chem. Chem. Phys.* **2004**, 6, 182.

[39] Nicholas, J. B.; Hess, A. C. *J. Am. Chem. Soc.* **1994**, 116, 5428.

[40] Rozanska, X.; Demuth, T.; Hutschka, F.; Hafner, J.; van Santen R. A. *J. Phys. Chem. B* **2002**, 106, 3248.

[41] Vanderbilt, D. *Phys. ReV. B* **1990**, 41, 7892.

[42] Perdew, J. P.; Wang, Y. *Phys. ReV. B* **1992**, 45, 13244.

[43] Raynaud, C.; Maron, L.; Jolibois, F.; Daudey, J. P.; Esteves, P. M.; Ramı´rez-Solı´s, A. *Chem. Phys. Lett.* **2005**, 414, 161.

[44] (a) Vos, A. M.; Rozanska, X.; Schoonheydt, R. A.; van Santen, R. A.; Hutschka, F.; Hafner, J. *J. Am. Chem. Soc.* **2001**, 123, 2799. (b) Termath, V.; Haase, F.;

Sauer, J.; Hutter, J.; Parrinello, M. *J. Am. Chem. Soc.* **1998**, 120, 8512. (c) Stich, I.; Gale, J. D.; Terakura, K.; Payne, M. C. *J. Am. Chem. Soc.* **1999**, 121, 3292.

[45] (a) Kresse, G.; Hafner, *J. Phys. ReV. B* **1994**, 49, 14251. (b) Kresse, G.; Furthmuller. *Comput. Mater. Sci*. **1996**, 6, 15.

[46] Godbout, N.; Salahub, D. R.; Andzelm, J.; Wimmer, E. *Can. J. Chem.* **1992**, 70, 560.

[47] (a) Parr, R. G.; Yang, W. *J. Am. Chem. Soc.* **1984**, 106, 4049. (b) Yang, Y.; Parr, R. G. *Proc. Natl. Acad. Sci. U.S.A.* **1985**, 821, 6723.

[48] Roy, R. K.; Krishnamuthy, S.; Geerlings, P.; Pal, S. *J. Phys. Chem. A* **1998**, 102, 3746.

[49] Roy, R. K.; Pal. S.; Hirao, K. *J. Chem. Phys.* **1999**, 110, 8236.

[50] Schmidt, M. W.; Baldrige, K. K.; Boatz, J. A.; Elbert, S. T.; Gordon, M. S.; Jensen, J. H.; Koseki, S.; Matsunga, N.; Nguyen, K. A.; Su, S.;Windus, T. L.; Dupuis, M.; Montgometry, J. A. *J. Comput. Chem.* **1993**, 14, 1347.

[51] (a) Wu, Q.; Yang, W. J. *J. Chem. Phys.* **2002**, 116, 515. (b) Zimmerli, U.; Parrinello, M.; Koumoutsakos, P. *J. Chem. Phys.* **2004**, 120, 2693. (c) Grimme, S. *J. Comput. Chem.* **2004**, 25, 1463.

[52] Dion, M.; Rydberg, H.; Schrder, E.; Langreth, D. C.; Lundqvist, B. I. *Phys. Rev. Lett.* **2004**, 92, 246401.

[53] Rappe, A. K.; Casewit, C. J.; Colwell, K. S.; GoddardIII, W. W.; Skiff, M. M. *J. Am. Chem. Soc.* **1992**, 114, 10024.

CHAPTER 4

Role of plane wave cut-off in structural and energy convergence

Abstract:

Periodic systems are best described by the pseudo-potential methods. However, the accuracy of its description depends on the cut-off of the plane wave basis. This is much more critical in the case of weak interactions, where a clear understanding on the influence of plane wave cut-off on the structural and electronic properties is not readily available in the literature. In the present chapter, we have taken a metal substituted beta zeolite–H_2O complex for understanding this objective. Our studies show that while a lower cut-off of 500 eV is sufficient for the convergence of the structural parameters, description of energy-dependent properties necessitates a high cut-off value.

4.1 Introduction

Among several theoretical methods, the total energy techniques such as Hartree–Fock (HF) and post-HF methods have been successfully applied to understand the structure and properties of systems containing 10–100 electrons [1]. The advances in density functional theory (DFT) [2,3] have facilitated the extension of these studies to large polyatomic molecules with more than 100 electrons. With the

advent of pseudo-potential (PP) based DFT methods [4], these studies were extended to periodic systems where core electrons are represented by pseudo-potentials and valence electrons are dealt with plane waves (PW). This reduces the computational expense of simulation [5] in dealing with large complex molecules and, in particular, for periodic systems. In addition, PW technique is popular as it is straight forward to use in solid state periodic simulations. PW periodic DFT (p-DFT) based methods have found an impressive range of applications [6–10].

An extremely appealing feature of PW basis is that the energies calculated do not suffer from the basis set superposition error (BSSE). This enables a better description of adsorption processes that are characterized by interaction energies of moderate strength. However, the quality of the PW basis set is specified by an important parameter: the electronic kinetic energy cut-off, E_{cut}. Therefore, for a given structure and a set of pseudo-potentials, the first task in any PW calculation is to choose appropriate cutoff energy for the basis. This is done by means of a convergence test, in which calculations are carried out with series of increasing cut-off energies. The convergence of a given quantity, usually the total energy, is monitored towards its large cut-off limit. However, as will be discussed later, this is not a sufficient test for studying weak interactions.

Many physical properties such as bulk moduli, piezoelectric constant, phonon, and phase transitions, are related to the total energy of a system. In contrast, chemical properties such as interaction energy, adsorption energy, intrinsic reaction barriers etc., are related to the differences in total energies of two systems. In p-DFT, truncation of PW at a finite cut-off may lead to an error in the calculation of the total energy and other energy-related properties. These errors are usually reduced by increasing the value of kinetic energy cut-off and hence the number of PW. In principle, the PW cut-off is increased until the calculated total energy is converged. However, a relative property, such as weak interaction energy need not converge at the same rate as that of the total energy. Hence, all these parameters, despite having some default values in the program, need to be carefully chosen in a given simulation.

Based on the above issues and inspired by the work of Ramirez-Solis and co-workers [11], we examine the convergence of total and interaction energies as a

function of PW basis. In the earlier work [11] the statistical and dynamical structure, energy convergence, and frequency convergence of Hydrogen Fluoride clusters were studied using standard norm conserving pseudo-potentials. The authors enclosed each molecular cluster in a box of 15 Å Here the vacuum region and the decaying wave functions are more delicate to handle with plane waves and the cut-off is crucial. Their study verified the need of a large plane wave cut-off for a proper description of ionic and hydrogen bonded interactions in a cluster. The authors mentioned that it would be interesting to have similar comparisons with the ultrasoft pseudo-potentials. It is to be noted that in the present study, we have used ultrasoft pseudopotentials, which are known to typically require 2.5 – 4 times lower cut-offs. Although similar attempts [12–17] have been previously made in the computational chemistry community, a clear description of the PW variation for a large periodic model is not yet available.

Consequently, we aim to examine the influence of PW cut-off on the convergence of a weakly interacting zeolite and water complex. These catalysts are so chosen because they are preferentially hydrophobic in nature [18,19]. In addition, zeolite beta (BEA) is a well known active catalyst for carrying out several organic reactions. Hence, the nature of its interaction, which is mainly weak attractive and coordinative, with several organic reagents and reaction media necessitates an understanding using such theoretical studies [20–22]. The incorporation of Ti- and Sn- at active sites (T-sites) finely tunes acidity and increases activity of the BEA (T-BEA). Several studies describe the structural and energetic features of these systems [23–27]. Structural details of Sn/Ti- BEA-complexes, their cohesive energies, interaction energies along with reactivity are well studied in the literature [22,28–34]. This system is an appropriate example as it features a rigid and flexible framework with a simultaneous presence of two types of bonding, a covalent one e.g. Si–O and a weak hydrogen bonding due to the adsorption of a water molecule, representing a wide range of chemical systems. Hence, the main focus of present study will be to examine the role of PW in describing the structural properties such as bond length, bond angle etc., total energies of each individual system and their respective interaction energies. We also include a short discussion on the density-dependent

HOMO, LUMO and ELF contours. These maps are calculated at PW cut-offs of 500 eV and 1000 eV to highlight the effect of basis extension.

4.2 Simulation Model

Since the zeolites are periodic and crystalline, their simulation is a challenging task. The most appreciated approximation for investigation of active sites within zeolites is a computationally cheap cluster model [35–38] approach. However, since a cluster model is an abbreviated form of a 3D structure, it introduces some artificial surface states and does not consider the long range interactions. In addition, the presence of a few substituted active sites in zeolites forces one to use periodic boundary conditions (PBC) in their representation. PBC corresponds to one or more unit cells replicated to form an infinite lattice. This ensures that the density of the system remains constant throughout the simulation and that the surface effects are absent. Despite the complexity to build such models, several reaction mechanisms of these catalytic materials are studied periodically [39–41]. However, as mentioned above, a clear understanding on the convergence of structure and energy with respect to PW cut-off is not available in the literature.

The unit cell of an ideal fully siliceous BEA zeolite consists of 192 atoms with 64 Si and 128 O atoms distributed within the tetragonal lattice of dimensions (12.6 * 12.6 * 26.2)Å. Figure 4.1 shows the unit cell of BEA zeolite. There are nine distinct crystallographically defined T-sites. We adopt the structure of BEA from our previous chapter [34] and incorporate the Sn- and Ti-atoms at T2 and T1 sites [42], respectively. The interaction of H_2O molecule at the active site is very important since it gives rise to geometric perturbations and energetic differences. Schematic representation of T-BEA/H_2O is given in Figure 4.1 (small molecule adsorbed on T-site). The most favorable H_2O ligand approach at the active T-site is along the b axis. Various other possible orientations of H_2O ligand at the active site result in high energy and high force values. The insertion of water molecule results in elongation of one of the T–O bonds compared to that of the others present in TO_4 unit. The four framework oxygen atoms are no longer equivalent and split into one axial ($T–O_{ax}$)

opposite to the adsorbed ligand and three equatorial ($T–O_{eq}$), respectively.

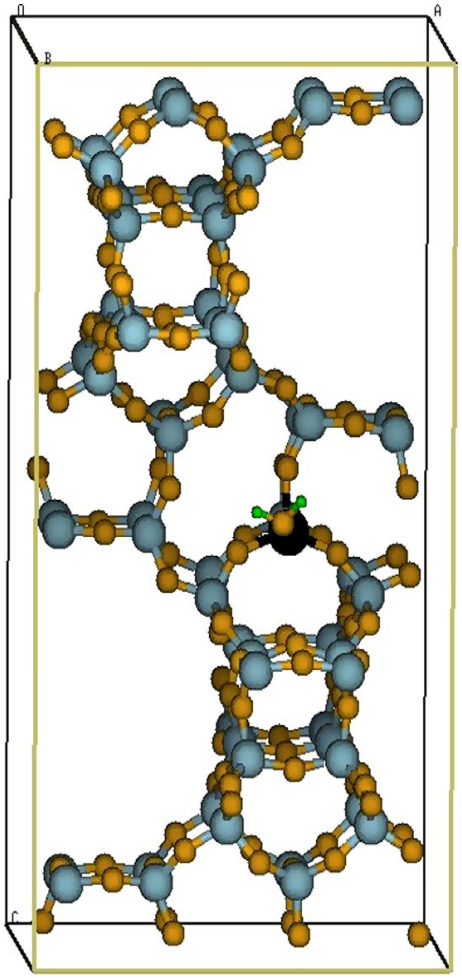

Figure 4.1: Optimized T-BEA unit cell with interaction of H_2O molecule at T1 site. Black sphere, Ti-atom; gray spheres, Si atoms; yellow spheres, O atoms; and small green spheres, H atoms.

Consequently, six O–T–O angles of the TO_4 unit give rise to two triplets, $O_{eq}–T–O_{eq}$ and $O_{eq}–T–O_{ax}$. These are labeled as a and b, respectively. This geometric distortion leading to more distorted bipyramidal geometry makes the structure more reactive.

4.3 Computational Details

All periodic calculations in the present study are carried out using VASP [9,10]. The PBC facilitates one to add long range electrostatic interactions through Ewald summations. As in standard DFT programs, the stationary ground state in p-DFT is calculated by solving iterative Kohn–Sham equations. We use Vanderbilt's ultrasoft pseudo-potentials [43] for describing the behavior of core electrons. Here we vary the number of PW for valence, and analyze the properties of the systems with respect to their number. The energy cut-off for plane waves is varied from 300 eV i.e. 21.83 Ry to 1200 eV i.e. 88.20 Ry. The exchange–correlation functional is expressed by the generalized gradient approximation (GGA) using Perdew–Wang 91 [44] functional (PW91). The calculations are restricted to gamma point in the Brillouin zone sampling. The structural optimization of Sn- and Ti-BEA is carried out using the conjugate gradient method. The structure is considered to be optimized when the maximum force on each atom is less than 0.08 eV/Å. Similar optimization procedures are repeated for the interaction of water molecule at Sn- and Ti-centers in BEA, and for that of periodic bare H_2O molecule. The above procedure of optimization is followed for all systems with PW cut-off varying from 300 eV to 1200 eV at an interval of 100 eV.

While calculating the total energy, one should take care of the charge density. The charge density is computed easily in real space, as it is simply the square of magnitude of the wave function. However, the charge density has components up to twice the cut-off wave vector in case of PW. Most programs assign some default grid size according to the need of the computation. However, the accuracy of such default values cannot be taken as granted for systems where a large number of PWs are required to explain weak interactions. As an illustration, Figure 4.2a shows a model convergence pattern of the total energy of Sn-BEA and H_2O complex as a function of cut-off value at default FFT grid assigned by the VASP program. Similarly, the total energy of each system converge smoothly until 700 eV cut-off, beyond which it fails to converge with default grid values. A consequence of this is also observed in the respective interaction energy. The Figure 4.2b highlights the oscillatory interaction

energies of the complexes as a result of bad convergence of the total energy of the individual system.

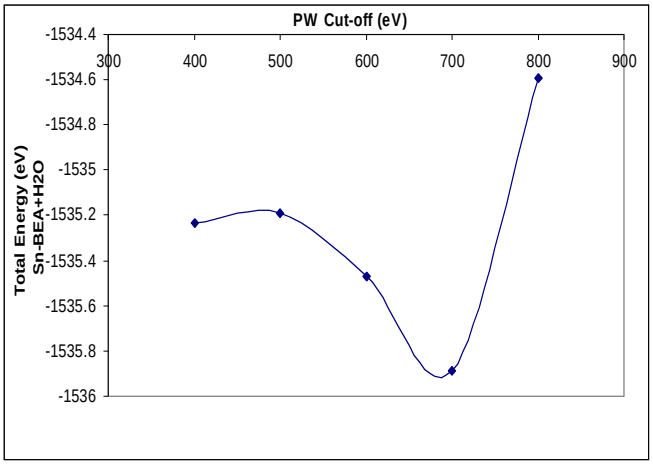

(a)

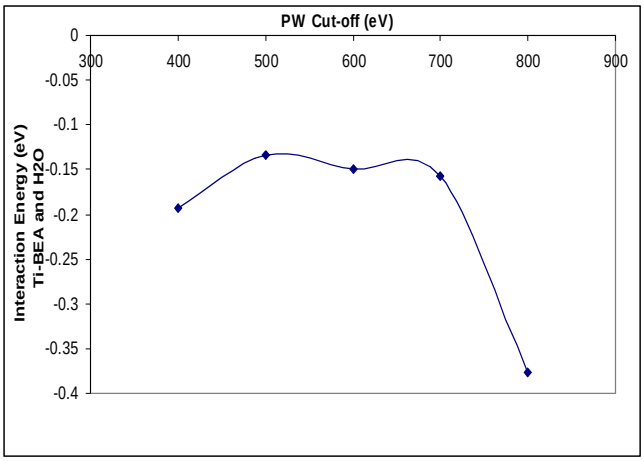

(b)

Figure 4.2: (a) Total energy of Sn-BEA + H_2O as a function of PW cut-off at default FFT grid. (b) Interaction energy of Ti-BEA and H_2O as a function of PW cut-off at default FFT grid.

As the energy-dependent relative property is far from the convergence, it is necessary to explore the energy surface of materials using higher cut-offs. Hence, to maintain a faithful representation of charge density one must compute it on a grid twice denser than that required in the representation of the wave function. In addition, considering the size of our periodic model and to achieve a better relative accuracy, we fix the

FFT grid to a cubical 96*96*96 mesh size. Further discussion of the results will be mostly in graphical form. The graphical figures are obtained from differential plots, where, we assume the converged values at limiting cut-off (1000 eV) as a reference zero and rest of the higher energies are subtracted from these reference values. Figure 4.3, taken as evidence for structural convergence, depicts nuclear–nuclear repulsion energy as a function of cut-off. Figure 4.4 gives the total energy of water as a function of cut-off. Figure 4.5a and b depicts the convergence. We have not presented figures for them. Figure 4.6 a and b displays the most important property, the fluctuations of interaction between Ti-BEA and Sn-BEA with water molecule,respectively.

4.4 Results and Discussion

We first examine the convergence of structural parameters over the range of PW cut-off, 300–1200 eV. Table 4.1 shows the convergence of some relevant geometrical parameters. The intra-molecular distances are quite stable from 400 eV. As a result of water adsorption, both the T-BEA–water adducts show an elongation of all T–O bond lengths as compared to the bare T-BEA systems. For Sn-BEA, it is stable at 1.91 Å, where as in water adduct, it gets elongated to 1.92 Å. For Ti-BEA, T–O distance converges to 1.80 Å. This gets elongated and converges to 1.82 Å in its water adduct. In TBEA–water adduct, T–Si bonds do not show much elongation as compared to the bare T-BEA. For bare T-BEA, T–Si distance converges to 3.33 Å and for the corresponding adduct, it converges to 3.36 Å. T–O–Si bond angle gets much widened in the respective water adducts. For Sn-BEA and H_2O complex, the T–O–Si angle widens from 143 to 145.2 deg, where as for Ti-BEA it changes from 152 to 157.7 deg. The most important inter-molecular interaction involves oxygen atom of water molecule with Sn- and Ti-atoms in BEA. In Sn-BEA, T–OH_2 distance varies from 2.43 Å to 2.44 Å, showing its convergence from 500 eV. However, in Ti-BEA, T–OH_2 distance varies from 3.84 Å to 4.13 Å and converges to 3.84 Å 600 eV cut-off.

Table 4.1: Convergence of various geometrical parameters of T-BEA+H_2O as a function of plane wave cut-off

Geometrical parameters	Sn-BEA	Sn-BEA+H_2O	Ti-BEA	Ti-BEA+H_2O
T-O Å (300 eV)	1.91	1.92	1.80	1.82
T-O Å (400 eV)	1.91	1.92	1.80	1.82
T-O Å (1000 eV)	1.91	1.92	1.80	1.82
T-Si Å (300 eV)	3.33	3.34	3.33	3.35
T-Si Å (400 eV)	3.33	3.36	3.33	3.36
T-Si Å (1000 eV)	3.33	3.36	3.33	3.36
T-O-Si deg (300 eV)	143.0	145.9	152.0	157.8
T-O-Si deg(400 eV)	143.0	145.2	152.0	157.7
T-O-Si deg(1000 eV)	143.0	145.2	152.0	157.7
T-OH_2 Å (300 eV)	-	2.43	-	4.07
T-OH_2 Å (600 eV)	-	2.44	-	3.84
T-OH_2 Å (1000 eV)	-	2.44	-	3.84

Thus, the structural convergence is less sensitive to the number of PW and the evidence of this fact is given through Figure 4.3. Figure 4.3 represents the variation of Ewald energy i. e. nuclear–nuclear repulsion energy for Ti-BEA over the plane wave basis. This figure depicts the model plot of nuclear repulsion energy as a function of cut-off as rest of the systems follow similar trend. The Ewald energy plot (Fig. 4.3) distinctly shows a plateau around 600 eV cut-off. This leads to conclusion that the nuclear positions are fixed at and above these cut-offs. However, for low cut-offs of 400 eV and 500 eV, the difference of repulsion energy from converged energies is negligible and hence one can assume the qualitative structural convergence even at 500 eV. Thus, the convergence of the structural parameters at lower PW cut-off validates the use of ultrasoft pseudo-potentials. These results certainly indicate that

for accurate structure one does not need very high kinetic energy cut-offs.

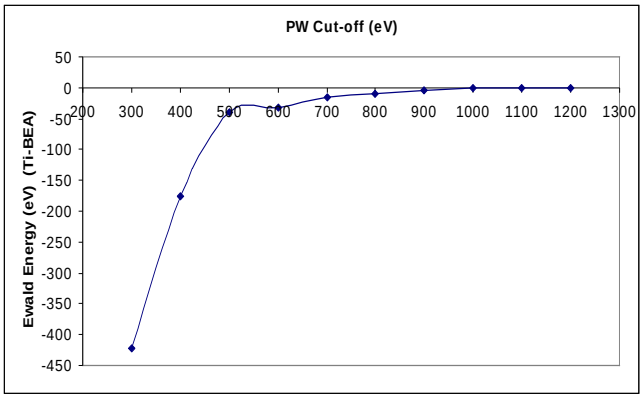

Figure 4.3: Ti-BEA nuclear–nuclear repulsion energy (Ewald energy) (eV) as a function of PW cut-off (eV).

The convergence of adsorption energies with respect to the PW cut-offs for zeolitic system is one of the most crucial issues to be investigated. These catalytic materials are expected to exhibit the hydrophobic nature and the water present is responsible in poisoning the active site. Discrepancy in calculation of the adsorption energy of water molecule on Sn- and Ti-BEA zeolite is already reported by us in our previous chapter [34]. We next analyze the convergence of total energy and the desired properties dependent on it as a function of plane wave cut-off. Figures. 4.4 and 4.5 a and b present the convergence of total energies of water and T-BEA systems, respectively. Figure 4.6 a and b depicts the interaction energies at variable cut-off for two different T-BEA systems with water molecule.

In our study of T-BEA and their weakly interacting water adduct, we attempt to determine properties that are essentially chemical in nature. Chemical properties are mostly determined by the electronic structure in the region between atoms, rather than in the space within atomic cores. This fact has already been made use of in the pseudo-potential approximation, and as we will see, it does not allow us to use a lower PW cut-off for the electronic energy convergence. The electronic energy is much more sensitive to the variation of PW cut-off. The total energy convergence of Ti-BEA–H_2O and Sn-BEA as a function of PW basis are plotted in Figure 4.5 a and b

(rest of the systems follow a similar trend). The total energies of T-BEA and their respective water complexes are seen to converge very slowly at lower cut-offs up to 500 eV. At these cutoffs the difference in total energy is around 1 eV between two successive cut-offs. However, 600 eV onwards, this difference reduces and the total energies of all systems converge much faster. Absolute convergence can be seen from 900 eV to 1000 eV cut-off. For water molecule (see Fig. 4.4), although the convergence is relatively faster even at lower cut-offs, we observe that at cut-offs beyond 700 eV, the electronic energy is well saturated.

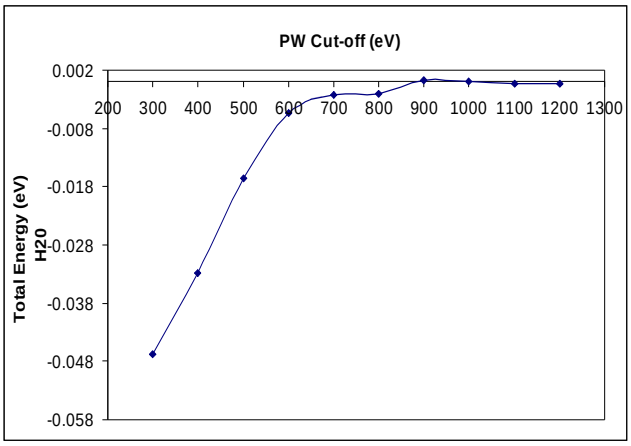

Figure 4.4: H_2O total energy (eV) as a function of PW cut-off (eV).

The total energy decreases linearly up to 700 eV cut-off, beyond which a smooth convergence is observed. Although a solid is known to converge at a faster rate than the gas phase molecules, Figure 4.4 shows a reverse trend. The electronic energy of molecular water converges at a lower cut-off of 600 eV. However, the interaction energy (defined as $\mathbf{E_{T\text{-}BEA+1H2O} - (E_{T\text{-}BEA}+E_{1H2O})}$) which is a relative term, converges only at cut-offs larger than 800 eV. The oscillatory behavior of interaction energy (Fig. 4.6 a and b) affirms the failure of low cut-offs in calculating the energy-dependent properties. Interaction energy greatly fluctuates for low PW cut-off: 300–700 eV. At the cut-off 300 eV, the interaction energy values are clearly misleading, since Ti-BEA turns out to be more hydrophilic in nature compared to Sn-BEA.

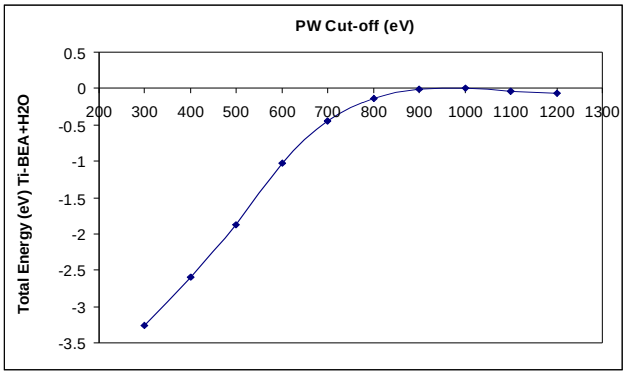

(a)

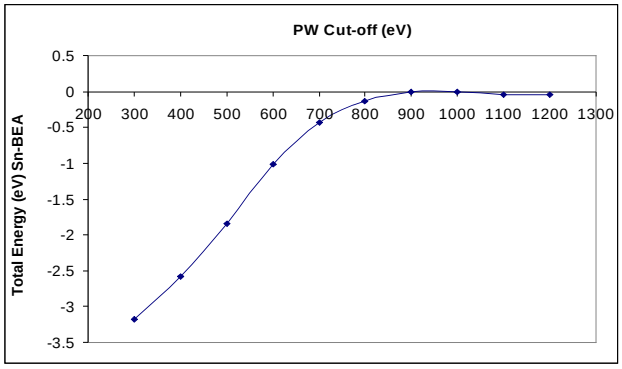

(b)

Figure 4.5: (a) Ti-BEA + H_2O total energy (eV) as a function of PW cut-off (eV). (b) Sn-BEA total energy (eV) as a function of PW cut-off (eV).

Several experimental and theoretical work [34,45] reports Sn-BEA to be strongly acidic and hydrophilic in nature. The variation in the convergence of interaction energy remains same even though the number of plane waves are increased. Thus, the evaluation of a relative property, such as the interaction energy, justifies role of exceptionally high cut-off in an energy-dependent property convergence.

A keen observation of Figures 4.5 a-b and 4.6 a-b highlights a slight error in the convergence of total and interaction energies above 1000 eV cutoff. A good convergence of energies, absolute or interactive, is obtained up to 1000 eV, beyond which these values violate the convergence pattern. In this case, as already described in the computational discussion, when the cut-off reaches its high limiting value a denser grid construction is advisable to accommodate this exceeded threshold of PW.

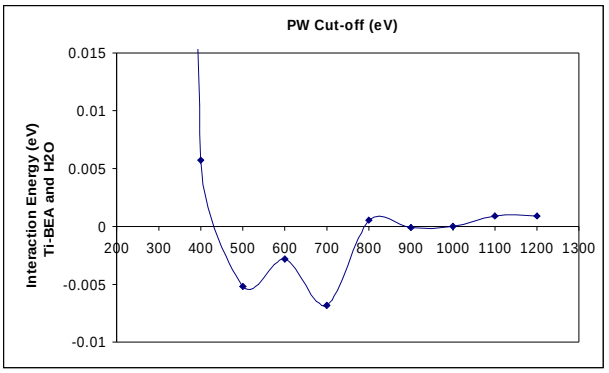

(a)

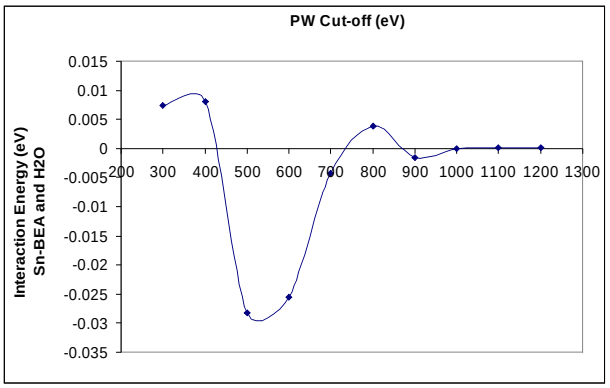

(b)

Figure 4.6: (a) Ti-BEA and H_2O Interaction energy (eV) as a function of PW cut-off (eV). (b) Sn-BEA and H_2O Interaction energy (eV) as a function of PW cut-off (eV).

Highest occupied molecular orbital (HOMO) and lowest unoccupied molecular orbital (LUMO) are characteristic of a particular system and are considered as the descriptors of global reactivity. Hence, for both individual T-BEA systems and their water adducts, we inspect the convergence of HOMO and LUMO with respect to the cut-off. HOMO, LUMO energies and their energy gap start to converge above 600 eV cut-off. For Sn-BEA, the converged values of HOMO and LUMO are 3.109 eV and 1.344 eV, respectively. For Ti-BEA, the HOMO converges to 3.144 eV and LUMO to 1.374 eV. For Sn-BEA adduct, the converged values of HOMO and LUMO are 2.891 eV and 1.659 eV, respectively. For Ti-BEA, adduct the corresponding values are 2.888 eV and 1.366 eV, respectively.

Analysis of HOMO orbital (see figure 4.7a) at 500 eV and 1000 eV shows a contribution from the framework oxygen (clearly showing p-orbital lobes) surrounding the T-atom. The oxygen of water molecule does not contribute to the HOMO.

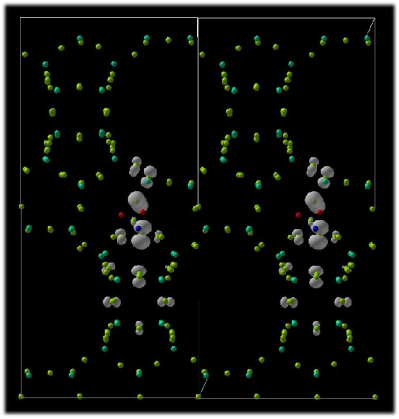

(a) HOMO at 500 eV

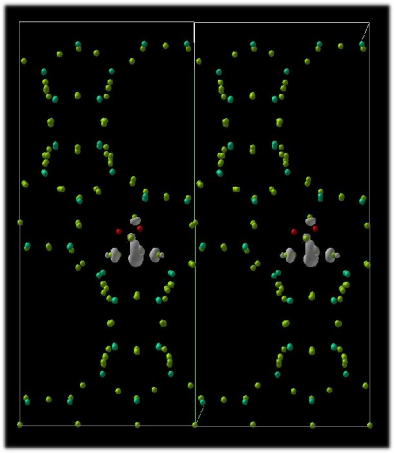

(b) LUMO at 500 eV

Figure 4.7: (a) HOMO and (b) LUMO of Ti-BEA+H_2O

Analysis of the LUMO orbital (see figure 4.7b) at 500 eV and 1000 eV highlights the polarization of the neighboring framework oxygen due to T-atoms. The LUMO is mostly concentrated on the T-atom. In addition, the density on the oxygen atom of the water molecule is also polarized due to the T-atom. This is a most important outcome

where a weak hydrogen bonding is observed between the framework oxygens (surrounding T-atom) and the H atom of the adsorbed water molecule. However, interestingly, we note that both the HOMO and LUMO orbital contour maps are converged by 500 eV cut-off, indicating that a lower cut-off is sufficient for studying the orbital contributions.

As an extension to this, we also evaluate a property, Electron Localization Function (ELF), which is often used to study the bonding pattern within molecules and solids [46,47]. Typically, the existence of an isosurface in the bonding region between two atoms at high values of ELF e.g. greater than 0.70 signifies a localized bonding. ELF is a function of q(r) and hence w(r). ELF contours for a isovalue of 0.80 (figure not shown) clearly show localized electron density around the oxygen atoms coming from the lone pair of electrons on them. The basins on the water molecule are merged showing them to be strongly covalent in nature. In contrast, the basins in zeolite cages are not merged. Around an isovalue of 0.65 (see figure 4.8), the basins in the zeolite cage also merge. The ELF contours converge for a plane wave cut-off of 500 eV indicating that structural and electron densities converge earlier than the total energy values. Hence, we state explicitly that density-dependent properties along with structure converge at much lower cut-offs.

In addition, variation of unit cell parameters i.e. a, b, c is also studied as a function of cut-off. For both T-BEA systems, a, b and c converge to 12.66 Å, 12.66 Å and 26.29 Å, respectively, above 600 eV cut-off. Unlike geometrical features, lattice vectors are very sensitive to the quality of plane wave cut-off chosen. All the above values describing geometrical data match very well with our earlier electronic structure studies [34]. Thus, although the pseudopotential techniques are easy to be applied for large complex systems, the evaluation of several properties, as described above, necessitates the need of proper selection of parameters like kinetic energy cut-off for the plane wave basis in their accurate description.

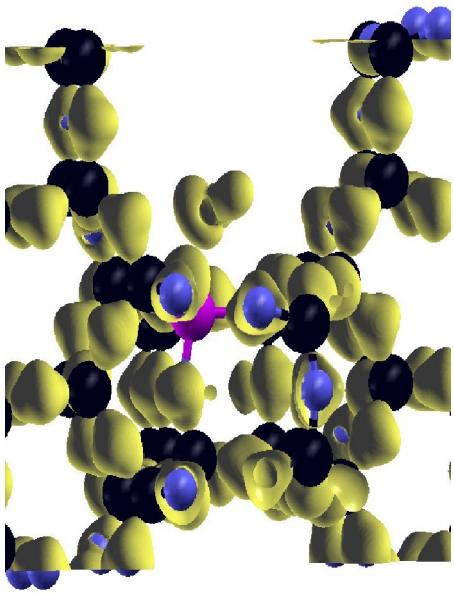

Figure 4.8: ELF at 0.65 of Sn-BEA+H_2O

4.5 Conclusion

In this paper, we study the role of a simple parameter, cut-off energy of a plane wave basis, required for an accurate description of periodic systems. Different types of bonding (intra- and intermolecular) can be described with reasonable accuracy by a low plane wave cut-off. This fact is proved by the description of ELF and HOMO–LUMO contours. However, the total energy and relative properties depending on it, such as interaction energy, require a cut-off which is larger than that required for structural convergence. The role of plane wave basis extension for these periodic solids is exactly the same as that reported in earlier studies [11,48,49] for finite molecular systems. Hence, for these particular periodic systems one can use 500 eV cut-off in structural convergence, where as total energy convergence requires more than 800 eV cut-off.

We conclude that caution must be exercised while choosing these control parameters, both from the structural and energetic point of view, for systems involving ionic and weak interactions. Also, as discussed in the methodology, in order to avoid artificial results, additional parameters like grid size need to be set up properly.

4.6 References

[1] I. N. Levine, Quantum Chemistry (4th edn), Prentice–Hall of India, 1995.

[2] P. Hohenberg, W. Kohn, Phys. Rev. B 140 (1964) 864.

[3] R.G. Parr, W. Yang, Density-functional Theory of Atoms and Molecules, Oxford University Press, 1989.

[4] M. C. Payne, M. P. Teter, D. C. Allan, T. A. Arias and J. D. Joannopoulos, Rev. Mod. Phys. 64 (1992) 1045.

[5] T. R. Cundari, M. T. Benson, M. L. Lutz, S. O. Sommerer, Reviews in Computational Chemistry, edited by K. B. Lipkowitz, D. B. Boyd, VCH, New York, 8 (1996) 145.

[6] X. Gonze, J.-M. Beuken, R. Caracas, F. Detraux, M. Fuchs, G.-M. Rignanese, L. Sindic, M. Vertraete, G. Zerah, F. Jollet, M. Torrent, A. Roy, M. Mikami, P. Ghosez, J.-Y. Raty, D. C. Allan, Comput. Mater. Sci, 25 (2002) 478.

[7] M. D. Segall, P. J. D. Lindan, M. J. Probert, C. J. Pickard, P. J. Hasnip, S. J. Clark, M. C. Payne, J. Phys.: Condens. Matter, 14 (2002) 2717.

[8] D. Marx, J. Hutter, Modern Methods and Algorithms of Quantum Chemistry, NIC, FZ, Julich, 2000, p.301. (c) W. Andreoni, A. Curioni, Parallel Comput, 26 (2000) 819.

[9] G. Kresse, J. Hafner, Phys. Rev. B, 48 (1993) 13115.

[10] G. Kresse, J. Furthermuller, Comput. Mater. Sci. 6 (1996) 15.

[11] C. Raynaud, L. Maron, F. Jolibois, J-P. Daudey, P.M. Esteves, A. Ramírez-Solís, Chemical Physics Letters, 414 (2005) 161.

[12] K. Lee, J. Yu, Y. Morikawa, Phys. Rev. B 75 (2007) 45402.

[13] T. Todorova, A. P. Seitsonen, J. Hutter, I. W. Kuo, C. J. Mundy, J. Phys. Chem. B 110 (2006) 3685.

[14] J. Paier, R. Hirschl, M. Marsman, G. Kresse, J. Chem. Phys. 122 (2005) 234102.

[15] S. Casassa, M. Catalayud, K. Doll, C. Minot, C. Pisani, Chem. Phys.Lett. 409 (2005) 110.

[16] G. Festa, M. Cossi, V. Barone, G. Cantele, D. Ninno, G. Iadonisi, J. Chem.

Phys. 122 (2005) 184714.

[17] C. Janfelt, F. Jensen, Chem. Phys. Lett. 406 (2005) 501.

[18] A. Corma, J. Catal. 216 (2003) 298.

[19] J. Stelzer, M. Paulus, M. Hunger, J. Weitkamp, Micropor. Mesopor. Mater. 22 (1998) 1.

[20] M. Boronat, A. Corma, M. Renz, G. Sastre, P. M. Viruela, Chem. Eur. J. 11 (2005) 6905.

[21] M. Boronat, A. Corma, M. Renz, R. M. Viruela, Chem. Eur. J. 12 (2006) 7076.

[22] S. Shetty, S. Pal, D. G. Kanhere, A. Goursot, Chem. Eur. J 12 (2006) 518.

[23] R. L. Wadlinger, G. T. Kerr, E. J. Rosinski, U.S. Patent (1967) 3308069

[24] V. A. Tuan, S. Li, R. D. Noble, J. L. Falconer, EnViron. Sci. Technol., 37 (2003) 4007.

[25] J. C. van der Waal, H. van Bekkum, J. Mol. Catal. 124 (1997) 137.

[26] A. Carati, C. Flego, P. Massara, R. Millini, L. Carluccio, W. O. Jr. Parker G. Bellussi, Microporous Mesoporous Mater. 30 (1999) 137.

[27] R. J. Saxton, J. G. Zajacek, G. L. Crocco, Zeolites 17 (1996) 315.

[28] T. Blasco, M. A. Camblor, A. Corma, PeÂ´rez-Pariente J. Am. Chem. Soc. 115 (1993) 11806.

[29] A. Corma, M. E. Domine, J. A. Gaona, M. T. Navarro, F. Rey, S. Valencia, Stud. Surf. Sci. Catal. 135 (2001) 1812.

[30] N. K. Mal, A. V. Ramaswamy, Chem. Commun. 425 (1997)

[31] A. Corma, L. T. Nemeth, M. Renz, S. Valencia, Nature 412 (2001) 423.

[32] G. Sastre, A. Corma, Chem. Phys. Lett. 302 (1999) 447.

[33] S. R. Bare, S. D. Kelly, W. Sinkler, J. J. Low, F. S. Modica, S. Valencia, A. Corma, L. T. Nemeth, J. Am. Chem. Soc. 127 (2005) 12924.

[34] S. Shetty, B. S. Kulkarni, S. Pal, D. G. Kanhere, A. Goursot, J Phys Chem B, 112 (2008) 2573.

[35] A. J. M. de Man, J. Sauer, J. Phys. Chem. 100 (1996) 5025.

[36] S. Krishnamurty, S. Pal, A. Goursot, R. Vetrivel, Microporous and Mesoporous Materials, 48 (2001) 383.

[37] S. Krishnamurty, S. Pal, J. Phys. Chem. A, 104 (2000) 7639.

[38] J. Sauer, Chem. ReV. 89 (1989) 199.

[39] C. Pisani, R. Dovesi, C. Roetti, C. Hartree-Fock Ab Initio Treatment of Crystalline Systems, Springer-Verlag, Berlin, 1988.

[40] E. H. Teunissen, C. Roetti, C. Pisani, A. J. M. de Man, A. P. J Jansen, R. Orlanso, R. A. van Santen, R. Dovesi, R. Simul. Mater. Sci. Eng. 2, 921 (1994).

[41] X. Rozanska, Th. Demuth, F. Hutschka, J. Hafner, R. A. van Santen, J. Phys. Chem. B, 106 (2002) 3248.

[42] J. M. Newsam, M. M. J. Treacy, W. T. Koetsier, C. B. de Gruyter, Proc. R. Soc. London, Ser. A 420 (1988) 375.

[43] D. Vanderbilt, Phys. ReV. B 41 (1990) 7892.

[44] J. P. Perdew, Y. Wang, Phys. ReV. B 45 (1992) 13244.

[45] A. Corma, M. E. Domine, S. Valencia, J. Catal. 215 (2003) 294.

[46] S. Krishnamurty, S. Chacko, D. G. Kanhere, G. A. Breaux, C. M. Neal, M. F. Jarrold, Phys. Rev. B 73 (2006) 045406.

[47] B. Silvi, A. Savin, Nature (London) 371 (1994) 683.

[48] F. C. E. Byrd, G. E. Scuseria, C. F. Chabalowski, J. Phys. Chem. B 108 (2004) 13100.

[49] S. Tosoni, C. Tuma, J. Sauer, B. Civalleri, P. Ugliengo, J. Chem. Phys. 127 (2007) 154102.

CHAPTER 5

Probing Lewis Acidity of Sn- and Ti-BEA using industrially important ligands

Abstract:

The Lewis acidic nature and reactivity of two industrially important catalysts, viz., Sn and Ti substituted beta zeolite (T-BEA) are analyzed using a unique combination of structural parameters, energetics and reactivity descriptors. To achieve this purpose, we adsorb the industrially important moieties (L) namely NH_3, H_2O, CH_3OH, CH_3CN on the active sites of T-BEA. The calculations were performed using a periodic density functional method where the valence electrons are described using a plane wave basis set in conjunction with pseudo-potentials for the core electrons. The analysis of the structural properties of these complexes reveals that TO_4 shows typical characteristic splitting 120°/90°, close to bipyramidal geometry as compared to tetrahedral symmetry observed in the bare T-BEA. This is associated with small variations in the framework bond lengths (≥ 0.08 Å) and a substantially large variation of bond angles (≤ 10˚) in all the ligand-zeolite complexes. Further in both cases of Sn and Ti substituted beta zeolite, ligand interacts at optimum inter-atomic bond distance. Our interaction energies show that adsorption of all ligand moieties is stronger at Sn center than that of Ti. In general, the order of stability of the different T-BEA adducts is NH_3>H_2O>CH_3OH>CH_3CN. The ligand interaction is associated with the corresponding bond elongation and bond reduction of the

adsorbed molecules on catalyst active site, which can be taken as measure of red or blue shifted frequencies. Finally, the global descriptors of reactivity justify the fact that soft acid, Sn-BEA, interacts strongly with soft bases following the Pearson's HSAB principle. However, hard acid, Ti-BEA interacts with soft bases to form a stable Lewis adduct. Furthermore, the HOMO-LUMO gap of all Sn-BEA--L adducts is lower than that of Ti-BEA--L adducts indicating to its higher Lewis acidic nature compared to Ti-BEA.

5.1 Introduction

The importance of the metal substituted BEA framework and its applications [1-21] are thoroughly discussed in the introduction section of chapter 3. Apart from the hydrophilic and/or hydrophobic nature comparison, we can take the water adsorption as the measure of the strength of Lewis acid base interaction. The strong interaction of the basic water molecule at the active Sn site than that of Ti assures its higher acidic nature. In general, the catalytic activity of a Lewis acid for oxidation is related to its ability to form acid–base adducts with either the substrate or the oxidizing agent, enhancing its reactivity. The formation of adduct implies an electron density transfer from the Lewis base to the Lewis acid which is directly proportional to the energy difference and degree of overlap between the occupied orbital of the base and the empty orbital of the acid. Therefore, the strength of a Lewis acid can be related to the energy of its LUMO in such a way that the lower the LUMO energy, the easier its interaction with a base molecule [22-25]. However, other factors influence the acid–base interaction. For example, one such factor is the HSAB (hard–soft acid–base) principle, which states that hard acids coordinate preferentially to hard bases and soft acids with soft bases [26, 27]. Another factor to be considered is the possibility of back-donation of electron density from the Lewis acid to the unoccupied orbital of the Lewis base [22]. An interaction may or may not occur, depending on the energy difference and degree of overlap between the orbital involved [23]. Modification of the electronic levels of both the metal and the

molecule, after the adsorption of a basic molecule on the metal center, should also be taken into account. Hence, the activity of a catalyst for a given reaction depends not only on the properties of the isolated active site, but also on the changes caused by its interaction with the reactant molecules [26,27]. This latter approach has been adopted by several experimentalists using *in situ* IR and EXAFS spectroscopies [15, 19] and theoreticians [21, 23, 25, 28-32] using simple adsorption model of basic moieties at catalyst active centers. The above mentioned parameters are analyzed in the present study on metal substituted beta zeolite-ligand complexes.

In the past, [21, 25, 28-32] main attention has been devoted to study of the Ti(IV) center reactivity in various zeolites such as TS-1, CHA etc. through the adsorption of NH_3 and H_2O. Bordiga et al. [28, 33, 34] study the adsorption of CD_3CN and pyridine on Ti centers of the TS-1. They confirm their results with the experimental vibrational spectra. Similarly, Corma et. al., [29] performed the *in situ* IR and DFT calculations with deuterated acetonitrile to outline the peculiarities of Sn-BEA. However, most of these studies consider a cluster model approach. The main drawback of the cluster model in the characterization of T(IV) Lewis centers using adsorption model is two fold: 1) the high dilution of the T(IV), where T/Si is lower than 1/30 (here in BEA also we have only one T/Si ratio) and 2) the presence of the framework defects (Si vacancies) generating internal hydroxyl groups.

Hence, in our present study, we execute periodic-DFT (p-DFT) for the interaction study of important basic moieties adsorbed at the active sites of Sn-BEA and Ti-BEA. To study the interaction, we consider the basic moieties such as NH_3, H_2O, CH_3OH, CH_3CN. The clear interest towards NH_3 and H_2O molecules is the direct comparison with previous results. In addition, the NH_3 molecule is used in ammoximation of cyclohexanone to give cyclohexanone ossime as reagent. Also it is a stronger base than the H_2O molecule which helps direct comparison due to the effect induced by the Lewis base of the increasing strength. The choice of other molecules such as CH_3OH and CH_3CN is justified by the important role played by these moieties in the industrial application of BEA. The Lewis acid-base adducts thus formed is taken as measure of strength of interactions to compare the acidity of Sn

and Ti centers in the BEA. The results are in qualitative agreement with previous studies. The bond elongation, bond reduction of adsorbed bases and deformation of TO_4 moiety is reported in detail for each adduct. In particular, we also report the discrepancy played by the weak bonds such as hydrogen bond in predicting misleading strength of interaction for that of Sn-BEA. In addition, difference in the interaction energies for Sn-BEA and CH_3CN using periodic and cluster model is clearly highlighted.

The work is organized as follows: Section II elaborates the periodic model of T-BEA and the respective adducts formed after adsorption of L. Section III discourse the computation used to model and calculate the systems. Section IV imparts the finding of these calculations, mainly, the comparative study of adsorption of the above mentioned basic moieties to study the deformation and hence resulted reactivity. Section V finally concludes the results.

5.2 Simulation Model

In this simulation, we use the periodic DFT (p-DFT) to built the Ti-BEA, Sn-BEA and their adducts with different basic molecules (L=NH_3, H_2O, CH_3OH, CH_3CN). The unit cell of BEA is shown in Figure 5.1. BEA is highly siliceous material, with a three-dimensional pore system of 12-membered ring aperture. The unit cell of an ideal fully siliceous BEA consists of 192 atoms with 64 Si and 128 O atoms distributed within the tetragonal lattice of dimensions (12.6*12.6*26.2) Å. There are nine distinct crystallographically defined T-sites. We adopt the structure of the BEA from our earlier theoretical study [22b]. In our earlier analysis[22b], we found that the Sn and Ti atom occupy T2 and/or T1 crystallographic positions in BEA. Hence, in the rest of the calculations we use single substituted Sn at T2 and Ti at T1 positions. The interaction of basic molecules at the active site is very important, since it gives rise to geometric perturbation and the energetic differences. We tried the various possible approaches of the basic molecule at the active site. Many of these resulted in high energy and high force values. The most favorable ligand approach at the active T-site is along the b axis (see Figure 5.2). This insertion gives rise to

geometric distortion [28-30]. Schematic representation of T-BEA--L is given in Figure 5.2-5.3. We built the same periodic environment i.e. size of unit cell, grid size etc for the T-BEA--L adducts and bare L molecules as that of the bare solid i.e. T-BEA.

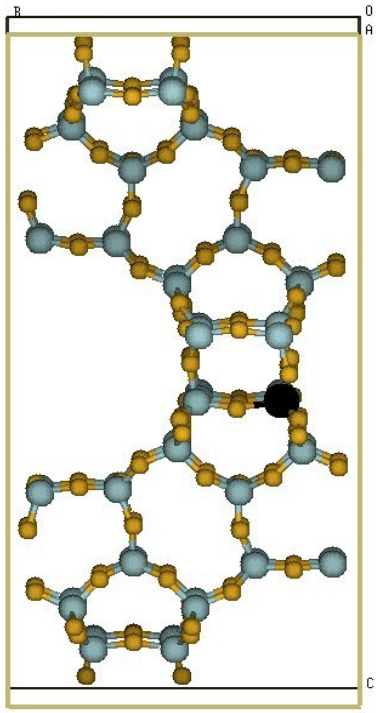

Figure 5.1: The Crystallographically defined BEA unit cell with Ti at T1 site. Black sphere:Ti atom. Gray spheres: Si atoms. Yellow spheres:O atoms.

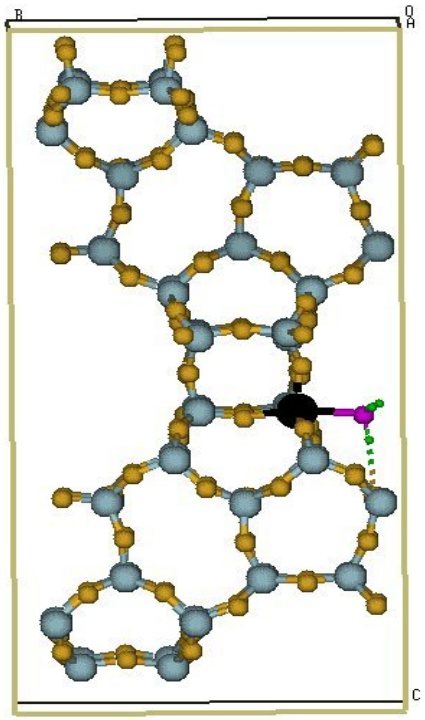

Figure 5.2: **Optimized T-BEA/NH_3.** Black sphere: T atom. Gray spheres: Si atoms. Yellow spheres: O atoms, Pink sphere: N atom and small green spheres: H atoms.

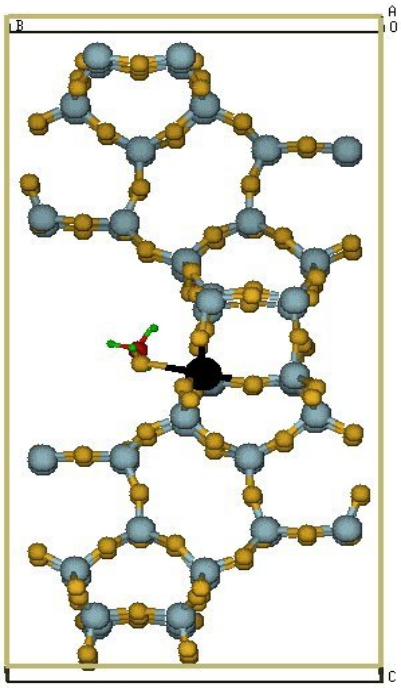

Figure 5.3: **Optimized T-BEA/CH_3OH.** Black sphere: T atom. Gray spheres: Si atoms. Yellow spheres: O atoms, Red spheres: C atoms and small green spheres: H atoms.

5.3 Computational Details

As in earlier chapters all the calculations are performed using VASP code which utilizes p-DFT [35] and Vanderbilt's ultrasoft pseudo-potentials [36]. The optimized T-BEA model obtained in chapter 3 [22b] was employed as the starting geometry to study the interaction of T-BEA zeolite with all probes. The adducts so formed have been fully optimized at 500 eV PW basis cut-off without any geometrical constraints. The interactions thus obtained are further evaluated at 1000 eV cut-off considering single point convergence keeping in mind the conclusions of

chapter 4 [37]. The exchange-correlation functional is expressed by the generalized gradient approximation (GGA) with the Perdew-Wang 91 functional [38]. The calculations were restricted to the gamma point in the Brillouin zone sampling. The structural optimization of the Sn- and Ti-BEA has been carried out using conjugate gradient method. The optimization was considered to be achieved when the maximum force on the atoms was less than 0.08 eV/Å. One should note that during the optimization, the cell shape of the unit cell has been fully relaxed, while keeping its volume constant. This is due to the fact that the percentage of Sn and Ti in BEA is only 1/u.c. Similar optimization procedure is repeated for the calculation of Sn-BEA and Ti-BEA with all basic molecules, L, interacting at the Sn and Ti centers, respectively. The optimization of bare L moieties is derived with same computational procedure.

5.4 Results and Discussion: Interaction of T-BEA with NH_3, CH_3CN, CH_3OH and H_2O

The least energetic approach of the ligand moieties on the active T-site in the BEA are shown in Figures 5.2 and 5.3. The NH_3 and CH_3CN interact with Sn and Ti centers via N atom as shown in Figure 5.2, where as CH_3OH and H_2O interact via O atom as shown in Figure 5.3. This section first discusses the common structural features of all adducts and further it investigates the comparative interaction energy differences and predicts the trend of reactivity of all moieties with the respective catalyst. Following this with the help of global descriptors of reactivity, LUMO (of catalyst) and HOMO (of ligands) we will summarize the inter-reactivity trend for Sn and Ti substitutions.

(a) Structural deformation of T-BEA framework upon ligand adsorption:

Table 5.1 presents the optimized structural details and the reactivity descriptors of Sn-BEA and Ti-BEA. These are the results obtained from chapter 3 but for the sake of simplicity repeated here. It should be noted that only the average bond distances and bond angles are presented. It can be seen from Table 5.1 that if we compare the Sn and Ti substitution in zeolite beta framework, we get expected order

of <T-O> bond lengths, viz., Sn-O > Ti-O. On the other hand, the <T-O-Si> bond angles vary as Sn-O-Si < Ti-O-Si. The particular T-O bond length difference is due to the larger atomic size of Sn with respect to Ti. On the other hand, smaller sized Ti shows better angular flexibility with greater Ti-O-Si angle and consequently resulting in larger Ti-Si bond distance (by ~0.04 Å from Sn-Si distance).

Table 5.1: Optimized structural parameters of Sn-BEA and Ti-BEA.

Average T-O Bond Lengths, T-Si Bond Distances, T-O-Si Bond Angles and the HOMO, LUMO energies.

T	T-O (Å)	T-Si (Å)	T-O-Si (deg)	HOMO (eV)	LUMO (eV)	Δ(H-L)(eV)
Ti	1.80	3.3	151.7	-3.13	1.42	- 4.55
Sn	1.91	3.34	144.2	-3.12	1.37	- 4.49

Thus, the adaptation of the BEA framework to Sn and Ti substitution results in a quite localized deformation of a pure siliceous framework. Hence, we can infer that the difference in adsorption properties between Sn- and Ti-BEA should be mainly due to the electronic differences of these sites and the changes caused by the interacting reactant molecules. Detailed understanding on the structural differences between Sn- and Ti-BEA zeolite is available in one of our earlier studies [22b]. Table 5.2 presents the optimized structural parameters of T-BEA--L adducts. We can see that after the adsorption of ligand molecules at the reactive center, the corresponding framework T-O bonds undergo the following perturbation with respect to that of bare T-BEA: In the bare T-BEA, T atoms were in perfect tetrahedral environment, however, in their respective adducts the four framework oxygen atoms of TO_4 unit split into one axial, $T\text{-}O_{ax}$, opposite to the adsorbed ligand and three equatorial, $T\text{-}O_{eq}$. Consequently, the T-Si distances are also perturbed. Figure 5.4 presents this detail splitting of the TO_4 unit. Table 5.2 gives this range of T-O and T-Si bond distances in the adducts. Here, the larger T-O bond length (or T-Si) corresponds to the respective $T\text{-}O_{ax}$ bond (or T-

Si_{ax}), thus, the oxygen atom which is exactly opposite to adsorbed ligand constitutes the most affected T-O (or T-Si) bond.

Table 5.2: Optimized structural parameters of T-BEA--L adducts.

Adducts	T-O (Å)	T-Si (Å)	T-L (Å)	H_L-O_T (Å)	α (deg)	β (deg)	T-O-Si (deg)
NH_3/Ti	1.80-1.88	3.24-3.45	2.35	2.23 (1)	110.9-131.2	95.0-104.9	144.1-161.9
NH_3/Sn	1.89-1.99	3.29-3.53	2.38	2.71 (0)	105.8-137.3	95.5-103.4	142.3-159.4
CH_3CN/Ti	1.79-1.88	3.29-3.45	2.35	2.45 (0)	110.1-125.5	93.9-102.5	146.6-163.2
CH_3CN/Sn	1.89-1.99	3.31-3.52	2.38	2.90 (0)	107.0-129.1	94.0-107.0	142.3-158.4
CH_3OH/Ti	1.80-1.86	3.26-3.43	2.46	2.54 (1)	111.3-123.7	102.4-105.9	146.4-160.2
CH_3OH/Sn	1.89-1.98	3.22-3.45	2.44	2.57 (1)	106.6-129.8	100.6-103.5	141.4-150.1

However, the rest three T-O_{eq} (or T-Si_{eq}) bonds correspond to the smaller value of this range. The impact of tetrahedral symmetry loss by framework oxygen atoms is not just restricted to bond distances but it also disturbs the corresponding T-O-Si framework bond angles. The resulting range of T-O-Si bond angle is given in last column of Table 5.2. In both T-BEA--L adducts, the largest bond angle of this range belongs to T-O_{ax}-Si where as the smallest to T-O_{eq}-Si. The most disturbed framework bond angle is O-T-O. The total six O-T-O angles of the original T-BEA TO_4 unit gives rise to two triplets O_{eq}-T-O_{eq}, **α**, and O_{eq}-T-O_{ax}, **β,** angles. Table 5.2 highlights the fact that these triplets are also not equal but fall in a range. In addition to these bonds and angles formed by framework atoms, Table 5.2 also reports the hydrogen bond (H_L-O_T) formed between framework oxygen (O_T) and ligand hydrogen (H_L).

Here, the bracketed values indicate the number of hydrogen bonds formed by ligand hydrogens. These structural deformations in the complexes are commonly seen in case of all ligands.

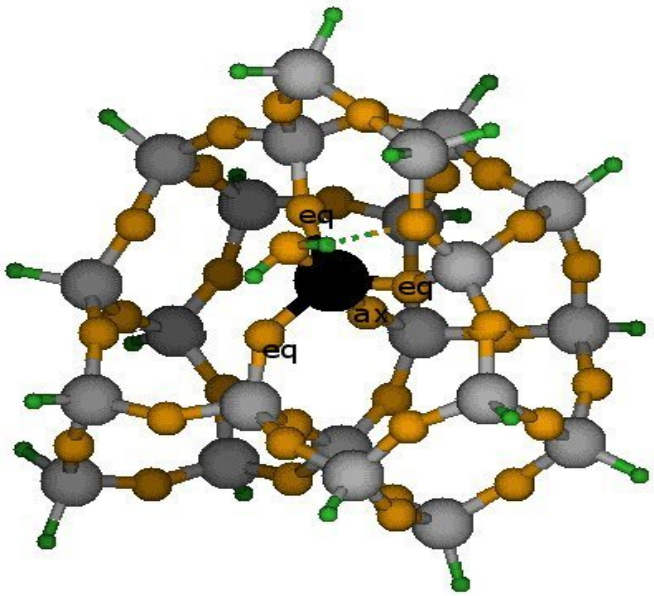

Figure 5.4: **Optimized T-BEA/H_2O showing axial (ax) and equatorial (eq) splitting of TO_4 unit.** Black sphere: T atom. Gray spheres: Si atoms. Yellow spheres: O atoms, and small green spheres: H atoms.

Note: An H atom of H_2O clearly shows hydrogen bonding with framework oxygen.

Coming to the details of the structural deformations, the T-O bonds in the respective T-BEA--L adduct show elongation to an equal extent. Thus, irrespective of the nature of adsorbed ligand, Ti-O_{ax} and Ti-O_{eq} comprise to 1.88 and 1.80 Å, respectively. Similarly, the Sn-O_{ax} and Sn-O_{eq} bonds correspond to 1.99 and 1.89 Å. The adsorption of L causes on an average 0.081 Å and 0.083 Å elongation of T-O_{ax} distance in Ti-BEA and Sn-BEA adduct, respectively. However, the rest three T-O_{eq}

bonds are closer to the T-O bonds of the bare T-BEA. Thus, we note an equal perturbation of T-O bonds in both the Sn- and Ti-BEA framework upon interaction with all ligands. The average variations of Ti-O bonds reported above agree well with the EXAFS data [33, 34]. Interestingly, earlier cluster calculations [39] also report a similar range of variations. Accordingly, the T-Si bond distances also show variation in the T-BEA--L complexes compared to the bare T-BEA. Unlike T-O_{eq} bonds, T-Si_{eq} bonds optimize to lower bond lengths compared to T-Si distances present in the bare T-BEA. Once again, irrespective of ligand nature and metal active center, T-Si_{eq} bond reduces by ~0.04 Å. However, the T-Si_{ax} bond further elongates by ~0.14 Å and ~0.18 Å in respective Ti- and Sn-BEA adducts. The Sn-BEA--CH_3OH adduct is exception here, where the Sn-Si_{eq} bond show strong reduction where as the Sn-Si_{ax} bond result in shorter elongation.

As discussed, hydrogen bond (H_L-O_T) is observed between the ligand hydrogen (H_L) and framework oxygen (O_T). At T1 site (Ti-substituted site) these hydrogen bonds formed are shorter in bond length but at T2 site (Sn-substituted site) these bonds result in weak bonding. In the case of Ti-BEA--NH_3 adduct, we report strong hydrogen bond of 2.23 Å which later on results in elevated interaction energy of NH_3 with Ti center as will be elaborated in next section. The most important inter-molecular bond length, distance between active site of zeolite and interacting atom of adsorbed ligand, T-L, is reported in Table 5.2. It is seen from the table that NH_3 molecule is optimized at a distance of 2.35 Å from the Ti center (T1-site) of BEA, being slightly shorter (about 0.017 Å) compared to that obtained on the Ti-CHA model [27b]. The Sn-BEA--NH_3 distance optimizes at 2.38 Å. Similarly, the CH_3CN interaction optimizes at 2.35 Å and 2.38 Å from Ti and Sn centers of BEA, respectively. In general, the ligands containing oxygen atom as donor atom converge to longer inter-molecular bond. The CH_3OH optimizes respectively to 2.46 Å and 2.44 Å at Ti and Sn centers. The Sn-BEA--OH_2 inter-molecular bond optimizes at 2.38 Å. The Ti-BEA--OH_2 bond length optimizes at 2.44 Å.

To conclude, the Ti-O-Si bond angles, which range between 144 and 163 degree, are larger than the Sn-O-Si angles (142-159 deg). This can be attributed to the

angular flexibility of small sized Ti. This angle reduces exceptionally during the formation of Sn-BEA--CH_3OH adduct. In addition, ligand approach at active T2 site is more linear, L-T-O_T angle being close to 180°, where as same angle at T1 site is close to ~170° (see Fig. 5.4). Consequently, six O-T-O angles in the respective adduct of Sn- and Ti-BEA split to different extent. The order of O-T-O angle splitting vary with respect to strength of ligand as NH_3 >CH_3CN>CH_3OH. Thus, the structural study of adducts conjecture that irrespective of the ligand nature, the bond length variation of the framework atoms is restricted in fixed range, however, bond angles deviates to different magnitudes. Similarly, irrespective of the catalyst active center, Sn or Ti, ligand interacts at optimum bond distance.

(b) Energetics of interacting T-BEA and Ligands (L): In this subsection, we discuss the strength of interaction of various ligands with Sn-BEA and Ti-BEA so as to highlight the distinct Lewis acidic nature of Sn and/or Ti centers. For this purpose, we calculate the interaction energy defined as the difference between the energy of adduct formed at equilibrium and the energy of the constituent molecules in their ground state. This is calculated as follows,

$$\textbf{Interaction Energy } (E_{int}) = (E_{T\text{-}BEA} + E_L) - E_{T\text{-}BEA\text{--}L} \qquad \text{....I}$$

In our earlier investigation on the hydrophilicity of Sn- and Ti-BEA [22b], we showed that the energy of H_2O interaction with Sn-BEA is 0.3323 eV and that of with Ti-BEA is 0.1342 eV. The Sn site in BEA is more hydrophilic compared to Ti site. This also confirms the higher Lewis acidic nature of Sn-BEA. As the water is the most common reaction medium, H_2O gains extreme importance in determining the catalyst activity study. Thus, water not only coordinates with catalyst active center but many times poisons the site and reduces its reactivity. Here, we do not consider the structural details of the T-BEA and H_2O adduct. The geometric features concerning the T-BEA--H_2O adducts are reported by us in the earlier study [22b]. For detailed interest one can refer to this study. We are going to extrapolate the analysis of this exothermic interaction of water to analyze the interaction of all ligands with both the Sn and Ti centers. The interaction energy of all ligands with Sn- and Ti-BEA

is reported in Table 5.3. The interaction energies reported in bracket are calculated at high PW cut-off of 1000 eV.

By the simple chemist intuition, we expect the higher acidic Sn center to result in stable interaction with the strong base NH_3 to form a better Lewis adduct than the less acidic Ti center. However, interaction energies of NH_3 ligand with the Sn and Ti substituted beta zeolite contradict these findings. Table 5.3 highlights the increase of interaction energy by 0.02 eV (0.06 eV at 1000 eV PW cut-off), while going from Sn to Ti center.

Table 5.3: HOMO, LUMO energies of Lewis bases and T-BEA--L adducts.

Systems	E_{int} (eV)	HOMO (eV)	LUMO (eV)	Δ(H-L) (eV)
NH_3	-	-6.03	-0.80	-5.23
NH_3/Ti	0.3156 (0.3459)	-2.69	1.43	-4.12
NH_3/Sn	0.2963 (0.2825)	-2.78	1.91	-4.70
CH_3CN	-	-8.10	-0.85	-7.25
CH_3CN/Ti	0.0325 (0.0083)	-2.80	1.36	-4.15
CH_3CN/Sn	0.1607 (0.1074)	-2.84	2.11	-4.95
CH_3OH	-	-6.33	-0.75	-5.58
CH_3OH/Ti	0.0716 (0.0980)	-2.65	1.43	-4.08
CH_3OH/Sn	0.2951 (0.3016)	-2.80	1.77	-4.57

Although this increase in the interaction energy is not considerable, we attribute this discrepancy to the distortion in the local environment after the adsorption of NH_3 as discussed below. The interaction of NH_3 is considered at T1 site of Ti-BEA where as for Sn-BEA it is at T2. Although the Sn-O-Si bond angles are smaller than Ti-O-Si, the Ti-center shows better angular flexibility due to its small atomic radius [22b]. As a result, hydrogen bond formed between the framework oxygen and the ligand hydrogen atoms (NH_3) is retained during the optimization. However, due to lack of Sn-O-Si angular flexibility there is no such hydrogen bonding observed for the adsorbed NH_3 in the case of Sn-BEA (ref. Table 5.2). The H_L-O_T bond lengths are reported in Table 5.2. The shortest bond distance between hydrogen atom of ammonia and framework oxygen in Ti-BEA--NH_3 adduct is 2.24 Å where as same for Sn-BEA--NH_3 adduct is 2.72 Å. This strong hydrogen bonding interaction of Ti-BEA--NH_3 adduct reflects in step up interaction energy compared to Sn-BEA--NH_3 adduct. We also carry a test calculations of NH_3 interacting with Sn-BEA, where, Sn is now substituted at T1 site. Surprisingly, interaction energy is 0.78 eV (an increase of 0.49 eV from its T2 site). At T1 site, Sn-BEA-- NH_3 does not fail to count the strong hydrogen bond. The shortest hydrogen bond thus formed is 2.33 Å and NH_3 optimizes at shorter bond length of 2.33 Å. Therefore, though the structural arrangement of atoms look equivalent in the unit cell model of BEA, the electronic difference in local environment of the active site plays an extensively important role in deciding materials catalytic behavior. The corresponding adsorbed N-H bonds are very weakly elongated in Ti-BEA--NH_3 adduct (about 0.001 Å). On the other hand, elongation is about 0.016 Å for Sn-BEA--NH_3 adduct. This elongation of interacting ligand N-H bond can be taken as evidence of red shift in IR frequency and hence measure of strength of interaction at catalyst active site.

An earlier experimental study of the vibrational properties of CH_3CN adsorbed on different zeolite, TS-1, as an evidence for the presence of Lewis acidic centers [28] associated with Ti(IV) was given by Bonino et. al. They found that acetonitrile forms a labile adduct with the Ti of TS-1 with a $\Delta\upsilon$(CN) stretching frequency of +37 cm^{-1}. Analogous experiment on Sn-BEA has been recently carried

out by Corma and co-workers [29, 30]. Their study also predicted a blue shifted $\Delta\upsilon$(CN) stretching frequency of +42 cm^{-1}. In addition, to study the structure-activity relation of catalyst they had carried out a computational study based on a cluster model approach. Interestingly, their model comprised of various reaction sites and various neighboring groups. For the comparison purpose, we restrict our self to pure siliceous environment of Sn center and do not consider their hydrolyzed model. In line with their frequency analysis, the CN distance in our calculation passes from 1.161 Å (bare one) to 1.156 Å (engaged one) predicting blue shift of the υ(CN) stretching frequency. This result is in qualitative agreement with the results reported in previous literature [28-30]. In particular, the interaction of probe molecule such as acetonitrile with Lewis acid center involves electron density transfer from lone pair of nitrogen to the catalyst LUMO, as a result CN bond reduces and υ(CN) frequency shifts to higher value. The computed blue shift, accompanied by a reduction of -0.005 Å of the C-N distance (compared to bare CN distance), proves the strong adsorption of the CH_3CN on the T-BEA active centers. This fact is well reproduced in the interaction energy calculation with the both T substituted BEA. Although, the cluster model predicted T-L bond lengths match well with our periodic model the interaction energy values differ from ours [29]. The interaction energy of Sn-BEA with CH_3CN predicted by the cluster model approach was 0.3 kcal/mol [29]. However, the additive long range interactions covered in periodic model results in an interaction energy increase of 3.45 kcal/mol. This difference can be attributed to the additive interaction. The interaction energy of CH_3CN with Ti-BEA adduct is 0.032 eV (0.008 eV at 1000 eV PW cut-off). Thus, the interaction of Sn-BEA is stronger with CH_3CN than that of Ti-BEA.

The CH_3OH is reagent of prime interest in several industrial reactions. The lone pair present on the O atom of CH_3OH should be more attractive towards the positive centers present in substituted BEA. Similar to CH_3CN interaction, the interaction energies computed for Sn-BEA, Ti-BEA and CH_3OH show large differences. The Sn-BEA and CH_3OH interaction is stronger and turns out to be 0.295 eV (0.301 eV at 1000 eV PW cut-off). On the other hand, the Ti-BEA and CH_3OH

interaction energy is 0.0716 eV (0.098 eV at 1000 eV PW cut-off). In the optimized structure of Ti-BEA--CH_3OH, C-O bond is 1.46 Å and O-H bond is 0.97 Å (i. e. elongates to +0.02 Å and +0.006 Å with respect to bare molecule). For Sn-BEA adduct, the C-O bond shows elongation by 0.013 Å and OH bond by 0.003 Å. The computed elongations can be accounted as measure of adsorption of CH_3OH on the active centers, resulting in the red shifted frequencies. This is a consequence of structural differences around T1 and T2 sites of the beta zeolite.

The present energetics of ligand interaction reveals that all the basic moieties result in exothermic interaction with Sn and Ti sites. Furthermore, the higher interaction energies of Sn-BEA--L adducts confirm their stability compared to Ti-BEA--L adducts. The ligand interaction is associated with the respective bond elongation and bond reduction of the adsorbed molecules on catalyst active site, which can be taken as measure of red or blue shifted frequencies. In general, the order of stability of the different T-BEA adducts is NH_3>H_2O>CH_3OH>CH_3CN. For Sn-BEA, this order is slightly reversed: viz., the H_2O interacts strongly with Sn-BEA compared to NH_3. However, in next section of reactivity descriptors, frontier orbital energies, justify the permanence of these respective interactions. The interactions of CH_3CN and CH_3OH are almost negligible with Ti-BEA. In conclusion, the higher acidic Sn site interacts strongly with all basic moieties compared to lesser acidic Ti site.

(C) Reactivity of T-BEA towards Ligands (L): We have applied the HSAB principle to understand the reactivity of Sn- and Ti-BEA towards ligand moieties. Pearson formulated the concept of HSAB principle for understanding reactivity of chemical systems and their interactions [26, 27]. This gave a new insight in interpreting the reactivity of chemical systems on the basis of their HOMO and LUMO energies [26, 27]. Thus a system can be categorized as soft acid (SA) with low lying LUMO, soft base (SB) with high lying HOMO and hard acid (HA) with high lying LUMO where as hard base (HB) with low-lying HOMO. It has been well established that the interactions between SA-SB are covalent, HA-HB are ionic and SA-HB or HA-SB are mostly weak electrostatic and form Lewis adducts. Here, we

must recall that the Lewis acidity, being related with an electron acceptor character, can be related with the global affinity of the solid [22b, 23, 24]. Qualitatively, LUMO energies can be used for a comparison between electron affinities of Sn- and Ti-BEA. The HOMO and the LUMO energies and their respective HOMO-LUMO gaps of Sn- and Ti-BEA are revised [22b] in Table 5.1. Globally the LUMO energy of Sn substituted BEA zeolite is lower than that of the Ti ones. Also the corresponding HOMO-LUMO gap of Sn-BEA is small which correlates this solid to a larger global softness. Thus, the Sn-BEA results in the most Lewis acidic and softer solid, hence, more reactive catalyst.

Table 5.3 describes the HOMO, LUMO energies, and the corresponding HOMO-LUMO gaps of all the ligand molecules. We observe decreasing order of HOMO energies of all the ligands as: H_2O (-5.99 eV) > NH_3 > CH_3OH > CH_3CN. Thus, here CH_3CN lead to hard base and rest three bases are soft bases based on their closely lying HOMO energies. However, NH_3 and H_2O are of equal strength. This is in line with our interaction energy analysis of the different T-BEA adducts (NH_3>H_2O>CH_3OH>CH_3CN) where we get less adsorption energy of CH_3CN with both Sn- and Ti-BEA. However, soft bases namely H_2O and NH_3 interact strongly with Sn and Ti-BEA. The global descriptors of reactivity thus explain the fact that soft acid, Sn-BEA, interacts strongly with soft bases H_2O, NH_3 and CH_3OH to give a covalent complex where as hard acid, Ti-BEA interacts with same bases to form a stable Lewis adduct. In addition, according to the above definition, interaction between CH_3CN with Ti-BEA is weakly ionic, (see Table 5.3: interaction energy is negligible) where as interaction of CH_3CN with Sn-BEA is weakly electrostatic (Lewis Acid-Base adduct) in nature. In general, interaction of Sn-BEA is strong with all ligands compared to Ti-BEA (compare interaction energies of respective adducts). Table 5.3 also summarizes the HOMO-LUMO gaps of all T-BEA--L adducts. The HOMO-LUMO gap of all Sn-BEA--L adducts is lower than that of Ti-BEA--L adducts. This thus explains the greater stability of all Sn-BEA--L complexes. Hence, we can once again state that globally Sn-BEA zeolite results in higher Lewis acidic catalyst forming stable interaction with all basic molecules than the Ti-BEA zeolite.

Other reactivity descriptors such as chemical potential, hardness and philicity of a molecule are also added in Table 5.4 for the sake of completeness.

Table 5.4: Chemical Potential, Hardness and Philicity descriptors for L and T-BEA--L.

Systems	μ	η	ω
NH_3	-3.42	-2.62	-2.23
CH_3OH	-3.54	-2.79	-2.25
CH_3CN	-4.48	-3.63	-2.76
NH_3/Sn	-0.44	-2.35	-0.04
CH_3OH/Sn	-0.61	-2.04	-0.09
CH_3CN/Sn	-0.37	-2.48	-0.03
NH_3/Ti	-0.63	-2.06	-0.1
CH_3OH/Ti	-0.52	-2.29	-0.06
CH_3CN/Ti	-0.72	-2.08	-0.12

However, it may be noted that none of these descriptors follow the trend reported by the interactions energies. The reason for this may be attributed to the sensitivity of these descriptors which applies to periodic density functional methods.

In addition to highlight the charge transfer in the interactions of T-BEA and L, we include a short discussion with the help of difference charge density (Δρ) plots. The Δρ plots for each type of interaction viz. covalent, Lewis adduct and ionic are reported in Figure 5.5. Here, the blue signifies charge gain where as red represents charge depletion. The Fig. 5.5a shows SA-SB, Sn-BEA--H_2O interaction. The charge transfer between H_2O and Sn- is indicated by small blue sphere. The blue sphere along inter-molecular bond, here, represents the bond critical point which can be taken as measure of a strong bonding such as covalent interaction. The Fig 5.5b and 5.5c shows, SA-HB and HA-SB, Lewis acid-base interactions forming Lewis adducts. As discussed in the beginning of this section these interactions are weakly

electrostatic in nature and this is well reflected in their Δρ plots. The presence of small red sphere along the inter-molecular bonding space here denotes loss of charge where as blue sphere on ligand donor atom indicates concentration of charge density on it. Similarly, HA-HB, Ti-BEA--CH_3CN, ionic interaction is shown in Fig. 5.5d (for clear visualization not color coded). Fig. 5.5d clearly shows a polarized charge density between Ti-BEA--CH_3CN bonding region which is an indication of ionic bond. Both the atoms, Ti- (blue sphere) and N- (red sphere), show polarization of electronic densities on them.

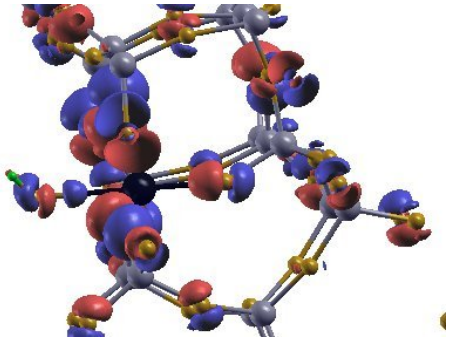

Figure 5.5a: **Sn-BEA--H_2O: SA-SB, covalent interaction** indicated by presence of blue sphere along inter-molecular bond.

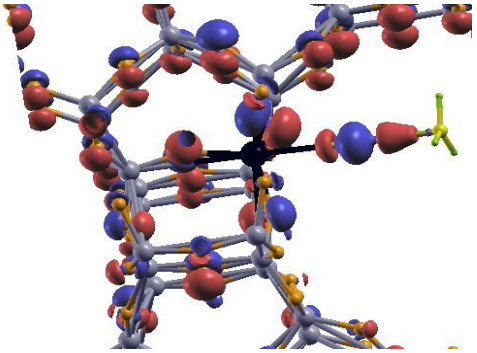

Figure 5.5b: **Sn-BEA--CH_3CN: SA-HB, weakly electrostatic interaction** indicated by red sphere along inter-molecular bond.

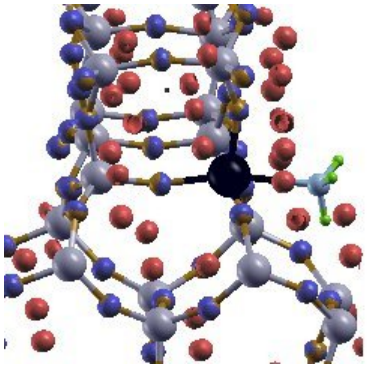

Figure 5.5c: **Ti-BEA--NH_3: HA-SB, weakly electrostatic interaction** indicated by red sphere along inter-molecular bond.

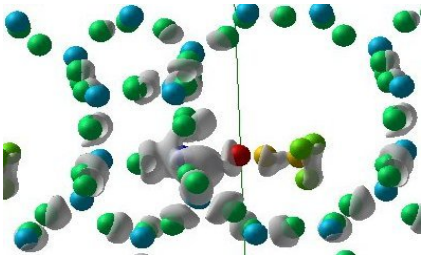

Figure 5.5d: **Ti-BEA--CH_3CN: HA-HB, ionic interaction** indicated by polarization of density along inter-molecular bond.

5.5 Conclusion

The reported geometries of the substituted beta and their respective interactions with NH_3, H_2O, CH_3OH and CH_3CN are obtained with the plane wave basis code VASP. Catalyst active site T2 and T1 are substituted by Sn and Ti, respectively. All the interactions are fully optimized without any geometrical constraints. The geometric and energetic deformations are discussed successfully using p-DFT.

In the bare T-BEA, TO_4 moiety is quite near to tetrahedral symmetry [22b, 28, 40]. However, the results discussed here predict the deformation of TO_4 moiety due to adsorption of basic molecules. In the optimized ligand adsorbed adducts, TO_4 shows typical characteristic splitting 120°/90° there by resulting into a nearly bipyramidal geometry. Irrespective of the adsorbed ligand nature, the bond length variation of the framework atoms is restricted in fixed range while the bond angles exhibit a larger variation. Similarly, irrespective of the catalyst active center, Sn or Ti, ligand interacts at an optimum bond distance. The interaction energy results demonstrate that all the basic moieties results in exothermic interaction with Sn and Ti sites. Furthermore, the higher interaction energies of Sn-BEA--L adducts confirm their stability compared to Ti-BEA--L adducts. This strength of interaction is also associated with a corresponding bond elongation and/or bond reduction of the adsorbed molecules on the catalyst active site, which can be taken as measure of red or blue shifted frequencies [28, 33, 34]. In general, the order of stability of the different T-BEA adducts is NH_3>H_2O>CH_3OH >CH_3CN. For Sn-BEA, this order is slightly reversed. The H_2O interacts strongly with Sn-BEA compared to NH_3. Overall the interaction of ligands with Sn and Ti substituted beta zeolite depend on a delicate balance of several factors such as substitution site of metal, angular flexibility around those sites and weak interactions like hydrogen bonds. All these factors reflect in global reactivity descriptors. The global descriptors of reactivity justify the fact that soft acid, Sn-BEA, interacts strongly with soft bases H_2O, NH_3 and CH_3OH to give a covalent complex where as hard acid, Ti-BEA interacts with same bases to form a stable Lewis adduct. In addition, the interaction energies and reactivity descriptors of

Ti-BEA--CH_3CN complex indicates it to be weakly ionic where as interaction of CH_3CN with Sn-BEA is weakly electrostatic in nature. The $\Delta\rho$ plots support these findings. The HOMO-LUMO gap highlights the greater stability of all Sn-BEA--L complexes which once again address the higher Lewis acidic nature of Sn-BEA than Ti-BEA.

5.6 References

[1] R. L Wadlinger, G. T. Kerr, E. J. Rosinski. U.S. Pat. 3 308 069 (1967).

[2] J. M. Newsam, M. M. J. Treacy, W. T. Koestsier, C. B. de Gruyter. Proc. R. Soc.London. A420 (1988) 375.

[3] (a) A. Corma, M. T. Navarro, F. Rey, J. Rius, S. Valencia, Angew. Chem. Int. Ed. 40 (2001) 2277. (b) A. Corma, M. T. Navarro, F. Rey, S. Valencia, Chem. Commun. (2001) 1486.

[4] G. Bellusi, G. Pazzuconi, C. Perego, G. Girotti, G. Terzoni. J. Catal. 157 (1995) 227.

[5] (a) J. A. Martens, J. Perez-Pariente, E. Sastre, A. Corma, P. A. Jacobs, Appl. Catal. 45 (1988) 85 (b) P. Ratnasamy, R. N. Bhat, S.K. Pokhriyal, S. G. Hagde, R. Kumar, J. Catal. 119 (1989) 65.

[6] L. Boretto, M. A. Camblor, A. Corma, J. Perez-Pariente, J. Appl. Catal. 82 (1992) 37.

[7] A.J. Hoefnagel, H. van Bekkum, Appl. Catal. A. 97 (1993) 87.

[8] A. Corma, J. L jorda, M. T. Navarro, F. Rey, Chem. Commun. (1998) 1899.

[9] T. Blasco, M. A. Camblor, A. Corma, P. Esteve, J. M. Guil, A. Martinez, J. A. Perdigon-Melon, S. Valencia, J. Phys. Chem. B 102 (1998) 75.

[10] a) A. Corma, L.T. Nemeth, M. Renz, S. Valencia. Nature 412 (2001) 423. b) A. Corma, M. E. Domine, L. T. Nemeth, S. Valencia. J. Am. Chem. Soc. 124 (2002) 3194.

[11] N. K. Mal, A. V. Ramaswamy. Chem. Commun. 425 (1997).

[12] (a) S. R. Bare, S. D. Kelly, W. Sinkler, J. J. Low, F. S. Modica, S. Valencia, A. Corma, L. T. Nemeth, J. Am. Chem. Soc. 127 (2005) 12924. (b) A. Corma, L. T. Nemeth, M. Renz, S. Valencia, Nature 412 (2001) 423.

[13] (a) A. Corma, V. Fornes, S. Iborra, M. Mifsud, M. Rez, J. Catal. 221 (2004) 67. (b) A. Corma, S. Iborra, M. Mifsud, M. Renz. J. Catal. 223 (2005) 96. (c) A. Corma, M. Renz, Chem. Commun. (2004) 550.

[14] (a) A. Corma, M. E. Domine, L. Newmeth, S. Valencia, J. Am. Chem. Soc. 124 (2002) 3194. (b) A. Corma, M. E. Domine, L. Nemeth, S. Valencia. J.

Catal. 215 (2003) 294.

[15] S. R. Bare, S. D. Kelly, W. Sinkler, J. J. Low, F. S. Modica, S. Valencia, A. Corma, L. T. Nemeth, J. Am. Chem. Soc. 127 (2005) 12924.

[16] I. Pbpai, A. Goursot, F. Fajula, J. Phys. Chem. 98 (1994) 4654.

[17] (a) N. Jardillier, D. Berthomieu, A.Goursot, J. U. Reveles, A. M. Koster, J. Phys. Chem. B 110 (2006) 18440. (b) A. Martınez, A. Goursot, B. Coq, G. Delahay. J. Phys. Chem. B 108 (2004) 8823.

[18] S. Krishnamurty, T. Heine, A. Goursot. J. Phys. Chem. B 107 (2003) 5728. (b) T. Heine, A. Goursot, G. Seifert, J. Weber. J. Phys. Chem. A 105 (2001) 620.

[19] K. Sun, W. Su, F. Fan, Z. Feng, T. A. P. J. Jansen, R. A. van Santen, C. Li. J. Phys. Chem. A 112 (2008) 1352.

[20] (a) M. Kubo, Y. Oumi, H. Takaba, A. Chatterjee, A. Miyamoto. J. Phys. Chem. B 103 (1999) 1876. (b) K. Teraishi, M. Ishida, J. Irisawa, M. Kume, Y. Takahashi, T. Nakano, H. Nakamura, A. Miyamoto. J. Phys. Chem. B, 101 (1997) 8079.

[21] (a) E. A. Pidko, P. Mignon, P. Geerlings, R. A. Schoonheydt, R. A. van Santen. J. Phys. Chem. C 112 (2008) 5510. (b) F. Tielens, J. F. M. Denayer, I. Daems, G. V. Baron, W. J. Mortier, P. Geerlings. J. Phys. Chem. B 107 (2003) 11065.

[22] (a) S. Shetty, S. Pal, D. G. Kanhere, A. Goursot. Chem. Eur. J. 12 (2006) 518. (b) S. Shetty, B. S. Kulkarni, S. Pal, D. G. Kanhere, A. Goursot.. J Phys Chem B 112 (2008) 2573.

[23] (a) M. Boronat, A. Corma, M. Renz, G. Sastre, P. M. Viruela. Chem. Euro. J. 12 (2006) 7067. (b) Boronat, M.; Corma, A.; Renz, M.; Sastre, G.; Viruela, P. M. Chem. Euro. J. 2005, 11, 6905.

[24] G. Sastre, A. Corma. Chem. Phys. Lett. 302 (1999) 447.

[25] A. M. Vos, K. H. L. Nulens, F. De Proft, R. A. Schoonheydt, P. Geerlings. J. Phys. Chem. B 106 (2002) 2026.

[26] R. G. Parr, R. G. Pearson, J. Am. Chem. Soc. 105 (1983) 7512 .

[27] R. G. Pearson. J. Am. Chem. Soc. 85 (1963) 3533.

[28] a) F. Bonino, A. Damin, S. Bordiga, C. Lamberti, A. Zecchina, Langmuir 19 (2003) 2155. b) A. Damin, S. Bordiga, C. Lamberti, A. Zecchina, K. Doll. J. Chem. Phys. 118 (2003) 10183.

[29] M. Boronat, P. Concepcion, A. Corma, M.Renz. Catalysis Today 121 (2007) 39.

[30] M. Boronat, P. Concepcion, A. Corma, M. T. Navarro, M.Renz, S. Valencia. Phys. Chem. Chem. Phys. 11 (2009) 2876.

[31] I. Phpai, A. Goursot, F. Fajula, D. Plee, J. Weber. J. Phys. Chem.99 (1995) 12925.

[32] (a) E. L. Meijer, R. A. van Santen, A. P. J. Jansen, J. Phys. Chem. A 103 (1999) 2553. (b) E. H. Teunissen, A. P. J. Jansen, R. A. van Santen, J. Phys. Chem. 99 (1995) 1873. (c) A. G. Pelmenschikov, R. A. van Santen, J. Phys. Chem. 97 (1993) 10678.

[33] (a) S. Bordiga, A. Damin, F. Bonino, A. Zecchina, G. Spano, F. Rivetti, V. Bolis, C. Prestipino, and C. Lambeti, J. Phys. Chem. B 106 (2002) 9892. (b) T. Blasco, M. A. Camblor, A. Corma, P. Esteve, J. M. Guil, A. Martinez, J. A. Perdigon-Melon, and S. J. valencia, J. Phys. Chem. B 102 (1998) 75. (c) A. Zecchina, S. Bordiga, G. Spoto, A. Damin, G. Berlier, F. Bonino, C. Prestipino and C. Lamberti, Top. Catal. 21 (2002) 67.

[34] (a) V. Bolis, S. Bordiga, C. Lamberti, S. Zecchina, F. Rivetti, G. Spano and G. petrini, Langmur, 15 (1999) 5753. (b) V. Bolis, S. Bordiga, C. Lamberti, S. Zecchina, A. Carati, F. Rivetti, G. Spano and G. petrini, Macroporous Mater. 30 (1999) 67.

[35] (a) G. Kresse, J. Hafner. Phys. Rev. B 48 (1993) 13115. (b) G. Kresse, J. Furthermuller, Comput. Mater. Sci. 6 (1996**)** 15.

[36] D. Vanderbilt. Phys. ReV. B 41 (1990) 7892.

[37] B. S. Kulkarni, S. Krishanamurti, S. Pal, Chem. Phys. Lett. 484 (2010) 374.

[38] Perdew, J. P.; Wang, Y. Phys. ReV. B 45 (1992) 13244.

[39] A. Damin, F. Bonino, G. Ricchiardi, S. Bordiga, A. Zecchina, and C.

Lamberti, J. Phys.Chem. B 106 (2002) 7524.

[40] M. Renz, T. Blasco, A. Corma, V. Formes, R. Jensen, L. Nemeth. Chem. Eur. J. 8 (2002) 4708.

CHAPTER 6

Role of Structure and Bonding of Al Clusters on the adsorption of N_2

Abstract:

Reactivity of aluminum clusters has been found to exhibit size sensitive variations. This work is motivated by a recent report [1] predicting higher reactivity of melted aluminum clusters towards the N_2 molecule as compared to the non-melted Al clusters. We attempt to understand the underlying electronic and structural factors influencing the adsorption of N_2 molecule (a prerequisite for the reactivity) on ground state geometry (a non-melted structure) of various Al clusters. The results show that the adsorption energy is of the order of 8-10 kcal/mol and does not vary with respect to the cluster size and the electronic properties of the ground state geometry. The structural and electronic properties of high energy conformations of Al clusters (a melted cluster) are further analyzed to explain their higher reactivity towards N_2 molecule. These findings are also validated with the help of activation barriers.

6.1 Introduction

The appearance of the bulk motif in small sized aluminum clusters has excited many researchers. As a consequence of this property, Al clusters are attracting a lot of

attention for their potential applications in optics, medicines [2], microelectronics [3] and nanocatalysis [4]. In addition to the appearance of bulk motif, ground state Al_n clusters ($n < 100$) show size specific features in their structures [5-8], cohesive energies [9-11], and thermodynamic properties [12-14]. For example, the ground state geometries of many clusters are seen to change from a disordered morphology to an ordered one (or vice-versa) with the addition of a single atom [15]. Adding an extra atom to some clusters also changes the melting transition from a first-order to a second order [16-22]. The above mentioned and many other size dependent characteristics make the study and application of aluminum nano clusters with up to a few hundred atoms both interesting and challenging.

One such application is the synthesis of aluminum nitride. Aluminum nitride, one of the industrially important materials, carries high impact as an electronic material and is usually synthesized through a direct reaction between Al surface or clusters and N_2 at a high temperature and pressure [23]. Nevertheless, one needs to modify a processing condition to smoothen such tedious and hard reactions. Consequently, recent experimental studies showing that Al clusters of range 25-100 have melting temperatures that are 450 K, well below the bulk melting temperature, 934 K, has excited several researchers [22]. Not only clusters in this range show a depressed melting temperature, they also show a size sensitive melting behavior. These results can be exploited to design the chemical reactions at desired temperature by choosing an appropriate cluster. In addition, the depressed melting temperature of clusters facilitates easier chemisorption and thus various chemical reactions at very low temperatures (around 450 K). It is noteworthy that N_2 molecule is only known to physisorb on the Al surfaces below the melting temperatures [24] and thus use of clusters for such reactions could be more advantageous.

The above aspect is demonstrated very nicely in a recent report by Jarrold *and co-workers* [1] where they discuss the reactivity of N_2 on Al_{100} cluster. They have determined the melting temperature of Al_{100} using heat capacity measurements following which the ion beam experiments are used to investigate the reaction between the cluster and molecular N_2. They show that on a melted structure, the activation barrier for N_2 adsorption decreases nearly by 1 eV. The importance of Al-N

reaction has also motivated Romanowski *et. al*. [25] to perform a theoretical study of N_2 reaction with liquid Al metal. They have determined the activation barrier for dissociative chemisorption of N_2 to be 3.0 eV. They propose that the melting decreases the surface energy, and atoms in liquid are mobile and better able to adjust the N_2 molecule. Hence, previous studies on N_2 adsorption conclude that the atoms on the surface of the liquid cluster move to minimize their energy lowering the activation barrier.

Apart from the enhanced mobility, very little understanding is available concerning the role of structure and bonding of Al clusters on the adsorption/reactivity of the cluster. The catalytic reactivity is always attributed to specific and precise structural rearrangement of atoms in the material. It is worthwhile to correlate the above two parameters to their reactivity. Thus, the interesting questions are: "Is the chemisorption of N_2 molecule a consequence of highly different structure of Al cluster following the phase transition? Do the changes in structure modify the chemical bonding property within the cluster thereby enhancing its reactivity or the higher reactivity is due the dynamical rearrangement of atoms within cluster? Does this reactivity vary as a function of cluster size?" To answer the above questions, we have studied systematically the adsorption behavior of N_2 on Al cluster as a function of cluster size. We also address the issue of conformational changes following the phase transition and their impact on N_2 adsorption.

To achieve this objective, we choose a series of Al clusters of variable size. It includes low energy conformers of Al_2, Al_3, Al_{13}, Al_{30} and Al_{100} clusters. Al_2 and Al_3 are the smallest of Al clusters that have been analyzed for understanding the adsorption of N_2 molecule. The reason for starting with such small clusters is to have a qualitative understanding on two issues viz., (a) to understand the electronic properties underlying the adsorption of the molecule on the cluster. (b) to analyze the adsorption of N_2 molecule as a function of Al cluster size. After analyzing various reactive sites of these clusters, N_2 is adsorbed on them to study the nature of its adsorption. The zero-temperature studies of adsorption is extended to a decahedron conformer as well as a few high energy conformers of Al_{13} (typically seen after the

phase transition) to analyze the ease of adsorption on high energy conformations. Since melting enhances distortion, these high energy structures help us to correlate the specific role of structure and bonding towards chemisorption of N_2. All considered structures were optimized and the bonding properties within them are analyzed through Electron Localization Function (ELF) and Frontier Molecular Orbital (FMO).

The rest of the work is organized as follows. In Section 6.2, we give a brief description of the computational method and descriptors of reactivity used in this work. Results and discussion are presented in section 6.3 for Al_n--N_2 interaction. Finally, our conclusions are summarized in section 6.4.

6.2 Computational Details

As mentioned, we have considered aluminum clusters of varying sizes viz.,: Al_2, Al_3, Al_{13}, Al_{30} and Al_{100} for the study. All the possible conformations of these clusters are optimized. Following the optimization, low lying structures are considered for further study of adsorption. All the structures were optimized using Density Functional Theory (DFT) based method. The optimization is carried out using VASP [26, 27]. As in standard DFT programs, the stationary ground state is calculated by solving iterative Kohn-Sham equations [28]. We use Vanderbilt's ultra-soft pseudo-potentials[29] within the Local Density Approximation (LDA) for describing the behavior of core electrons. An energy cut-off of 400 eV is used for the plane wave [30] expansion of Al and N atoms. The structural optimization of all geometries is carried out using the conjugate gradient method [31], except for the high energy conformers where, we use *quasi-Newton* method [32] in order to retain the local minima. The structure is considered to be optimized when the maximum force on each atom is less than 0.01 eV/Å. Similar optimization procedures are repeated for the interaction of N_2 molecule at all Al cluster reactive sites, and for that of bare N_2 molecule. All the molecules are enclosed in cubical box of 25 Å dimensions.

Various descriptors are used to analyze the reactivity of the Al clusters [33,

chapter 2]. We have analyzed the ELF for all clusters and their complexes of N_2 at isovalue where atomic basins start merging. Thus, as size and geometry of Al cluster changes, here, the ELF analysis helps us to understand the discrete bonding pattern. In addition, we also analyze the partial charge densities of FMO. The Highest Occupied Molecular Orbital (HOMO) and Lowest Unoccupied Molecular Orbital (LUMO) are the best used global descriptors of reactivity [34, 36a]. The N_2 adsorption at particular site is followed by HOMO and LUMO analysis, which helps to distinguish the most reactive site. Subsequently, after complex formation, same descriptors elaborate the peculiar Al-N bonding. In addition, to understand the over all charge distribution after complex formation, the charges on various atoms (in optimized bare clusters and respective complexes) are calculated through the GAMESS [36b] (following the single point energy convergence on the VASP optimized geometries).

Following the studies on the ground state conformations of Al clusters of varying sizes, as mentioned, we have considered few high energy conformations of Al_{13} for N_2 adsorption. This is done with an aim of elucidating the role of electronic properties of these high energy melted conformations on the chemisorption. One of the earlier theoretical works has reported that Al_{13} undergoes a solid to liquid transition between 1000-1700 K [37]. Hence, the high energy conformations are obtained from a finite temperature run of Al_{13} at 1200 and 1600K. It may be recalled that an earlier work [37] predicted 1600K to be nearly melting temperature of the cluster. The finite temperature calculations are performed by using Born-Oppenheimer molecular dynamics based on the Kohn-Sham formulation of DFT, employed in VASP. The ionic phase space of the cluster is sampled classically in a canonical ensemble using a method proposed by Nóse [38]. Pursuing the simulation of 10 pico seconds, few conformations were chosen from these high temperature runs. The structure, bonding and reactivity of these clusters are discussed and compared with those of the low lying conformation of the same cluster.

6.3 Results and Discussion

(A) Size dependence of the reactivity: Ground State Geometries of Al clusters and their Interaction with N_2

(i) Al_2:

Al_2 like any mono atomic dimer cluster is a covalently bonded one [39-43], while Al_3 is a widely studied system for adsorption of various molecules such as H_2 [44-46], O_2 [47] etc. Figure 6.1 gives the ground state geometry of Al_2 and its complex with N_2. The ELF contours and the frontier orbitals for these systems are given in the same Figure. Various inter atomic distances along with the Mulliken charges on each atom [in square bracket] for Al_2 and Al_2--N_2 are given in the same Figure.

We begin with a discussion of Al_2 followed by its complex with N_2. The inter atomic bond distance in Al_2 is 2.59 Å. This is in perfect agreement with the reported literature values [39-43]. The covalent nature of Al_2 is well seen from the contours of ELF, where both Al basins merge considerably around a value of 0.76. The FMO analysis predicts that HOMO orbital is bonding orbital (σ-overlap) and LUMO is localized on the two Al atoms (p-orbitals). The favorable mode of N_2 interaction with Al_2 is a linear structure as seen from Figure 6.1. Other modes of interaction (perpendicular to the Al-Al bond of Al_2 molecule) do not result in local minima. The Al_2--N_2 complex has an interaction energy of -0.57 eV (-13.10 kcal/mol). Following the adsorption of N_2 molecule, the Al-Al and N-N bond distances increase marginally from 2.59 to 2.61 Å and from 1.11 to 1.15 Å, respectively. The Al_2--N_2 interaction optimizes at an Al-N distance of 1.86 Å. The corresponding ELF contours at an isovalue of 0.76 reveals a polarized electron density on Al(2) and N(1) atoms (see Figure 6.1). There are no merged basins in the Al-N bonding region even at an isovalue of 0.50.

The HOMO of Al_2--N_2 complex is composed of 2p orbitals of N atoms while the LUMO is composed of p orbitals of interacting Al atom and N_2 atoms. To understand the charge redistribution following the adsorption of N_2, we study the difference charge density (Δρ) (Figure 6.1). The blue region indicates charge gained

where as the red region indicates the charge depletion. The presence of red region along the N_2 and Al_2 bonds and presence of blue region around the each atom shows a small polarization within the whole molecular space. Thus, Al_2 and N_2, in their interaction show an overall charge transfer from Al_2 to N_2. In order to quantify the charge transfer we have calculated the Mulliken charges for individual systems and the complex. The charges of Al atoms in the bare Al_2 are nearly zero. The corresponding charges on Al atoms in the complex are 0.123 a. u. (non-interacting Al atom) and 0.513 a. u (interacting Al atom). The N(1) atom (interacting N atom) in N_2 shows charge gain of -1.202 a. u. while N(2) is slight positively charged. Thus, both the difference charge density and Mulliken charges reveal an overall charge transfer from Al_2 to the N_2 molecule.

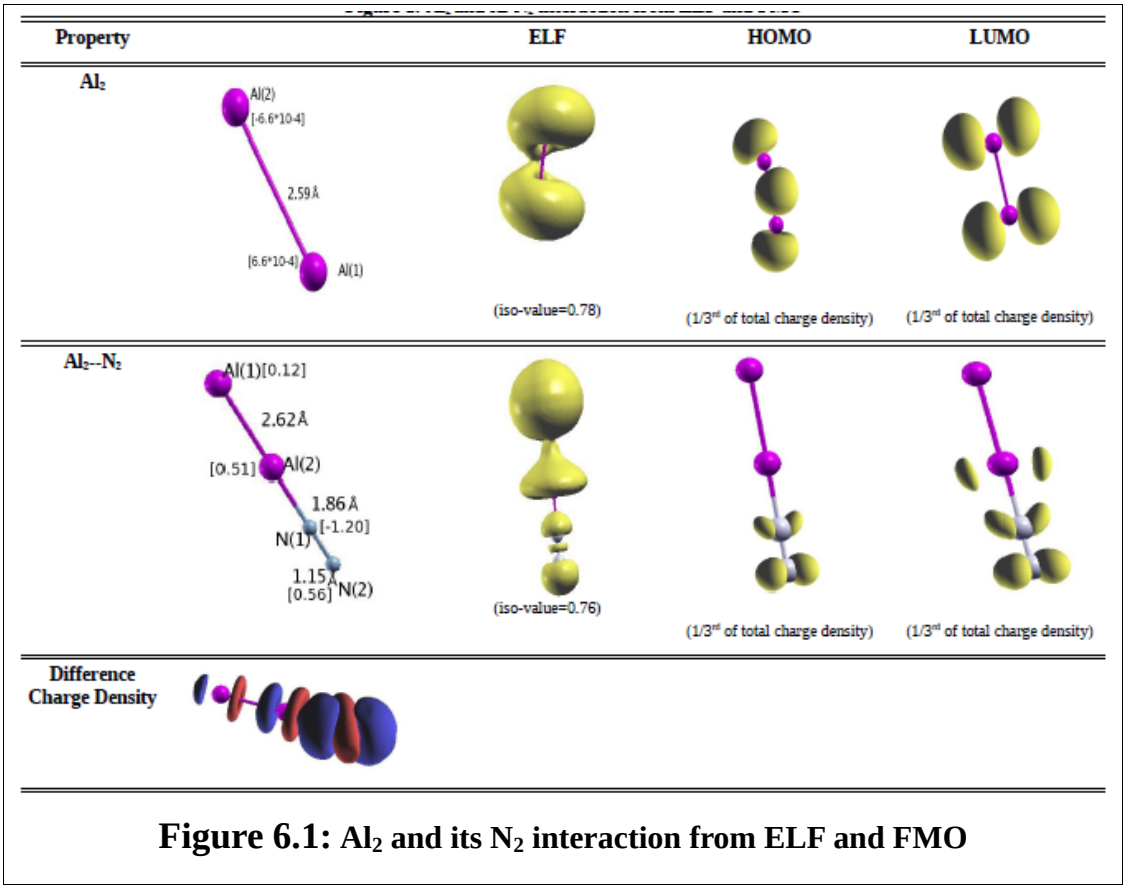

Figure 6.1: Al_2 and its N_2 interaction from ELF and FMO

The moderate interaction energy of N_2 with Al dimer promotes us to study the nature of N_2 interaction as a function of cluster size and geometry. Does the bonding

remain same for larger cluster sizes? Does interaction energy increase with the cluster size? Various such questions will be addressed in the next few sections.

(ii) Al_3:

A three atom cluster has three possible geometric configurations viz., linear conformation, zig-zag conformation and a cyclic conformation [48, 49]. The three conformations in Al_3 differ from each other by nearly 1 eV with cyclic Al_3 as the most stable configuration. This is consistent with earlier literature reports [48, 49]. Cyclic Al_3 is an equilateral triangle as shown in Figure 6.2 with Al-Al bond distances of 2.47 Å. Thus, we note a decrease in inter atomic bond distance within the Al atoms as compared to the Al_2. In spite of the decreased bond distances, the ELF basins merge only at a value of 0.74 as compared to 0.76 in Al_2. The HOMO of Al_3 shows a multi centered bonding arising from the overlap of s-p hybridized orbitals. The LUMO is made up of p orbitals of Al atoms. Considering the orbital contributions and their density contours, we verified two modes for N_2 adsorption. One perpendicular to the plane of triangle and another along one of the Al-Al bonds as shown in Figure 6.2. The first Al_3--N_2 conformation was found to be a meta stable one with N_2 getting desorbed. However, the second Al_3--N_2 configuration resulted in a stable minima with an interaction energy of -0.47 eV (i. e. -10.77 kcal/mol). Interestingly, this is nearly 3 kcal/mol lower than that of dimer complex.

N_2 adsorption reduces the symmetry of the Al_3 cluster from an equilateral triangle to an nearly isosceles triangle. The Al(2)-Al(3) (see Figure 6.2) increases to 2.64 from 2.47 Å with rest of the two Al-Al bond lengths remaining around their original values. The Al-N interaction converges to the same bond length as that in Al_2--N_2 complex i. e., 1.86 Å. The N_2 bond also increases to 1.15 Å from 1.11 Å like in the case of Al_2-N_2. The ELF contour of the complex (at an isovalue of 0.80) shows polarization of densities on Al(3) atom (the Al atom interacting with N_2) and N(1) atom. Similar to Al_2--N_2 complex, Al_3--N_2 complex does not show merged basins in the Al-N bonding region.

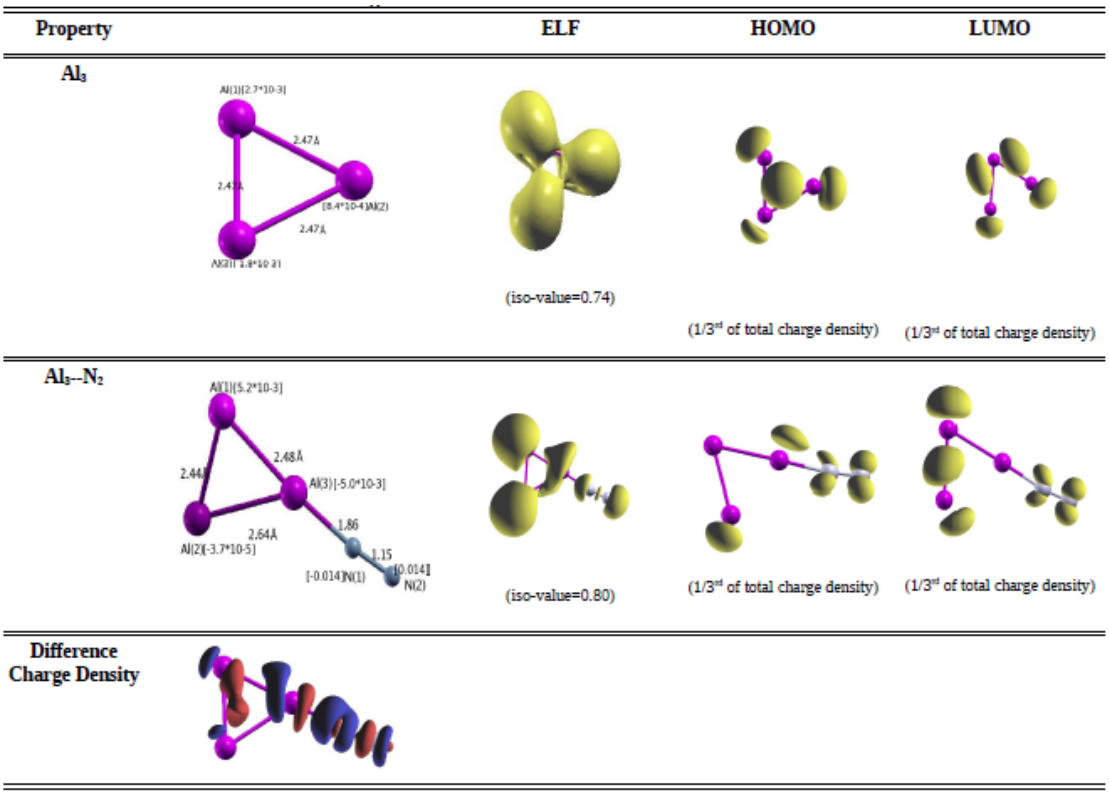

Figure 6.2: Al_3 and its N_2 interaction from ELF and FMO

The frontier orbital analysis shows that HOMO is contributed by the p orbitals of N_2, Al(3) and Al(2) atoms. The LUMO is composed of bonding orbital of Al(1) and Al(2) atoms (the two Al atoms not interacting with N_2). The charges derived by Mulliken population analysis for Al_3 and Al_3--N_2 are given in Figure 6.2. All the atoms in the Al_3 are nearly neutral in the cluster as well as the complex. However, the N_2 molecule is polarized following the complexation. However, the difference charge density plot shown in Figure 6.2 reveals that there has been some charge redistribution among the Al and N atoms. Each atom is seen to donate some electrons from one of its orbital and gain in another of its atomic orbital there by neutralizing the overall charge transfer. Thus, Al_3, shows a marginal decrease in the interaction energy.

(iii) Al_{13}:

Our next cluster to be studied for N_2 adsorption is an Al_{13} cluster. Al_{13} is the most well studied among the aluminum clusters. Icosahedra (I_h) is indebted global minima in all extensive static and dynamic studies of Al_{13} [50]. Hence, we found it

interesting to chose this as the next larger cluster for N_2 adsorption. Figure 6.3a shows optimized geometries of I_h, and its N_2 complex. We now classify atoms within the cluster in order to facilitate the discussion of various reactive sites with the cluster and the N_2 adsorption on them. Various atomic sites in the I_h conformation can be classified into three types viz., "A", "B" and "C" depending upon their chemical environment and their distances from the central atom (see Figure 6.3a). Site A is the single central atom. Site B and C are the surface atoms containing six atoms each. The atoms "B" lie at a distance of 2.66 Å from the central atom "A" and atoms "C" lie at a distance from 2.60 Å from central atom "A".

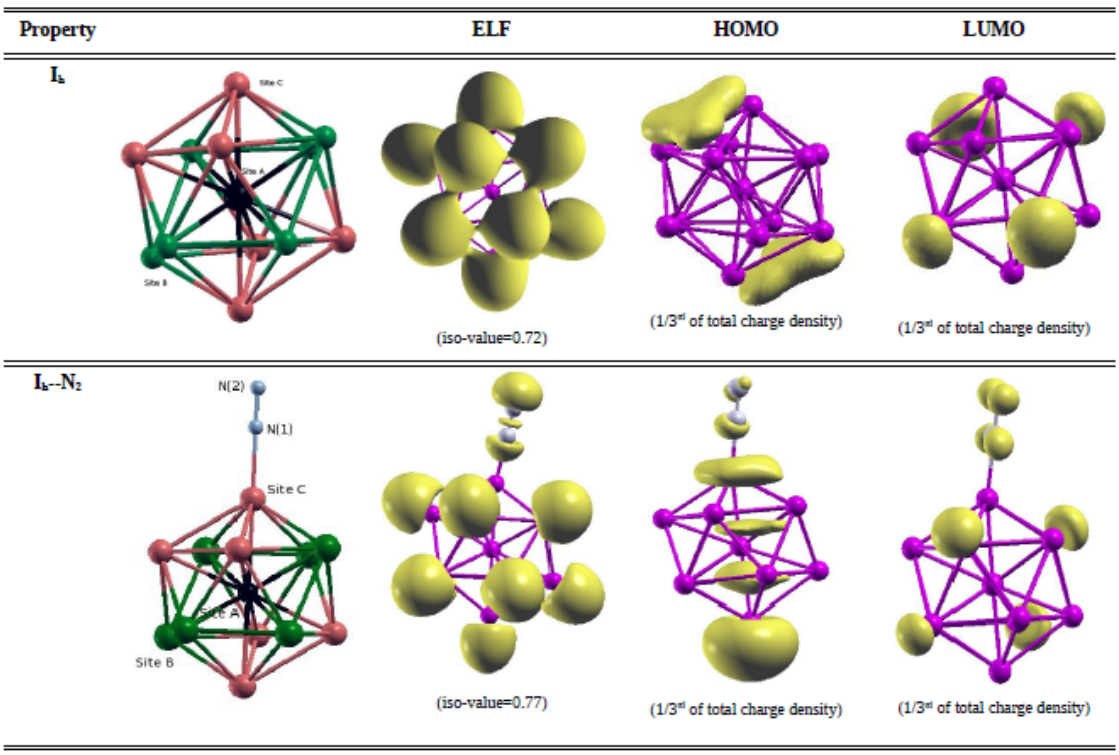

Figure 6.3a: Al_{13} (I_h) and its N_2 interaction from ELF and FMO

Figure 6.3b shows another perspective of the I_h conformation for a better understanding of the reactive sites. Thus, the structure is highly symmetric. Table 6.1 gives details of these inter atomic distances between various types of sites. Distances between two adjacent "B" atoms is 2.82 Å, while that of two adjacent "C" atoms is 2.90 Å. Owing to their different orientations with respect to the central atom "A", the

inter atomic distance between two diagonally placed "B" atoms is 5.32 Å while the distance between "C" atoms is 5.21 Å. The inter-atomic distance between site "B" and "C" is 2.70 Å.

This symmetry is reflected in Mulliken atomic charges (tabulated in Table 6.1) and ELF peculiarities of I_h geometry are also reproduced in the FMO's. Analysis of HOMO reveals a multi centered bonding contributed by "C" atoms in the same plane as seen in Figure 6.3a. However, the LUMO is contributed by only "B" atoms.

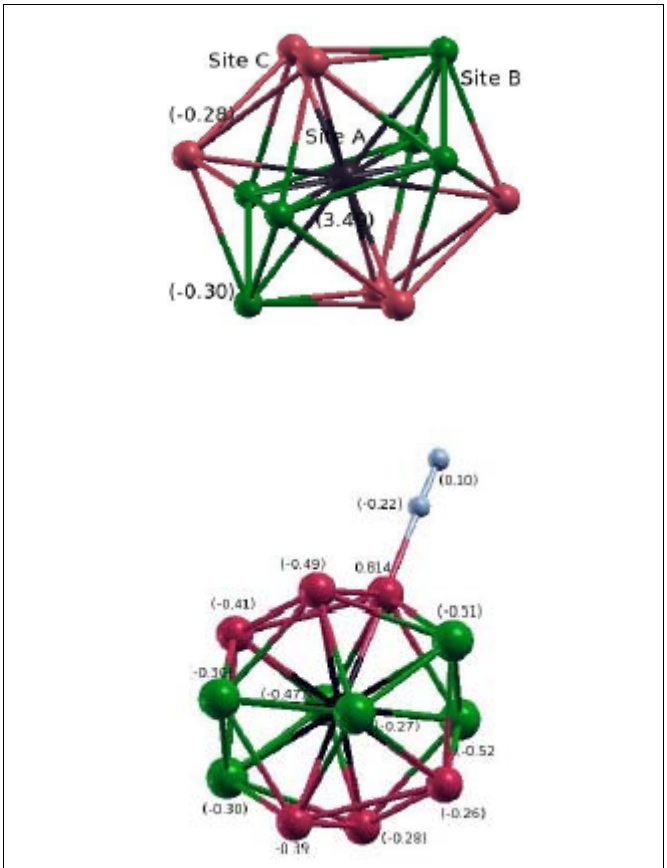

Figure 6.3b and 6.3c: Al_{13} (I_h) and its N_2 interaction another perspective

Following the analysis of FMO and ELF, site "B" and "C" appear to be susceptible [51] to the N_2 attack. Hence, we have studied the adsorption of N_2 on both these sites.

The adsorption of N_2 on site "B" results in a meta-stable structure with finally N_2, desorbing from it. The adsorption of N_2 on site "C" results on the other hand in a stable conformation with an interaction energy of -0.34 eV (-7.91 kcal/mol). Interestingly, this is nearly half of that found for O_2 molecule on Al_{13} (-0.77 eV) reported by Shiv Khanna and co-workers [47]. They attribute such a low interaction energy of Al_{13} to its magic cluster property (exceptional stability) and hence its nonreactive behavior towards many reagents. The marginally lower interaction energy of Al_{13} towards N_2 molecule as compared to Al_2 and Al_3 is reflected in its Al-N bond distance (which is 1.90 Å as compared to 1.86 Å in Al_2 and Al_3 complex). The N-N bond distance in the complex is 1.13 Å as compared to 1.15 Å in Al_2 and Al_3.

Table 6.1: Structural and Electronic Properties of Al_{13} (I_h) and its N_2 Complex

Distance (Å)	**I_h**	**I_h--N_2**
A-C_{int}	-	2.63
A-B	2.66	2.65
A-C	2.60	2.54
Al-N	-	1.90
N-N	1.11	1.13
B-C	2.70	2.78
B-B (diagonally placed)	5.32	5.50
B-B	2.82	2.85
C-C (diagonally placed)	5.21	5.28
C-C	2.90	2.86
Interaction energy (kcal/mol)	-	-7.91

Average Charges on various sites as obtained from Mulliken population analysis (a. u.)

Sites	**I_h**	**I_h--N_2**
A	3.43	3.49
B	-0.3	-0.51, -0.52, -0.49, -0.30, -0.30, -0.27
C_{int}	-0.3	0.81
C	-0.28	-0.49, -0.36, -0.41, -0.28, -0.26
N(1)	-	-0.22
N(2)	-	0.1

Following the N_2 adsorption there is a small loss of symmetry. For the sake of better understanding of structural changes following the adsorption we rename the interacting "C" atom as "C_{int}". The "A"-"C" bond distance in the $Al_{13}(I_h)$--N_2 complex reduces to 2.54 Å from 2.60 Å, "A"-"C_{int}" increases to 2.63 Å from 2.60 Å. Similarly, "B"-"C" bonds increase to 2.78 Å from 2.70 Å. The "A"-"B" and "B"-"B" bond distances in the complex remain around their original values. The distance between "C"-"C" is 2.86 Å in the complex as compared to "C"-"C" distance of 2.90 Å in I_h. The interatomic distances between the diagonally opposite "B" atoms in complex is 5.50 Å (as compared to 5.32 Å) and that between diagonally opposite "C" atoms is 5.28 Å (as compared to 5.21 Å). Thus, the volume of the cluster increases marginally following the N_2 adsorption.

Analysis of FMO's shows that HOMO is contributed by the interacting Al atom, and some lower plane of atoms in the cluster. The charge distribution in Al_{13}--N_2 complex is given in Table 6.1. There is an overall charge transfer of 0.21 electrons to N_2 from Al_{13} atom. It may be noted that this is less than that seen in Al_2 but more

than what is seen for Al_3. The Al atom bonded to the N_2 molecule acquires a positive charge of 0.81 a. u. As a consequence, following the charge transfer (see Figure 6.3c), the atoms on upper half (atoms above the central atom "A") of Al_{13} are more negatively charged compared to those on lower half (atoms below the central atom "A"). The finer details of the charge distribution (see Figure 6.3c) show that the positive charge on central atom "A" increases marginally by 0.05 a. u.

The ELF of Al_{13}--N_2 complex is shown in Figure 6.3a. It is interesting to note that there is lesser polarization of electron density around N_2 as compared to the case of Al_2 and Al_3. This and the fact that the first merging of the basins occurs only at 0.76 isovalue reflects the lower interaction between the Al_{13} and N_2.

(iv) Al_{30}:

To evaluate the adsorption energy of N_2 molecule as a function of cluster size, we next consider a 30 atom cluster. There have been quite a few recent reports on the lowest energy conformation of Al_{30}. One of the reports has suggested a double tetrahedron as a local minima for Al_{30} [52]. Recent reports, on the other hand have reported few other conformations as the lowest energy geometry for Al_{30} [6, 53]. However, we have used the double tetrahedron for the case of N_2 adsorption. The geometries of Al_{30} and its complex with N_2 and various other properties are given in Figure 6.4. Based on symmetry, the atoms in the cluster can be classified into 7 types of sites as shown in Figure 6.4. The inter-atomic distances between various sites are reported in Table 6.2. It is seen from the Table that the edge atoms are far from central atom ("E"). These bonds lay in the range 3.78 Å to 6.47 Å. On the other hand, surface atoms F and G lie at optimal distance of 2.75 Å from central atom while their corresponding distances with adjacent surface and edge atoms is slightly longer. The bond lengths among edge atoms viz., "A"-"B" (2.65 Å), "B"-"C" (2.65 Å) and "C"-"D" (2.59 Å) are the shortest ones. The short bond distance between the edge atoms is well reflected in the ELF plots (see Figure 6.4). At an isosurface of 0.86 the basins of all edge atoms merge. However, at the same value, the basins on surface atoms remain as such which merge at a lower value of 0.74. The HOMO of this conformation is mainly contributed by "A" and "B" atoms. The LUMO is contributed by "C" and "D". Considering the FMO contributions, N_2 can preferably adsorb on the

edge atoms “A”, “B” “C”, and “D” atoms.

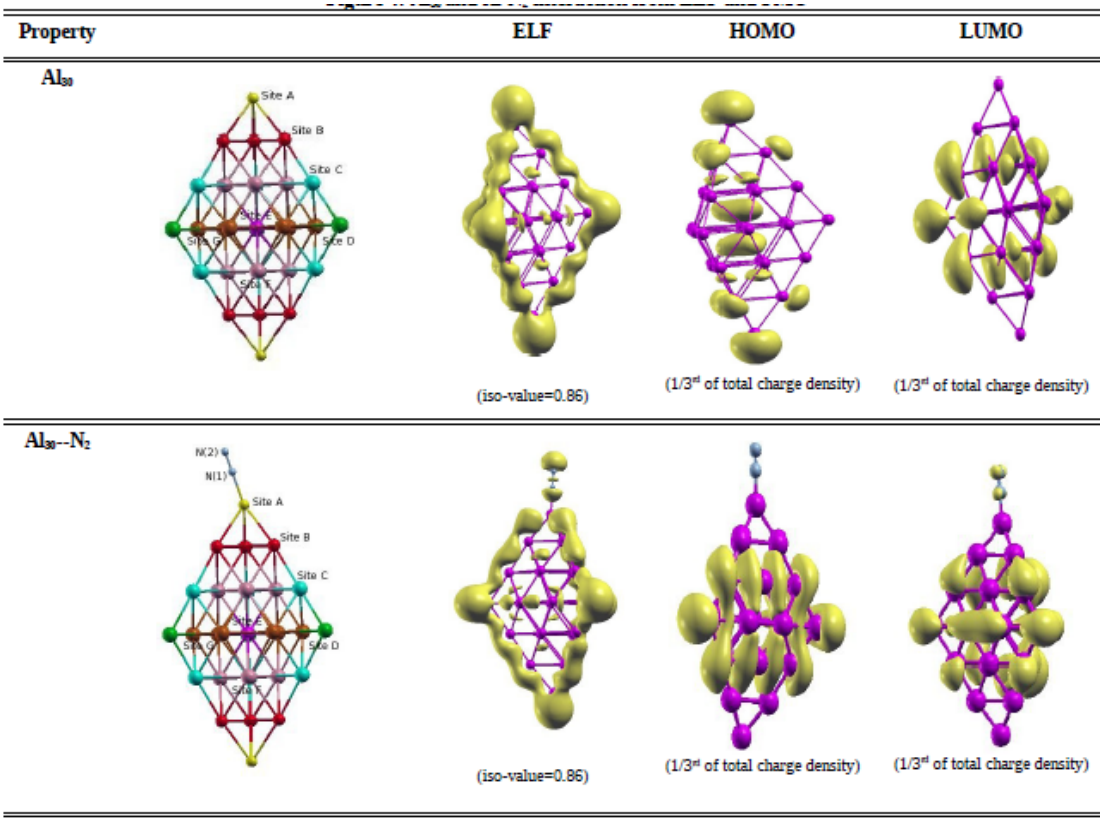

Figure 6.4: Al_{30} and its N_2 interaction from ELF and FMO

First, we consider site “A” for N_2 adsorption (see Figure 6.4). The Al-N and N-N bonds optimize to 1.86 Å and 1.13 Å respectively as in the case of Al_{13}. The interaction energy falls in the same range as observed for the earlier clusters, -8.01 kcal/mol. The structural details of Al_{30}-N_2 complex are reported in Table 6.2. Although, the original double tetrahedron is not distorted much, there are some small perturbations following the N_2 adsorption. Notable among them are the inter-atomic distances between site “C” and “D” which increases and consequently, ELF at 0.86 show some disconnected basins. The basin around site A atom, involved in Al-N bond, disappears. The HOMO of the complex is formed of P-P orbital overlap of site C, site D edge and site F, site G surface atoms. However, the LUMO is similar to the LUMO of bare Al_{30}. In addition to this, LUMO is also present on N_2 molecule. In the above Al_{30}--N_2 complex, the N_2 is adsorbed vertically on the site A. Adsorption of N_2

molecule on sites B and C result in similar interaction energies and electronic properties.

Table 6.2: Structural and Electronic Properties of Al_{30} and its N_2 Complex

Distance (Å)	Al_{30}	Al_{30}--N_2
A-B	2.66	2.54
A-E	6.47	6.00
B-B	2.86	2.91
B-C	2.65	2.58
B-F	2.76	2.69
B-E	4.69	4.60
C-C	2.68	2.70
C-F	2.68	2.74
C-D	2.59	2.63
C-G	2.74	2.64
F-G	2.64	2.62
C-E	3.78	3.90
F-E	2.75	2.84
D-G	2.65	2.68
G-G	2.52	2.65
G-E	2.75	2.80
D-E	4.51	4.77
Al-N	-	1.86
N-N	1.11	1.13
Interaction energy (kcal/mol)	-	-8.01

We have also attempted a case of multiple bonding where N_2 molecule adsorbs on site B with slight inclination towards site C, forming a bridge. However, this orientation results into a conformation where N_2 adsorbs only on site B atom with more or less

same interaction energy.

(v) Al_{100}:

We must not forget that the original work reported by Jarrold *et. al.* is on Al_{100} cluster [1]. Hence, to check the N_2 interaction with such a large cluster, we consider one of the potential minima of Al_{100} cluster. It is difficult to illustrate the in detail structural parameters of 100 atom clusters, hence, we only outline the peculiarities found in bonding those obtained from ELF and FMO reported in Figure 6.5. The Figure 6.5 shows that most of the Al atoms are clustered on the surface and very few of them form the core. The covalency of Al_{100} cluster is as good as that of symmetrical Al_{30} cluster. The basins on the surface atoms start merging at an 0.84 isovalue. The HOMO, is centered on many surface atoms, particularly showing the multi-centered bonding resembling that of Ih HOMO. The N_2 is adsorbed on one of the free sites.

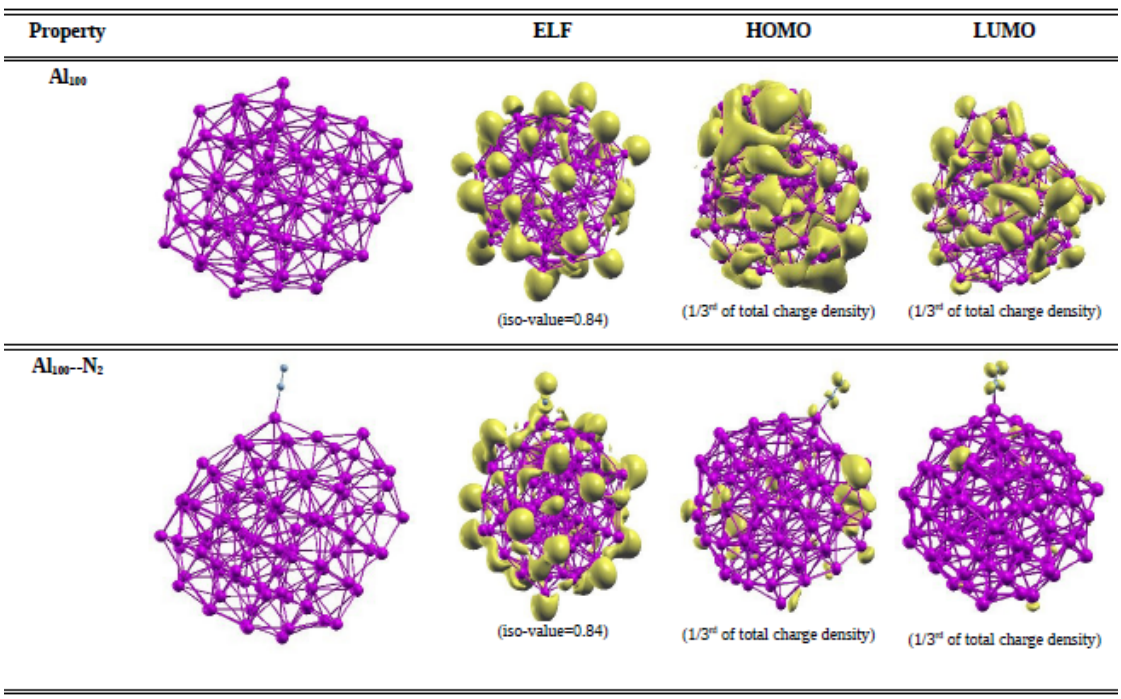

Figure 6.5: Al_{100} and its N_2 interaction from ELF and FMO

The interaction energy is -7 kcal/mol with an optimized Al-N bond of 1.91 Å. The N-N elongation, here, is to the same magnitude of 1.13 Å. Similar to small sized Al

cluster N_2 complex, ELF does not show any merged basins along Al-N bond. The ELF contours merge at lower isovalue of 0.80 resulting in further reduction of covalency. The HOMO of Al_{100}--N_2 is localized on both N atoms and interacting Al atom. On the contrary, N_2 also participates in LUMO formation. Thus, the interaction energy of N_2 molecule with the ground state conformation does not seem to vary substantially with respect to the cluster size.

(B) Influence of melting on the reactivity: High Energy Al_{13} cluster conformations and their Interaction with N_2

(i) Decahedron (D_h):

As discussed in Section I, N_2 adsorption on Al clusters increases dramatically above temperatures which correspond to the phase transition of the later. Just below and above the phase transition, clusters visit several high energy conformations. Such high energy conformations exhibit contrastingly different structural and electronic properties (particularly the surface atoms) as compared to the ground state conformations. One of the objectives of this work is to understand if such a change in surface properties can contribute to better adsorption of N_2 (and hence better reactivity) on Al clusters. Hence, we next study some of the high energy conformations of Al clusters and N_2 adsorption on them. For this purpose, we have chosen high energy conformations of Al_{13} as a case study. It has been reported earlier that Al_{13} undergoes a phase transition around 1400 K [37]. Decahedron is a dominant high energy conformation of Al_{13} seen from 400 K to 1200 K [37]. Hence, we found it interesting to study the adsorption of N_2 on this conformation. In addition, we have also chosen two high energy conformations from a finite temperature run of 1600 K. In the next few sections, we discuss the structure and bonding of these high energy conformations and their implications on the N_2 adsorption.

We begin with a discussion on decahedron (D_h). Figure 6.6 shows the structural details of this conformation. D_h having lower symmetry than that of I_h, the atoms within it can be classified into 5 types.

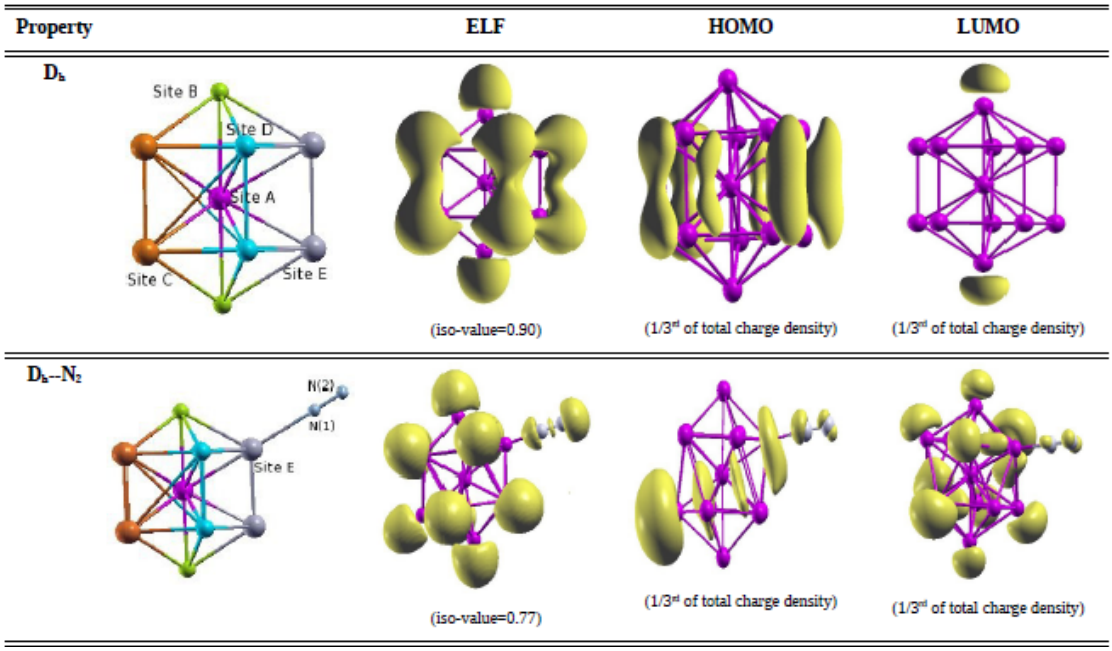

Figure 6.6: Al_{13} (D_h) and its N_2 interaction from ELF and FMO

Figure 6.6 shows five unique sites (as compared to three seen in I_h). The central atom, "A" is bonded to two vertex atoms "B" with an interatomic distance of 2.66 Å. Rest of the ten atoms form two planes between the central atom and two vertex atoms and are classified as "C", "D" and "E" based on the symmetry (See Figure 6.6).

The inter atomic distances between various sites are tabulated in Table 6.3. Interestingly, the inter atomic distances between sites "E" and "D" (i. e. "D"-"D" and "E"-"E" bond distances) are 2.59 Å, same as that of Al_2 dimer. Such a short bond distance is indicative of covalent bonding between these atoms. "C"-"C" bonds are the next shortest ones (2.63 Å) Thus, intra-planar atoms are bonded to each other with strong covalent bonds. The inter-planar bond distances viz., "C"-"D" and "D"-"E" are marginally longer with a reasonably large bond distances of 2.70 Å and 2.81 Å, respectively. Rest of the bond distances lay in the order of 2.66-2.72 Å. Analysis of ELF basins reveals the covalent nature of bonding across the two planes.

Table 6.3: Structural and Electronic Properties of Al_{13} (D_h) and its N_2 Complex

Distance (Å)	**D_h**	**D_h--N_2 (I_h--N_2)**
A-B	2.66	2.66
A-C	2.66	2.62
A-D	2.69	2.66
A-E	2.69	2.53
Al-N	-	1.90
N-N	1.11	1.13
B-C	2.69	2.79
B-D	2.72	2.73
B-E	2.67	2.70
B-B	5.32	5.28
C-D	2.70	2.78
C-E	4.42	4.31
C-C	2.63	2.78
D-E	2.81	2.68
D-D	2.59	2.77
E-E	2.59	2.74
Interaction energy (kcal/mol)	-	-15.86

Average Charges on various sites as obtained from Mulliken population analysis (a. u.)		
Sites	**D_h**	**D_h--N_2 (I_h--N_2)**
A	2.93	3.49
B	-0.10	-0.31, -0.51
C	-0.30	-0.26, -0.35, -0.30, -0.30
D	-0.26	-0.50, -0.34
E	-0.24	0.77, -0.40
N(1)	-	-0.21
N(2)	-	0.10

The ELF basins of same sites merge at a high isovalue of 0.90, whereas those across the two planes merge at 0.78 isovalue.(see Figure 6.6). Thus, D_h conformation is a more covalently bonded conformation as compared to the ground state I_h conformation of Al_{13}. The Mulliken charges on each site are given in Table 6.3. All the surface atoms are negatively charged resulting in a positively charged central atom. The atoms in the two planes are the most negatively charged ones.

The HOMO and LUMO of D_h are reported in the Figure 6.6. The HOMO contributed by the bonding orbitals of p-p overlap between the "C"-"C", "D"-"D" and "E"-"E" atoms while LUMO is concentrated only on site B i. e. vertex atom. Considering the contribution of various atoms to HOMO and LUMO, we finalize four sites for N_2 interaction, viz., "B", "C", "D" and "E". Interestingly, sites "B" and "C" do not show any reactivity towards N_2 adsorption. All orientations of N_2 on these two sites resulted in high energy structures with N_2 getting finally separated. The presence of highly covalent bonds around site "C" may be a probable reason for desorption on that site, site "B" being least negatively charged may be unfavorable for the N_2 adsorption. However, sites "D" and "E" are better for N_2 adsorption leading to stable complexes. The site E gives elevated interaction energy compared to site D. In both these optimizations although we started with initial D_h geometry, the final complex

obtained was nearly I_h--N_2 complex. That is during optimization D_h structure transforms into an I_h structure. This has been found to be the case irrespective of the optimization algorithm and initial orientations of N_2 molecule on these sites. Thus, N_2 adsorbed and stabilized complex is no more D_h--N_2 complex but it is same as original I_h--N_2 complex. This change of geometry reflects in ELF and FMO plots shown in Figure 6.6 which shows that the contours of this complex are analogous to those in original I_h--N_2 complex. However, the strength of interaction at both sites, D and E, is different. Site E shows almost double interaction energy than that of site D, The interaction energy at site E is -15.86 kcal/mol and the same at site D is -8.28 kcal/mol. These high energies of interaction are obtained from using definition of interaction energy as follows,

$$\text{Interaction Energy} = E_{complex} - (E_1 + E_2) \qquad (1)$$

Where, $E_{complex}$ is energy of complex which is converted to N_2 adsorbed I_h geometry. E_1 is energy of optimized D_h and E_2 is energy of optimized N_2. Since, final complex is no longer D_h, if we substitute E_1 as energy of optimized I_h, both interaction energies (at site D and site E) decrease significantly. In the later case site D is almost not bonded to N_2 (IE ~ 0.0 kcal) where as interaction of site E and N_2 is just same as original I_h--N_2 complex. As a consequence of this D_h turned I_h--N_2 complex shows similar behavior of bonding as described above in I_h section. Rest of the geometrical parameters of this final complex are same as those found in I_h--N_2 complex.

(ii) High Energy Conformations H1 and H2:

We next attempt the adsorption of N_2 molecule on some of the high energy Al_{13} conformations which are not so well known. As mentioned earlier, these conformations have been extracted from an molecular dynamical simulation of the Al_{13}--I_h cluster around 1600 K. Figure 6.7 gives one of the perspectives of both these two clusters. It is clearly seen that these high energy conformations are distorted leading to as many chemically unequal sites. H1 has nine chemically (Site "A" to Site "I" as shown in Figure 6.7) unequal sites while H2 has as many sites as the number of atoms within it. The high energy conformation H1 appears to be a hybrid of I_h and D_h conformations. The ELF at an isosurface of 0.90 reveals that both these conformations are characterized by the presence of covalent bonds at few pockets of

the clusters. The inter atomic distances between the atoms in the two clusters range from 2.54 to 2.84 Å. The charge distribution as obtained from the Mulliken population analysis for both the conformations is given in Table 6.4. It is seen from the Table that the atoms on the surface are mostly negatively charged and the central atoms are positively charged. Upon adsorption of N_2, H1 conformations results in a stable complex with an adsorption energy of -7.65 kcal/mol while adsorption of N_2 on H2 conformations leads to an interaction energy of -13.54 kcal/mol. Interaction energy increases by approximately -5 kcal/mol for a high melted and distorted structure H2, however, the case is not same for H1--N_2 complex.

Thus, interestingly it appears that varying the cluster size and just the reorientation of the bonds does not contribute significantly to the better adsorption of N_2 on Al clusters. The clear understanding of this elevated strength of interaction in case of H2 conformer can be understood with keen observation of the FMOs. The HOMO (see Figure 6.7) is dominantly spread over Al (7). In addition, this site is the least bonded and hence free site. The N_2 is adsorbed in a plane of triangle made up of Al(5), Al(7) and Al(12) atoms. This forms a stable complex with Al-N bond optimized to 1.90 Å. Here, the increase in interaction energy however is not ascribed by nature of H2 directly but is approved by additional Al-N bond formed between Al(12) and N(1). The characteristic bond formed so is 2.93 Å. The N-N elongation is 1.13 Å.

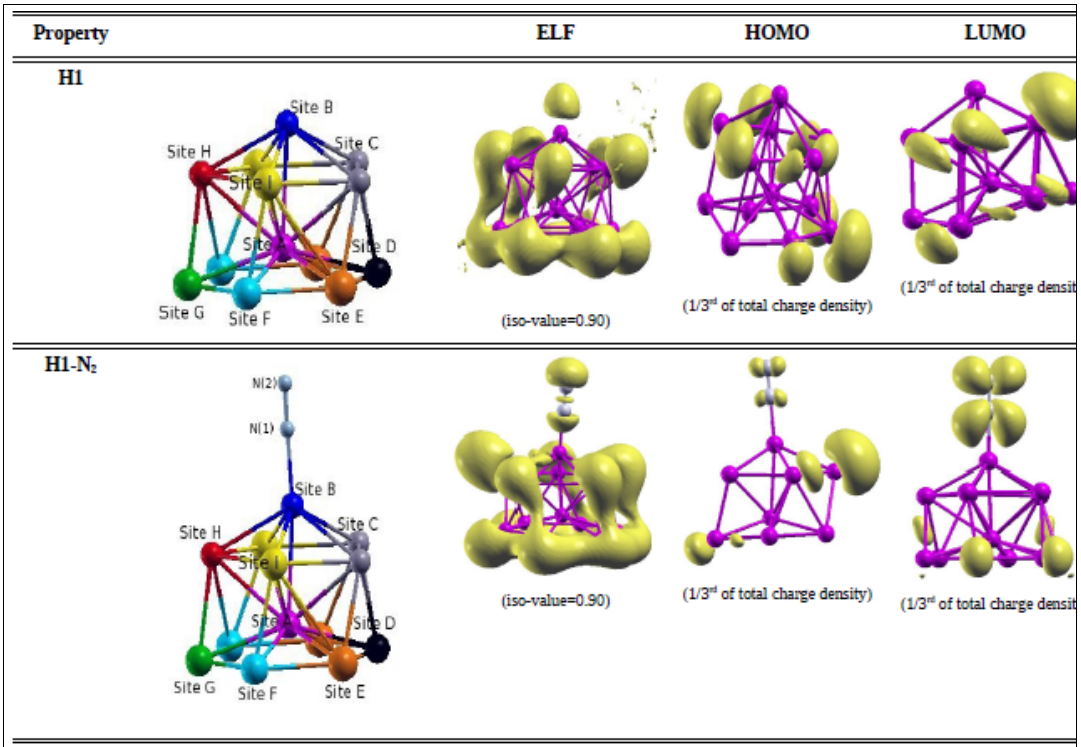

Figure 6.7(a): **Al_{13} (H1) and its N_2 interaction from ELF and FMO**

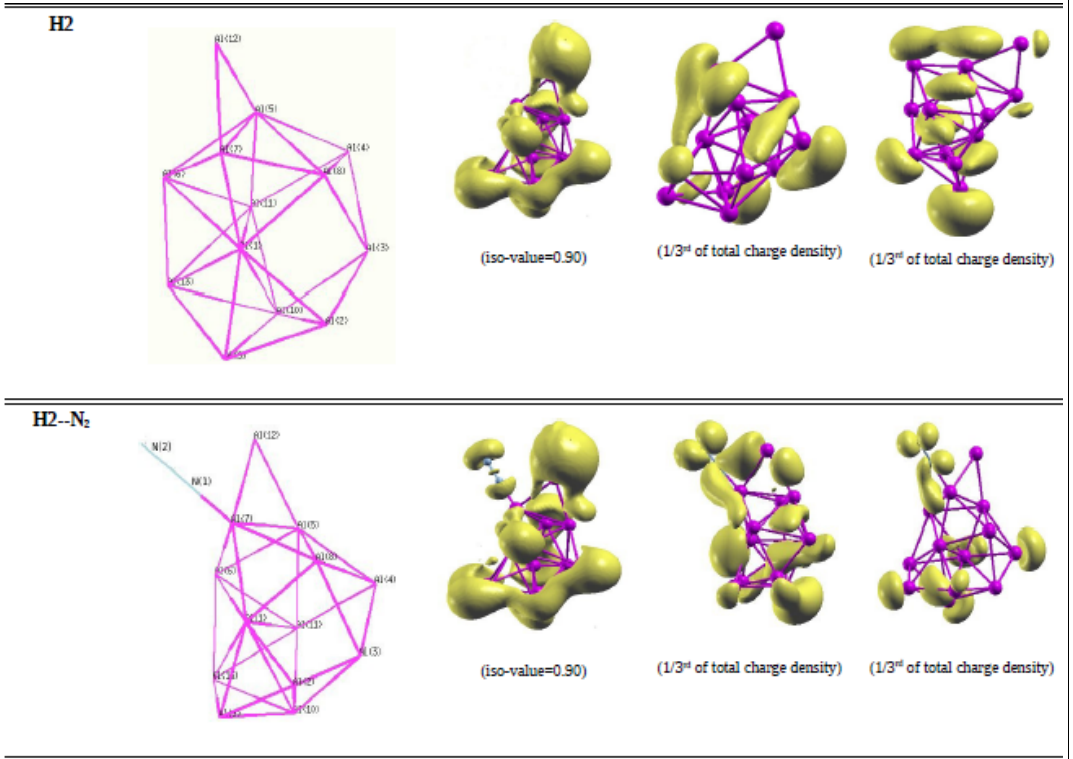

Figure 6.7(b): **Al_{13} (H2) and its N_2 interaction from ELF and FMO**

Table 6.4: Electronic Properties of H1, H2 (Al_{13}) and its N_2 Complex		
Sites	**H1**	**H1--N_2**
Average Charges on various sites as obtained from Mulliken population analysis (a. u.)		
A	2.07	1.61
B	-0.16	1.46
C	-0.01	-0.18
D	-0.20	-0.25
E	-0.36	-0.26
F	-0.28	0.00
G	-0.37	-0.43
H	-0.07	-0.25
I	0.01	0.00
N(1)	-	-0.22
N(2)	-	0.09
Interaction energy (kcal/mol)	-	-7.65
Sites	**H2**	**H2--N_2**
Average Charges on various sites as obtained from Mulliken population analysis (a. u.)		
1	1.22	1.20
2	-0.17	-0.38
3	0.11	0.22
4	-0.53	-0.46
5	0.34	0.17
6	-0.14	-0.34
7	-0.49	0.38
8	-0.13	-0.19
9	-0.54	-0.42
10	0.17	-0.02
11	0.42	0.44
12	-0.26	-0.34

N(1)	-	-0.18
N(2)	-	0.09
Interaction energy (kcal/mol)	-	-13.54

The Al(7)-Al(12) bond in bare H2 is 2.58 Å. In the respective complex, the Al(12) is close to Al(7). This bond reduces to 2.55 Å as N_2 approaches to Al(7) and thus retains a favorable geometry to form another Al-N bond (see Figure 6.7, H2--N_2 HOMO). There is no specific trend i. e. bond elongation or reduction observed in H2--N_2 complex formation. In general, the bonds in close vicinity of Al(7) show bond reduction. We also summarize the atomic charges on the interacting Al and N atoms. Let us concentrate on the atomic charges which participate in Al-N bond. A positive charge of 0.38 a .u. is built on the Al(7). The Al(12) atom is also bonded with N(1). Hence, the Al(12) pulls charge of -0.34 a. u. from N(1). The N(1) here, hence, acquires slightly less negative charge compared to other N_2 complexes.

Thus after studying various conformers of Al_{13} and their interaction with N_2, we can conclude that in case of Al_{13}, the N_2 interaction is not just dependent on structural arrangement of atom but is also a function of multiple bonding of N_2 with Al cluster. In other words, the highly melted or deformed structure where adjacent Al-Al bonds are not so strongly coordinated, N_2 can interact to form various Al-N bonds resulting in highly stable $(Al)_n$--N_2 complex. This is validated by the analysis of average interatomic Al-Al distances in Al_{13} clusters. The average interatomic distance shows a substantial increase in H2, a highly melted structure (3.91 Å) as compared to 3.59 Å, 3.65 Å and 3.70 Å in Ih, Dh and H1, respectively.

(C) Activation Barriers for interactive Al_{13}--N_2 complexes:

The relevance of the calculations presented in previous section can be verified by comparing the activation barriers of N_2 adsorption on the non-melted and melted Al clusters. To determine an accurate value for the activation barrier, we use the Nudge Elastic Band (NEB) method incorporated in VASP and calculate the barrier energies as a function of Al-N bond length. It adds to our surprise that activation barrier drops by ~0.85 eV i.e. 19.60 kcal/mol for the melted cluster. This outcome is agreeable with the original experimental result [1]. The large difference in the

activation energy for N_2 adsorption on melted and non-melted Al_{13} clusters and the fact that the N_2 remains adsorbed despite the relatively high barrier are both consistent with the idea that the N_2 molecule is chemisorbed on the Al_{13} cluster.

Finally, we must address that N_2 adsorption is carried out on a melted structure obtained after phase transition and no temperature effect is consider while its interaction. Thus, to count its chemisorption as mentioned by Jarrold *et. al.* we must bring in the thermal effects with the help of dynamics. Hence, in our next chapter, we plan to study the high temperature thermodynamics to obtain highly melted 100 atom cluster, followed by the room temperature reaction of N_2 adsorption.

6.4 Conclusion and Scope

Density Functional Calculations have been carried out to understand the adsorption of the N_2 molecule on the ground state geometries of Al_n clusters (n=2, 3, 13, 30, 100). The studies were also extended to few high energy conformations of Al_{13}. We summarize the adsorption energies of N_2 molecule on these ground state geometries and high energy conformations of Al_{13} clusters in Figure 6.8. With the exception of Al_2, all other ground state conformations show an interaction energy between -8 to -10 kcal/mol. As seen from the figure, the interaction energy is stable with respect to the cluster size. This interaction is mostly accompanied by a charge transfer from Al atoms to the nitrogen atoms in the complex. The bonding within ground state geometries in all cluster sizes is partially covalent and partially metallic. However, the extent of covalancy is seen to vary to some extent between the various sized clusters. Thus, independent of the electronic and structural properties, N_2 interacts weakly with the ground state geometries of Al clusters. The presence of high energy conformations of Al_{13} on the N_2 adsorption is seen to give mixed results with some high energy conformations leading to similar interaction energies as that of a ground state conformation (Decahedron and H1), whereas, high energy conformation of Al_{13}, viz., H2 is seen to favor the N_2 adsorption better due to the presence of more than one Al-N bond. Such multiple bonds between the ligand molecule and cluster are, thus, a characteristic phenomenon of high temperatures. This is a consequence of

increased interatomic distances between the Al-Al atoms (and thus weaker bonds) following the melting. These findings are also validated using the activation barrier energies. Thus, the above work indicates that the enhancement of reactivity of melted Al clusters is more due to thermodynamic factors and electronic factors play a minor role in the increasing adsorption energy of N_2 molecule.

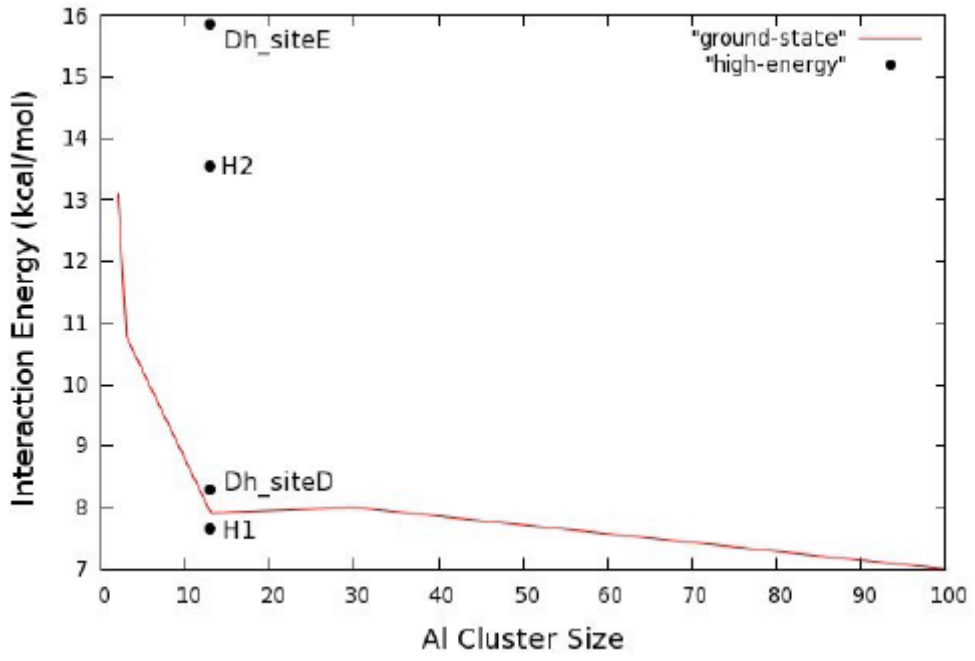

Figure 6.8: Interaction energy as a function of cluster size

6.5 References

[1] B. Cao, A. K. Starace, O. H. Judd, M. F. Jarrold, J. Am. Chem. Soc. **131**, 2446 (2009).

[2] R. Ferrando, J. Jellinek, R. L. Johnston, Chem. Rev. Washington, D. C. **108**, 845, (2008).

[3] A. O. Orlov, I. Amlani, G. H. Bernstein, C. S. Lent, G. L. Snider, Science **277**, 928 (1997).

[4] M. Valden, X. Lai, D. W. Goodman, Science **281**, 1647 (1998) .

[5] A. A. Shvartsburg, M. F. Jarrold, Phys. Rev. A **60**, 1235 (1999).

[6] A. Aguado and J. M. López, J. Chem. Phys. **130**, 064704 (2009).

[7] A. Lechtken, C. Neiss, M. M. Kappes, D. Schooss, Phys. Chem. Chem. Phys. **11**, 4344 (2009).

[8] E. C. Honea, A. Ogura, D. R. Peale, C. Felix, C. A. Murray, K. Raghavachari, W. O. Sprenger, M. F. Jarrold, W. L. Brown, J. Chem. Phys. **110**, 12161 (1999).

[9] C. Brcchignac, P. Cahuzac, J. Leygnier, J. Weiner, J. Chem. Phys. **90**, 1492 (1989).

[10] U. Ray, M. F. Jarrold, J. E. Bower, J. S. Kraus, J. Chem. Phys. **91**, 2912 (1989).

[11] D. A. Hales, L. Lian, and P. B. Armentrout, Int. J. Mass Spectrom. Ion Process. **102**, 269 (1990).

[12] M. Schmidt, R. Kusche, B. von Issendorf, and H. Haberland, Nature (London) **393**, 238 (1998).

[13] C. M. Neal, A. K. Starace, and M. F. Jarrold, Phys. Rev. B **76**, 054113 (2007).

[14] C. Hock, C. Bartels, S. StraŸburg, M. Schmidt, H. Haberland, B. von Issendorff, and A. Aguado, Phys. Rev. Lett. 102, 043401 (2009).

[15] S. M. Ghazi, S. Zorriasatein, and D. G. Kanhere, J. Phys. Chem. A **113**, 2659 (2009).

[16] G. A. Breaux, B. Cao, and M. F. Jarrold, J. Phys. Chem. B **109**, 16575

(2005).

[17] C. M. Neal, A. K. Starace, M. F. Jarrold, K. Joshi, S. Krishnamurty, and D. G. Kanhere, J. Phys. Chem. C **111**, 17788 (2007).

[18] E. G. Noya, J. P. K. Doye, D. J. Wales, and A. Aguado, Eur. Phys. J. D **43**, 57 (2007).

[19] K. Joshi, S. Krishnamurty, and D. G. Kanhere, Phys. Rev. Lett. **96**, 135703 (2006).

[20] K. Manninen, A. Rytknen, and M. Manninen, Eur. Phys. J. D **29**, 39 (2004).

[21] S. Chacko, K. Joshi, and D. G. Kanhere, Phys. Rev. Lett. **92**, 135506 (2004).

[22] (a) G. A. Breaux, C. M. Neal, B. Cao, M. F. Jarrold, Phys. Lett. **94**, 173401 (2005). (b) C. M. Neal, A. K. Starace, M. F. Jarrold, J. Am. Soc. Mass Spectrum. **18**, 74 (2007).

[23] (a) M. Costantino, C. Fipro, J. Mater. Res. **6,** 2397 (1977). (b) V. V. Zakorzhevskii, I. P. Borovinskaya, N. V. Sachkova, Inorg. **38**, 1131 (2002).

[24] O. Mayer, E. Z. Fromm, Mettallkunde **68**, 27 (1977).

[25] Z. Romanowski, S. Krukowski, I. Grzegory, S. Porowski, J. Chem. Phys. **114**, 6353 (2001).

[26] G. Kresse, J. Hafner, J. *Phys. Rev. B* **48**, 13115 (1993).

[27] G. Kresse, J. Furthermuller, Comput. Mater. Sci. **6**, 15 (1996).

[28] W. Kohn and L. J. Sham, Phys. Rev. **140**, 1133 (1965).

[29] D. Vanderbilt, Phys. ReV. B **41**, 7892 (1990).

[30] J. P. Perdew, Y. Wang, Phys. ReV. B **45**, 13244, (1992).

[31] M. C. Payne, M. P. Teter, D. C. Allan, T. A. Arias, J. D. Joannopoulos. Rev. Mod. Phys. **64**, 1045 (1992).

[32] P. Pulay, Chem. Phys. Lett. **73**, 393, (1980).

[33] B. Silvi, A. Savin, Nature (London) **371**, 683, (1994).

[34] R. G. Parr and W. Yang, J. Am. Chem. Soc. **106,** 4049 (1984).

[35] W. Yang and R. G. Parr, Proc. Natl. Acad. Sci. USA **82,** 6723 (1985).

[36] (a) W. Yang and W. Mortier, J. Am. Chem. Soc. **108**, 5708 (1986). (b) M. W. Schmidt, K. K. Baldrige, J. A. Boatz, S. T. Elbert, M. S. Gordon, J. H. Jensen, S. Koseki, N. Matsunga, K. A. Nguyen, S. Su, T. L. Windus, M. Dupuis and

J. A. Montgometry J. Comput. Chem. **14,** 1347 (1993).

[37] P. Chandrachud, K. Joshi. D. G. Kanhere, Phys. Rev. B, **76**, 235423 (2007).

[38] S. Nóse, Mol. Phys. **52**, 255 (1984).

[39] A. Bogicevic, P. Hyldgaard, G. Wahnstrom, B. I. Lumdqvist, Phys. Rev. Lett. **81**, 172 (1998).

[40] J. Akola, H. Hakkinen, M. Manninen, Phys. Rev. B **58**, 3601 (1998).

[41] A. I. Boldyrev, P. v. R. Schleyer, J. Am. Chem. Soc. **113**, 9045 (1991).

[42] R. O. Jones, J. Chem. Phys. **99**, 1194 (1993).

[43] B. K. Rao, P. Jena, J. Chem. Phys. **111**, 1890 (1999).

[44] Z.J. Li, J.H. Li, Solid state communications,**149**, 375 (2009).

[45] J. Moc, The European Physical Journal, D, **45**, 247 (2007).

[46] C. H. Yao, S. F. Zhao, J. R. Li, Y. W. Mu, J. G. Wan, M. Han and G. H. Wang, Eur. Phys. J. D., **57**, 197 (2010).

[47] A. C. Reber, S. N. Khanna, P. J. Roach. W. H. Woodward and A. W. Castleman. Jr. J. Am. Chem. Soc. **129**, 16098 (2007).

[48] R. O. Jones, Phys. Rev. Lett. **67**, 224 (1991).

[49] H. Basch, Chem. Phys. Lett. **136**, 289 (1987).

[50] U. Rothlisberger, W. Andreoni, P. Giannozzi, J. Chem. Phys. **96**, 1248 (1992).

[51] Theory of Orientation and Stereo Selection by K. Fukui (Springer-Verlag, Berlin 1975).

[52] W. Zhang, W-C. Lu, J. Sun, C. Z. Wang, K. M. Ho, Chem. Phys. Lett. **455**, 232 (2008).

[53] N. Drebov, R. Alrichs, J. Chem. Phys. 132, 164703 (2010).

CHAPTER 7

Thermodynamic study describing chemisorption of N_2

Abstract:

In this chapter, we address the dynamic interactions of N_2 with Al_{13} clusters at Room Temperature (RT). For this study, we obtain the high energy conformation (melted structures) of Al_{13} cluster from the high temperature simulations. The phase transition of the Al_{13} clusters among three distinct temperatures is verified using MSD and RMS-BLF descriptors. Similarly, we address the phase transition of Al_{100} cluster over three different temperatures. The results clearly show that the melted structure forms Al_n--N_2 cluster with more ease compared to non-melted structure. In addition, finite temperature simulation suggests the multiple Al-N bond formation which is not clearly seen from static calculations [chapter 6]. For understanding the interaction strength of N_2, this outcome is supported with various structural properties such as average bond lengths and average interaction energies.

7.1 Introduction and methodology

0 K calculations bring in considerable insight [chapter 6 (conclusion)] but it is important to remember that following the melting of aluminum clusters, the chemical reaction between Al cluster and N_2 occurs at the room temperature. For the sake of understanding the importance of thermodynamic factors playing role in the reactivity of the Al clusters we study these systems using dynamical

methods in the current chapter. Here, we briefly revise the original experimental conditions and set up used by Jarrold *et. al.*

Recently, Jarrold *et. al.* [chapter 6] mentions the chemical adsorption of N_2 on a melted hundred atom Al cluster. They performed heat capacity measurements for Al^+_{100} to determine its melting and used ion beam experiments to investigate the reaction between the cluster and molecular N_2. Briefly, aluminum nanoclusters are prepared by pulsed laser vaporization and then carried into a temperature variable extension where their temperature is set by collision with buffer gas. To investigate the reactivity of Al^+_{100} cluster as function of temperature, the high pressure collision cell is replaced by a low pressure reaction cell and N_2 is admitted to a pressure of < 1mTorr. The reaction cell and N_2 are at room temperature (300 K). They show for clusters obtained after the melting transition, the activation barrier for N_2 adsorption decreases nearly by 1 eV. The earlier studies proposed that melting decreases the surface energy; the atoms in the cluster are thus better able to adjust to the incoming N_2 molecule thereby lowering the activation barrier. In chapter 6, we determined the size sensitivity of these clusters towards the reactivity and the influence of melting on the reactivity. We have also calculated the activation barriers for the melted and non-melted Al_{13} clusters and conclude that it decreases by ~0.85 eV. Thus, considering the promising results presented in the previous chapter, in this chapter we would like to gain an insight on the dynamical behavior of Al cluster-N_2 complexes.

We have considered the Al clusters of two sizes 13 and 100 atoms. First we will focus on the 13 atoms cluster. We have carried out a constant-temperature dynamics of around 10 ps at temperatures of 200 K, 1200 K and 1600 K of bare Al clusters. We ensure the complete melting of Al clusters at 1600 K using the RMS-BLF and the MSD. From this trajectory, the few melted structures of Al_{13} clusters (conformations that are quite away from the initial icosahedra geometry) are further selected for the studying the Al_n--N_2 dynamics at 300 K (i.e. RT). To save the phase space during simulation, we consider three different modes of N_2 adsorption: vertical, inclined (H3) and embedded (H4). The H3 and H4 conformers are shown in Figure 7.1. Thermodynamic simulations are performed by using Born-Oppenheimer MD based on the Kohn-Sham formulation of Density Functional Theory (DFT). The ionic phase space of the clusters is sampled by using an isokinetic velocity scaling algorithm. The MD simulations have been

carried out by using Vanderbilt's ultra-soft pseudopotentials within the Local Density Approximation (LDA) for describing the core valance interactions as implemented in the VASP package. An energy cutoff of 400 eV is used for the plane wave expansion of Al an N atoms. We have used cubic super cells of length 25 Å and have ensured that the results converge with respect to a further increase in the energy cutoff and size of the simulation box.

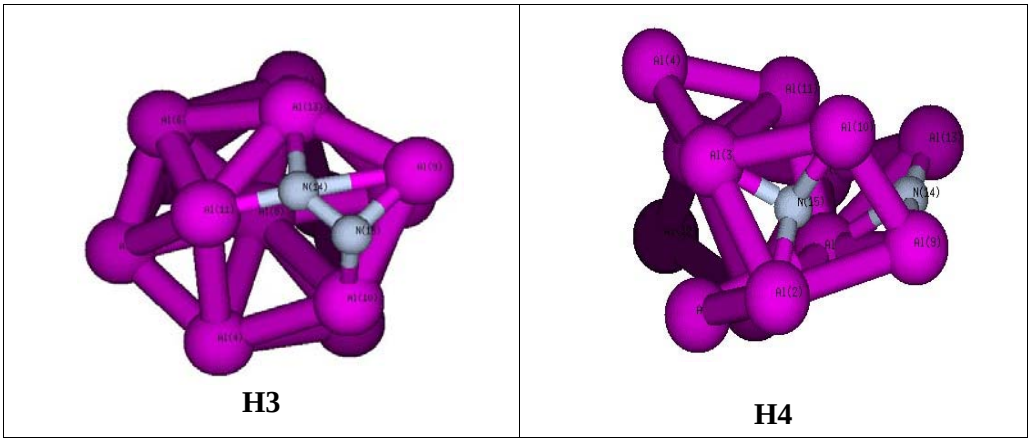

H3 **H4**

Figure 7.1: Two modes of N_2 interactions

Following the finite temperature study, various other thermodynamic indicators such as MSD and RMS-BLF as well as structural properties such as average bond lengths and average interaction energies are calculated for understanding the interaction strength of N_2. For further technical details concerning the extraction of thermodynamic averages and structural indicators one can refer to chapter 2.

7.2 Results and Discussion

A) Ionic motion of Al clusters: We first present the finite temperature behavior of the Al_{13} clusters. We begin with a discussion on the calculated MSD curves, Figure 7.2, and RMS-BLF values. It is possible to make a detailed analysis of the ionic motions by examining the trajectories of the cluster. An analysis of the ionic motions of Al_{13} cluster reveals that the atoms in cluster vibra

te around its ground state geometry (Ih) at 200 K (figure not shown). Around 1200 K, the cluster undergoes a peculiar structural arrangement so as to visit its several isomers. At this temperature, we found that the structure remains Ih around 20%

of simulation time. The other structures seen are D_h and few structures of intermediate geometry between Ih and Dh. This deviations of the structure can be clearly seen from the MSD plot at 1200 K, where MSD of the atoms is twice the largest inter atomic distance (5.31 angs) of the ground state geometry (see Figure 7.2). Further prominent melting of Al_{13} cluster is seen at higher temperature of 1600 K leading to a clear and relatively narrow melting transition. The RMS-BLF descriptor for Al_{13} comes out to be 0.34, 0.35 and 0.36 at 200 K, 1200 K and 1600 K, respectively. The increasing values of RMS-BLF descriptors support the MSD results.

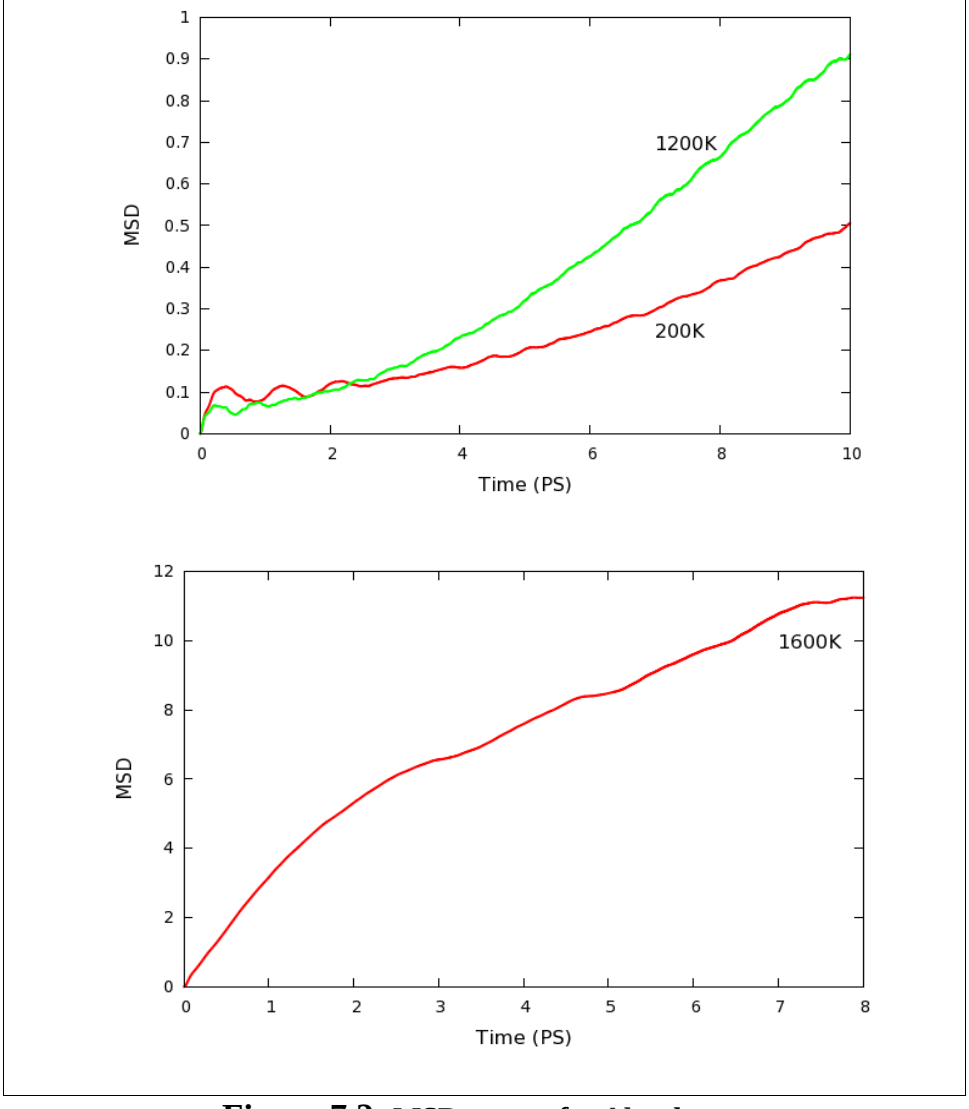

Figure 7.2: MSD curves for Al_{13} cluster

Similarly, the melting or phase transition of Al_{100} cluster is studied with MSD and RMS-BLF. The MSD curves of Al_{100} cluster are shown in the Figure 7.3. Considering the relatively large size of this cluster we reduce the simulation time, however, this does not affect the qualitative outcome. Around 300 K, only surface atoms move in their closed vicinity, withal, the core atoms

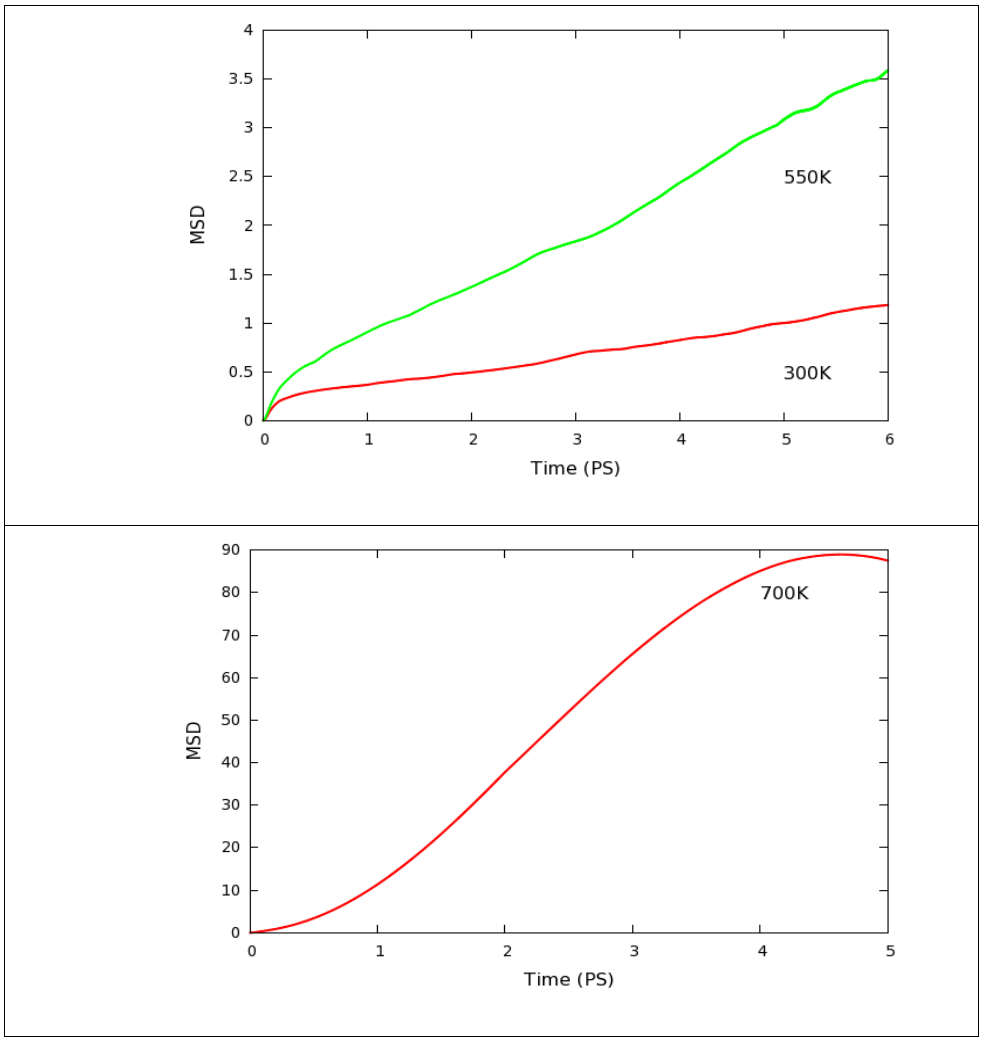

Figure 7.3: MSD curves for Al_{100} cluster

are at their original positions. Between, 550 K and 700 K, we see a continuous displacement of atoms over all the surface of cluster. Although, the cluster melts completely at 550 K with an MSD value of ~3.5, around 700 K spherical shape of the cluster is destroyed to such an extent that the atoms from core move drastically to surface and vice a verse. This leads to a unexpected hike in MSD value of ~90 at 700 K. The RMS-BLF descriptor also increases gradually with respect to

temperature of the cluster. These values are $5.6*10^{-2}$, $8.39*10^{-2}$ and 0.11 at 300 K, 550 K and 700 K, respectively. The phase transitions or the melting of both the Al cluster is in agreement with the recent experiment and theoretical predictions [chapter 6].

B) Molecular dynamic simulation of Al_{13}--N_2 complexes at RT: To model the experimental conditions, we carried out a RT simulation of Al_{13} clusters and N_2 molecule. The bare Al_{13} cluster is taken from the 1600 K simulation after examining its symmetry. It has almost same number of reactive sites as that of the number of atoms in the cluster. This ensures that the chosen Al_{13} cluster is highly melted conformer. To save the phase space of simulation, we consider three different modes of N_2 interaction on the Al_{13} cluster. The first mode considers the vertical approach of N_2 molecule at one of the open edge of cluster. However, this model failed to converged and both molecules got dissociated along the trajectory. In the second mode of interaction, N_2 approaches little inclined towards the core (H3) of the cluster. In the third mode (H4), N_2 molecule is protruding inside the cluster (nearly embedded) (see figure 7.1). The last two models could survive without N_2 dissociating from the Al_{13} cluster for the considerable time of simulation. We study the geometric parameters such as the characteristic bond length variations, particularly N-N bond elongations, Al-N bond formations and the Al-Al bond fluctuations of the H3--N_2 and H4--N_2 simulations. In addition, we also calculate the average interaction energy over the entire simulation time. The atoms in both complexes, viz., H3--N_2 and H4--N_2, show moderate vibrations at RT. The characteristic bond length fluctuations for H3 and H4 are plotted in the Figure 7.4 as a function of time. These values are averaged as a function of time.

In H3 complex, the N-N bond elongates from 1.13 Å to 1.40 Å. Here, although the N-N bond shows substantial elongation, it remains intact throughout the simulation time. Both the N atoms, N14 and N15, participate in the Al-N bond formation during the complex shaping (see Figure 7.1 and 7.4). The N14 atom is bonded to four neighboring Al atoms, namely, Al(9), Al(10), Al(11) and Al(13), on the contrary, N15 atom is bonded to only two neighboring Al atoms, Al(9) and Al(10). Thus, the H3 complex shows the multiple Al-N bond character with the bond length range 1.85 Å to 2.45 Å. In H3, interacting Al atoms show elongation of bonds with adjacent Al atoms in the range 2.75-2.95 Å compared to the normal Al-Al bonds observed in the bare cluster.

In H4 complex, the N-N bond elongates from 1.13 Å to 3.00 Å. The N-N bond elongation to such an extent suggests the N-N bond breaking during this simulation. Like the H3 complex, here both the N atoms, N14 and N15, participate in the Al-N bond formation during the complex shaping (see Figure 7.1 and 7.4). However, unlike the previous complex, both N atoms in H4 are bonded to four neighboring Al atoms. N(14) is bonded to Al(9), Al(10), Al(1) and Al(13). N(15) atom is bonded to Al(2), Al(3), Al(10) and Al(11). Thus, the H4 complex also shows the multiple Al-N bond character where the bond length ranges from 1.90 Å to 2.30 Å. In H4, interacting Al atoms do not show elongation of bonds with adjacent Al atoms. They show normal Al-Al bond length of 2.55-2.75 Å.

To understand the strength of N_2 adsorption, we calculate the average interaction energy (IE) of both complexes. The IE of H3 is -1.49 eV and that of for H4 complex is -4.14 eV. Although interaction energy of H4 complex is higher than that of H3, the fact that N-N bond breaks with inter atomic distance of ~3.0 Å and Al-Al bonds corresponds to the normal range of bond distance (same as in bare Al_{13}) suggest that the H4 is no longer N_2 adsorbed Al_{13} cluster at the end of given simulation. Instead this can be considered as the nitrogen doped Al_{15} cluster. However, the high interaction energy of H3 complex obtained from finite temperature simulation supports the chemisorption of N_2 and easier tendency to form Al_n-- N_2 clusters starting from the N_2 adsorption on melted Al clusters at room temperature.

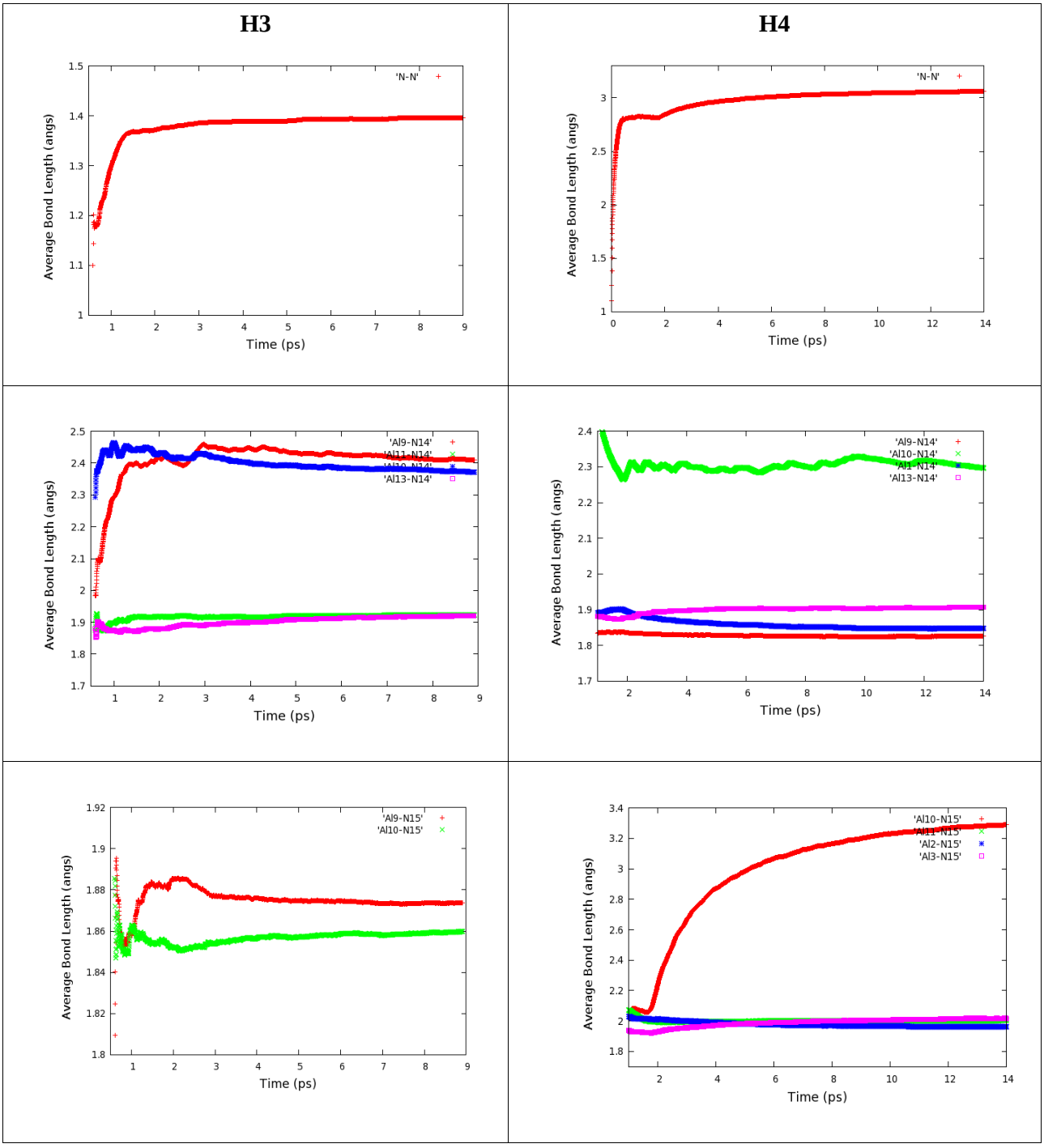

Figure 4: Characteristic Bond Length Fluctuations

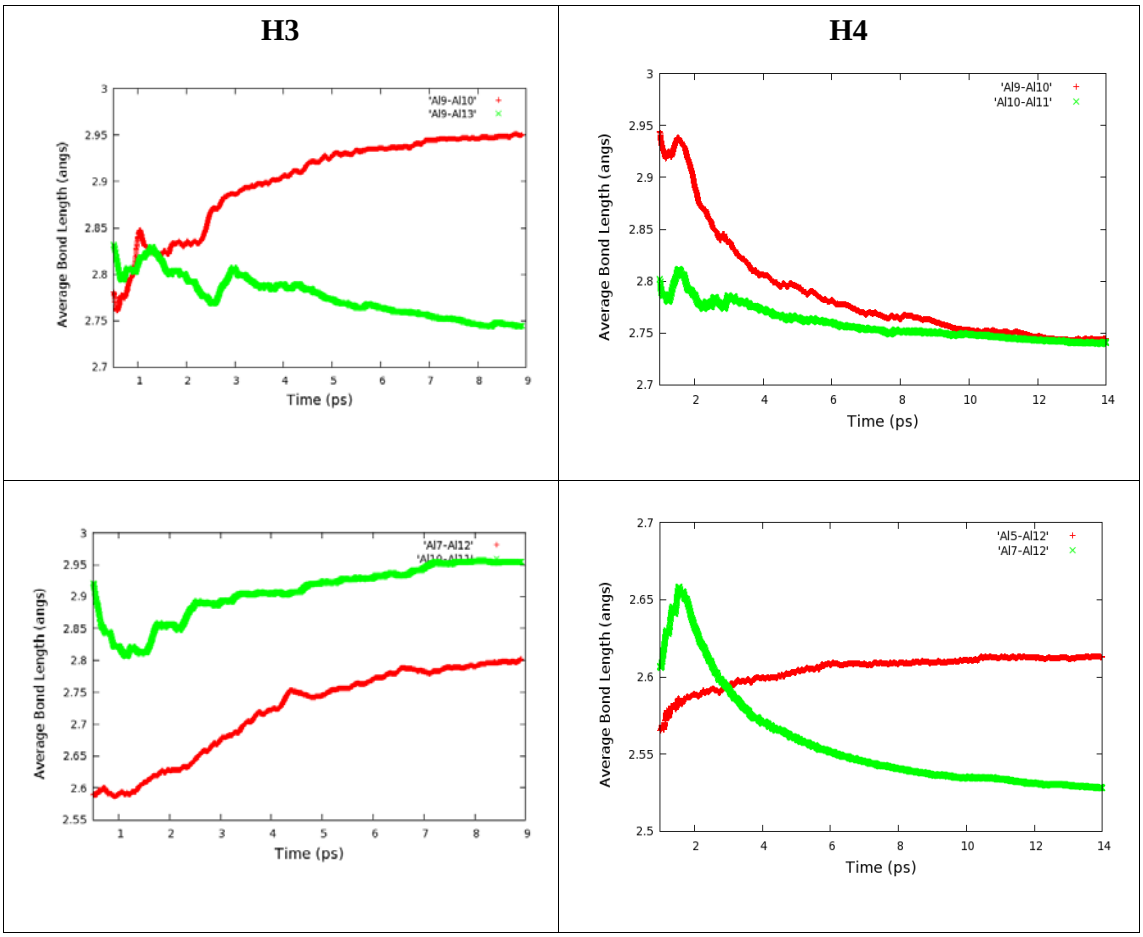

Figure 4: Characteristic Bond Length Fluctuations

7.3 Conclusion and Scope

To discuss the practical feasibility, the adsorption of nitrogen on Al_{13} clusters has been investigated using the BOMD approach. The dynamics of bare Al_{13} clusters is carried out at 200 K, 1200 K and 1600 K. We illustrate the complete melting of Al_{13} cluster around 1600 K using MSD and RMS-BLF descriptors. The few melted structures of Al_{13} clusters are further selected for studying the dynamical behavior of the Al_n--N_2 complex. The interactions of the N_2 and these clusters are thus examined at RT (300 K) using BOMD method for calculating various electronic properties. We optimized the three modes of N_2 adsorption: vertical, inclined (H3) and embedded (H4). The vertical N_2 adsorption model failed to optimize and finally dissociates. However, N-N bond remains intact during the simulation of H3--N_2 complex with a slight elongation of N-N bond to 1.40 Å, whereas, H4--N_2 complex turns out to be an Al-N cluster as N-N bond elongates to 3.0 Å. The average of Al-N bonds in H3 comes out to be around 2.40 Å. The average Al-N bonds in H4 reduce to ~1.90 Å. In addition, we also report the average Interaction Energies (IE) of these complexes. For the case of H3--N_2, IE comes out to be -1.49 eV, while average IE in H4--N_2 is - 4.14 eV. Both these values are considerably higher than the interaction energy values obtained over the ground state conformation in the earlier chapter. Thus, the finite temperature simulations for N_2 adsorption concludes that the melted structure (H3) with high interaction energy proves chemisorption of N_2 where as H4 can be consider as nitrogen doped 15 atoms Al cluster. The finite temperature studies also bring out multiple Al-N bonding. The high interaction energy of N_2 on Al_{13} clusters suggest the further investigation of Al_{100} clusters and chemisorption of N_2 on it.